Systematic Design of Particle Dampers for Passive Vibration Attenuation

Vom Promotionsausschuss der

Technischen Universität Hamburg

zur Erlangung des akademischen Grades

Doktor-Ingenieur (Dr.-Ing.)

genehmigte Dissertation

von
Niklas Joachim Meyer

aus
Hamburg

2023

1. Gutachter: Prof. Dr.-Ing. Robert Seifried
2. Gutachter: Prof. Dr.-Ing. habil. Alexander Düster

Tag der mündlichen Prüfung: 05. 05. 2023

MuM Notes in Mechanics and Dynamics

Editor: Prof. Dr.-Ing. Robert Seifried
Hamburg University of Technology
Institute of Mechanics and Ocean Engineering (MuM)
www.tuhh.de/mum

Volume 8
Niklas Joachim Meyer
“Systematic Design of Particle Dampers for Passive Vibration Attenuation”
Hamburg, 2023

DOI: https://doi.org/10.15480/882.5112
ORCID: https://orcid.org/0000-0001-9720-2693

Acknowledgments

The content of this document was created during my work at the Institute of Mechanics and Ocean Engineering (MuM) at the Hamburg University of Technology from 2017 to 2022. I had an amazing time at the MuM, with a lot of interesting discussions, a Corona pandemic, many months of working from home in my "Homeoffice", barbecues, mulled wine parties, workshops, conferences, student theses, and so much more ...
In fact, the content of this work was created during my time at the MuM, however, it is based on my whole life journey and it would be audacious not to name all the people who contributed to it. As everyone listed here plays an important role, not only due to their technical competence but often in a completely different fashion, I decided to address them in chronological order.

Hence, I would like to start and thank probably the most important people, my parents *Etu* and *Jo*. Without exaggeration, they made me the person who I am today. They have been part of my journey from the very beginning and continue to be an important part of my life by supporting me wherever possible. In contrast to people who only read this finished work, they have not only seen my positive but also negative moments whenever I struggled, but they still kept believing in me. Although this work is not written by them directly, between the lines you will find their handwriting.

Next, I would like to thank my brothers *Janick* and *Bennet*. You are part of this journey from (almost) the beginning and have seen my positive and negative moments as well. You have not only taught me to gain the upper hand against two brothers but also transfer these skills to real life. Likewise, I always had a person who could help me clear my head. Especially, our common training units in sports or one, two glasses of beer at the bar, were and still are awesome.

At this point, I would also like to thank all of my friends for being there and always having an open ear for me. Even though it is impossible to name them all, I would like to name *Jasmin*, *Monta* and *Sandra* for their mental support and grammar checking work during my whole time at the university.

It might seem uncommon, but I also would like to name the great dogs of my family, *Lotte* and *Nea*. We have taken so many walks together that not only helped me to relax but also come up with great new ideas for problems that

seemed unsolvable at the time.

Next, I would like to thank all of my students and colleagues for our wonderful time at the MuM. At first, *Eugen* who motivated me to become part of the MuM Ph.D. students. In addition, *der Zauberer (Merlin)*, who not only assisted my project and Master's theses but also taught me a lot about the work of a Ph.D. student. I should also name *Nathalie*, *Timo*, *Hollm (Marten)*, *Ali*, *Malte*, *Tobias* and *Svenja* who were always up for discussions about either technical or non-technical topics and free time activities. Many thanks go out to *Jana* for her awesome spelling correction of this work. However, the most important colleague to mention is *Mr. Dücki (Daniel)*, my office-mate in room *0517*. We had so many discussions, talks, barbecue events, drinks and further activities – I cannot even name all of them. It truly was an awesome time together.

Another very important group of people should not stay unnamed, our technical assistants *Wolfgang*, *Riza*, *Norbi (Norbert)* and senior engineer *MAP (Marc-André)*. They helped me whenever there were any technical difficulties in the lab. This ranged from the realization of experimental ideas or general technical support to last-minute repairs. It is not an overstatement to say, that this work would have been a different one without them.

I would also like to thank *Prof. Dr.-Ing. habil. Düster* for acting as my second advisor of this work and *Prof. Dr. Hoffmann* for supervising the doctoral defense.

Last but not least, I would like to thank the person on whose idea this whole project is based and who gave me the freedom to do what it did, the head of our institute *Robert (Prof. Dr.-Ing. Robert Seifried)*. Dear Robert, your expertise, your helpfulness and our fruitful discussions were great support during my time working with you. Your continuous support and excellent counsel are a major contribution not only to this work but also to many joint papers. For this and the awesome time I had at the MuM, I am very grateful.

Finally, this preface shall end with a quote from my office-mate *Mr. Dücki (Daniel)*, who always used to rib me due to my noisy experiments, which I choose not to comment on: "*Niklas, auch deine Kollegen bekommen es hin – ohne viel Lärm zu machen – nichts zu tun.*" (Niklas, your colleagues are also managing to accomplish nothing, without making so much noise.)

Enjoy reading!

Niklas Joachim Meyer

Hamburg, May 2023

To my family,
who always inspired me to stay focused and persistent.

Shaken, not stirred.

Abstract

Particle damping technology is a passive damping technique used to reduce structural vibrations. Either containers attached to the vibrating structure or cavities within the vibrating structure are filled with granular material. Through structural vibrations, momentum is transferred to the granular material causing granular interactions. Because of these interactions, energy dissipation occurs due to inelastic collisions and frictional losses. Thus, structural vibrations are reduced.

Although particle dampers have already been applied to some technical systems, their industrial application is still limited. The main reason for this is the nonlinear damping behavior of this technique and the multitude of influence parameters. Hence, the goal of this work is the development of a new design methodology in the form of a toolchain enabling a systematic damper design. To this end, various numerical models and experimental tests are combined. The toolchain commences with investigations of the micro-mechanical behavior of single particle impacts. It continues with analyzing the properties of vibrating granular matter inside sinusoidally driven containers and concludes with the design of a particle damper for a desired structure. The good agreement of the experimental and numerical models as well as their efficiency for the damper design and dimensioning are demonstrated for multiple examples.

Furthermore, with the use of the developed toolchain, single particle damper units with predefined characteristics are developed for non-specific applications. To this end, hybrid approaches, among others, are used to increase the efficiency of the individual particle dampers. In this way, it is possible to extend the use of particle dampers to a variety of vastly different applications.

Contents

List of Figures

List of Tables

Abbreviations and Symbols

In the following, the most important abbreviations and symbols are defined.

Abbreviations

CaC	collect-and-collide
COR	coefficient of restitution
DEM	discrete element method
FEM	finite element method
FFT	fast Fourier transform
FRF	frequency response function
LV	laser vibrometer
MuM	Institute of Mechanics and Ocean Engineering
ODE	ordinary differential equation
PD	particle damper
PVC	polyvinyl chloride
TUHH	Hamburg University of Technology

Scalars

i	imaginary unit
d	damping coefficient, distance
f	frequency
g	gravitational constant
h	clearance
k	stiffness
ℓ	length
m	mass
n	number
q	elastic coordinate
r	(particle) radius
t	time
v	velocity
x, y, z	cartesian coordinate system
A	acceleration amplitude
E	Young's modulus, energy
F	(contact) force
I	moment of inertia
L	container length
M	mass
P	power
R	radius
V	velocity amplitude
X	stroke amplitude
α	angle
δ	overlap
ϵ	error
ε	coefficient of restitution
η	loss factor
κ	scaling factor
μ	friction coefficient
ν	Poisson's ratio
ρ	density
σ	stress
τ	tolerance
ω	eigenfrequency
Δ	difference
Δt	time step size
Γ	excitation intensity
Ω	angular frequency

Vectors

$\boldsymbol{f}$	force vector
$\boldsymbol{\ell}$	torque vector
$\boldsymbol{n}$	normal direction
$\boldsymbol{q}$	elastic coordinates
$\boldsymbol{r}$	position vector
$\boldsymbol{t}$	tangential direction
$\boldsymbol{v}$	velocity vector
$\boldsymbol{x}$	(particles' translational) state vector
$\boldsymbol{z}$	nodal displacements
$\boldsymbol{\phi}$	mass normalized eigenvector
$\boldsymbol{\lambda}$	direction vector
$\boldsymbol{\omega}$	particles' angular state vector

Matrices

$\boldsymbol{D}$	damping matrix
$\boldsymbol{E}$	identity matrix
$\boldsymbol{I}$	inertia tensor
$\boldsymbol{K}$	stiffness matrix
$\boldsymbol{M}$	mass matrix
$\boldsymbol{S}$	rotation matrix
$\boldsymbol{\Phi}$	projection matrix
$\boldsymbol{\Omega}$	matrix of squared eigenfrequencies

Indices

0	initial
bed	particle bed
bou	bouncing
c	container
cp	container–particle
d	desired
dis	dissipation
eff	effective
ex	excitation
kin	kinetic
n	normal
max	maximum
min	minimum
opt	optimal
p	particle
pd	particle damper
rb	rigid body
rol	rolling
t	tangential
Ω	driving frequency
i	first contact partner
j	second contact partner
k	shape function index

Points and Sets

B	boundary point
O	origin of coordinate system
P	particle's center point
$\mathcal{J}$	contact partners
$\mathcal{P}$	all particles

Operators and Other Symbols

$\bullet$	scalar product
$\times$	cross product
$()^\top$	transpose
$\overline{()}$	conjugate
$\lvert() \rvert$	absolute value
$\lvert\lvert() \rvert\rvert_2$	euclidean norm
$\bar{()}$	effective value
$()^*$	complex amplitude

Introduction

Structural vibrations play a vital role in machines, buildings and processes. Very often, the emergence of these vibrations can not be prohibited, like a wind excited bridge or a car driving over a gravel road. Hence, these often undesired vibrations eventually lead to a higher noise emission, reduced comfort, reduced manufacturing precision, increased wear or even cause structural failure. In addition, nowadays, lightweight designs are becoming more and more important to reduce energy consumption and natural resources. These lightweight structures are even more prone to structural vibrations. Hence, in the last decades, a lot of effort has been investigated in structural control approaches to increase the vibration attenuation of such structures. These approaches can be separated into active control, passive control and semi-active control.
For active control, an actuator, a controller and sensors are needed. Often, a large power supply is necessary, making this control strategy costly in operation. Also, sensor failure or dynamic instabilities can be critical. For passive control strategies no external energy, actuators or sensors are necessary, making them in general much more robust and cost-efficient. Semi-active control is a hybrid version of active and passive control strategies. These are passive devices with some controllable properties, e. g. an air suspension where the air pressure is controlled to adjust the suspension's stiffness.

Due to the mentioned benefits, passive control is widely applied for structural vibration reduction. Passive control devices can be grouped into: metallic dampers, friction dampers, visco-elastic dampers, viscous dampers, particle dampers, tuned mass dampers, tuned liquid dampers and seismic isolation [SoongCostantinou94]. *Particle dampers* (PD), see Fig. 1.1, also referred to as *particle impact dampers* or *granular dampers*, are such a passive damping technology. Either containers attached to the vibrating structure or holes within the vibrating structure are filled with a granular material of various shape. Various different particle materials like steel, tungsten, carbide, polymers and many more can be used. The particle size normally ranges from the micrometer to the millimeter scale. Thus, a single particle damper can contain particles in the range of several dozens up to millions. Through structural vibrations, momentum is transferred to the granular material causing granular movement. Due to particle–particle and particle–wall interactions *energy dissipation* occurs by inelastic impacts and frictional effects. This energy dissipation reduces the

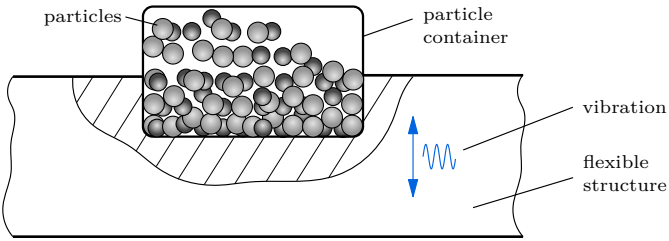

Figure 1.1: Schematic representation of a particle damper.

structural vibration. Therefore, particle damping technology belongs to the group of auxiliary-mass type vibration dampers [LuEtAl17].

Compared to other damping techniques, particle dampers show numerous advantages due to their conceptual simplicity and passive nature. They are cost-efficient devices, do not need an anchor point and do not degrade over time [Johnson95]. These properties make them attractive for long-lasting systems requiring high durability or where maintenance is not or only barely possible. Using appropriate particles, e. g. steel or tungsten, particle dampers can even operate in extreme environmental conditions [Panossian02, Simonian95, LuEtAl17]. This includes extreme temperatures, like in spacecraft applications [Panossian92, MooreEtAl95]. Furthermore, this includes operation under extreme pressure conditions [BannermanEtAl11, SackEtAl13] or for oil and dust contaminated particle damper cavities [LuEtAl17]. Additionally, particle dampers only add little mass to the primary system [Johnson95], causing no significant change in its mass and stiffness [Saeki02]. It is also reported that particle dampers can work in multiple directions [MichonEtAl13] or rather have a low sensitivity to excitation directions other than the principal one [WangEtAl15]. They can be applied to a wide frequency range [ChenEtAl01, SchönleEtAl22] and to deterministic, Gaussian, or random excitations [Ibrahim09].

Particle dampers have been successfully used in a few technical applications so far. They have been applied in spacecraft applications, like a space shuttle main engine liquid oxygen inlet tee [Panossian92], a spacecraft cantilever beam type appendage [Simonian04] or a spacecraft precision instrument [WangEtAl15]. They have also been utilized to damp a rotary printing equipment [SkiporBain80], an oscillatory saw [HeckelEtAl12], wind turbines [ChenGeorgakis13] and power transmission towers [TianGai15]. Furthermore, composite honeycomb structures [Panossian06] and a bond arm of electronic manufacturing equipment [ChanEtAl16] are being investigated. Other interesting application fields are high-rise buildings [LiDarby08, LuEtAl12, LuEtAl16].
Although particle dampers have already been applied to these technical applications, their wide industrial usage is still limited. Even today a general design guideline for the systematic development of particle dampers does not exist. The

main reason for this is the nonlinear damping behavior of this damping technique and the multitude of influence parameters, like particle material and shape, container geometry, excitation conditions, or filling ratio. These influencing factors strongly affect the particle motion, also called *state of matter* or *motion mode* (of the rheology behavior) [SaluenaEtAl98], which correlates in a non-trivial way with the damper's energy dissipation. These correlations are often only poorly comprehended, leading even nowadays to a trial and error-based design process of particle dampers, which is tedious and costly.

First analyses on particle dampers have been performed by different experimental tests and analytical studies, see e. g. [ArakiEtAl83]. Although, in this way the damping performance can be quantified, it is hard to gain insights into the complex processes inside the dampers, e. g. by visual observations. Hence, in the last ten years the *discrete element method* (DEM) [CundallStrack79] gained a lot of attention to obtain a better understanding of the mechanisms and motion modes inside particle dampers. Within the DEM, the particle dynamics are described by *Newton's and Euler's equation of motion* for every particle and are mainly influenced by particle contacts [Pöschel05, Matuttis14]. By time integration, the particle trajectories are obtained. This enables a deeper understanding of the influence parameters affecting the damper's energy dissipation. Hence, DEM simulations are a crucial tool for a systematic particle damper design process and are continuously used throughout this work.

1.1 Historical Development

The first particle damper can be traced back to [Paget37]. Paget proposed a single particle to damp the vibration attenuation of a turbine blade. Nowadays, this kind of damper is called *impact damper*. As the damper's whole mass is concentrated in one body, i. e. the particle, high contact forces occur during impacts with the container walls. Later, [LieberJensen45] studied an impact damper consisting of a single particle moving between two container walls to reduce structural vibrations. This form of an impact damper evolved to the most common design. In the following decades, impact dampers have been intensively studied due to their conceptual simplicity and robust properties against harsh environmental conditions, see e. g. [Kuphal65, Yamada74].
In [Masri69] the *multi-unit impact damper* is invented. Masri replaced a (single-unit) impact damper with multiple impact dampers of equivalent total particle mass operating in parallel. He reported that the effectiveness of the multi-unit impact damper stays unaffected, but lower force peaks are achieved.

Particle dampers are a derivative of impact dampers. Instead of a single impacting body, many particles are used within a container. First analyses of particle dampers go back to [ArakiEtAl83] and [ArakiEtAl85]. They studied analytically and experimentally the damping of a *single-degree-of-freedom* (SDoF) system, i. e. a spring-damper-mass system, and found good damping properties of particle dampers. In contrast to (multi-unit) impact dampers, particle dampers lead to lower force peaks and a reduced sound transmission [LuEtAl17], but share the good properties of impact dampers, i. e. simple design and robust behavior against harsh environmental conditions. In 1992, the *non-obstructive particle damper* was proposed by [Panossian92], where particle dampers are placed at strategic locations on a structure to absorb the energy of different structural modes. Hereby, the structural shape is not modified, but existing cavities within the structure are used.

1.2 Particle Damper Types

Since the invention of the particle damper, various different variants have been developed. These variants can be classified into four major groups: *traditional particle damper, particle material and shape improved particle damper, configuration improved particle damper* and *damper combinations* [LuEtAl17]. Each group and each damper type has its specific attributes and benefits. A schematic overview of these types is given in Fig. 1.2. Most variants aim for an improvement of the particle damper's efficiency concerning the amount of energy dissipation, efficient vibration frequency range, or efficient vibration amplitude range. Besides that, impact force reduction and noise emission reduction are also considered. The different groups are discussed in the following.

Traditional Particle Dampers

Traditional particle dampers can be subdivided into impact dampers, multi-unit impact dampers and particle dampers as discussed in the previous Sect. 1.1. Some authors additionally use the category of multi-unit particle dampers. However, studying the attributes of particle dampers without an underlying structure, this category is rather meaningless, as no real attribute change in the particle damper's properties is achieved. This category becomes important when coupling multiple particle dampers to a structure and damping optimization is the goal.

Traditional

- impact damper
  [Paget37, LieberJensen45]

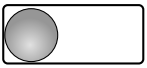

- multi-unit impact damper
  [Masri69]

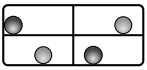

- particle damper
  [ArakiEtAl85, LuEtAl17]

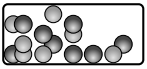

Particle Material and Shape Improved

- steel, ceramic, nickel, tungsten, lead, sand
  [Panossian92, MarhadiKinra05]
- polymers
  [DarabiRongong12, BustamanteEtAl16]
- shape and fragmentation
  [PourtavakoliEtAl16]
  [SanchezEtAl14]

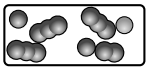

- soft hollow particles, fine particles,
  tangled metal wire particles, particle swarfs
  [MichonEtAl13, DuEtAl08]
  [TangEtAl15, AbbasEtAl14]

Configuration Improved

- container shape
  [WongEtAl09a]
  [FerreyraEtAl21]

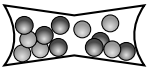

- spoliers & inner structures
  [YaoChen15, FerreyraEtAl21]
  [GnanasambandhamEtAl20]

- coated walls
  [LiDarby08, LuEtAl12]

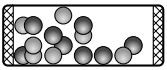

- liquid, honeycomb structures, vacuum-packed PD,
  linear particle chain, tuned rolling-ball, bean bag
  [GnanasambandhamEtAl19, BajkowskiEtAl15]
  [Panossian06, MichonEtAl13]
  [AhmadEtAl16, GharibKarkoub15]
  [ChenGeorgakis13, PopplewellSemercigil89]

Damper Combinations

- tuned impact/particle damper
  [SemercigilEtAl92]
  [YaoEtAl14, ZhangEtAl18]

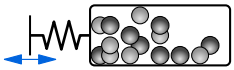

- piston-based PD
  [BaiEtAl09, ShahEtAl09]

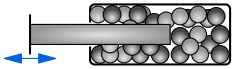

Figure 1.2: Overview of different particle damper types.

Particle Material and Shape Improved Particle Dampers

This kind of improvement is presumably the most obvious one. By changing either the particles' material or shape, the damper's properties are aimed to be improved. By [Panossian92] the effect of various materials, such as steel, ceramic, nickel and tungsten, were studied. It was found that the particle material has a great effect on the damping performance of particle dampers. Aside from metals, polymeric particle dampers are being investigated [DarabiRongong12, BustamanteEtAl16]. The effect of the particle shape is studied in [PourtavakoliEtAl16] using DEM simulations. Composite particles are being modeled using the multi-sphere method, i. e. rigidly connected spheres to form more complex particles. However, only a little effect of the particle shape on the efficiency of the damper is found [PourtavakoliEtAl16]. A similar numerical study on particle shape and particle fragmentation is performed by [SanchezEtAl14]. Using a sufficiently large number of particles, fragmentation is not affecting the efficiency of the damper. However, it is shown that the fusion of particles can reduce the efficiency of the damper. In [TerziogluEtAl20] the sphericity of particles is specifically analyzed. In contrast to [PourtavakoliEtAl16], a high sensitivity of the damper's efficiency is observed. Furthermore, special configurations are being investigated. This includes soft hollow particles [MichonEtAl13], particle swarfs [AbbasEtAl14] and tangled metal wire particles [TangEtAl15].

Configuration Improved Particle Dampers

In configuration improved particle dampers the structural configuration is changed, except for the particles' material and shape themselves. The most apparent change is using a different shape for the particle container. In this context, cuboidal and cylindrical container shapes are seen most commonly. Cylindrical shapes are also realized by drilled holes within a structure. In [JadhavAwasare16] a single container is divided into multiple cells and an improvement in the damping performance is found. In [WongEtAl09a] a significant effect of the container's geometry is demonstrated by presenting an extensive numerical study using various container prototypes. In [FerreyraEtAl21] a conical bottom inside a rectangular container is analyzed numerically. For this setting, only little influence on the damper's efficiency is found. Another design is presented by [YaoChen15]. They equipped the inside of the particle damper with loose spoilers to increase the damping performance at small vibration amplitudes. This approach is adopted by [GnanasambandhamEtAl20] to secured inner structures and by [FerreyraEtAl21] to secured obstacles. In all works, an improved damping performance at the studied frequency is obtained. In [LuEtAl12] and [LiDarby08] particle dampers with rubber coated container walls for applications in civil engineering are being investigated. These dampers show significantly lower force peaks caused by the particles and can increase the damping performance. Another interesting approach is presented by [GnanasambandhamEtAl19], where liquid-filled particle dampers are analyzed to damp low frequency vibrations. A

good damping performance is obtained as well.
Various additional configurations are under investigation. Honeycomb structures for example are addressed by multiple authors [Panossian06, MichonEtAl13, AhmadEtAl16]. A linear particle chain damper, i. e. a chain of alternating smaller and bigger particles, is proposed in [GharibKarkoub15]. Furthermore, a tuned rolling-ball damper using rolling particles in cylindrical containers for the suppression of wind turbine vibrations is presented in [ChenGeorgakis13]. By [BajkowskiEtAl15] a vacuum-packed particle damper for vibration reduction of a beam structure is used. Lastly, a bean bag damper is proposed in [PopplewellSemercigil89], whereby multiple particles are filled in an elastic bag.

Damper Combinations

For this type, the particle damping technology is combined with another damping technology. Hence, it is not solely a particle damper anymore, but rather a hybrid kind of damper. First of all, tuned impact dampers [SemercigilEtAl92] and tuned particle dampers [YaoEtAl14, ZhangEtAl18] should be mentioned. For these kinds of dampers, the mass of a classical tuned mass damper is replaced by an impact damper or a particle damper, respectively. It is found that these damper types are more efficient than particle dampers for low vibration amplitudes [YaoEtAl14].

In [BaiEtAl09, ShahEtAl09] a piston-based particle damper is presented. This type is similar to a classical viscous damper. Instead of a fluid, particles are filled in a cylindrical container. With the damper requiring an anchor point, the piston is mounted to the vibrating structure and can move within the particle bed. By this, good damping can be achieved. Even though comparisons to viscous dampers have not been performed, it is to be expected that piston-based particle dampers work more reliably in extreme temperature environments [BaiEtAl09, ShahEtAl09].

1.3 Analyses Methods

For the analyses of particle dampers, various different methods and techniques have been developed. Experimental tests as well as numerical studies using DEM simulations are performed. An overview of the most common techniques is given in Fig. 1.3. The analysis techniques can be separated into two major groups, i. e. *single damper* and *structural integrated damper*. Both groups can be supported by previously performed *single particle* analyses.

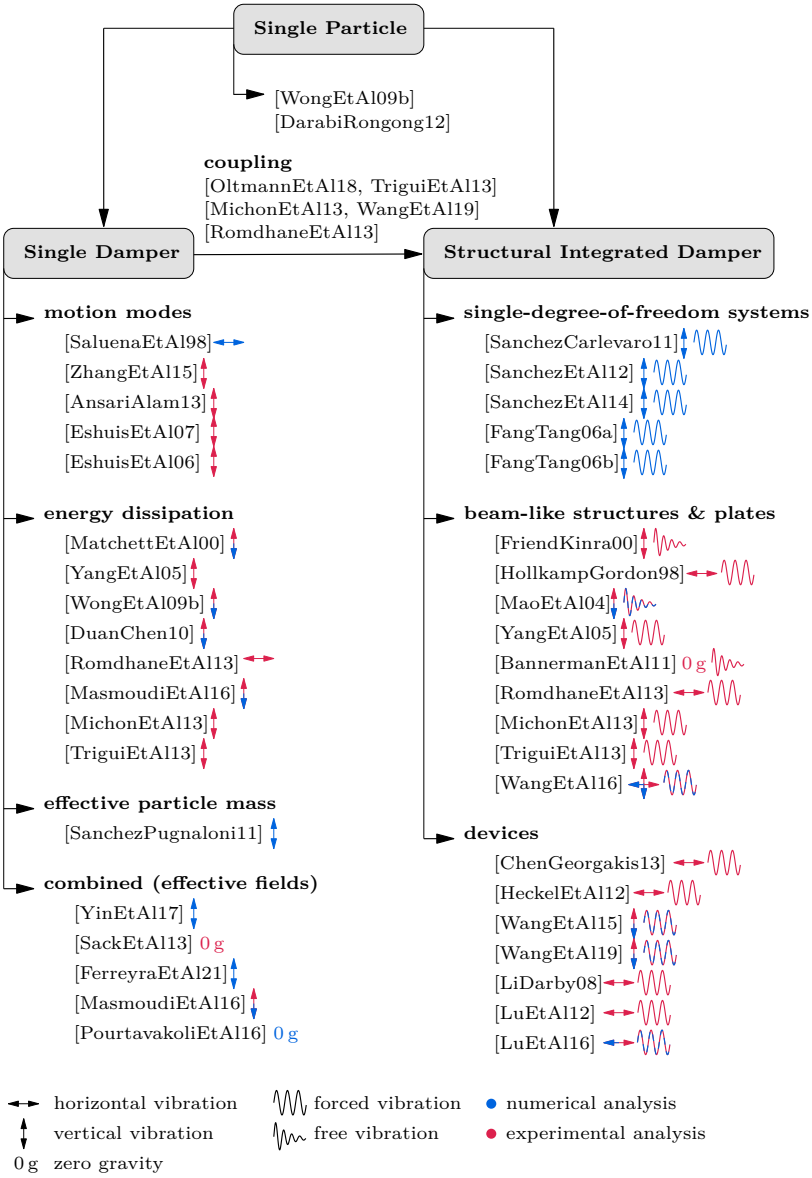

Figure 1.3: Overview of different analysis techniques for particle dampers.

Single Particle Analyses

Single particle analyses are only performed by a few authors dealing with particle dampers. On this level, the micro-mechanical behavior during an impact of two bodies of macroscopic size, i. e. particle–particle or particle–wall, is examined for different impact velocities obtained from experimental tests or numerical simulations. Thereby, the energy dissipation during the impacts is of major interest and can be calculated using the velocities of both collision partners before and after the impact. This kinetic energy loss is often described by the *coefficient of restitution* (COR), which can be used for DEM simulations within the single damper and structural integrated damper level. In addition, insights about noise transition, force peaks and damage during the impacts are obtained. Such analyses are performed by [WongEtAl09b] or [DarabiRongong12]. However, many authors apply a constant COR for their DEM simulations or use the COR as a tuning parameter to fit experiments and simulations, see e. g. [BannermanEtAl11].

Single Damper Analyses

For single damper analyses, the particle damper is studied without an underlying structure. Instead, the damper is subjected to a sinusoidal motion in either horizontal or vertical direction. Experimentally, controlled shaker setups or linear drives are prevalently used. Numerically, in DEM, the harmonic motion is applied perfectly to the particle container. In this way, *motion modes, energy dissipation* and *effective particle mass* inside the isolated damper are directly analyzed for a given excitation frequency range and amplitude range. Additionally, experimental or numerical parameter studies on different influence parameters can be performed, giving deeper insights into the nonlinear damping effects within the dampers.

An early work on motion modes of the granular matter is performed for vertical vibrations by [SaluenaEtAl98]. They determine numerically three different regimes for the conducted particle setting, namely the solid, convective, and gas-like motion modes. Based on experimental tests on vertical vibrations, [ZhangEtAl15] redefines this classification, introducing seven different motion modes, i. e. solid-like, local fluidization, global fluidization, convection, Leidenfrost effect, (bouncing) collect-and-collide and buoyancy convection. Further studies and detailed discussions on motion modes can be found in [EshuisEtAl06, EshuisEtAl07, AnsariAlam13].

Besides motion modes, the energy dissipation within the particle damper and the damper's efficiency can be investigated. By [YangEtAl05] the *complex power method* is introduced for this task. They experimentally analyzed a vertically shaken particle damper using different particle sizes and numbers. In [WongEtAl09b, DuanChen10] numerical and experimental studies are performed for vertically vibrating particle dampers and reasonable correlations between the numerical and experimental results are found. While [DuanChen10]

focuses on the *lost power*, in [WongEtAl09b] the *loss factor*, which is an efficiency factor, is additionally considered. Further studies for vertically excited dampers are presented in [MatchettEtAl00, WongEtAl09a, TriguiEtAl13, YaoChen15, BustamanteEtAl16]. Horizontal high frequency vibrations are studied in [RomdhaneEtAl13] using the loss factor. A more meaningful loss factor, namely the *effective loss factor*, is later introduced in [MasmoudiEtAl16] for numerical and experimental studies of a vertically vibrating particle damper.

Another important quantity is the *effective particle mass*. It describes how much the particle mass is influencing the driven container, i. e. to what degree the mass of the granular matter is coupled to the container's movement. Studies on this topic are presented in [SanchezPugnaloni11] and [MasmoudiEtAl16]. It is found that the effective particle mass varies mostly between zero and the mass of the particle bed. However, lower and higher values can also occur under special conditions [SanchezPugnaloni11].

Besides the stand-alone analyses of motion modes, energy dissipation and effective particle mass, combined analyses are performed as well. These combined results are also called *effective fields* throughout this work. By [YinEtAl17] numerical studies of vertically vibrating dampers are presented. They match the determined loss factor to the observed motion modes. [SackEtAl13] investigates the (bouncing) collect-and-collide motion mode experimentally under zero gravity, i. e. during parabolic flights, and low excitation frequencies. Different parameters affecting the efficiency of the damper are determined. A simple formula for an optimized damper under the condition of weightlessness is derived solely based on the gap clearance, i. e. the distance between the particle bed and opposite container wall. Further studies dealing with effective fields are presented for instance in [ZhangEtAl17] and [FerreyraEtAl21].

In Fig. 1.4 an overview of the various excitation ranges addressed by different authors is given. A lot of analyses have been performed within an excitation frequency range of $f = 10\,\mathrm{Hz} - 100\,\mathrm{Hz}$ and acceleration amplitudes $A = 0\,{}^{\mathrm{m}}/_{\mathrm{s}^2} - 100\,{}^{\mathrm{m}}/_{\mathrm{s}^2}$. The analyses are performed numerically as well as experimentally. Combined numerical and experimental studies are also considered. Vertical excitations are examined more often than horizontal ones. For low excitation frequencies $f \ll 10\,\mathrm{Hz}$ only little research is done and so far mostly for zero gravity environments [SackEtAl13, PourtavakoliEtAl16]. At high excitation frequencies $f \gg 100\,\mathrm{Hz}$ only few investigations have been conducted as well.

Structural Integrated Damper Analyses

The second possibility to analyze particle dampers is to couple them to an underlying structure. This structure can then be excited to exhibit either a free or forced vibration. By measuring the structural damping, conclusions on the particle damper's efficiency can be made. Furthermore, the influence of the damper on the system's eigenfrequencies, due to the effective particle mass, can

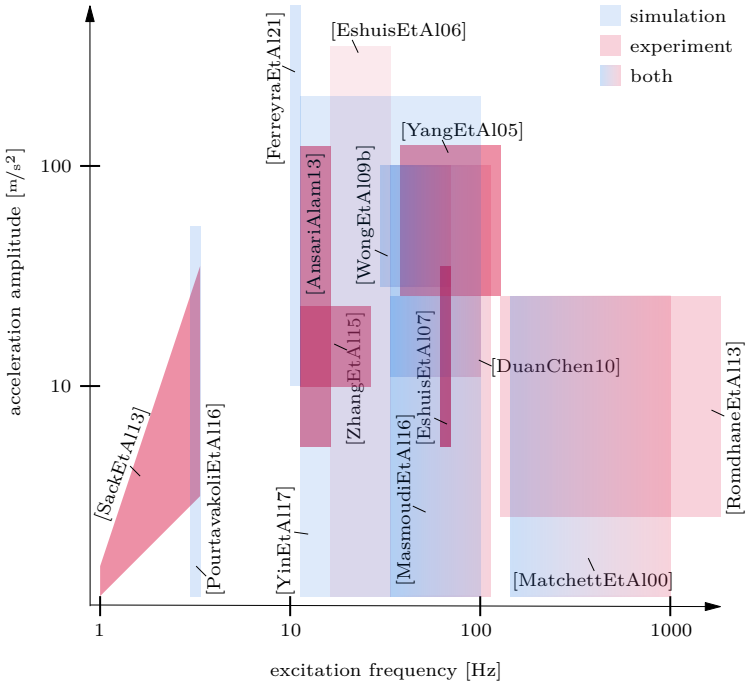

Figure 1.4: Diagram of excitation conditions for single particle damper analyses.

be extracted. These analyses are often performed experimentally, but numerical studies are also possible. Thereby, a model of the structure is coupled with a particle damper model. To model the underlying structures, the *finite element method* (FEM) and *model order reduction* techniques are used most commonly, see e. g. [Wriggers01]. For the particle damper either computationally expensive DEM models are used [SanchezEtAl12] or very simplified models such as a single particle model [MarhadiKinra05] or a particle chain model [MasmoudiEtAl16].

Unfortunately, both experimental and numerical studies on the overall structure can be extremely time-consuming. Hence, many researchers investigate into simplified systems, like single-degree-of-freedom systems and beam-like structures. Apart from that, also plates and more complex devices are under investigation. Single-degree-of-freedom systems are studied numerically by [FangTang06a, FangTang06b]. They apply a harmonic force to the system's mass and extract the static equilibrium for various excitation frequencies. Hereby, the *frequency response function* (FRF) is obtained. Multiple numerical studies [SanchezCarlevaro11, SanchezEtAl12, SanchezEtAl14] on single-degree-

of-freedom systems are performed by applying a harmonic motion to the system's base plate. Similar to [FangTang06a, FangTang06b], the FRFs are obtained by analyzing the system's static equilibrium of multiple excitation frequencies.

Beam-like structures under free and forced vibrations are investigated by various authors as well. Early experimental studies are presented by [FriendKinra00] for vertical free vibrations or by [HollkampGordon98] for horizontal forced vibrations. A combined experimental and numerical study on vertical free vibrations is presented by [MaoEtAl04]. [YangEtAl05] analyzed a particle damper on the single damper level, i. e. without underlying structure, and coupled later this damper to a beam-like structure under forced vibration. Similar experiments are performed by [RomdhaneEtAl13] and [MichonEtAl13]. [BannermanEtAl11] experimentally damped the free vibration of a beam-like structure under the effect of zero gravity and found a great effect of the (bouncing) collect-and-collide motion mode. Within this motion mode, the particle bed moves as one single particle block and collides inelastically with the container walls. Later, [SackEtAl13] described the (bouncing) collect-and-collide motion mode of the particle bed in full detail within the single damper level. Moreover, [WangEtAl16] carried out experimental and numerical analyses in the vertical plane using an L-shaped beam. Further studies are conducted in [Saeki02, MarhadiKinra05, SackEtAl15, BustamanteEtAl16, GnanasambandhamEtAl20].

Besides single-degree-of-freedom systems and beam-like structures, real technical devices and simplified models of devices are being investigated. Recently, [ChenGeorgakis13] developed and applied a tuned rolling-ball damper for low frequency vibration control in wind turbines. [HeckelEtAl12] studied the damping of an oscillatory saw. It is obtained that particle dampers are more efficient than solid mass dampers. [WangEtAl15] investigated particle dampers with a small damper weight and applied these to a spacecraft precision instrument. A considerable reduction of the instrument's response is achieved. A wheel structure is damped using multi-unit particle dampers in [WangEtAl19]. Particle dampers have also been applied to high-rise buildings. [LiDarby08] experimentally studied a particle damper on a model of a three-story building. In [LuEtAl12] real earthquake time history excitation signals are applied to a 6 m high three-story model. Numerical studies for this system are presented in [LuEtAl16]. Various other studies can be found in [SkiporBain80, Panossian92, Panossian02, Simonian04].

In Fig. 1.5 an overview of the different excitation ranges is given for applying particle dampers to an underlying structure. Most experimental implementations dealing with low frequencies $f \ll 10\,\mathrm{Hz}$ are either high-rise buildings or zero gravity applications. At medium frequencies $f \approx 10\,\mathrm{Hz}$ single-degree-of-freedom systems or beam-like structures are used most commonly. For high frequencies $f \gg 10\,\mathrm{Hz}$, beam-like structures and different other devices are investigated. In general, these systems are excited in multiple eigenfrequencies, e. g. by using a sine sweep excitation.

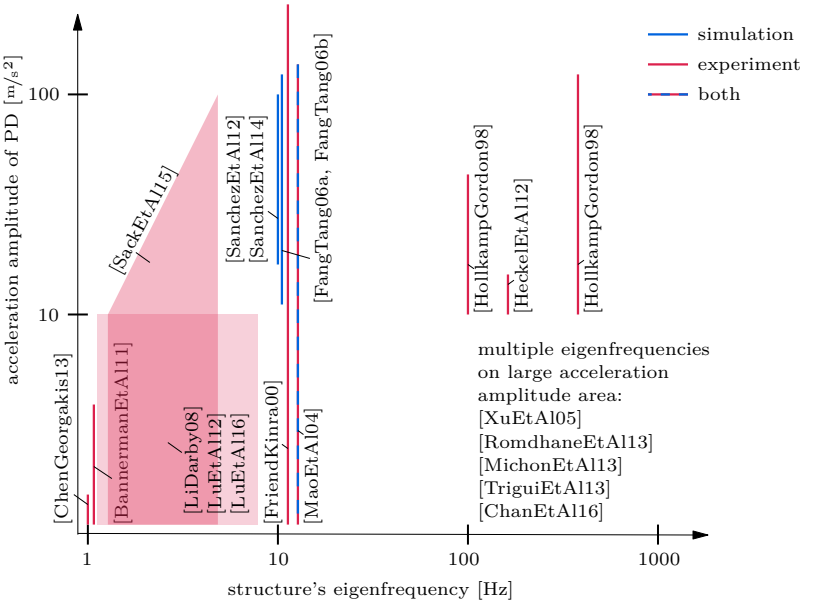

Figure 1.5: Diagram of excitation conditions for structurally integrated particle damper analyses.

Coupling

Besides the analysis of either the single damper level or the structural integrated damper level, a few authors also investigate the coupling of both approaches. Only in this way, it is possible to transfer knowledge between the levels, gain a deeper understanding of the processes and finally shorten the overall design procedure of particle dampers. [OltmannEtAl18] uses a frequency-based substructuring approach. However, this modeling approach is restricted to linear equations and, hence, its general precision is not clear. In [RomdhaneEtAl13] and [MichonEtAl13] a viscous damping parameter is determined on the single damper level describing the damper's energy dissipation. Later this viscous damping parameter is integrated into a full FEM model of a beam structure. However, the obtained FRFs are not of high accuracy. [TriguiEtAl13] coupled the energy dissipation field of a particle damper with a full FEM model of a plate. To calculate the overall damping they use the FRF obtained by time integration. A good agreement between experiments and numerical results is reported, but the investigated excitation range is small and the coupling with a full FEM model can be very time-consuming. Therefore, the above-presented approaches are not suited for fast analyses of the damping behavior using the single damper results for arbitrarily large and complex structures with reasonable accuracy.

1.4 Identified Research Gaps

Despite the huge potential of particle dampers to reduce undesired vibrations, so far they are rarely used in industrial applications. A major reason for this is the lack of a general and simple design guideline. This can be explained due to the damper's highly nonlinear behavior, the variety of influence parameters and the numerous, partially conflicting, statements found in the literature.
Various different particle damper types have been analyzed for horizontal and vertical vibrations, as well as in zero gravity environments, as shown in the previous Figures 1.2, 1.3, 1.4 and 1.5. The investigations are performed experimentally and numerically by DEM but are often restricted to a small frequency range or amplitude range. Moreover, two different analysis approaches are utilized. Either the particle damper is subject to a sinusoidal motion and its energy dissipation is directly analyzed, i. e. the single damper level, or the damper is attached to a structure and the structural damping is measured, i. e. the structural integrated damper level.

Within the single damper analyses, motion modes, energy dissipation and effective particle mass are often studied independently, see Fig. 1.3, even though these quantities are strongly correlated with each other. Furthermore, the energy dissipation, e. g. used by [DuanChen10], is not suitable to compare different damper settings. This quantity depends on the particle mass and can vary by multiple decades depending on the excitation conditions. The loss factor, used e. g. by [WongEtAl09b], is not appropriate either. It still correlates with the particle mass and in the case of experimental tests also with the container mass. The most suitable efficiency factor, the *effective loss factor*, is introduced recently by [MasmoudiEtAl16]. Being independent of the particle mass and the container mass, it allows the comparison of different particle settings. However, many authors still refer to the energy dissipation or loss factor, which is not convenient and hinders the comparison of different damper settings.

Within the structural integrated damper analyses, various different kinds of damping factors are used. However, all of these definitions depend on the structural mass as well as on the particle mass and do not allow the evaluation of the efficiency of the damper. Hence, a comparison between the different applications is hardly possible. A formula to obtain the damper's effective loss factor would be more meaningful and convenient in comparing results. Another problem is the number of different excitation frequencies and excitation amplitudes studied for the structural integrated damper analyses, see Fig. 1.4 and Fig. 1.5. Often, only a small frequency range or even a single frequency is analyzed. Horizontal and vertical vibrations are investigated but not compared and the container acceleration amplitude is mostly restricted to a specific range. Hence, the generality of derived results and findings is questionable, even resulting in recognizable contradictory statements, e. g. about the influence of the particle

shape or of the contact parameters, like friction coefficient or coefficient of restitution.

The above mentioned points demonstrate the problematic fields in the design process of particle dampers, which can be summarized in two major statements:

- The comparison of different design approaches and results is a challenging task, due to different investigated excitation ranges and utilized quantifying factors.
- The coupling of the different analysis levels, i. e. single particle, single damper and structural integrated damper, is currently not possible in reasonable time and accuracy.

Only by solving both points at the same time, reliable results and an efficient design of particle dampers can be achieved. Hence, in this work, a systematic multiscale design methodology in form of a *toolchain* is developed and introduced in Chap. 3. This design toolchain couples the different analysis levels efficiently and accurately, enabling a reliable damper design. The design toolchain is based on computational models as well as models derived from experiments. These models provide useful insights into the complex processes, nonlinear effects and design parameters influencing the efficiency of particle dampers. The computational models are hereby based on the DEM, which is discussed in detail in Chap. 2.

As the single particle analyses are independent of the other two levels, i. e. single damper and structural integrated damper levels, it is dealt with separately in Chap. 4. Afterward, the design toolchain is applied to the following four major excitation regimes:

Low-Excitation Horizontal Vibrations The vibrations at low excitation are going to be classified as frequencies $f < 5\,\mathrm{Hz}$ and acceleration amplitudes of the particle damper below the gravitational constant. These analyses are restricted to horizontal vibrations. For the vertical case particles normally remain on the container base, causing no significant damping. However, up to now, even in the horizontal case, only small energy dissipation rates have usually been obtained, due to sticking of particles. In this work, the rolling effect of spherical particles on flat container bases is used to significantly increase the damper's energy dissipation. An analytical equation is derived to accurately describe this rolling effect and the resulting energy dissipation. The derived analytical equation is validated by comparisons to experimental measurements using a linear drive. Based on this analytical equation, for structural free and forced vibrations, a systematic damper design approach is developed. A detailed discussion on this excitation regime is given in Chap. 5.

Medium-Excitation Horizontal Vibrations Medium-excitation vibration is going to be classified as a vibration range with frequencies $f \approx 5\,\mathrm{Hz}$ and acceleration

amplitudes of the particle damper below and above the gravitational constant. In the horizontal case, the transition from a rather bouncing particle motion at high container accelerations to a rolling particle motion at low container accelerations is analyzed by DEM. By coupling both analytical equations describing these motion modes, an efficient damper design guideline is found for structural integration. A detailed discussion on this excitation regime is given in Chap. 6.

Medium-Excitation Vertical Vibrations In the vertical case, particle dampers within medium-excitation vibrations show multiple different motion modes by DEM. For container acceleration amplitudes below the gravitational constant, the damper's efficiency is low. For container accelerations amplitudes above the gravitational constant, the observed motion modes are very sensitive to the excitation conditions and container dimensions, e. g. particles eventually reach the container top or not. A particle damper optimization procedure for an underlying structure is successfully applied here. A detailed discussion on this excitation regime is given in Chap. 7.

High-Excitation Vibrations High-excitation vibrations are going to be categorized as vibrations with frequencies $f \gg 5\,\mathrm{Hz}$ and acceleration amplitudes of the particle damper (significantly) above the gravitational constant. Due to the high acceleration amplitudes, the results of horizontal and vertical vibrations are very similar. Multiple influence parameters like particle shape and material, container shape and orientation, filling ratio, inner structures, coated container walls, and many more are studied on the single damper level. Depending on the excitation conditions, different design approaches are necessary to obtain an efficient damper. Multiple design guidelines are presented for the different excitation conditions. For structural coupling, a beam-like structure with free–free boundary conditions is utilized. The efficiency of different numerical coupling procedures between modal reduced model of the structure and particle damper are analyzed. A detailed discussion on this excitation regime is given in Chap. 8.

Discrete Element Method

Granular materials are of great importance for many industrial processes, natural sciences and also our everyday lives. To predict the behavior of granular materials and optimize industrial processes, numerical methods are widely applied. As granular materials are generally not linked with each other, i. e. can move freely in space, for their numerical description *meshfree particle methods* are widely applied [Fleissner10]. For these methods the discretization points, i. e. the particles, have no prior defined relations. Instead, these relations, e. g. for contact situations, are created and dissolved during the simulation.

For numerical analyses of particle dampers and their derivatives, the *discrete element method* (DEM) is most commonly used. The DEM was introduced by [CundallStrack79] for the simulation of systems consisting of discs and spheres. Its general concept can be applied to any system of many unconstrained particles where the system behavior is governed by the interaction of these particles [FleissnerEtAl07]. A particle is defined as a non-bounded object of finite dimensions, which dynamics are influenced by short-range forces [Pöschel05]. While the particles can have an arbitrary shape, spherical particles are used most frequently in simulations, due to their numerical efficiency. The particle dynamics are described by *Newton's* and *Euler's equation of motion* for every particle [Pöschel05, Matuttis14]. Hereby, the contacting partners are treated as rigid, thus only touching in a single overlapping point. To resolve these contacts, contact models obtained from *penalty approaches*, also called continuous contact models, are usually utilized. These contact models avoid large particle penetrations and can be, but do not need to be, based on physical laws.

The absolute translational acceleration of the center of mass $\ddot{\boldsymbol{x}}_i = [\ddot{x}_i^x,\, \ddot{x}_i^y,\, \ddot{x}_i^z]^\top$ of particle i is obtained by

$$m_i\, \ddot{\boldsymbol{x}}_i = \boldsymbol{f}_{\mathrm{a},i}, \tag{2.1}$$

with particle mass m_i and $\boldsymbol{f}_{\mathrm{a},i}$ being the vector of applied forces on particle i. The rotational acceleration $\dot{\boldsymbol{\omega}}_i = [\dot{\omega}_i^x,\, \dot{\omega}_i^y,\, \dot{\omega}_i^z]^\top$ of particle i is calculated as

$$\boldsymbol{I}_i\, \dot{\boldsymbol{\omega}}_i + \boldsymbol{\omega}_i \times \boldsymbol{I}_i\, \boldsymbol{\omega}_i = \boldsymbol{\ell}_{\mathrm{a},i}, \tag{2.2}$$

with the particle's inertia tensor $\boldsymbol{I}_i$ and $\boldsymbol{\ell}_{\mathrm{a},i}$ being the vector of applied torques on particle i in respect of the particle's center of mass. Since only spherical particles

are considered in this work, the inertia tensor $\boldsymbol{I}_i = I_i\,\boldsymbol{E}$ of the particles becomes diagonal, whereby all three entries of $\boldsymbol{I}_i$ are identical with a value of $I_i = \frac{2}{5}\,m_i\,r_i^2$ and r_i being the particle radius. Hence, Eq. (2.2) simplifies to

$$\boldsymbol{I}_i\,\dot{\boldsymbol{\omega}}_i = \boldsymbol{\ell}_{\mathrm{a},i}. \tag{2.3}$$

The vectors of applied forces $\boldsymbol{f}_{\mathrm{a},i}$ and torques $\boldsymbol{\ell}_{\mathrm{a},i}$ consist of the accumulated particle–particle (p) and particle–bounding geometry (b) contact forces $\boldsymbol{f}_{\mathrm{p/b},ij}$ and contact torques $\boldsymbol{\ell}_{\mathrm{p/b},ij}$ of particle i with contact partners j. In the case of spherical particles, the contact torques only result from frictional forces. If present, the vector of applied forces can additionally consist of external forces $\boldsymbol{f}_{\mathrm{e},i}$ and torques $\boldsymbol{\ell}_{\mathrm{e},i}$ as

$$\boldsymbol{f}_{\mathrm{a},i} = \boldsymbol{f}_{\mathrm{e},i} + \sum_{j\in\mathcal{J}_{i,\mathrm{p}}} \boldsymbol{f}_{\mathrm{p},ij} + \sum_{j\in\mathcal{J}_{i,\mathrm{b}}} \boldsymbol{f}_{\mathrm{b},ij}, \tag{2.4}$$

$$\boldsymbol{\ell}_{\mathrm{a},i} = \boldsymbol{\ell}_{\mathrm{e},i} + \sum_{j\in\mathcal{J}_{i,\mathrm{p}}} \boldsymbol{\ell}_{\mathrm{p},ij} + \sum_{j\in\mathcal{J}_{i,\mathrm{b}}} \boldsymbol{\ell}_{\mathrm{b},ij}, \tag{2.5}$$

with $\mathcal{J}_{i,\mathrm{p}}$ being the set of all particle contact partners with particle i, and $\mathcal{J}_{i,\mathrm{b}}$ being the set of all bounding geometry contact partners with particle i. The vectors of the external forces and torques may consist of gravitational forces, fluid forces, adhesive forces and many more [BandeiraZohdi18]. For particle systems of macroscopic size surrounded by air, the gravitational force is often the only one considered, whereas other external forces are neglected or do not exist.

Setting up the equation of motion, i. e. Eq. (2.1) and Eq. (2.3), for all n_p particles with set $\mathcal{P} \in \{1:1:n_\mathrm{p}\}$ results during particle contacts in a coupled nonlinear differential equation with $6\,n_\mathrm{p}$ degrees of freedom for 3D simulations. As particle systems can contain a large number of particles (up to millions), and all contacts between two particles as well as contacts of particles with bounding geometries need to be detected and resolved in every time step, efficient detection algorithms and contact laws are essential. Also, the choice of an appropriate time integration scheme is crucial [FleissnerEtAl07].

Besides the particles, granular systems also consist of bounding geometries. Each bounding geometry belongs to a rigid body, which is described by its translational and angular states, i. e. by $\boldsymbol{x}_{\mathrm{rb},j}$ and $\boldsymbol{\omega}_{\mathrm{rb},j}$. The rigid body movement can be static, be described by a rheonomic constraint or be characterized by an underlying *ordinary differential equation* (ODE). For the latter one, the DEM could be coupled to a (flexible) multibody system [Seifried14, Shabana13] or a *finite element method* (FEM) model.

In Fig. 2.1 a schematic procedure of a DEM simulation is shown. Each simulation starts with its initialization, where all necessary simulation parameters are defined. This includes the properties of particles and bounding geometries, initial conditions, contact search algorithm, contact force algorithms and time

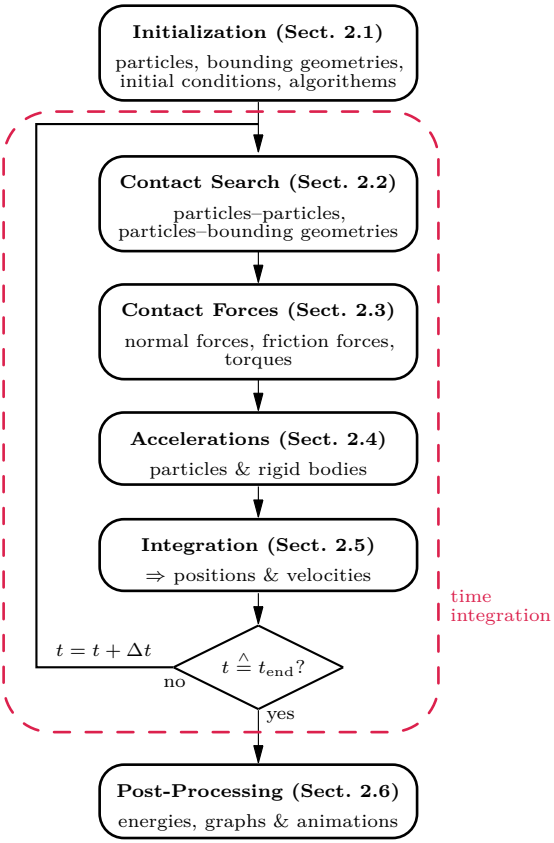

Figure 2.1: Work-flow of a DEM simulation.

integration scheme. Within the time integration, in every time step or corrector step (as discussed later) all contacts need to be resolved. Afterward, the resulting contact forces are calculated. These consist of normal forces, friction forces and the resulting torques. Through the contact forces, the accelerations of particles and rigid bodies are calculated. From the resulting accelerations, the positions and velocities follow by using an appropriate time integration scheme. At the end of a simulation, during post-processing, energies and user-defined outputs are calculated. In the following sections, the different parts of a DEM simulation are discussed in detail. For better readability, indices are dropped if the variables are still uniquely defined.

2.1 Initialization

During initialization, the particles' initial conditions are set. For very small particle numbers, this can be done manually for every particle. For higher particle numbers, however, appropriate algorithms are necessary for this task. As the initial conditions are only generated once per simulation, these algorithms do not require high performance. Especially, for highly dynamic particle systems, like the particle flow through a pipe, the overall long-term behavior of the particles is often independent of the chosen initial state. For such applications, the particles can be placed randomly within the bounding geometry. However, for applications requiring a high particle filling ratio, a random strategy might not be sufficient. Particles can be generated as a tight particle packing or created using a previous drop-down simulation. In the latter, initial contacts between the particles exist.

In Fig. 2.2 different pre-initialized initial conditions of 1000 particles are shown exemplary. Besides the shown pre-initialization of particles, particles can also be generated and removed dynamically during the simulation if required.

a) Tight packing.

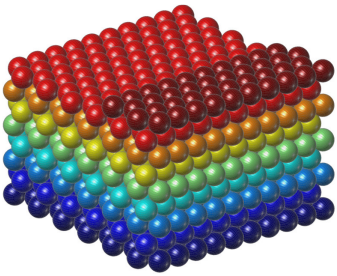

b) By previous drop-down simulation.

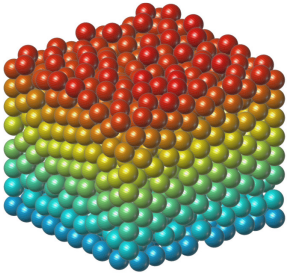

c) Randomly distributed: whole volume.

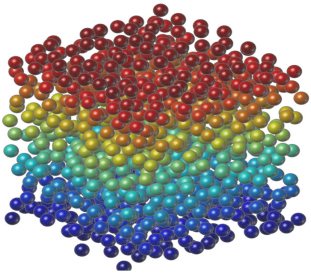

d) Randomly distributed: layer by layer.

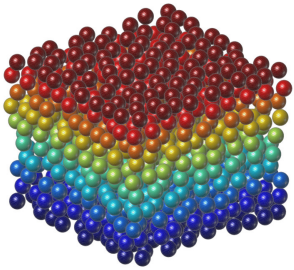

Figure 2.2: Different exemplary initial conditions of 1000 particles.

2.2 Contact Search

Within the time integration, the contact search takes place at the beginning of every new time step. Every particle–particle and particle–bounding geometry contact needs to be detected and the corresponding contact kinematics at the boundary point B have to be calculated, see Fig. 2.3. As the time integration possibly contains many time steps and granular systems can consist of a huge amount of particles, sophisticated algorithms are necessary for the contact search. In the following, some common and established contact search algorithms are presented.

2.2.1 Sphere–Sphere

In Fig. 2.3 a schematic contact of two spheres i and j is shown. Two spheres are in contact with each other if their overlap δ_{ij} is greater than zero. Otherwise, their overlap is negative. Their overlap δ_{ij} and the normal direction of contact $\boldsymbol{n}_{ij}$ of two spheres are obtained by

$$\delta_{ij} = r_i + r_j - ||\boldsymbol{x}_i - \boldsymbol{x}_j||_2 \,, \tag{2.6}$$

$$\boldsymbol{n}_{ij} = \frac{\boldsymbol{x}_j - \boldsymbol{x}_i}{||\boldsymbol{x}_j - \boldsymbol{x}_i||_2}, \tag{2.7}$$

with $r_{i/j}$ being the radii of the spheres. The simplest algorithm to check for such sphere–sphere contacts is to calculate the overlap δ_{ij} for all possible contact pairs. This results in a computational complexity of $\mathcal{O}(n_\mathrm{p}^2)$. While for small

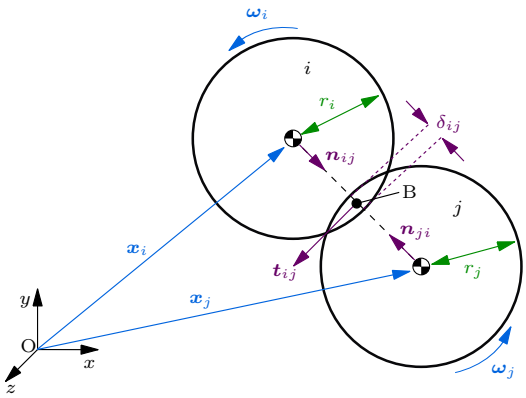

Figure 2.3: Contact of two spheres.

particle numbers, this algorithm is quickly implemented and sufficient, for larger particle systems it is too inefficient. Hence, this algorithm is called *naive search* in the following. There exist a variety of other algorithms, such as cell-based, tree-based or sort-based ones, decreasing the search complexity to an optimum of $\mathcal{O}(n_\mathrm{p})$ [NorouziEtAl16, Pöschel05]. A very common cell-based search algorithm is the *non-binary search* algorithm, shown in Fig. 2.4. The simulation domain is discretized into cube cells and every particle is assigned to its corresponding cell, see Fig. 2.4a. The cell size is chosen as large as the largest particle. Thus, to search for particle contacts, only the target and neighboring cells have to be checked for contact partners, i. e. one target cell and 26 neighboring cells for 3D simulations. Additionally, the fact is used that if particle i is a neighbor of particle j, particle j is conversely also a neighbor of particle i. Therefore only 13 of the 26 neighboring cells have to be checked for contact partners, as shown in Fig. 2.4b.

Although the non-binary search algorithm is a very efficient one, it still has to be run in every time step. In contrast, the *Verlet list* algorithm [Verlet67] makes use of the particles' property that their movement is continuous and the timescale of changing contact partners is much larger than the contacts themselves. For every particle i a Verlet list is created, saving all particles with index $j > i$ in a certain Verlet distance d_v, i. e. for

$$||\boldsymbol{x}_i - \boldsymbol{x}_j||_2 - r_i - r_j < d_\mathrm{v}, \tag{2.8}$$

see also Fig. 2.5. The condition $j > i$ is considered to be established because particle j is in the Verlet range with particle i if particle i is in Verlet range with particle j. In the next time steps, only particles in the Verlet list have to be checked for contacts. In this work, the used Verlet distance d_v depends on the current time step size Δt, the current maximum particle velocity, and the list shall last about 1000 time steps. To prevent the Verlet distance from becoming

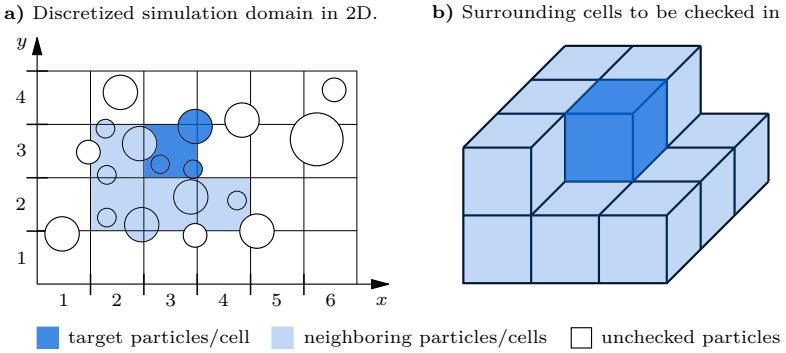

Figure 2.4: Sketch of the non-binary search algorithm.

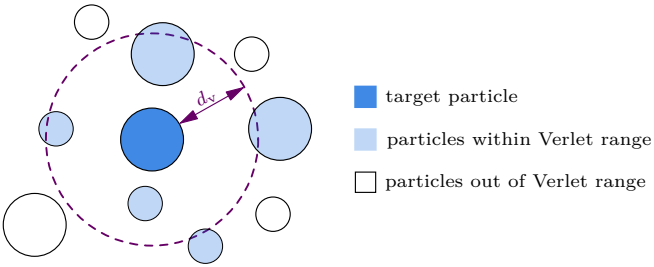

Figure 2.5: Verlet list algorithm.

too small or too large, threshold values d_v^{min} and d_v^{max} are utilized. The Verlet distance is obtained by

$$d_v = 1000\,\Delta t \cdot \max ||\dot{\boldsymbol{x}}_i||_2\,, \quad \forall i \in \mathcal{P}. \tag{2.9}$$

$$d_v = \max\left(d_v^{min}, \min\left(d_v, d_v^{max}\right)\right), \tag{2.10}$$

with $d_v^{min} = 1 \cdot 10^{-10}$ and $d_v^{max} = 0.8 \cdot \min(r_i)$. The value of d_v^{max} is based on the shortest distance between two particles in a tight particle packing without contact. This prevents unnecessary overhead for rather static particle packings with only single dynamical particles with high velocity.

The Verlet list is updated when the abort criterion is fulfilled. The abort criterion is obtained by comparing the state vector of the time step when the Verlet list was created (index 0) with the current state vector (index 1). Here, the distance traveled by the two fasted particles is used, i. e.

$$\max\left|\left|\boldsymbol{x}_i^1 - \boldsymbol{x}_i^0\right|\right|_2 + \max\left|\left|\boldsymbol{x}_j^1 - \boldsymbol{x}_j^0\right|\right|_2 \geq d_v, \quad \forall i \in \mathcal{P} \ \wedge\ \forall j \in \mathcal{P} \ \wedge\ j \neq i. \tag{2.11}$$

This is a very conservative abort criterion, as it is extremely unlikely that the two fastest particles are only separated by a distance slightly higher than d_v and move directly towards one another. More sophisticated abort criteria use a greater distance than the Verlet distance in Eq. (2.11), see e. g. [Pöschel05]. However, in these cases, it is necessary to examine whether unrecognized contacts have occurred during the time the Verlet list is updating. If this is the case, the simulation has to be restarted from the point in time at which the Verlet list was created utilizing a smaller Verlet distance.

To update the Verlet list, algorithms like the naive search as well as the non-binary search algorithm can be used. Updating the Verlet list with the non-binary search algorithm yields an efficient contact search, even for systems with a large number of particles.

Contact Kinematics Besides the individual contact partners of each particle, the contact kinematics need to be calculated as well [Luding08b]. This includes especially the normal and tangential velocities at the boundary point B, see Fig. 2.3.

Introducing the effective radius $\bar{r}_{i/j} = r_{i/j} - \frac{1}{2}\delta_{ij}$, the relative velocity at boundary point B follows to

$$\boldsymbol{v}_{\mathrm{B},ij} = \dot{\boldsymbol{x}}_i + \bar{r}_i\ (\boldsymbol{\omega}_i \times \boldsymbol{n}_{ij}) - \dot{\boldsymbol{x}}_j - \bar{r}_j\ (\boldsymbol{\omega}_j \times \boldsymbol{n}_{ji}). \tag{2.12}$$

The scalar penetration velocity $\dot{\delta}_{ij}$, i. e. in normal direction, and the vectorial, relative velocity in normal direction $\boldsymbol{v}_{ij}^{\mathrm{n}}$ are obtained by the scalar product $\bullet$ as

$$\dot{\delta}_{ij} = \boldsymbol{n}_{ij} \bullet\ (\dot{\boldsymbol{x}}_i - \dot{\boldsymbol{x}}_j), \tag{2.13}$$

$$\boldsymbol{v}_{ij}^{\mathrm{n}} = \dot{\delta}_{ij}\, \boldsymbol{n}_{ij}. \tag{2.14}$$

The relative, tangential velocity at boundary point B is obtained by

$$\boldsymbol{v}_{\mathrm{B},ij}^{\mathrm{t}} = \boldsymbol{v}_{\mathrm{B},ij} - \boldsymbol{v}_{ij}^{\mathrm{n}}. \tag{2.15}$$

Finally, the tangential contact direction follows to

$$\boldsymbol{t}_{ij} = \frac{\boldsymbol{v}_{\mathrm{B},ij}^{\mathrm{t}}}{\left|\left|\boldsymbol{v}_{\mathrm{B},ij}^{\mathrm{t}}\right|\right|_2}. \tag{2.16}$$

2.2.2 Sphere–Bounding Geometry

To model bounding geometries, numerous approaches exist, see e. g. [Fleissner10, NorouziEtAl16, Pöschel05]. Bounding geometries can be modeled using simple analytical forms, like *planes, circles* or *cylinders* yielding an efficient description. However, such forms are not suited to model complex structures and are thus limited in their application. Hence, *triangular surface meshes* are often used for complex structures. The following sections will briefly introduce the most important types.

Every bounding geometry belongs hereby to a rigid body, defined in the body-fixed frame of the rigid body. If existing, the rotation of the rigid body can be described by different descriptions, like Cardan- and Euler angles, Quaternion or Rodriguez-parameters, see e. g. [Shabana13]. By this, the rigid body's rotation matrix $\boldsymbol{S}_j \in \mathbb{R}^{3\times3}$ follows, describing the orientation between the body-fixed and inertial frame. As the geometrical properties $\boldsymbol{c}_0$ of the bounding geometries, like their relative position to the rigid body, are defined in the body-fixed frame of rigid body j, they need to be transformed into the inertial frame for contact search. The description of the geometrical properties within the inertial frame is obtained by $\boldsymbol{c} = \boldsymbol{S}_j\, \boldsymbol{c}_0$.

Sphere–Plane

In Fig. 2.6 a schematic sphere–plane contact is shown. An infinite plane k belonging to a rigid body j is described by a point on the plane and the plane's normal direction $\boldsymbol{n}_k$. The point on the plane is described by $\boldsymbol{r}_k$, i. e. the relative vector originating on the rigid body. The distance d_{ik} and overlap δ_{ik} of particle and plain are obtained by

$$d_{ik} = \boldsymbol{n}_k \bullet (\boldsymbol{x}_i - \ (\boldsymbol{x}_{\mathrm{rb},j} + \boldsymbol{r}_k)) \,, \tag{2.17}$$

$$\delta_{ik} = r_i - |d_{ik}|. \tag{2.18}$$

Using the naive search algorithm, the computational complexity to calculate all contacts of the n_P planes is $\mathcal{O}(n_\mathrm{p}\, n_\mathrm{P})$. As the number of (infinite) planes is usually small, the computational effort is much lower than for the particle–particle search. To increase the efficiency of the contact search, the Verlet list can be used as well. All planes within a certain distance of the particles are saved and checked in the next time steps until the abort criterion is fulfilled. If existing, the planes' rotations also have to be considered. To update the Verlet list the naive search is used.

Contact Kinematics As the particles can be positioned on both sides of the plane, during contact the particle normal direction $\boldsymbol{n}_{ik}$ is calculated first, as

$$\boldsymbol{n}_{ik} = -\boldsymbol{n}_k \cdot \mathrm{sgn}(d_{ik}). \tag{2.19}$$

Next, the relative vector from the rigid body's center of mass (point R) to the boundary point B, denoted as $\boldsymbol{r}_{\mathrm{RB},ik}$, is necessary, see Fig. 2.6. It is calculated

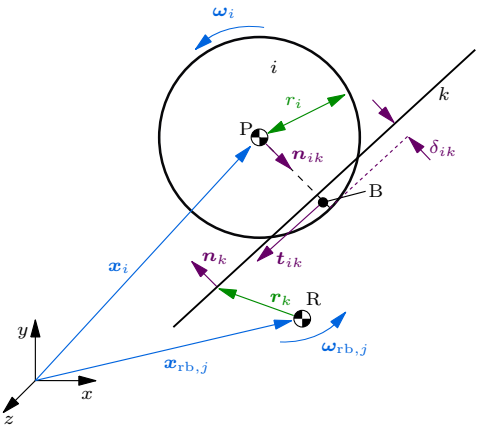

Figure 2.6: Sphere–plane contact.

using the relative vector from the particle's center of mass to the boundary point $\boldsymbol{r}_{\mathrm{PB},ik}$ and the effective particle radius $\bar{r}_{ik}$. It follows to

$$\bar{r}_{ik} = r_i - \frac{1}{2}\delta_{ik}, \tag{2.20}$$

$$\boldsymbol{r}_{\mathrm{PB},ik} = \bar{r}_{ik}\,\boldsymbol{n}_{ik}, \tag{2.21}$$

$$\boldsymbol{r}_{\mathrm{RB},ik} = \boldsymbol{x}_i + \boldsymbol{r}_{\mathrm{PB},ik} - \boldsymbol{x}_{\mathrm{rb},j}. \tag{2.22}$$

The relative velocity at boundary point B follows to

$$\boldsymbol{v}_{\mathrm{B},ik} = \dot{\boldsymbol{x}}_i + \bar{r}_{ik}\,(\boldsymbol{\omega}_i \times \boldsymbol{n}_{ik}) - \boldsymbol{x}_{\mathrm{rb},j} - \boldsymbol{\omega}_{\mathrm{rb},j} \times \boldsymbol{r}_{\mathrm{RB},ik}. \tag{2.23}$$

The penetration velocity $\dot{\delta}_{ik}$ and the relative velocity in normal direction $\boldsymbol{v}^{\mathrm{n}}_{ik}$ are computed as

$$\dot{\delta}_{ik} = \boldsymbol{n}_{ik} \bullet \boldsymbol{v}_{\mathrm{B},ik}, \tag{2.24}$$

$$\boldsymbol{v}^{\mathrm{n}}_{ik} = \dot{\delta}_{ik}\,\boldsymbol{n}_{ik}. \tag{2.25}$$

The relative, tangential velocity at boundary point B is obtained by

$$\boldsymbol{v}^{\mathrm{t}}_{\mathrm{B},ik} = \boldsymbol{v}_{\mathrm{B},ik} - \boldsymbol{v}^{\mathrm{n}}_{ik}. \tag{2.26}$$

Finally, the tangential contact direction follows to

$$\boldsymbol{t}_{ik} = \frac{\boldsymbol{v}^{\mathrm{t}}_{\mathrm{B},ik}}{\left|\left|\boldsymbol{v}^{\mathrm{t}}_{\mathrm{B},ik}\right|\right|_2}. \tag{2.27}$$

Sphere–Cylinder

In Fig. 2.7 a schematic sphere–cylinder contact is shown. The infinitely long cylinder o is described by its radius $r_{\mathrm{cyl},o}$, its longitudinal direction $\boldsymbol{\ell}_o$ and its relative vector from the rigid body to the cylinder's center point C by $\boldsymbol{r}_o$. The absolute position vector of the cylinder's center point $\boldsymbol{r}_{\mathrm{OC}}$ and the relative vector between particle's and cylinder's center points $\boldsymbol{r}_{\mathrm{CP}}$ are obtained by

$$\boldsymbol{r}_{\mathrm{OC}} = \boldsymbol{x}_{\mathrm{rb},j} + \boldsymbol{r}_o, \tag{2.28}$$

$$\boldsymbol{r}_{\mathrm{CP}} = \boldsymbol{x}_i - \boldsymbol{r}_{\mathrm{OC}}. \tag{2.29}$$

The shortest distance between the cylinder's surface and a particle is described by d_{io}. The distance d_{io} and the particle–cylinder overlap δ_{io} are obtained by

$$d_{io} = r_{\mathrm{cyl},o} - \left|\left|\boldsymbol{\ell}_o \times \boldsymbol{r}_{\mathrm{CP}}\right|\right|_2, \tag{2.30}$$

$$\delta_{io} = r_i - |d_{io}|. \tag{2.31}$$

Just as described for the particle–plane contacts, a pure naive search or a Verlet list with naive search update can be used for contact detection.

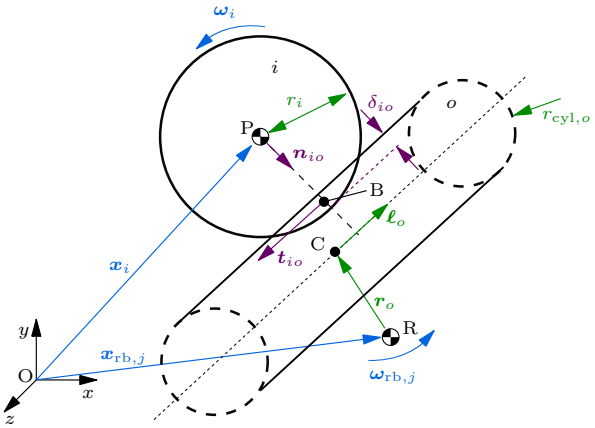

Figure 2.7: Sphere–cylinder contact.

Contact Kinematics The normal direction $\boldsymbol{n}_{io}$ is obtained by

$$\boldsymbol{n}_{io}^0 = -\boldsymbol{r}_{\mathrm{CP}} + (\boldsymbol{r}_{\mathrm{CP}} \bullet \boldsymbol{\ell}_o)\ \boldsymbol{\ell}_o, \tag{2.32}$$

$$\boldsymbol{n}_{io} = \frac{\boldsymbol{n}_{io}^0}{||\boldsymbol{n}_{io}^0||_2}. \tag{2.33}$$

All other quantities are calculated analogously to Eq. (2.20)–Eq. (2.27) and $o \mathrel{\widehat{=}} k$.

Particle–Triangle

In the last two sections, two simple analytical forms for bounding geometries are introduced and many more, like disks, spheres or coils, could be presented. From a numerical point of view, these bounding geometries are highly efficient, robust and quickly implemented. The drawback of these geometries is, however, that it is not possible to model arbitrary complex structures, as it is often necessary for industrial applications. A common approach is to use triangular surface meshes [FleissnerEtAl07, HuEtAl13, KremmerFavier01, NorouziEtAl16]. These meshes can be exported from CAD (computer-aided design) programs using the *STL* format.

At first, during pre-processing of a DEM simulation, the obtuse triangles are split up into two acute triangles. For such triangles, in Fig. 2.8 a sphere–triangle contact is shown. Each triangle l is defined by its three points T_1, T_2, and T_3 and the corresponding local position vectors $\boldsymbol{r}_{\mathrm{RT}_{1/2/3},l}$, originating from the rigid body's center of mass R. The midpoint M of a triangle l is obtained using the

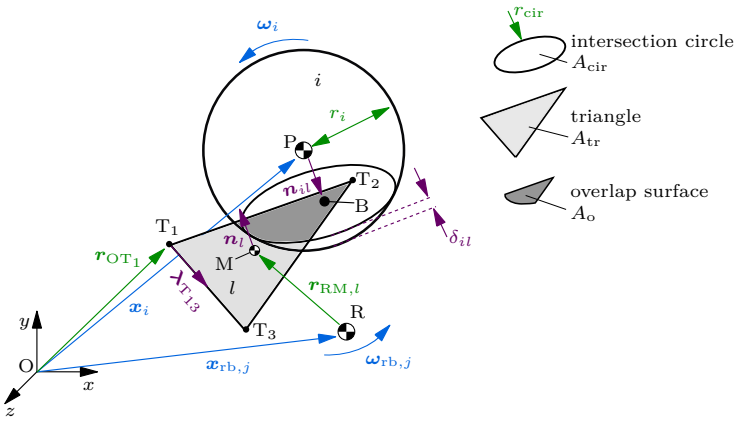

Figure 2.8: Sphere–triangle contact.

triangle's global position vectors $\boldsymbol{r}_{\mathrm{OT}_{1/2/3}}$ as

$$\boldsymbol{r}_{\mathrm{OT}_{1/2/3}} = \boldsymbol{x}_{\mathrm{rb},j} + \boldsymbol{r}_{\mathrm{RT}_{1/2/3,l}}, \tag{2.34}$$

$$\boldsymbol{r}_{\mathrm{OM}} = \frac{1}{3}\left(\boldsymbol{r}_{\mathrm{OT}_1} + \boldsymbol{r}_{\mathrm{OT}_2} + \boldsymbol{r}_{\mathrm{OT}_3}\right). \tag{2.35}$$

The following contact search is divided into three steps: *coarse*, *medium* and *fine* search.

Coarse Search For the coarse search, the individual triangles are treated as quasi spheres with midpoint M and effective radius $\bar{r}_l$. The latter is defined as the largest distance between the triangle's midpoint M to the points T_1, T_2 and T_3. It follows to

$$\bar{r}_l = \max \left|\left| \boldsymbol{r}_{\mathrm{OM}} - \boldsymbol{r}_{\mathrm{OT}_{1/2/3}} \right|\right|_2. \tag{2.36}$$

Hence, Eq. (2.6) of the particle–particle contact search can be used to determine the virtual "particle–particle" overlap. The naive search algorithm results in a computational complexity of $\mathcal{O}(n_\mathrm{p}\, n_\mathrm{tr})$, with n_tr being the number of triangles. As particle and triangle numbers can be large, the naive search is inefficient for these systems. As in the particle–particle search, the non-binary search algorithm can be applied, yielding an efficient search algorithm even for large systems.

Medium Search For the medium search, only contacting particles and triangles detected in the coarse search are considered. Now, the particles are tested against the (infinite) triangle planes defined by the triangle midpoint M and normal

vector $\boldsymbol{n}_l$. To determine the triangle's normal vector, first, the three triangle sides are defined by the directional vectors

$$\boldsymbol{\lambda}_{\mathrm{T}12} = \boldsymbol{r}_{\mathrm{OT}_2} - \boldsymbol{r}_{\mathrm{OT}_1}, \tag{2.37}$$

$$\boldsymbol{\lambda}_{\mathrm{T}13} = \boldsymbol{r}_{\mathrm{OT}_3} - \boldsymbol{r}_{\mathrm{OT}_1}, \tag{2.38}$$

$$\boldsymbol{\lambda}_{\mathrm{T}23} = \boldsymbol{r}_{\mathrm{OT}_3} - \boldsymbol{r}_{\mathrm{OT}_2}, \tag{2.39}$$

see also Fig. 2.8. Introducing the set $\mathcal{S} = \{\mathrm{T}_{12}, \mathrm{T}_{13}, \mathrm{T}_{23}\}$ for the three triangle sides, the normalized forms of the direction vectors are defined as

$$\boldsymbol{\lambda}_s^0 = \frac{\boldsymbol{\lambda}_s}{||\boldsymbol{\lambda}_s||_2}, \quad \forall s \in \mathcal{S}. \tag{2.40}$$

The area of the triangle follows to

$$A_{\mathrm{tr}} = \frac{1}{2} \left|\left|(\boldsymbol{\lambda}_{\mathrm{T}12} \times \boldsymbol{\lambda}_{\mathrm{T}13})\right|\right|_2 . \tag{2.41}$$

The normal direction of the triangle is obtained by

$$\boldsymbol{n}_l = \frac{\boldsymbol{\lambda}_{\mathrm{T}12} \times \boldsymbol{\lambda}_{\mathrm{T}13}}{||\boldsymbol{\lambda}_{\mathrm{T}12} \times \boldsymbol{\lambda}_{\mathrm{T}13}||_2}. \tag{2.42}$$

Using analogously Eqs. (2.17) and (2.18) of the sphere-plane contact search, the distance between a particle's center of mass and the triangle infinite plane d_{il} and their overlap δ_{il} are determined. Only those particles and triangles being in contact are further considered for the fine search. Using the overlap δ_{il}, the radius and area of the intersection circle, see Fig. 2.8, are obtained to

$$r_{\mathrm{cir}} = \sqrt{2\, r_i\, \delta_{il} - \delta_{il}^2}, \tag{2.43}$$

$$A_{\mathrm{cir}} = \pi\, r_{\mathrm{cir}}^2. \tag{2.44}$$

Fine Search Within the fine search, the particle–triangle contact region needs to be determined next. First, the particle's center of mass P projection onto the contact plane, i. e. boundary point B, is determined as

$$\boldsymbol{r}_{\mathrm{OB}} = \boldsymbol{x}_i - d_{il}\, \boldsymbol{n}_l, \tag{2.45}$$

see Fig. 2.8. As shown in Fig. 2.9, three different contact regions exist, i. e. the position of boundary point B relative to the triangle: one interior region, three vertex regions and three edge regions. Note, even if the sphere–triangle boundary point B lies not within the triangle, a contact is still possible, see e. g. Fig. 2.9b. To determine the particle's contact region, the *barycentric coordinates* u and w are used. By defining the directional vector $\boldsymbol{\lambda}_{\mathrm{T}_1\mathrm{B}}$, pointing from triangle point T_1 to boundary point B, as

$$\boldsymbol{\lambda}_{\mathrm{T}_1\mathrm{B}} = \boldsymbol{r}_{\mathrm{OB}} - \boldsymbol{r}_{\mathrm{OT}_1}, \tag{2.46}$$

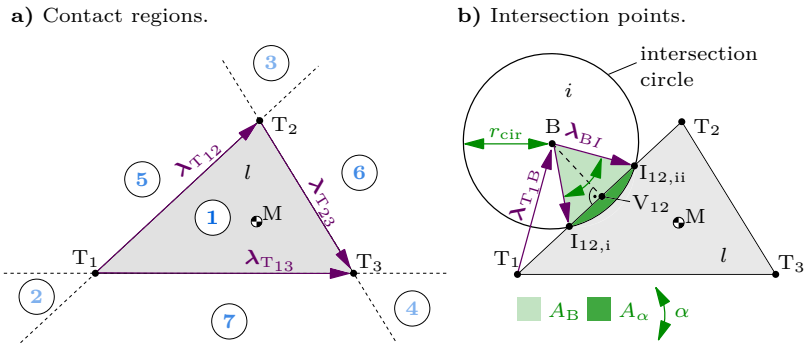

Figure 2.9: In-plane view on sphere–triangle contact.

the equations for determining the barycentric coordinates can be set up

$$u\,(\boldsymbol{\lambda}_{\mathrm{T}_{12}} \bullet \boldsymbol{\lambda}_{\mathrm{T}_{12}}) + w\,(\boldsymbol{\lambda}_{\mathrm{T}_{12}} \bullet \boldsymbol{\lambda}_{\mathrm{T}_{13}}) = \boldsymbol{\lambda}_{\mathrm{T}_{12}} \bullet \boldsymbol{\lambda}_{\mathrm{T}_1\mathrm{B}}, \tag{2.47}$$

$$u\,(\boldsymbol{\lambda}_{\mathrm{T}_{13}} \bullet \boldsymbol{\lambda}_{\mathrm{T}_{12}}) + w\,(\boldsymbol{\lambda}_{\mathrm{T}_{13}} \bullet \boldsymbol{\lambda}_{\mathrm{T}_{13}}) = \boldsymbol{\lambda}_{\mathrm{T}_{13}} \bullet \boldsymbol{\lambda}_{\mathrm{T}_1\mathrm{B}}. \tag{2.48}$$

The Eqs. (2.47) and (2.48) can be solved using *Cramer's rule*. Depending on the values of the barycentric coordinates the contact region of the particle within the triangle is obtained from Tab. 2.1.

It is obvious that the particle is in contact with the triangle for contact region 1, see Fig. 2.9a. But also for the other regions, the particle could be in contact with the triangle. This is the case if the penetration depth with the neighboring triangle is high enough, such that the intersection circle touches the triangle, see Fig. 2.9b. To check for such an intersection, the vertical distances between point B and the triangle sides are determined. Each triangle side is defined by a starting point $\mathcal{T} = \{\mathrm{T}_1, \mathrm{T}_1, \mathrm{T}_2\}$ and the corresponding direction vectors $\boldsymbol{\lambda}_s$. The vertical projections of B on the triangle sides are defined by the set $\mathcal{V} = \{\mathrm{V}_{12}, \mathrm{V}_{13}, \mathrm{V}_{23}\}$,

Table 2.1: Contact regions of Fig. 2.9 by barycentric coordinates.

Region	Condition
1	$u \geq 0$ and $w \geq 0$ and $u + w \leq 1$
2	$u \leq 0$ and $w \leq 0$ and $u + w < 0$
3	$u \geq 1$ and $w \leq 0$ and $u + w > 1$
4	$u \leq 0$ and $w \geq 1$ and $u + w > 1$
5	$u > 0$ and $w < 0$ and $u + w < 1$
6	$u \geq 0$ and $w \geq 0$ and $u + w > 1$
7	$u < 0$ and $w > 0$ and $u + w < 1$

see Fig. 2.9b. First, the directions vectors between $\mathcal{T} = \{\mathrm{T}_1, \mathrm{T}_1, \mathrm{T}_2\}$ and B are obtained

$$\boldsymbol{\lambda}_{TB} = \boldsymbol{r}_{\mathrm{OB}} - \boldsymbol{r}_{OT}, \quad \forall T \in \mathcal{T}, \tag{2.49}$$

see Fig. 2.9b. The vertical distances between boundary point B and the three triangle sides $\boldsymbol{\lambda}_s$ are achieved to

$$d_{\mathrm{BV}} = \left|\left|\boldsymbol{\lambda}_s^0 \times \boldsymbol{\lambda}_{TB}\right|\right|_2, \quad \forall V \in \mathcal{V}, \tag{2.50}$$

and $\mathcal{S} = \{\mathrm{T}_{12}, \mathrm{T}_{13}, \mathrm{T}_{23}\}$. If the vertical distance d_{BV} is smaller than the radius of the intersection circle, i. e. $d_{\mathrm{BV}} < r_{\mathrm{cir}}$, the intersection circle intersects the corresponding triangle side. Every triangle side can be intersected up to two times by the intersection circle depending on the contact region. The set $\mathcal{I} = \{\mathrm{I}_{12,\mathrm{i/ii}}, \mathrm{I}_{13,\mathrm{i/ii}}, \mathrm{I}_{23,\mathrm{i/ii}}\}$, see also Fig. 2.9b, defines all possible intersection points on the triangle. First, the global vectors $\boldsymbol{r}_{OV}$ to the vertical projection points $\mathcal{V}$ are calculated using the distance d_{TV} between $\mathcal{T} = \{\mathrm{T}_1, \mathrm{T}_1, \mathrm{T}_2\}$ and $\mathcal{V} = \{\mathrm{V}_{12}, \mathrm{V}_{13}, \mathrm{V}_{23}\}$ as

$$d_{TV} = \boldsymbol{\lambda}_{TB} \bullet \boldsymbol{\lambda}_s^0, \tag{2.51}$$

$$\boldsymbol{r}_{OV} = \boldsymbol{r}_{OT} + d_{TV}\, \boldsymbol{\lambda}_s^0. \tag{2.52}$$

Then, the distance between the vertical projections points $\mathcal{V}$ and the intersection points $\mathcal{I}$ are obtained as

$$d_{VI} = \sqrt{r_{\mathrm{cir}}^2 - d_{\mathrm{BV}}^2}, \quad \forall I \in \mathcal{I}. \tag{2.53}$$

The points of intersection $\boldsymbol{r}_{OI}$ can finally be described by

$$\boldsymbol{r}_{OI} = \boldsymbol{r}_{OV} \pm d_{VI}\, \boldsymbol{\lambda}_s^0. \tag{2.54}$$

Only if these intersection points exist and lie within the triangle sides, they are real intersections. Hence, the number of triangle intersections n_{int} is obtained. Finally, the distance between the triangle's midpoint M and point B is calculated

$$d_{\mathrm{BM}} = ||\boldsymbol{r}_{\mathrm{OB}} - \boldsymbol{r}_{\mathrm{OM}}||_2\,. \tag{2.55}$$

In conclusion, a particle is in contact with a triangle if one of the following pertains, see again Fig. 2.9:

- Case 1: contact in region 1,
- Case 2: if any intersection of the intersection circle with the triangle sides is present as shown in Fig. 2.9b, i. e. $n_{\mathrm{int}} > 0$,
- Case 3: if no intersection of the intersection circle with the triangle sides exists but the intersection circle is bigger than the triangle, i. e. $n_{\mathrm{int}} = 0 \wedge r_{\mathrm{cir}} > d_{\mathrm{BM}}$.

Similar to the sphere–sphere contact search, contact partners within a certain Verlet distance can be saved and checked in the following time steps for contact. To do so, the spheres are modeled with a higher imaginary radius, i. e. as $r_i + d_{\mathrm{v}}$. This increases the computational efficiency noticeably.

Contact Area For the contact force calculation, the area of the triangle within the intersection circle, named A_o, is necessary, see also dark gray area in Fig. 2.8 and Fig. 2.10. In sum eight different overlap scenarios exist, as defined in Fig. 2.10. Note, that there is no direct correlation between the three different contact regions of Fig. 2.9a, i. e. interior, vertex and edge region, and the eight overlap scenarios shown in Fig. 2.10. For instance, a particle with contact region 1, i. e. inside the triangle, could be bigger than the triangle, could have intersections with the triangle, or could be small and have no intersections with the triangle. To calculate the overlapping areas, the angle α between point B and two neighboring intersection points I and J $\forall I, J \in \mathcal{I} = \{\mathrm{I}_{12,\mathrm{i/ii}}, \mathrm{I}_{13,\mathrm{i/ii}}, \mathrm{I}_{23,\mathrm{i/ii}}\}$ & $J \neq I$ is necessary, see also Fig. 2.9b. The angle α is calculated by the direction vectors $\boldsymbol{\lambda}_{\mathrm{B}I}$ and $\boldsymbol{\lambda}_{\mathrm{B}J}$ pointing from boundary point B to the intersection points I and J, respectively. The angle α follows to

$$\boldsymbol{\lambda}_{\mathrm{B}I/J} = \boldsymbol{r}_{OI/J} - \boldsymbol{r}_{\mathrm{OB}}, \tag{2.56}$$

$$\alpha = \arccos\left(\frac{\boldsymbol{\lambda}_{\mathrm{B}I} \bullet \boldsymbol{\lambda}_{\mathrm{B}J}}{||\boldsymbol{\lambda}_{\mathrm{B}I}||_2 \cdot ||\boldsymbol{\lambda}_{\mathrm{B}J}||_2}\right). \tag{2.57}$$

For all angles $\alpha > \pi$, e. g. for contacts within contact region 1 of Fig. 2.9b, the angle needs to be adopted as $\alpha = 2\,\pi - \alpha$. Point B and the intersection points I

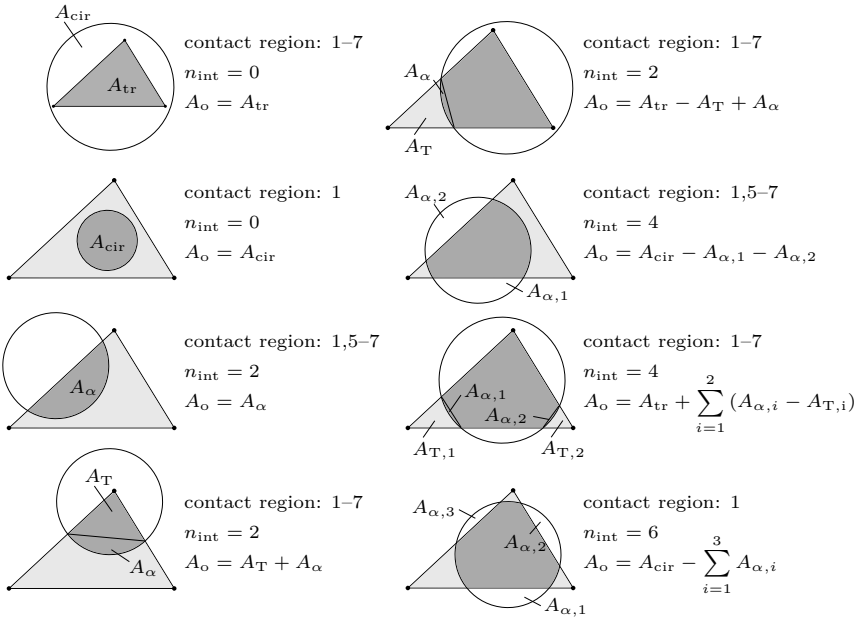

Figure 2.10: Sphere–triangle overlap scenarios.

and J span the area

$$A_{\mathrm{B}} = \frac{1}{2}\, r_{\mathrm{cir}}^2 \cdot \sin(\alpha), \tag{2.58}$$

see also light green area in Fig. 2.9b. The circle sector defined by point B and the intersection points, shown as a dark green area in Fig. 2.9b, is obtained as

$$A_\alpha = \frac{1}{2}\, r_{\mathrm{cir}}^2\, \alpha - A_{\mathrm{B}} = \frac{1}{2}\, r_{\mathrm{cir}}^2\, (\alpha - \sin(\alpha))\,. \tag{2.59}$$

If the intersection points I and J lie on two different triangle sides, the corresponding triangle edge point between those two intersection points $T \in \hat{\mathcal{T}} = \{\mathrm{T}_1, \mathrm{T}_2, \mathrm{T}_3\}$ and the intersection points I and J span the area A_{T}, see Fig. 2.10. For this, the direction vectors $\boldsymbol{\lambda}_{TI}$ and $\boldsymbol{\lambda}_{TJ}$ are defined, pointing from triangle point T to intersection point I and J, respectively. The area A_{T} is obtained to

$$\boldsymbol{\lambda}_{TI/J} = \boldsymbol{r}_{\mathrm{O}I/J} - \boldsymbol{r}_{\mathrm{O}T}, \tag{2.60}$$

$$A_{\mathrm{T}} = \frac{1}{2}\, ||(\boldsymbol{\lambda}_{TI} \times \boldsymbol{\lambda}_{TJ})||_2\,. \tag{2.61}$$

Finally, the area ratio of the overlap surface A_{o} to the area of the intersection circle A_{cir}, see Fig. 2.10, is obtained as

$$\kappa_{\mathrm{A}} = \frac{A_{\mathrm{o}}}{A_{\mathrm{cir}}}. \tag{2.62}$$

For the later normal contact force calculation, κ_{A} is used as a scaling factor for sphere–triangle contacts.

Edge and Corner Contacts Besides contact with the triangle's surface, a particle can also have contact with the edges and corners of the bounding geometry. In Fig. 2.11 a schematic representation of a sphere's contact with a triangle's surface and with a triangle's edge or corner is shown.

For a particle contact with multiple triangle surfaces, the contact forces of all penetrated triangles act at the boundary point B, even if this point is not located within the triangle. The normal contact force points in the normal direction of the triangle. If all triangles are coplanar, the normal contact force can be obtained as if it was a sphere–plane contact.
If a particle comes in contact with an edge or a corner of the bounding geometry, the calculation of the penetration depth and normal force direction changes. A property of impacts is that the penetration depth is small compared to the particle size, i. e. $\delta_{il} \ll r_i$. This is used to efficiently detect these edge/corner contacts. If a sphere has contact with the triangle's surface, Eq. (2.18) is used to determine the penetration depth, i. e. the triangle is treated as a plane. However, for an edge/corner contact this results in an unrealistically high penetration, as indicated by $\widetilde{\delta}$ in Fig. 2.11. The maximum penetration of a sphere into a triangle

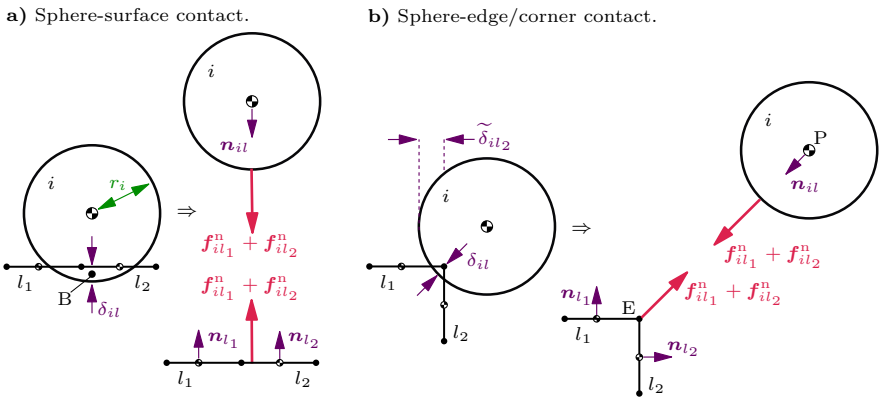

Figure 2.11: Different sphere–triangle contact situations.

surface $\delta_{\max}$ can be calculated by Hertz impact theory [Hertz82] and will be introduced later, see Eq. (2.80). Here, an edge or corner contact is assumed if the sphere is not within contact region 1 and $\widetilde{\delta}_{il} > 2\,\delta_{il,\max}$, with two as a safety factor.

The vector between the sphere's midpoint P and edge/corner E is calculated as

$$\boldsymbol{r}_{\mathrm{EP}} = \boldsymbol{x}_i - \boldsymbol{r}_{OT} \quad \text{for contact regions } 2-4, \tag{2.63}$$

$$\boldsymbol{r}_{\mathrm{EP}} = \boldsymbol{x}_i - \boldsymbol{r}_{OV} \quad \text{for contact regions } 5-7, \tag{2.64}$$

with T and V being the intersection points with the triangle's edge or side, respectively, see also Fig. 2.9. The distance, overlap and normal direction of the edge/corner contacts are obtained by

$$d_{il} = ||\boldsymbol{r}_{\mathrm{EP}}||_2\,, \tag{2.65}$$

$$\delta_{il} = r_i - d_{il}, \tag{2.66}$$

$$\boldsymbol{n}_{il} = \frac{\boldsymbol{r}_{\mathrm{EP}}}{||\boldsymbol{r}_{\mathrm{EP}}||_2}. \tag{2.67}$$

As an edge or corner is made up of two or more triangles, the contact force needs to be distributed over these. For this, the area ratio κ_{A} is used as

$$\kappa_{\mathrm{A}} = \frac{1}{n_{\mathrm{E},i}}, \tag{2.68}$$

with $n_{\mathrm{E},i}$ being the number of edge/corner contacts of the i-th particle.

Contact Kinematics All quantities are calculated analogously to Eq. (2.19)–Eq. (2.27) and $l \mathrel{\widehat{=}} k$.

2.3 Contact Forces and Torques

In DEM simulations, continuous particle–particle and particle–bounding geometry contacts occur. The contact partners are treated as rigid, thus only touching in a single point, i. e. the contact point B. Because of this, the contact partners are allowed to overlap and are virtually connected by unilateral springs and dampers, as shown in Fig. 2.12. Thus, normal and frictional contact forces and resulting torques occur. While normal contact forces counteract the overlap, friction forces occur due to the surface roughness.

Normal Contact Forces For the calculation of the normal contact forces, various models have been developed, see e. g. [Hertz82, Johnson03, WaltonBraun86]. The contact law of Hertz [Hertz82] is widely used for a sphere–sphere contact, as it is based on physical parameters of the contact partners i and j, namely the particle radius $r_{i/j}$, Young's modulus $E_{i/j}$ and Poisson's ratio $\nu_{i/j}$. The Hertz force law is also suitable for contacts of a sphere with other elliptical shapes or planes [Goldsmith60]. Hertz contact law follows from continuum mechanic considerations and reads

$$F_\mathrm{n} = k_\mathrm{n}\, \delta_{ij}^{3/2}, \tag{2.69}$$

with normal stiffness

$$k_\mathrm{n} = \frac{4}{3}\, \bar{E}\, \sqrt{\bar{R}}. \tag{2.70}$$

The effective Young's modulus $\bar{E}$ and effective radius $\bar{R}$ follow to

$$\frac{1}{\bar{E}} = \frac{1-\nu_1^2}{E_1} + \frac{1-\nu_2^2}{E_2}, \tag{2.71}$$

$$\frac{1}{\bar{R}} = \frac{1}{r_1} + \frac{1}{r_2}. \tag{2.72}$$

If the contact partner of a sphere is a bounding geometry, the radius r_2 needs to be adjusted [Goldsmith60] to approximate the geometries as

$$r_2 = \infty \quad \text{for planes \& triangles,} \tag{2.73}$$

$$r_2 = 2\, r_\mathrm{cyl} \quad \text{for cylinder outside contacts,} \tag{2.74}$$

$$r_2 = -2\, r_\mathrm{cyl} \quad \text{for cylinder inside contacts.} \tag{2.75}$$

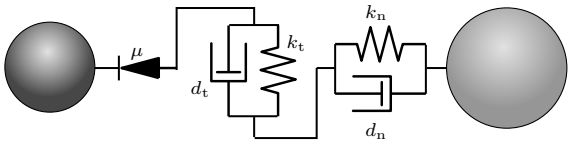

Figure 2.12: Contact model for a sphere–sphere contact.

It should be noted that for sphere–triangle contacts, the normal contact force needs to be scaled by the area ratio κ_A, see Eqs. (2.62) and (2.68) as $F_\mathrm{n} = \kappa_\mathrm{A}\, F_\mathrm{n}$. The normal contact force is projected onto the coordinate axes via

$$\boldsymbol{f}_{ij}^\mathrm{n} = -F_\mathrm{n}\, \boldsymbol{n}_{ij}. \tag{2.76}$$

The drawback of Hertz's contact law is that no energy loss is modeled during the normal contact. Such an energy loss could occur due to plastic deformations of the contact zone for metal contact partners or visco-elastic dissipation of polymers. [LankaraniNikravesh90] therefore extended the force law of Hertz by a dissipative term depending on the *coefficient of restitution* (COR) ε to introduce an energy dissipation. The COR ($0 < \varepsilon < 1$) controls the amount of energy dissipation during the contact. [LankaraniNikravesh90] force law reads

$$F_\mathrm{n} = k_\mathrm{n}\, \delta_{ij}^{3/2} \left(1 + \frac{3}{4}\left(1-\varepsilon^2\right)\frac{\dot{\delta}_{ij}}{\dot{\delta}_0}\right), \tag{2.77}$$

with $\dot{\delta}_0$ being the initial penetration velocity in normal direction of both collision partners. The force law of [LankaraniNikravesh90] is suitable for high COR values, i. e. $\varepsilon > 0.8$. For lower COR values [GonthierEtAl04] adapted [LankaraniNikravesh90] force law by introducing the effective nonlinear damping parameter $\bar{d}$ as

$$F_\mathrm{n} = k_\mathrm{n}\, \delta_{ij}^{3/2} \left(1 + \frac{\bar{d}}{\varepsilon}\frac{\dot{\delta}_{ij}}{\dot{\delta}_0}\right). \tag{2.78}$$

This normal force law is used as default in this work if not stated differently. The nonlinear parameter $\bar{d}$ follows from

$$\frac{1 + \bar{d}/\varepsilon}{1 - \bar{d}} = \mathrm{e}^{\bar{d}(1+1/\varepsilon)}. \tag{2.79}$$

The nonlinear Eq. (2.79) is only depending on ε and can be solved offline and stored as a lookup table [GonthierEtAl04]. The solution to Eq. (2.79), i. e. $\bar{d}$, is shown in Fig. 2.13.

Based on Hertz impact theory the maximum penetration δ_max of two colliding bodies can be calculated [Barber18] as

$$\delta_\mathrm{max} = \left(\frac{5\,\bar{M}\,\dot{\delta}_0^2}{4\,k_\mathrm{n}}\right)^{\frac{2}{5}}, \tag{2.80}$$

with effective mass $\bar{M}$

$$\frac{1}{\bar{M}} = \frac{1}{M_1} + \frac{1}{M_2}, \tag{2.81}$$

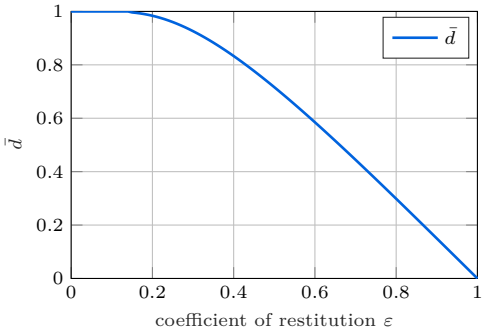

Figure 2.13: Nonlinear damping parameter $\bar{d}$.

and $M_{1/2}$ being the mass of each body. The recoverable strain energy stored during contact, i. e. due to the contact stiffness k_n, follows to

$$E_\mathrm{con} = \int_0^\delta \left(k_\mathrm{n}\, \delta^{3/2}\right) \mathrm{d}\delta = \frac{2}{5}\, \mathrm{k_n}\, \delta^{5/2}. \tag{2.82}$$

This energy is completely resolved after contact and hereafter referred to as *contact energy*. Some time integrators make use of the so-called linear contact eigenfrequency of two identical spheres, see [Luding08a], which is defined as

$$\omega_\mathrm{con} = \sqrt{\frac{k_\mathrm{n}}{m_i}}. \tag{2.83}$$

Friction Contact Forces For many particle systems, friction needs to be taken into account. Whenever a particle collision is oblique, friction forces occur due to the surface roughness of the colliding bodies. To model friction, an appropriate force law needs to be chosen, based on the dynamics of the particle system. For highly dynamic systems, sticking friction can often be neglected, while for quasi-static applications it is very important [FleissnerEtAl07]. Pure sliding friction, see [BrendelDippel98], reads

$$\boldsymbol{f}_{ij}^\mathrm{t} = -\mu\, F_\mathrm{n}\, \boldsymbol{t}_{ij}, \tag{2.84}$$

with μ being the coefficient of friction. However, pure sliding friction can cause numerical instabilities, due to the jump in friction force at zero relative tangential velocity. To avoid these jumps in the friction forces, Eq. (2.84) is extended by a smoothing hyperbolic tangent function by [AnderssonEtAl07] to

$$\boldsymbol{f}_{ij}^\mathrm{t} = -\mu\, F_\mathrm{n}\, \boldsymbol{t}_{ij} \cdot \tanh(\eta \left|\left|\boldsymbol{v}_{\mathrm{B},ij}^\mathrm{t}\right|\right|_2), \tag{2.85}$$

with η being a smoothing parameter. This friction force law is used as default in this work if not stated differently. To model friction including sticking more

sophisticated force algorithms are necessary. These penalty laws often extend sliding friction by a tangential stiffness coefficient k_t and damping coefficient d_t, see also Fig. 2.12. An early model is proposed by [CundallStrack79]. Since then, various improved models have been proposed, see e. g. [Di RenzoDi Maio05, Kruggel-EmdenEtAl07, Luding08a, WaltonBraun86]. Besides the friction forces due to the tangential relative motion, also rolling and torsion resistance torques could be considered [Luding08a]. However, for many applications, these are negligible.

Contact Torques In DEM simulations, different contact torques can occur. Normal and tangential contact forces create torques that are acting on the particles' and rigid bodies' centers of mass. Rolling and torsion resistance torques also have to be considered if used. The total torques $\boldsymbol{\ell}_{ij}$ between particle i and contact partner j are obtained using the total contact force $\boldsymbol{f}_{ij}$ as

$$\boldsymbol{f}_{ij} = \boldsymbol{f}_{ij}^\mathrm{n} + \boldsymbol{f}_{ij}^\mathrm{t}, \tag{2.86}$$

$$\boldsymbol{\ell}_{ij} = \boldsymbol{\ell}_{ij}^\mathrm{t} + \boldsymbol{r}_{\mathrm{PB},ij} \times \boldsymbol{f}_{ij}, \tag{2.87}$$

with $\boldsymbol{\ell}_{ij}^\mathrm{t}$ being rolling and torsional resistance torques, see [Luding08a], and $\boldsymbol{r}_{\mathrm{PB},ij}$ the direction vector from the particle's center of mass P to the boundary point B. For spherical particles, the normal contact forces are always pointing towards the center of mass of the particles. Hence, the contact torques simplify to

$$\boldsymbol{\ell}_{ij} = \boldsymbol{\ell}_{ij}^\mathrm{t} + \bar{r}_i \, \boldsymbol{n}_{ij} \times \boldsymbol{f}_{ij}^\mathrm{t}. \tag{2.88}$$

The torques on the rigid body are obtained analogously to Eq. (2.87) as

$$\boldsymbol{\ell}_{\mathrm{rb},ij} = -\boldsymbol{\ell}_{ij}^\mathrm{t} - \boldsymbol{r}_{\mathrm{RB},ij} \times \boldsymbol{f}_{ij}. \tag{2.89}$$

2.4 Particle and Rigid Body Accelerations

To obtain the particles' translational and rotational accelerations, Eq. (2.1) and Eq. (2.2) are solved. The particle translational accelerations follow to

$$\ddot{\boldsymbol{x}}_i = \frac{1}{m_i} \boldsymbol{f}_{\mathrm{a},i}. \tag{2.90}$$

Written in the body-fixed frame, the inertia tensor of arbitrary particles is diagonal and constant as $\boldsymbol{I}_i = \mathrm{diag}\left([I_i^x,\, I_i^y,\, I_i^z]^\top\right)$ and the angular accelerations

expressed in the body-fixed frame follow to

$$\dot{\boldsymbol{\omega}}_i = \begin{bmatrix} \dfrac{\ell^x_{\mathrm{a},i}}{I^x_i} + \omega^y_i\,\omega^z_i\,\dfrac{I^y_i - I^z_i}{I^x_i} \\ \dfrac{\ell^y_{\mathrm{a},i}}{I^y_i} + \omega^x_i\,\omega^z_i\,\dfrac{I^z_i - I^x_i}{I^y_i} \\ \dfrac{\ell^z_{\mathrm{a},i}}{I^z_i} + \omega^x_i\,\omega^y_i\,\dfrac{I^x_i - I^y_i}{I^z_i} \end{bmatrix}, \tag{2.91}$$

with all quantities given in the body-fixed frame. For spherical particles, the angular accelerations can be set up in the inertial frame and follow to

$$\dot{\boldsymbol{\omega}}_i = \frac{1}{I_i}\,\boldsymbol{\ell}_{\mathrm{a},i}. \tag{2.92}$$

The rigid body accelerations only need to be solved if the rigid body is described by an underlying *ordinary differential equation* (ODE), e. g. a multibody system. Otherwise, the rigid body's movement is static or is described by a rheonomic constraint, i. e. its movement is given by the user. In the case of a description by an ODE, the rigid body's contact forces and contact torques are applied to the ODE resulting in the rigid body's translational acceleration $\ddot{x}_{\mathrm{rb},j}$ and angular acceleration $\dot{\boldsymbol{\omega}}_{\mathrm{rb},j}$.

2.5 Time Integration

Another very important part of the DEM is the time integration of Eq. (2.90) and Eq. (2.92). The contact detection and computation of contact forces are the most time-consuming elements in DEM simulations and thus the numerical effort for the time integrator itself is negligible. However, the number of evaluations of the equation of motion during time integration and the stability of the simulation are highly dependent on it. Therefore, the time integrator needs to be chosen carefully.
In *molecular dynamics*, the *Verlet* integrator [Verlet67] is often used. As the DEM evolved from molecular dynamics, the Verlet integrator can also be applied to the DEM. It is a rather simple algorithm but might lack in stability [Fleissner10, Matuttis14]. Hence, more sophisticated time integration schemes are necessary. Due to dissipative normal forces and friction forces, the right-hand side of Eq. (2.90) and Eq. (2.92) are generally non-smooth. That is why higher-order time integration schemes do not apply to the DEM as they are too

sensitive to jumps of the contact forces [Fleissner10]. There is much literature about the proper choice of a time integration scheme with partially oppositional statements [Fleissner10, Pöschel05, Matuttis14, NorouziEtAl16].
Common integrators in DEM are the *central difference* [O'SullivanBray04], *Gear's predictor-corrector* algorithm of different orders [Gear67], the *Newmark−β* method and the *Generalized−α method* [Fleissner10]. A comparison of various integration algorithms is presented in [RougierEtAl04] and [TuleyEtAl10]. In the following, first, the Verlet integration scheme is presented in detail due to its simplicity. Afterward, the Gear predictor-corrector integration scheme is discussed and applied for all the following simulations in this work.

2.5.1 Verlet Integration Scheme

The symplectic Verlet integration scheme [Verlet67] is commonly used for DEM simulations, even though particle systems are not symplectic. This scheme can also be found under the names *classical Verlet* scheme or *Störmer-Verlet* scheme. The algorithm is based on the second-order equations of motion and is mainly applied for the integration of the translational particle states [Matuttis14]. The positions of the particle system at time $t + \Delta t$, with Δt being the time step size, are obtained by the previous two positions and the resulting particle acceleration of the last time step as

$$\boldsymbol{x}_i(t + \Delta t) = 2\,\boldsymbol{x}_i(t) - \boldsymbol{x}_i(t - \Delta t) + \Delta t^2\,\ddot{\boldsymbol{x}}_i(t). \tag{2.93}$$

The particle velocities can be obtained from central finite differences

$$\dot{\boldsymbol{x}}_i(t) = \frac{1}{2\,\Delta t}\left(\boldsymbol{x}_i(t + \Delta t) - \boldsymbol{x}_i(t - \Delta t)\right). \tag{2.94}$$

The Verlet algorithm is not "self-starting", i. e. at starting time t_0 the position $\boldsymbol{x}_i(t_0 - \Delta t)$ is necessary but unknown. Hence, for the first time step either a different integration scheme is used or $\boldsymbol{x}_i(t_0 - \Delta t) = \boldsymbol{x}_i(t_0)$ is applied if the details of the initial conditions are not of high importance. This is e. g. the case for many highly dynamic systems. From Eq. (2.94) follows that the velocities of the particle system are known one time step after the corresponding accelerations. The particle accelerations are, however, necessary to calculate the particle positions, see Eq. (2.93). Thus, velocity-dependent forces should not be used with the Verlet integration scheme, being another disadvantage of this method.

Besides the classical Verlet method, different derivatives like the *velocity-Verlet* method and *higher-order velocity-Verlet* methods [Matuttis14] exist. All of these Verlet integration schemes are, however, only conditionally stable. The proper choice of the time step size depends consequently on the granular system and can be a time-consuming task.

2.5.2 Gear Predictor-Corrector Integration Scheme

The Gear predictor-corrector integration scheme [Gear67] is particularly suited to handle a non-smooth right-hand side with steep gradients of the equation of motion and leads to good stability [Pöschel05]. The algorithm is more complicated than others, e. g. the Verlet integrator. However, as the time spent within the time integration scheme is small compared to contact detection and contact force evaluation in DEM simulations, significant time savings can be achieved with this integration scheme. Hence, this time integration scheme is used as default in this work.

For better readability, only the integration of the translational degrees of freedom is described here. The algorithm can be applied analogously for particle rotations or rigid body dynamics. It should be considered that for spherical particle systems, the rotational dynamics can be integrated straightforwardly. However, for more complex shapes, quaternions should be used [FleissnerEtAl07].

The Gear algorithm can be implemented at any desired order p. Here, the algorithm up to order five is presented. The Gear algorithm consists of two parts. First, the states of the next time step including higher-order time derivatives are computed by using a Taylor expansion in the predictor step:

Predictor Step:

$$\boldsymbol{x}_i^{\mathrm{p}}(t+\Delta t) = \boldsymbol{x}_i(t) + \Delta t\, \dot{\boldsymbol{x}}_i(t) + \frac{1}{2}\Delta t^2\, \ddot{\boldsymbol{x}}(t) + \frac{1}{6}\Delta t^3\, \dddot{\boldsymbol{x}}_i(t) + \frac{1}{24}\Delta t^4\, \ddddot{\boldsymbol{x}}_i(t), \tag{2.95}$$

$$\dot{\boldsymbol{x}}_i^{\mathrm{p}}(t+\Delta t) = \dot{\boldsymbol{x}}_i(t) + \Delta t\, \ddot{\boldsymbol{x}}_i(t) + \frac{1}{2}\Delta t^2\, \dddot{\boldsymbol{x}}(t) + \frac{1}{6}\Delta t^3\, \ddddot{\boldsymbol{x}}_i(t), \tag{2.96}$$

$$\ddot{\boldsymbol{x}}_i^{\mathrm{p}}(t+\Delta t) = \ddot{\boldsymbol{x}}_i(t) + \Delta t\, \dddot{\boldsymbol{x}}_i(t) + \frac{1}{2}\Delta t^2\, \ddddot{\boldsymbol{x}}_i(t), \tag{2.97}$$

$$\dddot{\boldsymbol{x}}_i^{\mathrm{p}}(t+\Delta t) = \dddot{\boldsymbol{x}}_i(t) + \Delta t\, \ddddot{\boldsymbol{x}}_i(t), \tag{2.98}$$

$$\ddddot{\boldsymbol{x}}_i^{\mathrm{p}}(t+\Delta t) = \ddddot{\boldsymbol{x}}_i(t). \tag{2.99}$$

Next, the predicted positions $\boldsymbol{x}_i^{\mathrm{p}}(t+\Delta t)$ and velocities $\dot{\boldsymbol{x}}_i^{\mathrm{p}}(t+\Delta t)$ are used to calculate the new particle accelerations $\ddot{\boldsymbol{x}}_i^{\mathrm{c}}$ by evaluating Eq. (2.90) and Eq. (2.92). The difference in accelerations between predicted and re-calculated accelerations $\Delta\ddot{\boldsymbol{x}}_i$ is used to correct the state vector. For this, the coefficients c_i, which depend on the Gear algorithm's order p, are defined as listed in Tab. 2.2. For an algorithm of p-th order, p coefficients are necessary. The correction step is either performed once or until the error ϵ, see Eq. (2.103), falls below the threshold value of one. For this, the relative error tolerance τ_{rel} and absolute error tolerance τ_{abs} are defined. Additionally, a maximum counter of correction steps $n_{\mathrm{max}}^{\mathrm{c}}$ is used. The corrector steps follow as:

Table 2.2: Coefficients of Gear integration scheme.

p	c_0	c_1	c_2	c_3	c_4	c_5
4	$\frac{1}{6}$	$\frac{5}{6}$	1	$\frac{1}{3}$	0	0
5	$\frac{19}{90}$	$\frac{3}{4}$	1	$\frac{1}{2}$	$\frac{1}{12}$	0
6	$\frac{3}{16}$	$\frac{251}{360}$	1	$\frac{11}{18}$	$\frac{1}{6}$	$\frac{1}{60}$

Corrector Steps:
Calculate new accelerations by Eq. (2.90) and Eq. (2.92) utilizing the predicted positions $\boldsymbol{x}^{\mathrm{p}}(t+\Delta t)$ and velocities $\dot{\boldsymbol{x}}^{\mathrm{p}}(t+\Delta t)$ as

$$\ddot{\boldsymbol{x}}_i^{\mathrm{c}}(t+\Delta t) = \ddot{\boldsymbol{x}}_i\left(\boldsymbol{x}^{\mathrm{p}}(t+\Delta t), \dot{\boldsymbol{x}}^{\mathrm{p}}(t+\Delta t)\right). \tag{2.100}$$

Difference between predicted and re-calculated accelerations

$$\Delta\ddot{\boldsymbol{x}}_i = \ddot{\boldsymbol{x}}_i^{\mathrm{c}}(t+\Delta t) - \ddot{\boldsymbol{x}}_i^{\mathrm{p}}(t+\Delta t). \tag{2.101}$$

Correct whole state vector

$$\begin{bmatrix} \boldsymbol{x}_i^{\mathrm{c}}(t+\Delta t) \\ \dot{\boldsymbol{x}}_i^{\mathrm{c}}(t+\Delta t) \\ \ddot{\boldsymbol{x}}_i^{\mathrm{c}}(t+\Delta t) \\ \dddot{\boldsymbol{x}}_i^{\mathrm{c}}(t+\Delta t) \\ \ddddot{\boldsymbol{x}}_i^{\mathrm{c}}(t+\Delta t) \end{bmatrix} = \begin{bmatrix} \boldsymbol{x}_i^{\mathrm{p}}(t+\Delta t) \\ \dot{\boldsymbol{x}}_i^{\mathrm{p}}(t+\Delta t) \\ \ddot{\boldsymbol{x}}_i^{\mathrm{p}}(t+\Delta t) \\ \dddot{\boldsymbol{x}}_i^{\mathrm{p}}(t+\Delta t) \\ \ddddot{\boldsymbol{x}}_i^{\mathrm{p}}(t+\Delta t) \end{bmatrix} + \begin{bmatrix} c_0 \\ c_1 \frac{1}{\Delta t^1} \\ c_2 \frac{2}{\Delta t^2} \\ c_3 \frac{6}{\Delta t^3} \\ c_4 \frac{24}{\Delta t^4} \end{bmatrix} \frac{\Delta t^2}{2} \Delta\ddot{\boldsymbol{x}}_i. \tag{2.102}$$

Calculate error

$$\epsilon = \max\left(\frac{||\Delta\ddot{\boldsymbol{x}}_i||_2}{\tau_{\mathrm{abs}} + \tau_{\mathrm{rel}} \cdot ||\ddot{\boldsymbol{x}}_i^{\mathrm{c}}||_2} \right). \tag{2.103}$$

Update predictor states by corrector states for all time derivatives if multiple correction steps are used and if $\epsilon > 1$ as

$$\frac{\mathrm{d}^\iota}{\mathrm{d}t^\iota}\boldsymbol{x}^{\mathrm{p}}(t+\Delta t) = \frac{\mathrm{d}^\iota}{\mathrm{d}t^\iota}\boldsymbol{x}^{\mathrm{c}}(t+\Delta t), \quad \forall \iota \in \{0:1:p-1\}, \tag{2.104}$$

and perform the corrector step again. If $\epsilon > 1$ and the maximum number of correction steps is reached, the step is rejected and the states are not updated. Instead, the time step size is reduced using a time step controller and the time step is calculated again.

Time Step Control:
The proper choice of the time step size is a very important quantity for the integration as it affects the integrator's stability, accuracy and overall simulation

time. As a particle system can exhibit completely different dynamics during the time integration, the use of an undersized time step size can result in an immense overhead. Therefore, an appropriate time step control algorithm should be used to match the desired accuracy while using the largest possible time step size throughout the simulation.

Many time step controllers are indeed not applicable to DEM due to the special right-hand side of the equation of motion [Fleissner10]. In [Zohdi04] a time step control is proposed for multi-field particulate flows, using the rate of convergence of the error ϵ. In [Fleissner10], this algorithm is applied to the DEM. Finding appropriate tolerances can be a challenging task, however. By simplifying the algorithm, in [MeyerSeifried20] a robust and still efficient time step controller is achieved using the number of correction steps needed for the last time step n^{c} and the maximum allowed number $n^{\mathrm{c}}_{\mathrm{max}}$. The algorithm updates the time step size such that $n^{\mathrm{c}} \to 0.5\, n^{\mathrm{c}}_{\mathrm{max}}$. The new time step size is calculated as

$$\Delta t = \Delta t \cdot \kappa_{\mathrm{s}} \left(\frac{n^{\mathrm{c}}_{\mathrm{max}}}{2\, n^{\mathrm{c}}} \right)^{\frac{1}{p}}, \tag{2.105}$$

with $\kappa_{\mathrm{s}} = 0.9$ as a safety factor increasing the probability that the next time step is accepted [HairerEtAl08]. To prevent the time step size from decreasing and increasing too much, it is limited by

$$\Delta t = \max\left(\Delta t_{\mathrm{min}}, \min\left(\Delta t_{\mathrm{max}}, \Delta t\right)\right), \tag{2.106}$$

with Δt_{min} and Δt_{max} being the minimum and maximum time step sizes allowed. Established parameters of the Gear integration scheme, yielding a good accuracy and efficiency for various simulations, are shown in Tab. 2.3.

Table 2.3: Established parameters of the Gear integration scheme.

Δt_{min}	Δt_{max}	τ_{abs}	τ_{rel}	$n^{\mathrm{c}}_{\mathrm{max}}$
$1 \cdot 10^{-16}$	$\frac{\pi}{\max\left(\omega_{\mathrm{con},i}\right)}$	$1 \cdot 10^{-6}$	$1 \cdot 10^{-6}$	10

2.6 Post-Processing

When the predefined simulation time is reached, the time integrator stops and the post-processing starts, where all necessary and defined quantities are calculated from the resulting states. In Fig. 2.14 and Fig. 2.15 the simulation procedure and post-processing results of the drop-down test to generate the initial conditions of Fig. 2.2b using the fifth order Gear predictor-corrector algorithm with sliding friction and Gonthier's normal force law are shown and summarized.

The simulation starts with a high time step size, as no particle contacts exist, see Fig. 2.15a. With an increasing number of contacts, see Fig. 2.15d, the time step size reduces, but almost no time steps are rejected at the beginning. Simultaneously, the potential energy of the particle system decreases as its kinetic energy increases, see Fig. 2.15c. When the particles come to rest, the number of contacts is continuously increasing, see Fig. 2.15d. The kinetic energy converges to zero and the potential energy is dominant. Within the quasi-static phase, i. e. $t > 0.4\,\mathrm{s}$ the number of rejected time steps increases. In total 3 % of the 88 520 time steps are rejected. Within each time step, five correction steps are mostly necessary as forced by the time step controller, see Eq. (2.105) and Fig. 2.15b.

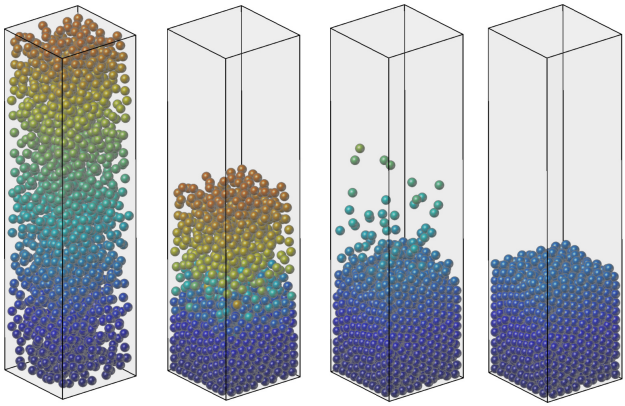

Figure 2.14: Snapshots of drop-down simulation of 1000 particles for times $t \in \{0\,\mathrm{s}, 0.1\,\mathrm{s}, 0.2\,\mathrm{s}, 0.5\,\mathrm{s}\}$.

a) Accepted and rejected time step sizes over time.

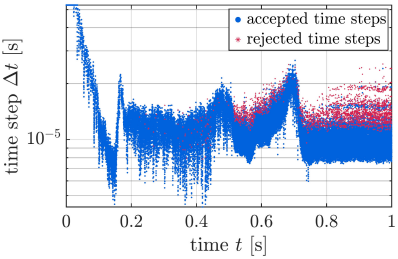

b) Frequency distribution of correction steps.

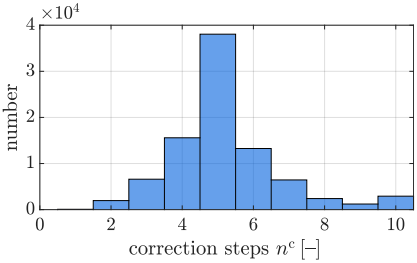

c) Energy distribution over time.

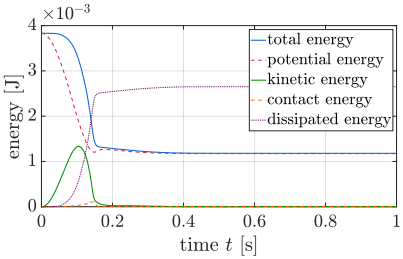

d) Number of contacts over time.

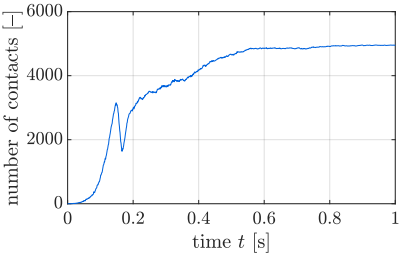

Figure 2.15: Post-processing results of the drop-down procedure shown in Fig. 2.14.

2.7 Applications

The DEM applies to a wide field of applications. In Fig. 2.16 various different examples are shown. As mentioned before, the DEM is not restricted to spherical particles, see for instance [BoonEtAl13, LuEtAl15, NetoWriggers21] and even complicated particle shapes can be modeled, see Fig. 2.16a and Fig. 2.16b for elliptical and multi-sphere particle shapes. Complicated bounding geometries can be modeled by triangular surface meshes, see Fig. 2.16c. Even very high particle numbers can be realized as shown in Fig. 2.16d. Finally, two examples of the later realized particle damper simulations are shown in Fig. 2.16e and Fig. 2.16f. While for most simulations no a-prior defined relations between particles exist, as demanded by its original concept, the DEM has also been modified, e. g. to model cutting processes of materials or elastic membranes [FleissnerEtAl07]. The DEM can also be coupled to another computation method. Multiple DEM-FEM coupling approaches have been developed, e. g. in [ChaudryEtAl22, WellmannWriggers12]. Also, DEM-CFD couplings are investigated [NorouziEtAl16].

a) Elliptical particle shape.

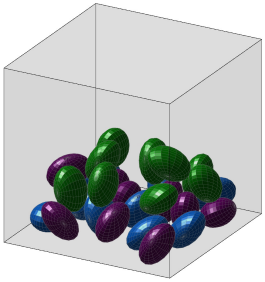

b) Multi-sphere particle shape.

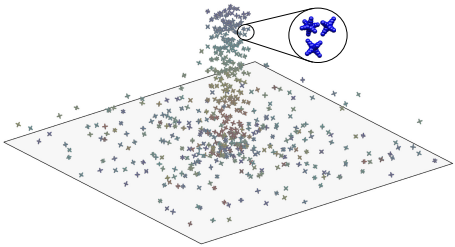

c) Particle extruder.

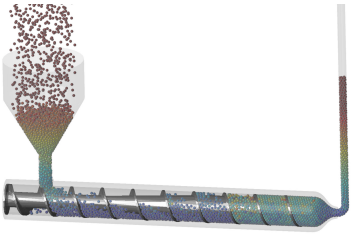

d) Wave channel.

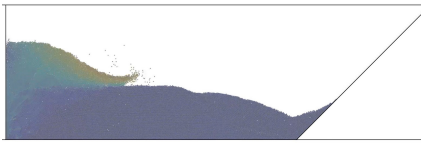

e) Cuboid particle damper.

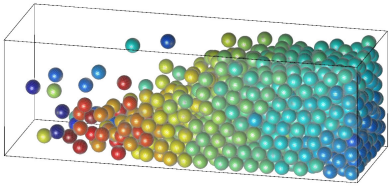

f) Cylindrical particle damper.

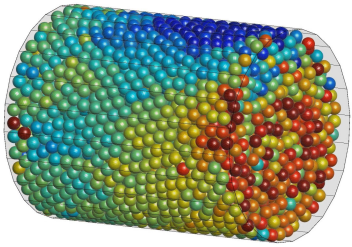

Figure 2.16: Examples of DEM simulations.

2.8 Simulation Parameters

For the DEM simulations in this work, mostly the same algorithms and parameters are used. These are summarized in the following. For time integration, the fifth order Gear predictor-corrector integration scheme is used, see Sect. 2.5.2. The utilized integration parameters are listed in Tab. 2.3. For contact search, the Verlet list updated by the non-binary search algorithm is applied, discussed in Sect. 2.2. The normal contact forces are calculated by Gonthier's formula, see Eq. (2.78). As particle dampers are highly dynamic systems, sliding friction by Andersson, i. e. Eq. (2.85), is applied. Rolling and torsion resistance torques are neglected.

Design Toolchain

Particle dampers show a nonlinear dynamical behavior, starting at the micromechanical effects during single particle impacts and sliding contacts, continuing with the energy dissipation inside the particle container and ending at the interaction within a structure. For a better understanding of particle dampers, and thus also for an efficient design, investigations on these different scales or levels, respectively, are necessary. A *systematic multiscale design methodology* in form of a *toolchain* is therefore developed, see Fig. 3.1 and [MeyerEtAl21]. Insights gained on one level can be transferred to the next level to better understand the dynamical properties of particle dampers and shorten the overall design process for an underlying structure. On all levels, numerical models, as well as experimental tests, can be used for analyses. The proper choice depends on the specific requirements at each level.

The **Single Particle Level**, see Sect. 3.1, analyzes single particle–particle and particle–wall interactions. A spherical particle collides with the collision partner in a defined manner. Experimentally, a spherical particle is suspended by thin wires and released from different heights to obtain different impact velocities with the collision partner. Numerically, the *finite element method* (FEM) is used and accurate material models are utilized. The energy dissipation during the impacts is of major interest and can be obtained from the velocities of both collision partners before and after the impact. The energy dissipation occurs due to *visco-*

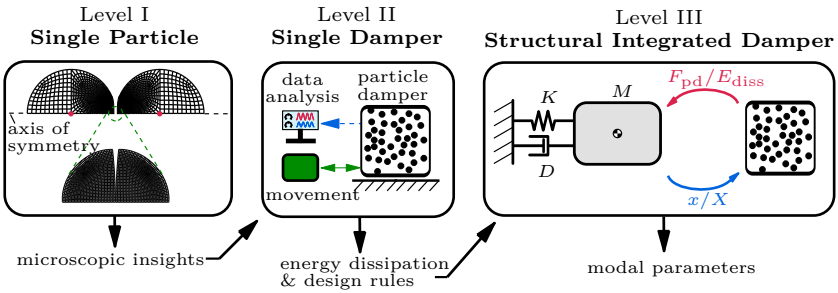

Figure 3.1: Toolchain for the analysis of particle dampers.

elastic or *elastic-viscoplastic* material behavior during the impacts, depending on the chosen materials. This kinetic energy loss is often described by the *coefficient of restitution* (COR), which can be used in the **Single Damper Level** for DEM (discrete element method) simulations. In addition, insights about noise transition, contact force and damage during these impacts are achieved.

The **Single Damper Level**, see Sect. 3.2, represents investigations of an isolated particle damper subjected to a defined horizontal or vertical vibration. The energy dissipation of the particle damper is determined for the given excitation frequency range and excitation amplitude range. The particle container is excited by a sinusoidal motion using a rheonomic constraint. This can be investigated numerically using DEM or experimentally. Experimental investigations can be realized using a closed-loop controlled shaker setup [MeyerSeifried21c] or a linear drive [MeyerSeifried22].
From the numerically given or experimentally measured velocity of the particle container and the excitation force, the *complex power* is determined [YangEtAl05]. Using the complex power, the *energy dissipation* and the *effective loss factor*, i. e. an efficiency factor, are obtained and displayed as characteristic diagrams over the excitation frequency and excitation amplitude. In addition, the *effective particle mass* is determined, describing how much the mass of the particles is coupled to the container movement. These characteristic diagrams are henceforth called *effective fields*. The calculated effective fields can be stored and used on the third level of the toolchain for the integration process of the particle dampers in a vibrating structure. If applicable, the effective fields might be approximated by analytical formulas, which can also be integrated on the next level. All these aspects help to shorten the design phase on the last level.

The **Structural Integrated Damper Level**, see Sect. 3.3, represents the integration of particle dampers in a vibrating structure to evaluate their overall damping effect. For numerical investigations, three different particle damper models are coupled to a numerical model of the structure. The flexible structure could be described by a reduced linear finite element model or a (flexible) multibody system [Shabana13]. In the first coupling approach, the complete DEM model describing the particle damper from the **Single Damper Level** is coupled to the model of the structure. While this approach is very accurate and useful for verification purposes, it is computationally very expensive. Alternatively, for coupling approach two and three, the flexible structure model can be coupled with the previous on the **Single Damper Level** determined effective fields or the analytical formulas. These couplings are easily implemented and lead to accurate results and significantly reduced computation times. Especially, the analytical formulas are very efficient and can be used for quick testing of different damper settings. Hence, an optimized damper can be found quickly by evaluating all possible damper variants. Also, insights from the analytical formulas can be used to derive systematic design guidelines for particle dampers.

In the following, the different levels of the toolchain are discussed in detail, see Sect. 3.1 for the **Single Particle Level**, Sect. 3.2 for the **Single Damper Level** and Sect. 3.3 for the **Structural Integrated Damper Level**. Furthermore, for all levels, the applied evaluation methods are presented. Afterward, in Chap. 4 the results of the **Single Particle Level** are expounded, as these analyses are independent of the other two following levels. In the following chapters, particle dampers are analyzed and applied to

- Chap. 5: Low excitation horizontal vibrations.
- Chap. 6: Medium excitation horizontal vibrations.
- Chap. 7: Medium excitation vertical vibrations.
- Chap. 8: High excitation vibrations.

Within these chapters on the **Single Damper Level**, single particle damper units with predefined characteristics are developed. These single particle damper units do not rely on a specific application. Mostly, simple particle systems are analyzed, but also different hybrid approaches are developed to increase the efficiency of the individual particle dampers. Afterward, these single particle damper units are applied to a vibrating structure on the **Structural Integrated Damper Level** and the overall damper efficiency is determined.
This chapter has partly been published in [MeyerSeifried20, MeyerEtAl21] as well as [MeyerSeifried21a, MeyerSeifried21b, MeyerEtAl22].

3.1 Level I: Single Particle Impacts

The micro-mechanical behavior during an impact of two bodies of macroscopic size, i. e. particle–particle or particle–wall, can mainly be characterized by the *coefficient of restitution* ε (COR) and the *friction coefficient* μ [Stronge18, PöschelBrilliantov01]. While the COR describes the energy loss due to the normal impact of two bodies, the friction coefficient models the losses by the tangential relative motion, due to the surface roughness of the bodies.

In many DEM simulations, a constant COR is used. However, this is not the case in reality, as the COR can depend on a variety of influence parameters, like the impact velocity [Goldsmith60]. These influence parameters are mainly associated with the energy dissipation effect of the material pairings. For metal bodies, the energy dissipation comes mainly from plastic deformations in the contact zone. For polymer bodies, visco-elastic energy dissipation occurs, due to compression

of the material. For both materials, the impact velocity has a big influence on the COR. Different authors investigated the COR, e. g. [PöschelBrilliantov01, Goldsmith60, SeifriedEtAl10]. For two impacting bodies (I and II) the kinematic COR is evaluated by the normal velocities v of the bodies before (0) and after (1) the collision, reading

$$\varepsilon = -\frac{v_{\mathrm{I}}^{1} - v_{\mathrm{II}}^{1}}{v_{\mathrm{I}}^{0} - v_{\mathrm{II}}^{0}}, \quad 0 \leq \varepsilon \leq 1. \tag{3.1}$$

Numerical and experimental models can be used to determine the COR as discussed in detail in Chap. 4 and [MeyerEtAl22]. The exact determination of the friction coefficient is indeed problematic. As the later particle dampers are highly dynamic systems, it is sufficient to neglect static friction [FleissnerEtAl07]. In [MeyerSeifried21c] it is shown that the usage of a constant coefficient of friction is often sufficient for accurate simulation results.

3.1.1 Impact Process

An impact is characterized by a short contact duration of two or more colliding bodies while a high contact force is exerted [Goldsmith60]. Figure 3.2 shows the general structure of a direct central impact problem. When two bodies collide on their line connecting their center of gravity, a central impact is achieved. As the resulting contact forces are only acting along this connecting line, the common center of gravity stays unaffected. However, due to possible dissipation losses during the impact, the normal velocities of the collision partners can change. This ranges from *fully elastic* contacts – no energy loss to *fully inelastic* contacts – both contact partners move with the same velocity afterward. Fully inelastic contacts are also referred to as *plastic contacts*. However, a plastic contact does not necessarily imply plastic deformations within the contact zone, as this depends on the used materials [Goldsmith60].

The impact process can be divided into two phases: *compression* and *restitution phase*. Both phases are described briefly in the following. See [Goldsmith60] for further discussions about this topic. The compression phase starts with the first contact of both bodies at $t = 0$ and ends at $t = t'$. At this time point, both bodies

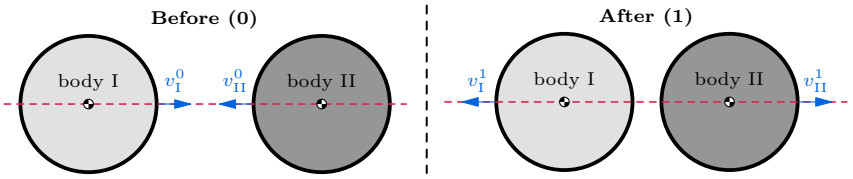

Figure 3.2: General central impact problem.

have the same rigid body normal velocity, i. e. zero relative movement. The normal contact force F_n first increases with time until it reaches its maximum value. If no wave propagation is present and the material behavior is rate-independent, the maximum normal contact force is achieved at $t = t'$ [Stronge18]. The linear impulse of the compression phase is described by

$$p_\mathrm{c} = \int_0^{t'} F_\mathrm{n}(t)\,\mathrm{d}t. \tag{3.2}$$

After the compression phase follows the restitution phase. Depending on the level of plasticity of the collision, the deformation will (partially) vanish or not. The contact force decreases starting from its maximum value down to zero at $t = t_\mathrm{e}$. The linear impulse follows to

$$p_\mathrm{r} = \int_{t'}^{t_\mathrm{e}} F_\mathrm{n}(t)\,\mathrm{d}t. \tag{3.3}$$

The compression and restitution phases are visualized in Fig. 3.3 for the cases of a *fully elastic, partly plastic* and *fully plastic* collisions. In case of a fully elastic contact, the linear momenta of compression and restitution phase are identical, hence, $p_\mathrm{c} = p_\mathrm{r}$. However, for (partly) plastic contacts this is no longer true. For partly plastic contacts $p_\mathrm{r} < p_\mathrm{c}$ and for plastic contacts $p_\mathrm{r} = 0$ holds.
The kinematic COR ε of Eq. (3.1) is a widely used key indicator to describe the occurring velocity change. For $\varepsilon = 1$ the impact is fully elastic, while for $\varepsilon = 0$ it is fully plastic. The linear impulse of the compression and restitution phase correlate as

$$p_\mathrm{r} = \varepsilon_\mathrm{kin}\, p_\mathrm{c}, \tag{3.4}$$

with ε_kin being the kinetic coefficient of restitution. For a central straight impact, kinematic and kinetic COR are identical [Stronge18]. If one of the impacting bodies is static, e. g. in case of a wall, Eq. (3.1) simplifies to

$$\varepsilon = -\frac{v_\mathrm{I}^1}{v_\mathrm{I}^0}. \tag{3.5}$$

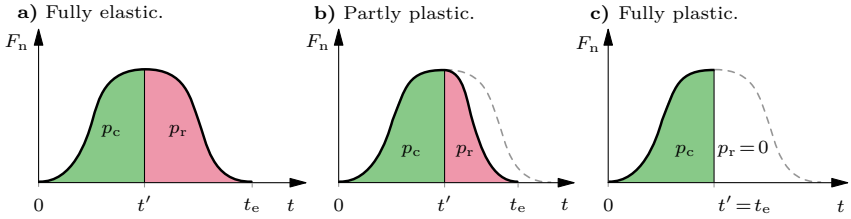

Figure 3.3: Contact force over time for different collision types.

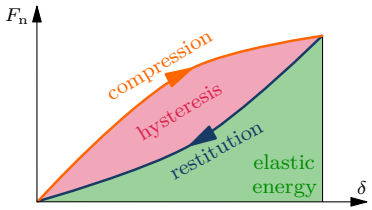

Figure 3.4: Compression and restitution phase for a direct central impact.

The COR can also be used as a measurement for the energy dissipation (hysteresis) caused by the collision as indicated in Fig. 3.4. In the compression phase, energy is stored in both collision partners. During the subsequent restitution phase, only a part of the elastic energy is transformed back into kinetic energy. The rest is dissipated by plastic deformations or heat. The dissipated energy E_diss can be calculated via the ring integral of the contact force F_n over the indentation δ to

$$E_\mathrm{diss} = \oint F_\mathrm{n}\,\mathrm{d}\delta. \tag{3.6}$$

If one body is static and the mass of the moving body is m, this simplifies to

$$E_\mathrm{diss} = \frac{1}{2}m\left(\left(v_\mathrm{I}^0\right)^2 - \left(v_\mathrm{I}^1\right)^2\right) = \frac{1}{2}m\left(v_\mathrm{I}^0\right)^2\left(1-\varepsilon^2\right). \tag{3.7}$$

3.2 Level II: Single Damper

On this level, investigations of an isolated particle damper, subjected to horizontal or vertical sinusoidal motion, are performed. The particle damper's effective fields, i. e. energy dissipation, effective loss factor and effective particle mass, for the given excitation frequency range and amplitude range are obtained using the *complex power method*. Additionally, insights about the movement of the particle bed, called *motion mode*, are gained. These motion modes are strongly related to the effective fields.
These investigations can be performed experimentally using a closed-loop controlled shaker setup, see e. g. [DuanChen10, MeyerSeifried21c, WongEtAl09b] or linear drives, see e. g. [MeyerSeifried22, SackEtAl13]. A linear drive is utilized in Chap. 5 and shown in Fig. 5.1. A shaker setup is shown in Fig. 8.1 of Chap. 8. Numerically, the DEM is used, see e. g. [MeyerSeifried21c, WongEtAl09b, YaoChen15]. An exemplary DEM model is shown in Fig. 3.5a.

The particle container is excited by a sinusoidal motion using a rheonomic constraint as

$$x_c = X \sin(\Omega t), \tag{3.8}$$

with container amplitude X and angular frequency $\Omega = 2\,\pi\,f$. The corresponding container velocity and acceleration follow as

$$\dot{x}_c = V \cos(\Omega t), \tag{3.9}$$

$$\ddot{x}_c = -A \sin(\Omega t), \tag{3.10}$$

with container velocity amplitude $V = X\,\Omega$ and container acceleration amplitude $A = X\,\Omega^2$. The dimensionless *excitation intensity* Γ is defined as

$$\Gamma = \frac{A}{g}, \tag{3.11}$$

with g as gravity constant.

3.2.1 Motion Modes

If a particle bed inside a container is subjected to a sinusoidal vibration, different motion modes can be observed depending on the particle properties and excitation conditions [SaluenaEtAl98, ZhangEtAl15]. To distinguish these motion modes, *animations, particle trajectories, velocity fields* and *experimental observations* can be used. Indeed, this task is not always trivial and unambiguous as the transition between the motion modes is smooth.
In Fig. 3.5 some examples of the *bouncing collect-and-collide* motion mode are shown to outline the differences between the analyses methods. Animations and experimental observations are especially suited for low-frequency vibrations with rather high amplitude, as the particle motion is easily observed, see Fig. 3.5a. The particle trajectories, obtained by DEM simulations, are meaningful for synchronized particle motions with the container, even if the excitation frequencies are high as shown in Fig. 3.5b. Velocity fields, also obtained by DEM simulations, apply to all kinds of vibrations but are not always as clear as animations or particle trajectories, see Fig. 3.5c.

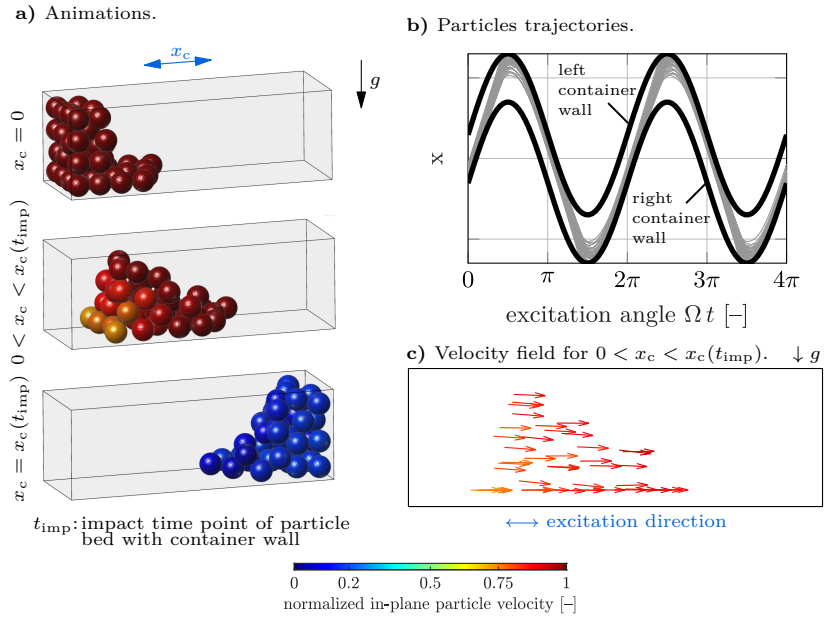

Figure 3.5: Bouncing collect-and-collide motion mode characterized by different techniques. The colors show the magnitude of the particle velocity normalized by the container velocity amplitude V from low (*blue*) to high (*red*).

3.2.2 Effective Fields

The effective fields, i. e. energy dissipation, effective loss factor and effective particle mass, of particle dampers can be analyzed by the complex power method, introduced by [YangEtAl05]. The complex power is calculated using the velocity of the particle container and its excitation force. Through experimental tests, both quantities are measured as discussed later in the individual chapters. For DEM simulations, the container's velocity is given by Eq. (3.9) and the excitation force is the sum of the container's inertia and the particles' contact forces onto the container walls in the corresponding excitation direction. The complex power is determined as

$$P^* = \frac{1}{2}\, F^*\, \overline{V}^{*\top}. \tag{3.12}$$

Variable F^* denotes the complex amplitude obtained by the *fast Fourier transform* (FFT) of the driving force signal acting on the particle container, while $\overline{V}^*$ is the conjugate complex amplitude found via FFT of the velocity signal of the container motion. See [OppenheimSchafer75, ProakisManolakis92] for further information on the FFT. The dissipated energy per cycle $\widetilde{E}_{\mathrm{diss}}$ follows from the

complex power to

$$\widetilde{E}_{\mathrm{diss}} = 2\,\pi\,E_{\mathrm{diss}} = \frac{2\,\pi}{\Omega}\cdot \mathrm{Real}(P^*). \tag{3.13}$$

Following [YangEtAl05] the loss factor η is defined as the ratio of the dissipated energy/power to the maximum energy/power stored in one vibration cycle, i. e.

$$\eta = \frac{P_{\mathrm{diss}}}{P_{\mathrm{max}}} = \frac{E_{\mathrm{diss}}}{E_{\mathrm{max}}} = \frac{\mathrm{Real}(P^*)}{\mathrm{Imag}(P^*)}. \tag{3.14}$$

However, this classical definition of the loss factor is not very informative for an application to particle dampers due to the scaling with the maximum power/energy. For instance, using a higher container mass in experiments with the same particle setting, changes the loss factor although the dissipated energy stays constant. Likewise, if the particle system is only weakly coupled to the container movement, e. g. a single particle with no or almost no contact to the container walls, the stored energy/power of the particle bed is low. This leads to a misinterpreting of the loss factor. Hence, the loss factor cannot be used as a meaningful efficiency factor.
Therefore, the approach of [MasmoudiEtAl16] is adopted. To assess the damper's efficiency the effective loss factor $\bar{\eta}$ [MeyerSeifried21c] is used. It is calculated by scaling the dissipated energy of the damper with the maximum kinetic energy of the particle system E_{kin} if the particles are added as a static mass. By using the mass of the particle bed m_{bed}, i. e. the mass of all particles, the effective loss factor is obtained to

$$\bar{\eta} = \frac{E_{\mathrm{diss}}}{E_{\mathrm{kin}}} = \frac{E_{\mathrm{diss}}}{\frac{1}{2}\,m_{\mathrm{bed}}\,|V_\Omega^*|^2}, \tag{3.15}$$

with V_Ω^* being complex amplitude by FFT of the velocity signal at driving frequency. Consequently, the effective loss factor is independent of the container and particle mass and enables the comparison of different particle settings. It should be noted that due to the definition of the effective loss factor, it is not limited by a value of one. However, to compare different particle damper settings and to ensure a unique coloring of the later utilized surface plots throughout this work, a value of one and higher are indicated by the same yellow color. Such an effective loss factor is shown exemplary in Fig. 3.6. The effective loss factor depends on the excitation frequency Ω as well as on the excitation amplitude X and shows the full range of values from low to high. This behavior occurs due to the strong coupling of the effective loss factor to the motion modes of the particle damper and is further discussed in the next chapters.
For certain motion modes, it is even possible to describe the energy dissipation and effective loss factor analytically. These equations describe or approximate the physical behavior of the particles. However, there is no general concept to derive these equations, but DEM simulations often give useful insights. An example of such an analytical formula is given in Fig. 3.6 as well. For this example,

the effective loss factor only depends on the container amplitude X. Further discussions are given in the following chapters.

Another relevant quantity is the effective moving mass $\bar{M}^*_{\mathrm{mov}}$ of the particle damper [SanchezPugnaloni11]. It is determined by dividing the complex amplitude of the excitation signal at driving frequency F^*_Ω by the complex amplitude of the acceleration signal at driving frequency A^*_Ω to

$$\bar{M}^*_{\mathrm{mov}} = \frac{F^*_\Omega}{A^*_\Omega} = \frac{F^*_\Omega}{\mathrm{i}\,\Omega\,V^*_\Omega}, \tag{3.16}$$

with i being the imaginary unit. By using the effective moving mass, the effective particle mass $\bar{m}_{\mathrm{bed}}$ can be obtained as

$$\bar{m}_{\mathrm{bed}} = |\bar{M}^*_{\mathrm{mov}} - m_{\mathrm{con}}|. \tag{3.17}$$

The effective particle mass describes how much mass of the particle bed is "felt" by the container, i. e. how much the mass of the granular matter is coupled to the container movement. When mounting a particle damper to an underlying structure, this effective particle mass leads to a change in the structure's eigenfrequency. The lower and upper bounds for the effective particle mass can be approximated to

$$0 \lessapprox \bar{m}_{\mathrm{bed}} \lessapprox m_{\mathrm{bed}}. \tag{3.18}$$

It seems counterintuitive that Eq. (3.18) is just an approximation. Indeed, it is shown by [SanchezPugnaloni11] that under certain conditions slightly lower values than zero and higher values than the particle bed mass can occur. Later, the ratio between the effective particle mass and the mass of the particle bed is used, i. e. $\bar{m}_{\mathrm{bed}}/m_{\mathrm{bed}}$, also called *effective particle mass ratio*. Values close to zero mean that the mass of the particle bed is only weakly coupled to the container movement. Values close to one or even higher indicate a strong particle mass coupling.

3.3 Level III: Structural Integrated Damper

The last level of the toolchain, shown in Fig. 3.1, represents the integration of one or multiple particle dampers into a vibrating structure to evaluate their overall damping effect. The individual testbeds are introduced in the corresponding Chap. 5–Chap. 8. To obtain numerically the motion of the structure, the different particle damper models acquired on the **Single Damper Level** of the

toolchain have to be coupled to a structure's model. This coupling procedure is illustrated in Fig. 3.6 for the three different particle damper models used in this work. These models are:

- **1)** Full DEM model.
- **2)** Effective fields, i. e. energy dissipation and effective particle mass.
- **3)** Analytical formulas.

For numerically coupling, an accurate model of the structure is necessary. In this work, the *finite element method* (FEM), see e. g. [Wriggers01], is used for this task. The underlying structure is discretized with a sufficient number of suitable elements. Setting up the linear equation of motion leads to a system of the form

$$\boldsymbol{M}\,\ddot{\boldsymbol{x}}_\mathrm{e} + \boldsymbol{D}_\mathrm{e}\,\dot{\boldsymbol{x}}_\mathrm{e} + \boldsymbol{K}\,\boldsymbol{x}_\mathrm{e} = \boldsymbol{f}. \tag{3.19}$$

Here, $\boldsymbol{x}_\mathrm{e} \in \mathbb{R}^{f_\mathrm{e}}$ are the f_e nodal displacements. The entries $\boldsymbol{M} \in \mathbb{R}^{f_\mathrm{e} \times f_\mathrm{e}}$ and $\boldsymbol{K} \in \mathbb{R}^{f_\mathrm{e} \times f_\mathrm{e}}$ are the mass and stiffness matrices, respectively, of the elastic body. The vector $\boldsymbol{f} \in \mathbb{R}^{f_\mathrm{e}}$ denotes the force vector acting on the structure, including the particle damper force $\boldsymbol{f}_\mathrm{pd}$ and other external forces $\boldsymbol{f}_\mathrm{ex}$. The structural damping, i. e. without particle dampers, is first not considered, i. e. $\boldsymbol{D}_\mathrm{e} = 0$, and

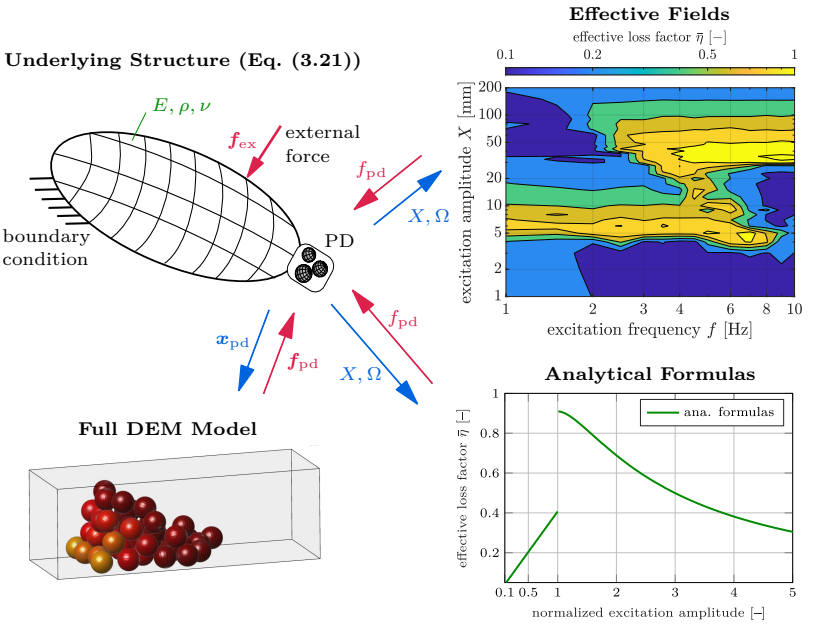

Figure 3.6: Coupling procedure of structure with particle damper models.

is added later based on measurements.
To reduce the FEM model in size, i. e. Eq. (3.19), a modal reduction is performed. See e. g. [NowakowskiEtAl12] for further information on model order reduction techniques. In this work, the reduction is performed by transforming Eq. (3.19) to elastic coordinates $\boldsymbol{q} \in \mathbb{R}^{f_\mathrm{q}}$ and neglecting certain modes to achieve $f_\mathrm{q} \ll f_\mathrm{e}$. Thereby, the computational cost can be significantly reduced and the efficient use and analysis of complex structures can be accomplished. By solving the general eigenvalue problem

$$\left(\boldsymbol{K} - \omega_k^2\, \boldsymbol{M}\right)\, \bar{\boldsymbol{\phi}}^{(k)} = \boldsymbol{0}, \tag{3.20}$$

with $\bar{\boldsymbol{\phi}}^{(k)}$ being the k-th mode shape, the reduced model can be stated as

$$\boldsymbol{E}\, \ddot{\boldsymbol{q}} + \boldsymbol{D}\, \dot{\boldsymbol{q}} + \boldsymbol{\Omega}\, \boldsymbol{q} = \boldsymbol{\Phi}^\mathrm{T} \boldsymbol{f}, \tag{3.21}$$

$$\boldsymbol{x}_\mathrm{e} \approx \boldsymbol{\Phi}\, \boldsymbol{q}. \tag{3.22}$$

The matrix $\boldsymbol{E}$ denotes hereby the identity matrix. The structural damping matrix $\boldsymbol{D}$, i. e. without particle dampers, with the damping parameters D_k on its diagonal, is included using Rayleigh damping and is extracted from experimental results, see e. g. [SchwarzRichardson13]. The matrix $\boldsymbol{\Omega}$ contains the squared eigenfrequencies ω_k^2 of the system on its diagonal and $\boldsymbol{\Phi} = [\boldsymbol{\phi}^{(1)}, \boldsymbol{\phi}^{(2)}, ..., \boldsymbol{\phi}^{(f_\mathrm{q})}]$ contains the corresponding mass normalized mode shapes $\boldsymbol{\phi}^{(k)}$. Hence, Eq. (3.21) is a decoupled differential equation with f_q degrees of freedom with Eq. (3.22) describing the structural displacements $\boldsymbol{x}_\mathrm{e}$.
In the following, it is assumed that the external force and the particle damper act at a single point in one direction on the structure. The mode shapes evaluated at these two points are denoted as $\phi_\mathrm{ex}^{(k)}$ and $\phi_\mathrm{pd}^{(k)}$, respectively. As Eq. (3.21) is a decoupled differential equation, a single mode can be written as

$$\ddot{q}_k + D_k\, \dot{q}_k + \omega_k^2\, q_k = \phi_\mathrm{ex}^{(k)}\, f_\mathrm{ex} + \phi_\mathrm{pd}^{(k)}\, f_\mathrm{pd}, \tag{3.23}$$

with f_ex and f_pd being the external and particle damper force, respectively. The translational particle damper state x_pd and its derivatives are obtained by the k-th mode shape value at the damper position $\phi_\mathrm{pd}^{(k)}$ as

$$x_\mathrm{pd} = \phi_\mathrm{pd}^{(k)}\, q_k, \tag{3.24}$$

$$\dot{x}_\mathrm{pd} = \phi_\mathrm{pd}^{(k)}\, \dot{q}_k, \tag{3.25}$$

$$\ddot{x}_\mathrm{pd} = \phi_\mathrm{pd}^{(k)}\, \ddot{q}_k. \tag{3.26}$$

For many later utilized systems, it is sufficient to only consider the first (bending) eigenmode of the structure if this one is dominant for the system's deformation. Since for these systems the particle damper position is here generally used as output, Eq. (3.24)–Eq. (3.26) are inserted into Eq. (3.23) and only $k = 1$ is

considered. Thereby, one obtains

$$\underbrace{\frac{1}{\phi_{\mathrm{pd}}^{(1)^2}}}_{M}\,\ddot{x}_{\mathrm{pd}} + \underbrace{\frac{D_k}{\phi_{\mathrm{pd}}^{(1)^2}}}_{D}\,\dot{x}_{\mathrm{pd}} + \underbrace{\frac{\omega_1^2}{\phi_{\mathrm{pd}}^{(1)^2}}}_{K}\,x_{\mathrm{pd}} = \frac{\phi_{\mathrm{ex}}^{(1)}}{\phi_{\mathrm{pd}}^{(1)}}\,f_{\mathrm{ex}} + f_{\mathrm{pd}}, \tag{3.27}$$

Hence, this equation can also be written as

$$M\,\ddot{x}_{\mathrm{pd}} + D\,\dot{x}_{\mathrm{pd}} + K\,x_{\mathrm{pd}} = \frac{\phi_{\mathrm{ex}}^{(1)}}{\phi_{\mathrm{pd}}^{(1)}}\,f_{\mathrm{ex}} + f_{\mathrm{pd}}. \tag{3.28}$$

In the following, the coupling procedure of the different damper models, i. e. full DEM model, effective fields and analytical formulas, to Eqs. (3.21),(3.23) and (3.28) is discussed in detail.

1) Full DEM Model For the first approach, the full DEM model of the particle damper, already used on the **Single Damper Level** of the toolchain, is coupled to the model of the underlying structure, i. e. Eq. (3.21), see Fig. 3.6. The position vector $\boldsymbol{x}_{\mathrm{pd}}$ of the particle damper is obtained from the reduced model and applied to the DEM model. Within the latter, the particle interactions are determined. The resulting reaction forces and torques onto the container walls $\boldsymbol{f}_{\mathrm{pd}}$ are transferred back to the underlying structure, i. e. Eq. (3.21), resulting in its elastic accelerations $\ddot{\boldsymbol{q}}$. Finally, all accelerations including particle and elastic states are integrated. This approach leads to accurate results, as a precise particle damper model is used. However, as not only the elastic states but also the particle states need to be integrated, high numerical costs can be expected.

2) Effective Fields The effective fields, i. e. energy dissipation and effective particle mass, are either pre-computed via DEM or obtained by experimental measurements, see Sect. 5.1.1 and Sect. 8.1.1 for the experimental testbeds. These effective fields are determined for discrete excitation frequencies and amplitudes. To couple the effective fields, a computation scheme different from the one used in **approach 1**, i. e. the DEM model, is necessary, see also Fig. 3.6. Since the modal reduced model of the structure, i. e. Eq. (3.21), is a decoupled differential equation, only the k-th mode at a time has to be considered for general systems, i. e. Eq. (3.23). This is justified, as the deformation of the system is dominated by the k-th mode if it is vibrating in or near the k-th eigenfrequency. Since the effective fields are determined for purely one-dimensional translational excitations, e. g. by a shaker, only this translational state is coupled between underlying structure and particle damper model, see Eq. (3.24)–Eq. (3.26). Furthermore, the particle damper contact force f_{pd} is replaced by an equivalent damper force. This equivalent damper force consists of the additional inertia term caused by the effective particle mass $\bar{m}_{\mathrm{bed}}$ and the damping forces due to the energy dissipation

of the damper expressed as *effective viscous damping* $\bar{d}$. The damper force is replaced as

$$f_{\mathrm{pd}} = -\left(\bar{m}_{\mathrm{bed}}\,\ddot{x}_{\mathrm{pd}} + \bar{d}\,\dot{x}_{\mathrm{pd}}\right). \tag{3.29}$$

Inserting Eq. (3.29) into Eq. (3.23), one obtains for the k-th mode

$$\ddot{q}_k + D_k\,\dot{q}_k + \omega_k^2\,q_k = \phi_{\mathrm{ex}}^{(k)} F_{\mathrm{ex}}\cos(\Omega\,t) - \phi_{\mathrm{pd}}^{(k)}\left(\bar{m}_{\mathrm{bed}}\,\ddot{x}_{\mathrm{pd}} + \bar{d}\,\dot{x}_{\mathrm{pd}}\right), \tag{3.30}$$

with $f_{\mathrm{ex}} = F_{\mathrm{ex}}\cos(\Omega\,t)$ being a harmonic external excitation. Inserting the particle damper states x_{pd} and $\dot{x}_{\mathrm{pd}}$, i. e. Eqs. (3.25) and (3.26), into Eq. (3.30) and rewriting it, one obtains

$$\underbrace{\left(1 + {\phi_{\mathrm{pd}}^{(k)}}^2\,\bar{m}_{\mathrm{bed}}\right)}_{m}\ddot{q}_k + \underbrace{\left(D_k + {\phi_{\mathrm{pd}}^{(k)}}^2\,\bar{d}\right)}_{d}\dot{q}_k + \underbrace{\omega_k^2}_{k}\,q_k = \underbrace{\phi_{\mathrm{ex}}^{(k)} F_{\mathrm{ex}}}_{R}\cos(\Omega\,t). \tag{3.31}$$

Thus, Eq. (3.31) can also be written as

$$m\,\ddot{q}_k + d\,\dot{q}_k + k\,q_k = R\cos(\Omega\,t). \tag{3.32}$$

As the particle mass is temporarily coupled to the structure, the structure's eigenfrequencies decrease [BannermanEtAl11]. The angular eigenfrequency influenced by the effective particle mass, in the following referred to as *effective eigenfrequency* $\bar{\omega}$, follows to

$$\bar{\omega}_k = \sqrt{\frac{k}{m}} = \omega_k\sqrt{\frac{1}{1 + {\phi_{\mathrm{pd}}^{(k)}}^2\,\bar{m}_{\mathrm{bed}}}}. \tag{3.33}$$

The lower and upper bounds for the effective eigenfrequency are approximated as

$$\omega_{\mathrm{bed}} \lessapprox \bar{\omega}_k \lessapprox \omega_k, \tag{3.34}$$

with ω_{bed} being the eigenfrequency of the system if the mass of the particle bed is added as a static mass

$$\omega_{\mathrm{bed}} = \omega_k\sqrt{\frac{1}{1 + {\phi_{\mathrm{pd}}^{(k)}}^2\,m_{\mathrm{bed}}}}. \tag{3.35}$$

Note, Eqs. (3.33) and (3.35) only slightly differ by m_{bed} and $\bar{m}_{\mathrm{bed}}$. The limits for the effective eigenfrequency arise due to the range of values for the effective particle mass, see Eq. (3.18). As a consequence, the effective eigenfrequency will be approximately between the undamped eigenfrequency ω_k and the eigenfrequency of the system with the mass of the particle bed added as a static mass ω_{bed}.
If only the first bending eigenmode of the structure is considered, i. e. $k = 1$, the

equivalent damper force, i. e. Eq. (3.29), is inserted in Eq. (3.28). Thereby, one obtains

$$(M + \bar{m}_{\mathrm{bed}})\,\ddot{x}_{\mathrm{pd}} + \left(D + \bar{d}\right)\dot{x}_{\mathrm{pd}} + K\,x_{\mathrm{pd}} = R'\cos(\Omega\,t), \tag{3.36}$$

with $R' = \dfrac{\phi_{\mathrm{ex}}^{(1)}}{\phi_{\mathrm{pd}}^{(1)}}\,F_{\mathrm{ex}}$. The effective eigenfrequency follows to

$$\bar{\omega}_1 = \omega_1 \sqrt{\frac{M}{M + \bar{m}_{\mathrm{bed}}}}. \tag{3.37}$$

To solve Eq. (3.32) or Eq. (3.36) the effective particle mass $\bar{m}_{\mathrm{bed}}$ and the effective viscous damping coefficient $\bar{d}$ are required. At this point, it is assumed that the elastic coordinate of the k-th mode and thus the particle damper are vibrating in a quasi-stationary state with frequency Ω and damper amplitude X. These assumptions will be discussed in detail later. Thus, the effective particle mass can directly be determined from its corresponding field as

$$\bar{m}_{\mathrm{bed}} = \bar{m}_{\mathrm{bed}}(\Omega, X), \tag{3.38}$$

see e. g. Fig. 3.6. The effective viscous damping coefficient in a stationary state is calculated by the dissipated energy per cycle $\widetilde{E}_{\mathrm{diss}}$, which is obtained from its corresponding field, and the excitation conditions [Shabana19]. The effective viscous damping coefficient follows to

$$\bar{d} = \frac{\widetilde{E}_{\mathrm{diss}}}{\pi\,\Omega\,X^2}. \tag{3.39}$$

As the values for the energy dissipation and the effective particle mass are only available at discrete frequencies and amplitudes, see e. g. Fig. 3.6, a linear interpolation is performed to obtain intermediate values.
The numerical costs for solving Eq. (3.32) or Eq. (3.36) are much lower compared to **approach 1**, i. e. the DEM model, as only the elastic coordinates need to be solved but no particle states. However, this approach contains high offline costs as the effective fields need to be either pre-computed by DEM or experimental measurements. The accuracy of the coupling approach depends mainly on how well a pure one-dimensional particle damper movement is obtained and how well the assumption of a quasi-stationary state is fulfilled. It is also assumed that the mass of the particle bed is much lower than the structure's mass and, hence, the structure's mode shapes are only negligible affected by the particle mass.

3) Analytical Formulas The coupling of the analytical formulas to the model of the structure is identical to the coupling of the effective fields, i. e. either Eq. (3.32) or Eq. (3.36) is solved, see also [MeyerEtAl21] and Fig. 3.6. The energy dissipation and the effective particle mass follow from previously derived formulas general of form $f = f(X, \Omega)$. These formulas are case-depending and developed

in Chap. 5–Chap. 8. Analogously to **approach 2**, the numerical cost for solving Eq. (3.32) or Eq. (3.36) are low. However, the analytical formulas need to be developed first, which can result in high offline costs. As with the effective fields, the accuracy of the coupling approach depends mainly on how well a pure one-dimensional particle damper movement is obtained and, of course, how well the analytical formulas approximate the damper's energy dissipation and effective particle mass.

3.3.1 Free Vibration Analysis

For numerical and experimental free vibration analysis, no external force is used, i. e. $F_{\mathrm{ex}} = 0$ or $\boldsymbol{f}_{\mathrm{ex}} = \mathbf{0}$, respectively. Instead, the structure is subjected to a defined initial condition, numerically by $q_{k,0} = q_k(t_0)$ and $\dot{q}_{k,0} = \dot{q}_k(t_0)$. Experimentally, this can be realized for instance by manual bending, the release of a counterweight or an impulse hammer. Then, the transient vibration amplitude attenuation of the structure is measured or simulated, respectively, and analyzed. During the transient vibration of the structure, the dissipated energy of the particle dampers changes. Thus, for the numerical **approaches 2-3**, the effective viscous damping coefficient and the effective particle mass need to be updated as the vibration amplitude reduces. To calculate the new effective damping coefficient and effective particle mass, Eq. (3.38) and Eq. (3.39) are used with vibration frequency being the structure's effective eigenfrequency, i. e. $\Omega = \bar{\omega}$. However, the effective eigenfrequency in Eq. (3.33) is also depending on the effective particle mass, which depends on Ω. Hence, a fixed point iteration scheme is used to solve these equations. The update time points of the effective particle mass and effective viscous damping parameter depend on the vibration form of the underlying structure, i. e. horizontal or vertical vibration, and are discussed in detail in the corresponding sections.
To evaluate and compare different damper models and experimental measurements, the damping ratio ζ is used. It follows from the logarithmic decrement ϑ as

$$\vartheta = \ln\left(\frac{X_n}{X_{n+1}}\right), \tag{3.40}$$

$$\zeta = \frac{\vartheta}{\sqrt{4\pi^2 + \vartheta^2}}, \tag{3.41}$$

with X_n being the vibration amplitude of the n-th vibration cycle. As logarithmic decrement and damping ratio change with the damper amplitude, for comparison the mean damper amplitude $X_{n+\frac{1}{2}} = \frac{1}{2}\left(X_n + X_{n+1}\right)$ is used as sampling point for the damping ratio of the n-th vibration cycle.

3.3.2 Forced Vibration Analysis

For the experimental forced vibration analyses, a sine sweep excitation with a slow frequency change rate [GlothSinapius05] is generally used. Thus, a stationary state of the structure can be assumed for every instant of time. By measuring the structure's excitation $\boldsymbol{f}_{\mathrm{ex}}$ output $\boldsymbol{x}_{\mathrm{out}}$, the structure's *frequency response function* (FRF) can be calculated [Brandt11]. The FRF is based on the complex amplitude by fast Fourier transform of the input $\boldsymbol{f}_{\mathrm{ex}}$ and output $\boldsymbol{x}_{\mathrm{out}}$, resulting in $\boldsymbol{F}^*_{\mathrm{ex}}$ and $\boldsymbol{X}^*_{\mathrm{out}}$. Thus, it reads

$$\boldsymbol{H}^*(\Omega) = \frac{\boldsymbol{X}^*_{\mathrm{out}}}{\boldsymbol{F}^*_{\mathrm{ex}}}. \tag{3.42}$$

By means of the structure's FRF, the effective eigenfrequencies and damping ratios are extracted by using the software *BK Connect* and the function *rational fraction polynomial-z* [Brandt11]. To calculate these values numerically using the damper **models 1**–**3**, different approaches are necessary and presented in the following.

1) Full DEM Model For the coupling of Eq. (3.21) to a full DEM model, two different analysis approaches are used to extract the damping ratios [MeyerSeifried20]. For the first approach, henceforth referred to as *frequency domain approach*, the structure's FRF is calculated. Likewise, in the experiments, a sine sweep excitation over all considered eigenfrequencies is utilized. Since the simulation would be very time-consuming, if carried out for multiple eigenfrequencies, the frequency range is divided up into multiple overlapping segments and calculated simultaneously. The initial transient vibration parts of each simulation are cut off. For each segment, the FRF is calculated separately. Afterward, all FRFs are combined into a single FRF using a peak hold algorithm. Subsequently, the modal parameters are extracted from the resulting FRF with the MATLAB function *Modalfit* using the *Least-Squares Complex Exponential Method* [Brandt11]. For the second approach, hereafter referred to as *time domain approach*, the idea is not to sweep over the complete frequency range, but only over a small area around the eigenfrequencies of the structure. The resulting time domain results are analyzed using the analytical solution of Eq. (3.32), i. e. the damper is assumed to be included via its effective mass and effective viscous damping coefficient. The analytical solution of Eq. (3.32) follows to

$$q_k(t) = Q\cos(\Omega\, t - \psi_k) + \Psi\ (q_{k,0}, \dot{q}_{k,0}), \tag{3.43}$$

with

$$Q = \frac{R}{m\,\sqrt{\left(\bar{\omega}_k^2 - \Omega^2\right)^2 + \left(2\,\delta\,\Omega\right)^2}}, \tag{3.44}$$

and

$$\delta = \frac{d}{2\,m} = \bar{\omega}_k\,\zeta_k. \tag{3.45}$$

Hereby, ζ_k denotes the k-th structural damping ratio. The phase angle between excitation and response is denoted by ψ_k, while Ψ is the homogeneous solution, which converges to zero in finite time if damping is present, see e. g. [Shabana19]. The maximum vibration amplitude of the elastic coordinate $Q_k^{\max}$ is obtained at the resonance frequency

$$\Omega_{\mathrm{R}} = \sqrt{\bar{\omega}_k^2 - 2\,\delta_k^2} = \bar{\omega}_k\,\sqrt{1 - 2\,\zeta_k^2}. \tag{3.46}$$

For small damping ratios $\zeta_k \ll 1$ the resonance frequency approaches the effective eigenfrequency $\Omega_{\mathrm{R}} \approx \bar{\omega}_k$, see Eq. (3.33). Inserting this relation into Eq. (3.44), the damping ratio can be calculated by

$$\zeta_k = \frac{R}{2\,m\,Q_k^{\max}\,\Omega_{\mathrm{R}}^2}. \tag{3.47}$$

The resonance frequency Ω_{R} is determined at the time of the maximum vibration amplitude $Q_k^{\max}$. For the system to constantly be in a steady state, a sufficient small sweep rate has to be selected, i. e. of about $0.003\,\omega_k$ for the applications here. In contrast to the frequency domain approach, the simulation time can be significantly decreased with factors around 20 and higher. It should be noted that an excitation solely within the eigenfrequency of the structure is not possible. This is because the structure's eigenfrequency slightly shifts due to the effective particle mass, which cannot be determined precisely enough beforehand.

2 & 3) Effective Fields and Analytical Formulas To obtain the damping ratios of the underlying structure under forced vibrations utilizing the effective fields and analytical formulas, the analytical solution of Eq. (3.32), i. e. Eq. (3.43), is used [MeyerSeifried21a, MeyerSeifried21b]. Assuming a stationary state, an excitation within the resonance frequency, i. e. $\Omega = \bar{\omega}_k$, and small damping ratios, the amplitude of the elastic coordinate Q_k and the damping ratio ζ_k can now be expressed as

$$Q_k = \frac{R}{2\,m\,\zeta_k\,\bar{\omega}_k^2}, \tag{3.48}$$

$$\zeta_k = \frac{d}{2\,m\,\bar{\omega}_k}. \tag{3.49}$$

The vibration amplitude of the particle damper is calculated by

$$X = \phi_{\mathrm{pd}}^{(k)}\,Q_k. \tag{3.50}$$

As Eqs. (3.38), (3.39), (3.48) and (3.49) are depending on each other via the energy dissipation and effective particle mass, an iteration scheme is used to

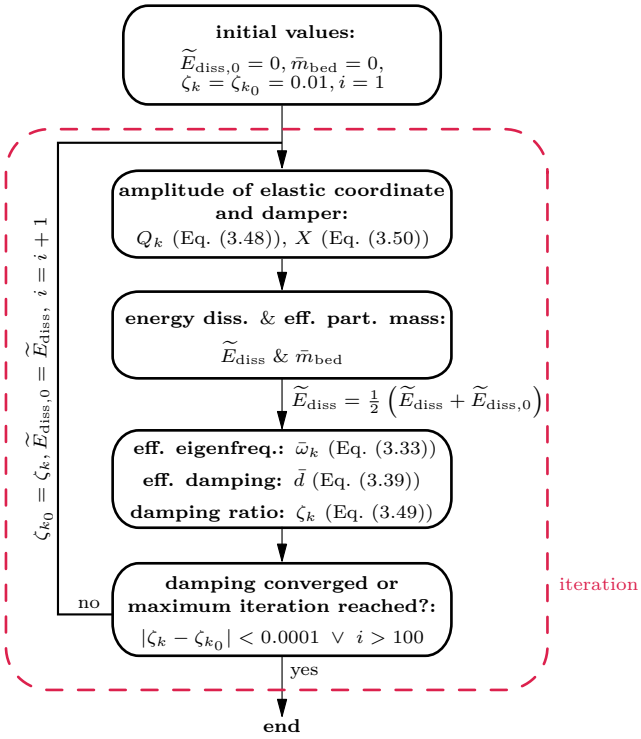

Figure 3.7: Iteration scheme to find equilibrium state of structure coupled to particle damper model utilizing effective fields or analytical equations.

solve these equations for the damping ratio, see Fig. 3.7. First, energy dissipation and effective particle mass are set to zero. Then, the iteration process starts. By Eqs. (3.48) and (3.50) the amplitude of the elastic coordinate Q_k and the damper amplitude X, respectively, are determined. By the given excitation frequency, i. e. $\Omega = \bar{\omega}_k$, the damper's energy dissipation and effective particle mass are obtained from the effective fields or analytical formulas, respectively. For the energy dissipation, the mean value of the current and previous iteration step is taken, as this increases the convergence speed of the iteration scheme. The Eqs. (3.33), (3.39) and (3.49) are than solved successive for the effective eigenfrequency $\bar{\omega}_k$, the effective viscous damping parameter $\bar{d}$ and the damping ration ζ_k, respectively. When the damping ratio has converged, i. e. is only changing marginally, the procedure stops. Otherwise, the iteration is repeated with the new calculated energy dissipation and effective particle mass as updated start values. In most cases, the iteration scheme converges in five to ten iterations, see [MeyerSeifried21a].

The underlying structure reaches a stationary state during resonance if the excitation input energy is equal to the dissipated energy [Shabana19]. While the input energy is increasing linearly with the vibration intensity, the energy dissipation of a perfect viscous damper with a constant coefficient is increasing quadratically. Thus, only one single point of equilibrium exists. For particle dampers, however, the viscous damping coefficient is not constant. Therefore, the question arises if multiple equilibrium points are possible. Here, this has never been observed but it is still part of ongoing research.

3.3.3 Evaluation of Efficiency

For the free and forced vibration analyses, the damping ratio ζ is used as a damping measurement. However, using the damping ratio provides no further information on whether the particle damper works efficiently concerning the used particle mass. The particle damper can be considered as efficient though, if its effective loss factor $\bar{\eta}$ is high, e. g. for a value of one or higher [MeyerSeifried21a]. The effective loss factor is an efficiency factor, which correlates the dissipated energy of the particle damper to the kinetic energy of the particle bed. See Sect. 3.2.2 for a detailed description. Inserting the damper's energy dissipation expressed by the effective loss factor $\widetilde{E}_{\mathrm{diss}}{=}2\,\pi\,\bar{\eta}\,E_{\mathrm{kin}}$ into Eq. (3.49) by using Eq. (3.39) and neglecting the structural damping, i. e. $D_k = 0$, Eq. (3.49) can be solved for the resulting damping ratio. As the effective particle mass $\bar{m}_{\mathrm{bed}}$, i. e. the coupled mass of the particle bed to the container, is unknown, it is approximated by the mass of the particle bed, i. e. $\bar{m}_{\mathrm{bed}} \approx m_{\mathrm{bed}}$. This is justified, as a high effective loss factor goes along with a high effective particle mass [MeyerSeifried21a]. Hence, the damping ratio of the structure in dependency on the effective loss factor of the particle damper $\bar{\eta}$ results in

$$\zeta_k(\bar{\eta}) = \frac{{\phi_{\mathrm{pd}}^{(k)}}^2\,\bar{d}}{2\,m\,\bar{\omega}_k} = \frac{{\phi_{\mathrm{pd}}^{(k)}}^2\,m_{\mathrm{bed}}\,\bar{\eta}}{2\left(1+{\phi_{\mathrm{pd}}^{(k)}}^2\,\bar{m}_{\mathrm{bed}}\right)} \approx \frac{\bar{\eta}}{2\left(1+\dfrac{1}{{\phi_{\mathrm{pd}}^{(k)}}^2\,m_{\mathrm{bed}}}\right)}, \tag{3.51}$$

with $\phi_{\mathrm{pd}}^{(k)}$ being the k-th mode shape value at the particle damper position. Thus, the efficiency of the particle damper can be judged by simply comparing the experimentally measured damping ratio to this theoretical value for any desired effective loss factor. This formula could also be used further for quick efficiency testing of possible mounting points of the particle damper on the structure. Changing the mounting points means to change $\phi_{\mathrm{pd}}^{(k)}$.
If the structure is described by Eq. (3.36), i. e. only its first bending eigenmode is considered, and using $M = 1/{\phi_{\mathrm{pd}}^{(1)}}^2$, Eq. (3.51) can also be written as

$$\zeta_1(\bar{\eta}) = \frac{1}{2}\,\bar{\eta}\,\frac{m_{\mathrm{bed}}}{M+m_{\mathrm{bed}}}. \tag{3.52}$$

Single Particle Impact Analyses

The dynamics of particle dampers are mainly influenced by impacts of the granular particles with each other and the surrounding damper walls. However, these impacts are very complex processes that depend on a variety of influence parameters, like impact velocity, material pairing, shape of contact partners and surface roughness. These parameters significantly influence the contact duration, penetration depth, contact force and energy dissipation of the contacting bodies [Goldsmith60]. A special focus is put on the energy dissipation, which stems for normal impacts, for instance, from *elastic-viscoplastic* deformations in metals or *visco-elastic* deformations in polymers [Goldsmith60, WangEtAl17]. Additionally, kinetic energy is dissipated by frictional effects. Also, kinetic energy of the rigid body action might be transformed during impact into wave propagation. This happens especially in impacts involving slender bodies [SeifriedEtAl10]. These are, however, not being considered in this work, since the focus lies on impacts occurring in particle dampers, i. e. granular matter of macroscopic size. For the description of the global normal contact behavior, a simplified description by the *coefficient of restitution* (COR) is often used to summarize the energy dissipation during normal contacts, see Eq. (3.1). The kinematic COR correlates the velocities of both contact partners before and after impact. It varies between zero and one, with a value of one implying no energy dissipation and a value of zero meaning maximum energy dissipation, i. e. both bodies move with the same velocity after impact, see Sect. 3.1 and [Goldsmith60] for further details. Frictional effects are often described by a *static* and *sliding friction coefficient*, i. e. μ_0 and μ, respectively. However, these friction coefficients strongly depend on the surface roughness, adhesion and lubrication of the colliding bodies and are, hence, difficult to determine [UrbakhEtAl04]. Thus, the friction coefficients could be used as a tuning parameter in the simulation for later particle damper analyses. Indeed, it turned out that the use of the same friction coefficient for various simulations is mostly sufficient.

As the COR is a key parameter for simulations of contact procedures, in the past various numerical [AryaeiEtAl10, MinamotoEtAl11, SchiehlenEtAl06, SeifriedEtAl10, Wriggers06] and experimental [AryaeiEtAl10, CioccaWang11, Goldsmith60, MinamotoEtAl11, PatilHiggs17, SchiehlenEtAl06, SeifriedEtAl10, TataraMoriwaki82] studies have been performed. These studies can be further subdivided into different classes, like the used test apparatus, body materials, material

models, shape of bodies, etc. As test apparatus drop-down tests [AryaeiEtAl10, PatilHiggs17] or pendulum tests [SeifriedEtAl10] are often used. With drop-down tests, sphere–wall impacts are analyzed. Pendulum tests allow for the analysis of sphere–sphere [TataraMoriwaki82], sphere–rod [SeifriedEtAl10] or sphere–wall impacts [Goldsmith60]. Due to their high importance for industrial applications, metal impacts have already been analyzed experimentally by numerous authors, see e. g. [AryaeiEtAl10, MinamotoEtAl11, PatilHiggs17, SeifriedEtAl10, WeirTallon05]. But also other materials like brass, glass or polymers have been investigated as well [Goldsmith60, TataraMoriwaki82, WangEtAl17].

In the last decade, numerical impact analyses by the *finite element method* (FEM) gained more and more attention. These simulations enable a deeper understanding of the contact procedure and allow quick sensitivity analyses. Many different material models have been investigated until now. It was shown that an accurate material model is very important for precise results as the material model has a major influence on the energy dissipation during contact and thus on the COR [SeifriedEtAl10].

In the following, intensive analyses of impacts between a steel sphere and different wall materials using experiments and FEM simulations are presented in the next sections. Hereby, the materials within the later used particle dampers are investigated. The particles and walls within the particle dampers are made of steel, aluminum and polymers. Thus, different material models are necessary for FEM simulations. Multiple influence parameters are studied, like impact velocity and sphere size. Using FEM simulations, deeper insights into the conversion of energy during the impacts are given. Additionally, contact duration and contact forces are measured experimentally and compared for the different material pairings. By using the validated numerical model, the COR results are extended to purely steel sphere–sphere contacts for future particle damper analyses.

First, in Sect. 4.1, the different material models for metals and polymers are presented. In the following Sect. 4.2, the experimental and numerical setups for impact analyses are introduced. A comprehensive overview of the impact results is given in Sect. 4.3. Finally, in Sect. 4.4, a summary of the chapter is provided. The following results have been published in [MeyerEtAl22] and this chapter follows this publication.

4.1 Material Models

To be able to use FEM simulations to describe the deformation behavior of a body, a meaningful material model is required. Though, the choice does not only depend on the body's material but also on the forces acting on it. Thus, the material model should be based on the expected deformation behavior. In this work, metals and polymers are used for the subsequent particle dampers. For impacts, high contact forces and high strain rates in the contact zone are expected. The utilized material models should be able to reproduce this behavior.

4.1.1 Metals

Initially, during tensile testing, metals show a *linear-elastic* material behavior, conforming to Hooke's law

$$\sigma = E\,\epsilon, \tag{4.1}$$

where σ denotes the stress, ϵ the strain and E the Young's modulus. After reaching the yield stress, metals start to deform plastically. The plastic flow depends on the strain-rate $\dot{\epsilon} = \frac{\mathrm{d}\epsilon}{\mathrm{d}t}$ [Jones90]. Thus, to describe metals accurately, an *elastic-viscoplastic* material model is necessary for impact problems including steel bodies [SeifriedEtAl10]. For this task, many different models have been developed, like the Bingham model, the Perzyna model, Prager's rule or the Armstrong–Frederick kinematic hardening law [Souza NetoEtAl08]. Here, the widely used model by [Perzyna66] is employed [Souza NetoEtAl08]. Using a factor β, this model brings the dynamic yield stress σ_d in relation to the quasi-static yield stress σ_y and the effective plastic strain-rate $\dot{\epsilon}_\mathrm{pl}$ resulting in

$$\sigma_\mathrm{d} = \beta\,\sigma_\mathrm{y} \quad \text{with} \quad \beta = 1 + \left(\frac{\dot{\epsilon}_\mathrm{pl}}{\varsigma}\right)^{\lambda}. \tag{4.2}$$

The material viscosity parameter is denoted by ς and the strain-rate hardening parameter by λ. Both parameters have to be obtained from the split-Hopkinson pressure bar test [GamaEtAl04].
In Fig. 4.1 the piecewise linear approximations of the quasi-static yield stress σ_y for the later used metals steel S235 and aluminum Al6060 are shown. The data stems from [SeifriedEtAl10]. These curves are used in later FEM simulations with the corresponding material data and Perzyna coefficients listed in Tab. 4.1.
To give an impression of the dynamic yield stress σ_d, it is shown in Fig. 4.2 for S235 and Al6060 using different plastic strain rates from the Perzyna model, see Eq. (4.2). For both metals, the dynamical yield stress increases for higher strain rates. Aluminum is showing only little dependency on the plastic strain rate. Only for the highest plotted plastic strain rate of $\dot{\epsilon}_\mathrm{pl} = 1000\,{}^1/_\mathrm{s}$ minor differences in the dynamical yield stress are visible. For steel instead, a high dependency

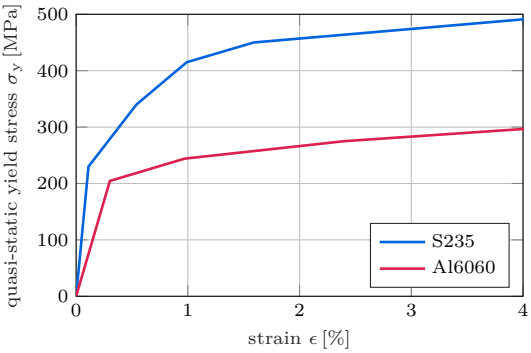

Figure 4.1: Piecewise linear approximations of quasi-static stress–strain curves for steel and aluminum [SeifriedEtAl10].

Table 4.1: Material parameters and Perzyna coefficients obtained by the split-Hopkinson pressure bar test [SeifriedEtAl10].

Material	E [GPa]	ν [–]	ρ [kg/m^3]	σ_y [MPa]	ς [–]	λ [–]
Steel S235	208	0.3	7800	230	305	0.403
Aluminum Al6060	67.7	0.33	2702	205	5548	1

can be observed. At the plastic strain rate of $\dot{\epsilon}_{pl} = 1000\,1/s$ a factor of about three between dynamic and quasi-static yield stress is achieved.

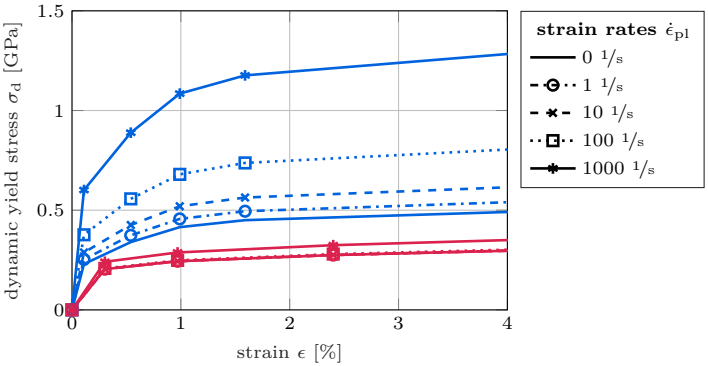

Figure 4.2: Stress–strain curves of steel S235 (*blue*) and aluminum Al6060 (*red*) for different plastic strain rates by the Perzyna model.

4.1.2 Polymers

The numerically analyzed elastomeric material is a KRAIBON® compound *SAA9579-52* supplied by Gummiwerk KRAIBURG GmbH & Co. KG. Based on preliminary experimental investigations, this elastomer has not shown any dependence on the load amplitude and is therefore considered isotropic and linear visco-elastic. The time- and rate-dependent constitutive relation for this material is expressed by

$$\tau(t) = \int_0^t G_{\mathrm{R}}(t-s)\,\dot{\gamma}\,\mathrm{d}s, \tag{4.3}$$

where τ represents the shear stress as the response to the uniaxial shear strain rate $\dot{\gamma}$. G_{R} is the time-dependent shear relaxation modulus. These, as well as the following relations describing linear visco-elasticity, can be found in [Bergström15] and [Christensen82]. The normalized relaxation shear modulus can be written as

$$g_{\mathrm{R}}(t) = \frac{G_{\mathrm{R}}(t)}{G_0}, \tag{4.4}$$

where G_0 describes the instantaneous linear elastic response of the material under infinitely fast loading. The relaxation function g_{R} is modeled using a generalized Maxwell model in terms of a Prony series

$$g_{\mathrm{R}}(t) = 1 - \sum_{i=1}^{n} g_i \left(1 - e^{-\frac{t}{\tau_i}}\right). \tag{4.5}$$

The material parameters g_i and τ_i are determined from experimental DMA (dynamic mechanical analysis) tests as described in [SessnerEtAl19]. Here, the tests have been conducted at the Institute of Vehicle System Technology at the Karlsruhe Institute of Technology for this material. Figure 4.3 shows the experimentally determined storage and loss moduli G' and G'', respectively. The complete list of Prony parameters is summarized in Tab. 4.2. The storage and loss moduli are given by the Fourier transform of the relaxation modulus $G_{\mathrm{R}}(t)$ denoted as the complex shear modulus [Bergström15] as

$$G^*(\omega) = G'(\omega) + \mathrm{i}\,G''(\omega), \tag{4.6}$$

with i being the imaginary unit. Furthermore, the long-term relaxation modulus relates to the instantaneous modulus by

$$G_\infty = G_0 \left(1 - \sum_{i=1}^{n} g_i\right). \tag{4.7}$$

The long-term shear modulus is calculated from the long-term Young's modulus $E = 54.97\,\mathrm{MPa}$ and the Poisson ratio $\nu = 0.4477$.

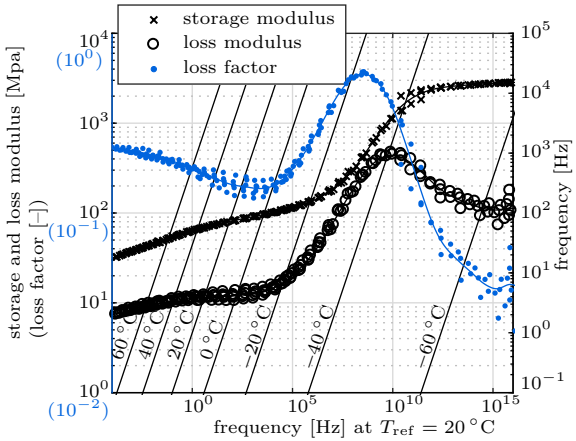

Figure 4.3: Storage modulus, loss modulus and loss factor determined from experimental DMA tests [SessnerEtAl19].

Table 4.2: Prony parameters determined from experimental DMA data of Fig. 4.3 [SessnerEtAl19].

i	$g_i[-]$	τ_i[s]
1	0.035 841 4	5.4×10^{-15}
2	0.032 541 3	9.2×10^{-14}
3	0.032 340 2	1.59×10^{-12}
4	0.034 239	2.61×10^{-11}
5	0.046 502 6	3.78×10^{-10}
6	0.076 279 9	3.31×10^{-9}
7	0.109 384	1.83×10^{-8}
8	0.013 587 7	5.48×10^{-8}
9	0.142 179	1.12×10^{-7}
10	0.141 801	4.73×10^{-7}
11	0.113 87	1.7×10^{-6}
12	0.084 679 7	6.33×10^{-6}
13	0.051 767 8	2.75×10^{-5}
14	0.027 910 7	0.000 163
15	0.012 778 9	0.001 49
16	0.007 076 92	0.0226
17	0.005 633 9	0.57
18	0.005 381 53	21.7
19	0.005 425 48	700.0
20	0.005 109 43	23 500.0
21	0.003 982 99	805 000.0
22	0.009 474 23	4.36×10^{7}

4.2 Experimental and Numerical Setups

In the following, the experimental and numerical setups are introduced to analyze particle–wall impacts within this chapter.

4.2.1 Experimental Setup

For the studies here, a pendulum testbed is used to observe sphere–wall impacts in detail, see Fig. 4.4 and [MeyerEtAl22]. The utilized steel sphere of 30 mm diameter impacts different planar material probes in normal direction in a reproducible way. Therefore, the sphere is suspended with thin Kevlar wires and collides with the material probe that is glued or otherwise fixed to a rigid steel block. The latter is assumed to be grounded, as the armature is very stiff. In the initial position of the sphere, only a minimal gap between itself and the wall probe is set. To achieve the deflected state, the sphere is moved and held by an electromagnet. As the position of the electromagnet is variable, different initial impact velocities can be achieved. The measurement range for this experimental setup is $v_{\mathrm{I}}^{0} = 0.1\,\mathrm{m/s} - 2.5\,\mathrm{m/s}$. Repeated impacts on the same spot of the wall can be measured as well. During the contact procedure, the sphere's velocity is measured using a laser scanning vibrometer (LV), the *PSV-500* from Polytec with a sampling frequency of 250 kHz. The laser is adjusted in the initial state of the sphere. By applying a reflective foil on the sphere, the measuring performance is enhanced.
Each measurement cycle consists of multiple impacts, i. e. the sphere is not caught after the first impact but the first three rebounds are measured as well. Thereby, the effect of repeated impacts on the same spot can be investigated. After each

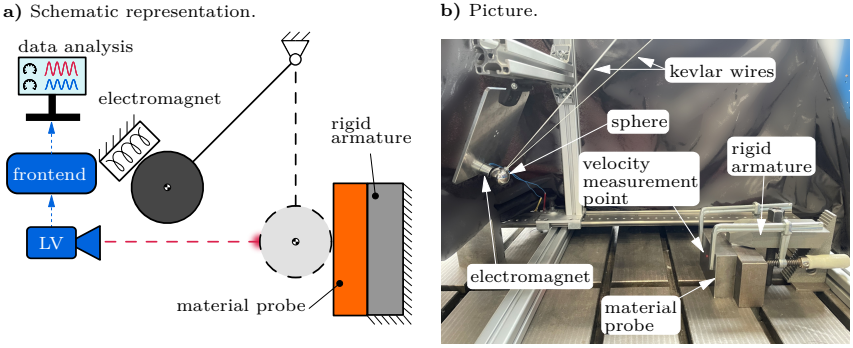

Figure 4.4: Testbed to determine the COR for a sphere–wall impact.

measurement cycle, the wall material probe is slightly moved to an undeformed spot and the sphere is smoothed with sandpaper to remove hardening.
Due to the high sampling frequency of the laser vibrometer, the contact process is measured very accurately. This makes it possible to compute the derivative of the sphere's velocity signal, i. e. its acceleration a, by central finite differences. This acceleration can then be used to calculate the normal contact force $F_\mathrm{n} = m\,a$ acting on the sphere with mass m during impact.

4.2.2 Numerical Setup

Besides the experimental analyses, FEM simulations are performed to determine the COR numerically. The commercial software program Abaqus is used for this task. A schematic representation of the sphere–wall model is shown in Fig. 4.5. The sphere is modeled with an initial radius of 5 mm. The wall is modeled as a cylinder with its diameter and length being the diameter of the sphere. The contour of the cylinder is completely clamped. As the contact zone during impact is much smaller than the sphere's diameter, see [Barber18], and due to the comparably high length and diameter of the cylinder, the influence of the boundary condition is negligible and the wall, i. e. the cylinder, can be seen as semi-infinite. Both bodies, i. e. sphere and cylinder, can be scaled for different sizes. This is done by multiplying the nodal coordinates by a constant scaling coefficient. The sphere consists of 5907 axisymmetric 2D elements, called *CAX4R* in Abaqus. The wall consists of 9019 *CAX4R* elements. The element size varies between 0.5 mm outside the contact zone to 0.015 mm inside the contact zone for the sphere's initial radius of 5 mm. As the cylinder, representing the wall, is clamped, the sphere is assigned with the impact velocity v_I^0, see also Sect. 3.1.1.

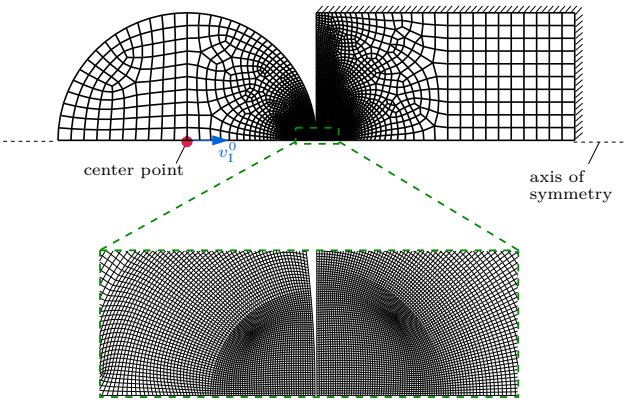

Figure 4.5: Schematic representation of the sphere–wall FEM impact model.

The kinematic COR is evaluated by the normal velocity of the sphere before and after the collision. While the velocity before impact is known a priori, the velocity after impact is evaluated at the center point of the sphere. As the velocity is slightly oscillating, due to mechanical vibrations of the sphere induced by the collision, the mean value of the last few time steps is taken. Since different material pairings are used, the contact duration and thus the necessary simulation time can vary by multiple decimal powers. This makes it important to approximate the contact duration beforehand, e. g. by using the formula by [Barber18] based on Hertz's impact theory [Hertz82]. The contact time t_e, i. e. the end of impact, reads

$$t_\mathrm{e} = 2.868 \left(\frac{\bar{M}^2}{v_\mathrm{I}^0 \, \bar{R} \, \bar{E}^2} \right)^{\frac{1}{5}} . \tag{4.8}$$

The effective Young's modulus $\bar{E}$, the effective radius $\bar{R}$ and the effective mass $\bar{M}$ follow from Eqs. (2.71),(2.72) and (2.81). To remove the unnecessary overhead after contact, the simulation is stopped when the contact force turns zero.
The nonlinear material behavior of steel, aluminum and polymer are here described by the relationships and data presented in Sect. 4.1. The metal behavior of steel and aluminum is implemented with the data of Tab. 4.1 and Fig. 4.2. The implementation of the SAA polymer is done with the so-called *Prony series* shown in Tab. 4.2.

4.3 Experimental and Numerical Results

In this section, experimental and numerical results are compared for steel–metal and steel–polymer impacts. Furthermore, sensitivity analyses on the sphere's diameter and impact velocity are performed. Finally, to gain insights into the micromechanical processes during impact, such as energy conversion, contact time and contact force, these are compared for the different utilized material pairings.

4.3.1 Steel–Metal Impacts

This section deals with steel–metal collisions. For that, a steel sphere impacts different planar steel and aluminum walls of about 50 mm thickness. These metals are part of the particles and walls in the later utilized particle dampers. Precise material models for FEM simulations are available for aluminum and steel, see

also Sect. 4.1. It should be noted that the used metals are of the same type, but not from the same production batch.

Steel–Steel Impacts

In Fig. 4.6 the results of simulations and experiments of the COR for steel–steel impacts with a 30 mm diameter sphere are shown. The simulation relates only to the first impact of the sphere against the wall. For the experiments, only the first impact, as well as an exponential fit, is plotted. As each impact velocity is measured five times, the mean values and their maximum deviations are shown. Since every measurement cycle consists of multiple impacts on the same spot, those results are plotted as well in Fig. 4.6 and are labeled with "exp. repeated impacts".
A high dependency on impact velocity is observed in simulations and experiments. For very small impact velocities, which can not be measured experimentally, the COR is close to one in the simulations. When the impact velocity increases the COR starts to decrease rapidly in simulations as well as in experiments. For high impact velocities, the COR drops below 0.55 and converges to an almost constant value. For low impact velocities, i. e. $v_{\mathrm{I}}^{0} < 0.5\,\mathrm{m/s}$, simulations and experiments match very well. For higher impact velocities, a slight difference of about 0.03 is seen in the COR. Hence, a good qualitative and quantitative agreement is achieved between experiments and simulations.
Comparing the repeated impacts from the experiments with the corresponding first impacts, it can be seen that a higher COR is obtained for the collisions after the first rebound. Thus, during the initial impact, a considerable amount of energy dissipates by plastic deformations. Due to the hardening of the contact zone after initial contact, a repeated impact with the same spot cannot be accompanied by an energy dissipation of the same high amount. In consequence, the energy dissipation is lower, resulting in a higher COR. See [MinamotoEtAl11,

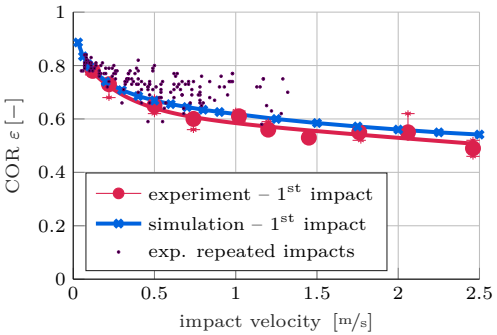

Figure 4.6: CORs for the impact of a 30 mm steel sphere against a steel wall.

WeirTallon05] for further discussion on this topic.
The high CORs for low impact velocities can be explained by considering Hooke's law. Only if the metal yield stress is exceeded plastic deformations occur and thus energy is dissipated. For low impact velocities, only very little plastic deformation occurs. With increasing impact velocity, plastic deformations are rising as well, leading to lower CORs. The COR finally converges to an almost constant value due to the elastic-viscoplastic material behavior of steel, i. e. the yield stress raises for higher strain rates, see also Fig. 4.2. This leads to lower plastic deformations compared to a purely plastic material behavior and vanishes the effect of higher impact velocity.

As the numerical model is suitable for calculating CORs of steel–steel impacts, it can be used in the next step for sensitivity analyses of the sphere's diameter. The results for the first impact are shown in Fig. 4.7 for sphere diameters between 1 mm to 50 mm. All COR curves show a similar progression but with an offset in the COR. The higher the sphere's diameter, the lower the COR. Similar results were gained in [AryaeiEtAl10] for a more limited diameter range. Only for very low impact velocities, the COR seems to converge to the same high value. Getting closer to the smallest/biggest sphere diameter the difference in the COR decreases. Thus, it is expected that even lower/higher sphere diameters do not have a significant influence on the COR anymore.

Next, the energy dissipation during impact is analyzed in more detail using the simulation. In this study, the plastic deformation `ALLPD` (name in Abaqus) and the recoverable strain energy `ALLSE` are gathered from the simulation. Figure 4.8 shows the time course of those two energy types for an impact of a 30 mm steel sphere with an impact velocity of 1 m/s against a steel wall. In addition to that, the time points of maximum contact force, maximum indentation and end of impact are indicated. At the beginning of impact, strain energy and plastic dissipation are

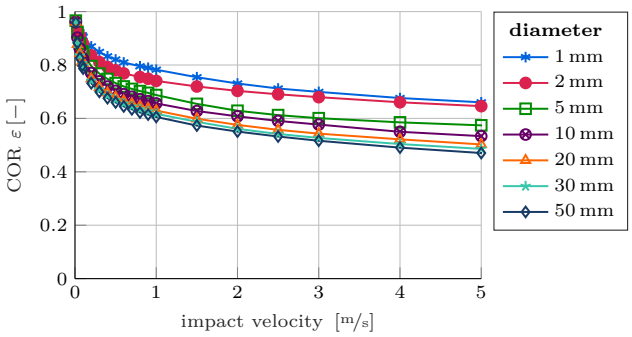

Figure 4.7: CORs by FEM simulations for first impacts of steel sphere of different diameters against steel wall.

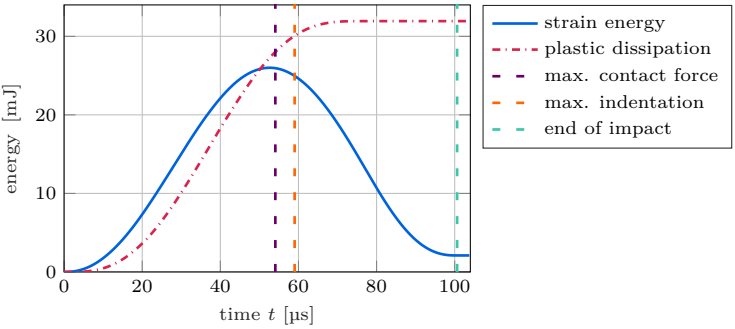

Figure 4.8: Time course of energy dissipation by FEM simulation of a 1 m/s impact between 30 mm steel sphere and steel wall.

increasing and showing an almost constant slope for 20 µs $< t <$ 40 µs. However, the plastic dissipation lags a bit in time. The strain energy reaches its maximum value approximately at the time of maximum contact force. The maximum indentation follows shortly after the maximum contact force, i. e. 5 µs later. This can mainly be explained by the elastic-viscoplastic material behavior of steel. A pure elastic-plastic material model, i. e. if only the quasi-static yield stress is considered, leads to a time delay of just 1 µs. Here, the time the compression wave takes to travel from the contact zone to the sphere's center point is the only cause of the time delay. After the maximum contact force is exceeded, the slope of plastic dissipation decreases a lot. Shortly after the maximum indentation occurred, the energy dissipated by plastic deformations reaches its maximum. Thus, plastic dissipation mainly takes place in the compression phase. Throughout the restitution phase, the strain energy decreases drastically. At the end of the impact, some strain energy is still left and does not vanish. This happens due to permanent plastic deformations inhibiting a full strain release. Thus, this remaining strain energy can also be categorized as energy dissipation. The next step is to determine in which contact partner, i. e. sphere or wall, the energy dissipation takes place. Figure 4.9 shows the energy dissipation as the relative distribution over different impact velocities for a 30 mm sphere. The dissipation is approximately identical in both contact partners, i. e. in sphere and wall, with impact velocity only having a minor influence. Moreover, there is a negligible dependency on the sphere's diameter. This is not depicted in Fig. 4.9. Hence, the influence of the body's geometry seems to play a subordinate role in this case.

For the particle damper analyses of the following chapters, the CORs for impacts between two steel spheres are required. At first, in Fig. 4.10 steel sphere–sphere and steel sphere–wall impacts are compared by FEM simulations for 30 mm sphere size. Both COR curves show the same qualitative behavior. Quantitatively, a

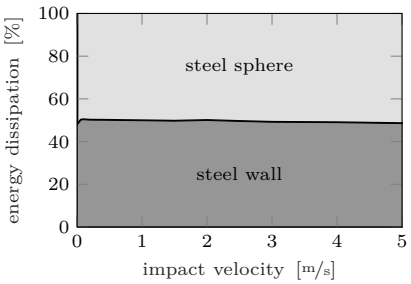

Figure 4.9: Location of energy dissipation obtained by FEM simulations between 30 mm steel sphere and steel wall.

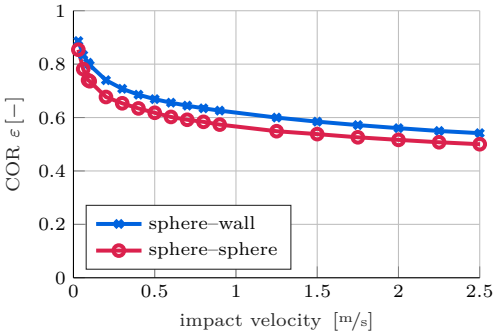

Figure 4.10: Comparison of CORs for steel sphere–sphere and steel sphere–wall impacts of 30 mm sphere size by FEM simulations.

small offset of about 0.04 can be seen, while the sphere–sphere impacts lead to lower CORs. This could occur due to a smaller contact area of a pure sphere–sphere contact, leading to higher stresses in the contact zone.
For the sake of completeness, Fig. 4.11 shows the CORs for steel sphere–sphere contacts of same diameters between 1 mm to 50 mm, which are used for later DEM (discrete element method) simulations. Similar to the sphere–wall contacts, the COR curves show the same qualitative progression. Quantitatively, the bigger the spheres' diameters, the lower the COR. Getting closer to the smallest/biggest sphere diameters the difference in the COR decreases. Thus, it is expected that even lower/higher sphere diameters do not have a significant influence on the COR anymore.

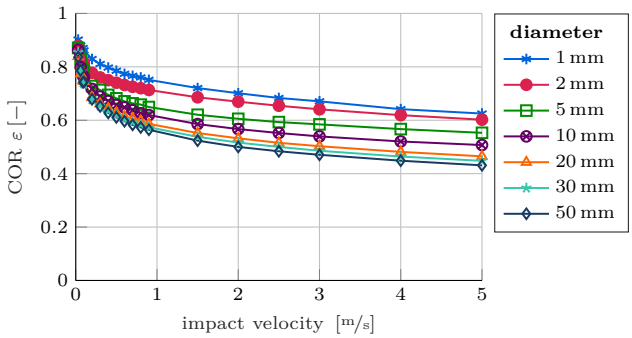

Figure 4.11: CORs by FEM simulations for the impact of two same sized steel spheres for different diameters.

Steel–Aluminum Impacts

In this section, the impact of a steel sphere against an aluminum wall is examined. The results of the COR for experiments and simulations are shown in Fig. 4.12. The COR's curve progression looks similar compared to the pure steel impacts, i. e. high CORs for low impact velocities with a high decrease at the beginning and converging to an almost constant value of about 0.5 at high impact velocities. As in the previously described observations, the experimental results show only a small deviation within each impact velocity. A good qualitative agreement with a quantitative difference of about 0.05 is obtained through simulations. The experimentally repeated impacts yield a higher COR than the corresponding first impacts once again.

Comparing steel–steel and steel–aluminum impacts, i. e. Fig. 4.6 and Fig. 4.12,

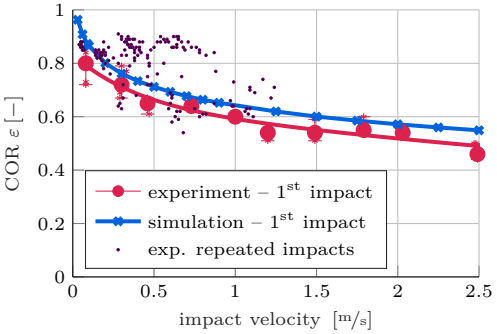

Figure 4.12: CORs for the impact of a steel sphere against an aluminum wall.

the experimental COR values are very close to each other. Obtaining COR values that are so similar might seem counterintuitive as aluminum is a softer material than steel. One could therefore expect more plastic deformations and energy dissipation and thus lower CORs. However, as will be shown in Sect. 4.3.3, due to the lower Young's modulus and lower weight of aluminum, the contact force for steel–aluminum impacts is smaller than the one for steel–steel impacts. For the latter, the energy dissipation occurs equally in both bodies, i. e. wall and sphere, see Fig. 4.9. For impacts of a steel sphere against an aluminum wall, the energy dissipates predominantly in the aluminum wall, as shown in Fig. 4.15 and discussed later in more detail. Hence, the steel sphere shows almost no plastic deformations. These combined effects lead to a similar energy dissipation for steel–steel and steel–aluminum impacts. As the energy dissipation is concentrated to the aluminum wall, its contact zone is more hardened compared to pure steel–steel impacts. This could explain the fact that the CORs of repeated impacts for aluminum are higher compared with pure steel impacts. For details on repeated impacts see [MinamotoEtAl11, SeifriedEtAl10, WeirTallon05]. In consequence, general statements about the CORs for other metal material pairings can merely be drawn from these investigations.

In Fig. 4.13 the dependency of the sphere's diameter regarding the COR is depicted. These curves are utilized for the later DEM simulations. The curves look-alike for steel–steel and steel–aluminum impacts, i. e. a lower sphere diameter leads to a higher COR, compare Fig. 4.7 and Fig. 4.13. However, for steel–aluminum impacts the dependency on the sphere's diameter is much lower. This behavior could be due to a lower slope in the stress–strain curve at high strains for aluminum, see Fig. 4.1.

As explained in Sect. 4.3.1, the location of the energy dissipation can be gathered from FEM analysis. The same is done for the steel–aluminum impacts and shown

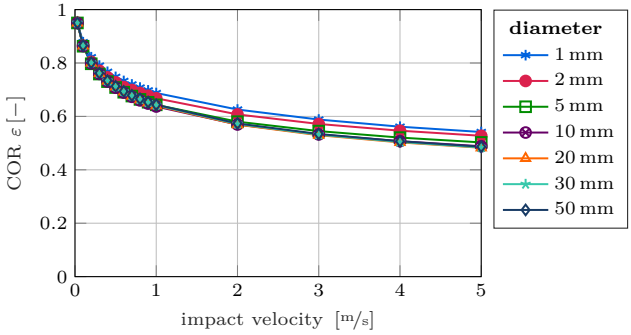

Figure 4.13: CORs by FEM simulations for first impacts of steel spheres of different diameters against aluminum wall.

in Fig. 4.14 for a 30 mm steel sphere of 1 m/s impact velocity. The time course of the energy dissipation is qualitatively similar to the pure steel dissipation, compare Fig. 4.8 and Fig. 4.14. However, for the steel–aluminum impact the time delay between maximum contact force and maximum indentation is much lower with only 2.5 µs to 5 µs although the total contact time is higher, i. e. 133 µs to 101 µs. This happens due to the significantly lower dependency of the plastic flow on the strain rate of aluminum compared to steel, see Fig. 4.2. After the maximum indentation, i. e. during the restitution phase, almost no plastic dissipation occurs anymore.

Figure 4.15 shows where the energy in the sphere and wall dissipates relatively. It can be seen that approximately 90 % of the energy dissipation occurs in the aluminum wall almost independent of impact velocity. Only for very low impact velocities, the dissipation ratio decreases to roughly 85 % within the aluminum wall. The difference to steel–steel is significant, i. e. equal dissipation in both bodies, see Fig. 4.9. This effect can be explained by the lower yield stress of aluminum compared to steel. Thus, considerably more plastic deformation occurs in the aluminum wall. This can also be observed after the experiments as the visual impact zone deformations on the aluminum block are far more noticeable than the ones on the steel block.

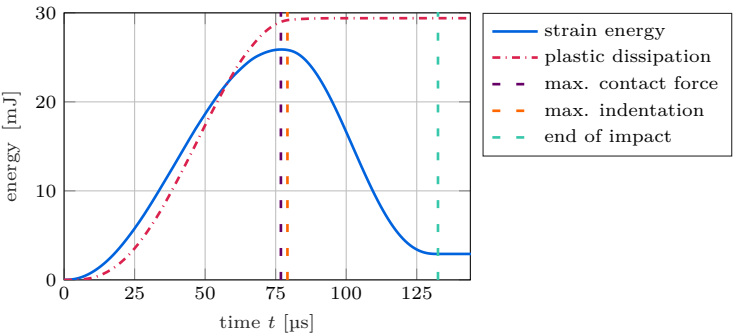

Figure 4.14: Time course of energy dissipation obtained via FEM simulation for 1 m/s impact velocity between 30 mm steel sphere and aluminum wall.

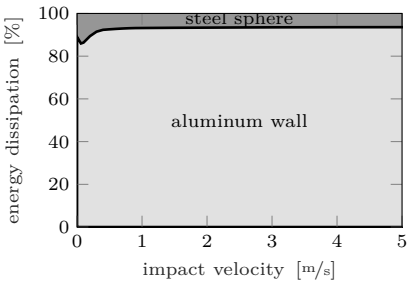

Figure 4.15: Location of energy dissipation obtained by FEM simulations between 30 mm steel sphere and aluminum wall.

4.3.2 Steel–Polymer Impacts

In the previous sections, pure metal contacts were discussed. Now, contacts between hybrid material combinations are investigated. A same-sized steel sphere of 30 mm diameter is used. As wall material, three different types of polymers are analyzed. All materials are investigated experimentally. The available material data of the polymers are listed in Tab. 4.3. The Young's moduli can only be seen as rough approximations due to the visco-elastic material behavior of polymers. However, they give an impression of the material stiffness.
The first investigated polymer is a KRAIBON® compound *SAA9579-52*, henceforth referred to as *SAA*. The second polymer is the widely used Polyvinyl chloride (PVC). The third one is a cold vulcanizing silicone rubber manufactured by Zhermack SpA (Badia Polesine, Italy) distributed through Troll Factory Rainer Habekost e.K. (Riede, Germany) under the name *TFC Type 2*. In the following, it is referred to as *T2*. The polymer T2 is significantly softer than SAA and substantially softer than PVC. All densities are on a similar scale. However, due to a lack of proper material models, only the SAA is investigated numerically to obtain deeper insights into the contact procedure. Its visco-elastic material behavior is introduced in Sect. 4.1.2.

Table 4.3: Material data of used polymers.

Material	T2	SAA	PVC
Color	● light green ●	● Black ●	● Gray ●
Density [kg/m³]	1193	1180	1400
Young's Modulus [MPa]	≈ 1	≈ 55	1000 – 3500

Steel–SAA Impacts

The used SAA probe is 2.4 mm thick and glued to the rigid steel block of the test armature. Due to this setup, the question arises whether the material thickness affects the COR. However, this could not be observed, see [MeyerEtAl22] for further discussion. In contrast to pure metal impacts, no effect of repeated impacts is seen for polymers, i. e. repeated impacts have the same COR as corresponding first impacts [MeyerEtAl22]. Thus, it is not differentiated between first or repeated impacts anymore. This effect can be explained as the used polymers show a visco-elastic material behavior. Hence, no or almost no plastic deformations occur in the contact zone. Instead, the material fully recovers and no history-dependent behavior takes place. Here, for each measurement cycle, the sphere rebounds until it comes to rest. Thus, the lowest measurable impact velocity decreases to about 0.01 m/s. The measurements are repeated five times. Hence, the mean value and the maximum derivation are shown for the experiments.

In Fig. 4.16 the experimental and numerical results for the COR are shown. These differ significantly from the investigated steel–steel and steel–aluminum impacts, i. e. the dependency of the COR on impact velocity is recognizably smaller, compare with Fig. 4.6 and Fig. 4.12. However, the effect of higher CORs at lower impact velocities resembles. Already at the lowest impact velocity of 0.01 m/s the COR has a value of $\varepsilon = 0.68$. At low impact velocities, the investigated metals have shown a tendency towards $\varepsilon \to 1$. Additionally, for the metals, a rapid decrease of the COR over impact velocity is observed on a large measurement range. Here, this can only be noticed up to impact velocities of 0.2 m/s. Afterward, only a slight almost linear decay is seen in the experiments.

The COR values measured for impact velocities below 1 m/s coincide very well with the simulation results. At higher velocities, there is a notable difference.

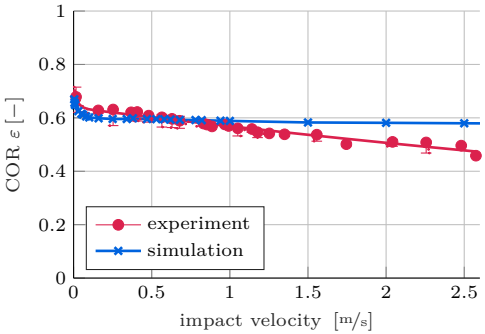

Figure 4.16: CORs for impact of 30 mm steel sphere against 2.4 mm thick SAA wall.

While in the experiments a small linear decay of the COR over impact velocity is seen for impacts velocities above 1 m/s, the simulations COR stays almost constant. A possible explanation for this behavior could be the method with which the visco-elastic material data is gained from the experimental DMA tests, see [SessnerEtAl19]. Thus, the used simulation data might only fit for a specific range of impact velocities. In this case, for impact velocities up to 1 m/s.

Similar to the previous sections, for this kind of material pairing a parameter study regarding the diameter of the sphere is performed. As for high impact velocities experimental and numerical results begin to diverge, the analyses are limited to impact velocities up to 1 m/s. The results are shown in Fig. 4.17. The dependency on the sphere's diameter is small. It is seen that bigger sphere diameters lead to higher CORs. This is opposite to steel–steel and steel–aluminum impacts, see Fig. 4.7 and Fig. 4.13, respectively. Yet, for very small sphere diameters, like 1 mm and 2 mm, the convergence does not hold anymore as the COR values rise again. However, it is hard to judge if this is a physical effect or happens due to numerical inaccuracies, like within the material model.

Next, the evolution of energy dissipation is investigated. This is shown for an impact velocity of 1 m/s for a 30 mm steel sphere in Fig. 4.18. In addition to the outputs mentioned in Sect. 4.3.1, for the visco-elastic SAA it is necessary to take the energy dissipation by viscoelasticity `ALLCD` into account. Figure 4.18 displays that the energy stored in the material due to strain rises very quickly at the beginning of contact, i. e. within the compression phase. During this phase, the visco-elastic energy dissipation rapidly increases as well. Shortly before the strain energy reaches its maximum value, the maximum contact force occurs. Then, at about half the collision time, the maximum strain energy and afterward the maximum indentation is reached. The maximum strain energy lags behind the maximum contact force, due to the propagation of the compression waves within

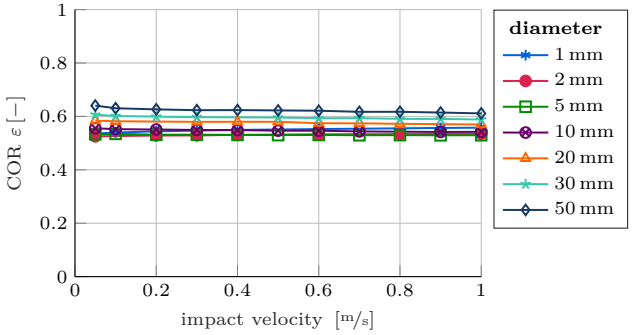

Figure 4.17: CORs by FEM simulations for impact of steel sphere of different diameters against SAA wall.

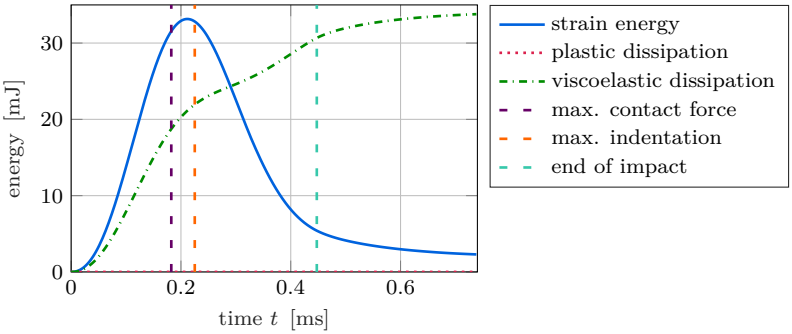

Figure 4.18: Time course of energy dissipation of a 1 m/s impact between 30 mm steel sphere and SAA wall obtained via FEM simulation.

both bodies. After the strain energy's maximum, it decreases with a high slope. However, the gradient of visco-elastic dissipation decreases. At the end of the contact, the strain energy has not reached zero and still has a negative slope. The visco-elastic dissipation increases the same amount as the strain energy decreases in this area. This effect is also known as the *elastic after effect* [BrinsonBrinson08]. This is different to the steel–steel and steel–aluminum progressions, see Fig. 4.9 and Fig. 4.15, as both of them show a constant remaining strain energy after impact. The amount of energy dissipation due to plasticity in the steel sphere is negligibly small during the whole contact procedure.

The energy dissipation ratio between 30 mm steel sphere and SAA wall is shown in Fig. 4.19. It can be seen that more than 99 % of the energy dissipates in the SAA wall. The result does not surprise as for aluminum, see Fig. 4.15, which is much softer than steel, already 90 % of the energy dissipation happens in the aluminum wall. The Young's modulus of SAA is several orders of magnitude

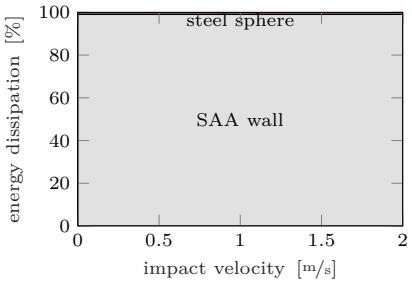

Figure 4.19: Location of energy dissipation by FEM simulations between 30 mm steel sphere and SAA wall.

lower than the ones of steel or aluminum. Due to this lower Young's modulus, the strain in the SAA wall is significantly higher but the resulting contact forces are considerably lower. Consequently, the steel sphere shows almost no plastic deformations and most energy dissipates through the visco-elasticity of the SAA.

Steel–PVC Impacts and Steel–T2 Impacts – Experimental Results

The previous section has shown a significantly lower dependency of the COR on impact velocity for the polymer SAA than for pure metal impacts. To further investigate this behavior, two additional polymers PVC and T2 are analyzed. However, due to a lack of material models, this is purely done experimentally. To prevent a break through the materials during impact, the material probes have a high thickness of 8 mm (PVC) and 10 mm (T2). The material data are summarized in Tab. 4.3. Each measurement is repeated five times. Hence, the mean value and the maximum derivation are shown for the experiments.
Figure 4.20 shows the experimental results for the COR of both materials getting impacted by a 30 mm steel sphere. It can be seen that there is only a minor dependency of the PVC's COR on impact velocity. A slight linear reduction of the COR towards higher velocities is obtained. The COR starts at $\varepsilon = 0.92$ and decreases to $\varepsilon = 0.87$. The deviations in the measurement results are very small. The material T2 has an even lower dependency of the COR on impact velocity. The COR is almost constant with values of $\varepsilon \approx 0.77$ and a small measurement deviation is obtained. Thus, all steel–polymer tests have shown a much lower dependency on impact velocity and a lower measurement deviation than the steel–metal impacts. Also, no damage of the material probes is observed after tests and the COR does not change for repeated impacts. Hence, it has to be analyzed in the following chapters if this could be a beneficial property of particle dampers.

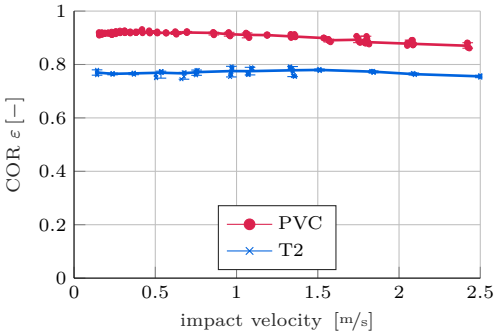

Figure 4.20: Experimental CORs for impact of 30 mm steel sphere against 8 mm thick PVC and 10 mm thick T2 wall.

As a numerical sensitivity analysis regarding the sphere's diameter is not possible, because no accurate material models are available for PVC and T2, the COR of Fig. 4.20 is used for all later DEM simulations independent of the diameter of the spheres. Indeed, it is expected that the sphere's diameter is of much lower influence for steel–polymer impacts compared to steel–metal impacts. Compare Fig. 4.17 of the SAA material with Fig. 4.7 and Fig. 4.13 of the metal materials.

4.3.3 Contact Duration and Contact Force

In the following, the contact duration and contact force for the different material pairings are analyzed. Figure 4.21 shows the results for the contact duration for all conducted experiments. A general observation is that for lower impact velocities, the contact duration increases in an exponential manner. For pure metal impacts, this is consistent with Hertz's impact theory [Hertz82], but can also be applied to the polymer impacts.
The metal–metal contacts are in a region of 100 µs and thus clearly shorter than metal–polymer contacts. Steel is harder than aluminum, therefore, the duration is shorter. The same rationale can be applied to the polymer contacts since PVC is harder than SAA and T2. Each PVC contact lasts around 0.3–1.5 ms. SAA and T2 are in a region of 1–10 ms.

In Fig. 4.22 contact force profiles of impacts by a 30 mm steel sphere of 1 $^{m}/_{s}$ impact velocity against the different wall material probes are compared by experiments. As described in Sect. 4.2.1, the acceleration and thus the contact

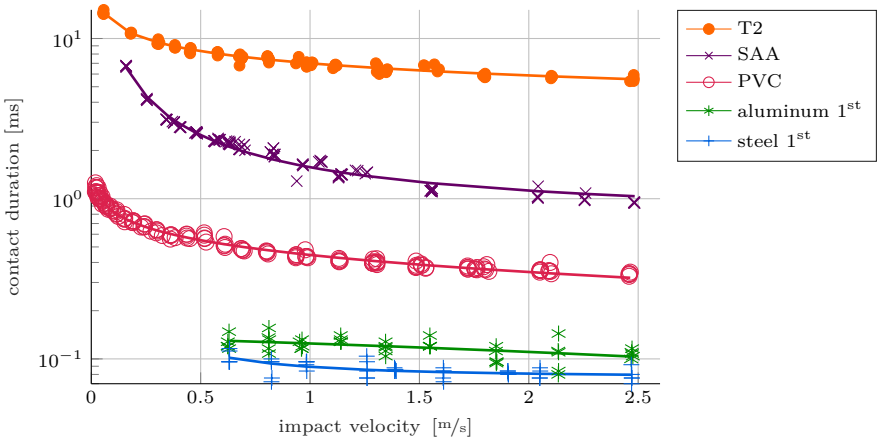

Figure 4.21: Measured contact durations of a 30 mm steel sphere for different wall materials.

force are calculated using central finite differences of the velocity signal of the laser vibrometer with a sampling frequency of 250 kHz. As expected, the maximal values of the contact force of the metal–metal impacts, i. e. steel–steel and steel–aluminum, are much higher than those of metal–polymer contacts, i. e. steel–PVC/SAA/T2. The force peaks are 3027 N and 2180 N for steel and aluminum compared to 865 N, 388 N and 50 N for PVC, SAA and T2. Hence, the maximal value of the contact force is directly correlated to the Young's moduli of the material, i. e. higher Young's moduli result in higher force peaks but lower contact times.

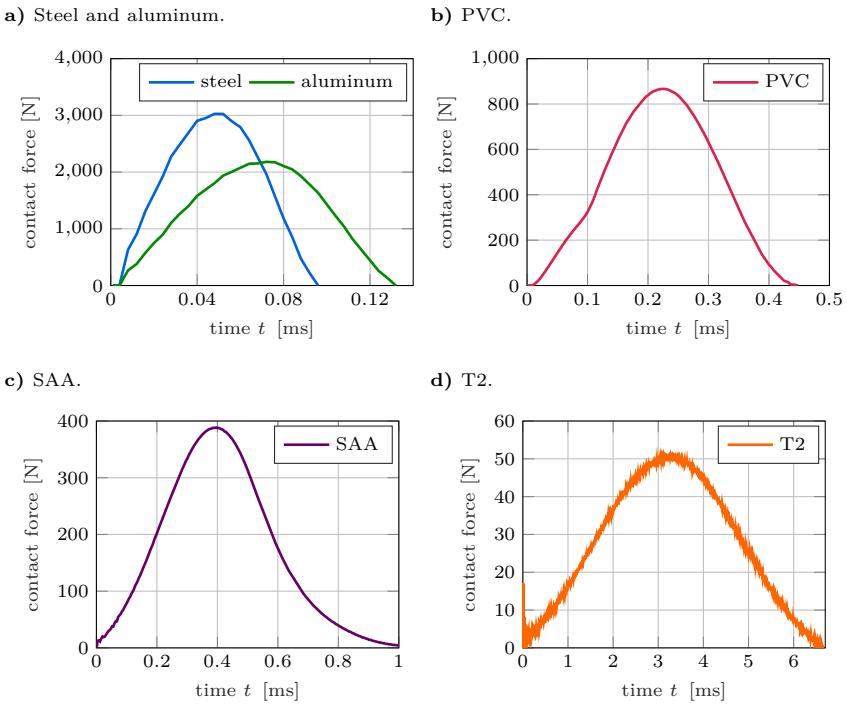

Figure 4.22: Measured contact force profiles for 1 m/s impact velocity of a 30 mm steel sphere for different wall materials.

4.4 Summary

The analyzed steel–steel and steel–aluminum contacts show a high dependency on impact velocity. They start at high COR values for low-impact velocities and show a degressive decay towards higher impact velocities. Due to plastic deformations, repeated impacts onto the same spot show a substantially higher COR. The contact times are short compared to steel–polymer impacts, which results in high contact forces and much higher noise emission. The finite element simulations are capable of reproducing the qualitative progression of the COR observed in experiments. However, small quantitative differences remain. Especially, for steel–steel impacts an effect on the sphere's diameter is observed. Bigger diameters lead to lower CORs. Indeed, a convergence to extreme diameters is visible. While for the steel–steel impacts the energy dissipation is distributed almost equally between sphere and wall, for steel–aluminum impacts this is dominated by the aluminum wall. Visible plastic deformations within the aluminum wall are observed after experiments.
Besides the steel–metal impacts, three different steel–polymer combinations are investigated. The used polymers can be roughly classified as soft, medium and hard. The steel–polymer contacts show only little dependency on impact velocity. Often, only a slight linear decrease of COR with impact velocity is observed. Also, the effect of repeated impacts vanishes as no plastic deformation occurs in the contact zone. The medium-stiff polymer is also analyzed numerically. A good agreement with experimental measurements is achieved for low-impact velocities. At high impact velocities, bigger differences are seen. The effect of the sphere size is small for this polymer. The energy dissipation predominantly takes place in the polymer wall and lasts even after contact has ended, due to the "elastic after effect" of polymers.

Low-Excitation Horizontal Vibration Analyses

Vibrations at low-excitation are going to be classified with vibration frequencies $f < 5\,\mathrm{Hz}$ and acceleration amplitudes of the particle damper below the gravitational constant, i. e. $A < g$. Early studies including this frequency range go back to [MehtaLuck90]. Thereby they studied the completely inelastic bouncing ball motion mode. Inspired by this, recently, the *bouncing collect-and-collide* motion mode was described by [BannermanEtAl11] and [SackEtAl13] under the condition of weightlessness, i. e. in absence of gravity. In this motion mode, the particles move as one single particle block synchronously with the vibrating particle container and collide inelastically with the container walls. To describe the motion mode, [BannermanEtAl11] and [SackEtAl13] derived an analytical equation for the energy dissipation of the particle bed. To validate their analytical predictions, experiments during parabolic flights, i. e. $A \approx 0$, were performed. While [SackEtAl13] subjected their particle container to a sinusoidal motion via a linear drive, [BannermanEtAl11] mounted their damper at the tip of a simple beam-like structure. Either way, a good agreement between the analytical equations and the performed experiments was found. Finally, in [BannermanEtAl11, SackEtAl13] it is concluded that the optimal working point of the bouncing collect-and-collide motion mode is only depending on the filling ratio of the damper but not on the excitation frequency.
However, for applications under the effect of gravity and of low acceleration intensities, i. e. an acceleration amplitude of the particle damper below the gravitational constant $A < g$, the formula of [BannermanEtAl11] and [SackEtAl13] is losing validity. This can be explained because particles begin to stick and the synchronous motion with the particle container is no longer observed [LuEtAl16]. To overcome this problem, the rolling attribute of spherical particles can be used for horizontal vibrations, i. e. perpendicular to gravity [ChenGeorgakis13, HuangEtAl21, LuEtAl10]. Instead of sticking, particles slide and roll over the container base. In this chapter, the spheres' rolling attribute is used within flat container bases. It is observed that a synchronous particle motion with the driven container is achieved, which furthermore can even be accurately described analytically. As high energy dissipation rates are obtained for this synchronous particle motion, structural vibrations can be damped efficiently.

At first, in Sect. 5.1, the **Single Damper Level** of the toolchain is considered, see also Fig. 3.1. Various experimental and numerical studies of a cuboid and

cylindrical particle container subjected to a horizontal sinusoidal motion are performed. Afterwards, in Sect. 5.2 the **Structural Integrated Damper Level** is analyzed. Free and forced vibrations of a simple beam-like structure and of a lightweight manipulator are damped efficiently by utilizing the previously described rolling effect of spheres.

5.1 Single Damper

To investigate the rolling effect of spheres inside a driven container, a cuboid container shape instead of a cylindrical one is utilized here for the first time. This container is studied experimentally and numerically using the *discrete element method* (DEM). Two different *motion modes* are observed within this container for sinusoidal motions. For vibration amplitudes below a certain threshold stroke a random particle motion, namely the *scattered motion mode*, is obtained. This motion mode results in a comparatively low energy dissipation. Increasing the amplitude of the vibration above the threshold stroke, a synchronous particle motion with the container is seen. The particles start to move as one particle bed and collide inelastically with the container walls. This results in high energy dissipation rates and is called *rolling collect-and-collide*. It becomes apparent that the highest damper efficiency occurs at the transition between both motion modes, i. e. at the so-called *optimal stroke*. It turns out that this optimal stroke is only depending on the filling ratio of the damper. Analogous to [BannermanEtAl11] and [SackEtAl13], analytical descriptions for the energy dissipation for both motion modes are derived in this section. A simple analytical equation for the optimal stroke is found as well.
In this section, also, sensitivity analyses are performed using the experimental setup and DEM simulations. Multiple particle properties, like Young's modulus, density, coefficient of restitution, friction coefficient, particle radius and particle number are studied. Additionally, the effect of a tilt around the different container's axis is investigated. Besides the cuboid container shape, the effect of a cylindrical container shape with its longitudinal axis oriented in the direction of gravity is analyzed at the end.

This section is organized in the following way: In Sect. 5.1.1, the experimental setup and numerical model are introduced to analyze the motion modes and energy dissipation inside the particle container. The results of these studies are given in Sect. 5.1.2. Subsequently, in Sect. 5.1.3, analytical equations for the energy dissipation of the scattered and rolling collect-and-collide motion modes are derived and compared to experimental measurements and numerical

simulations. Further influence parameters on the damper's energy dissipation are investigated by sensitivity analyses in Sect. 5.1.4. Finally, the content of this section is summarized in Sect. 5.1.5. The following results in this section have been published in [MeyerSeifried22].

5.1.1 Experimental and Numerical Setups

The experimental and numerical setups to analyze the particle damper for low-excitation horizontal vibrations are presented in the following. The particle container is subjected hereby to a sinusoidally motion of amplitude X and angular excitation frequency $\Omega = 2\,\pi\,f$ as $x_\mathrm{c} = X\sin(\Omega\,t)$, see Eq. (3.8). The container's velocity and acceleration amplitudes follow to $V = X\,\Omega$ and $A = X\,\Omega^2$, respectively, see Eqs. (3.9) and (3.10). The damper's *energy dissipation, effective loss factor* and *effective particle mass* are extracted using the *complex power method*. See Sect. 3.2.2 for a detailed description.

The main idea of the new damper design is to use the rolling attribute of spheres to obtain a high damper efficiency for low acceleration intensity vibrations. In contrast to the design of other authors, e. g. [BannermanEtAl11], a particle container with a cuboid shape and spherical particles is installed. By using less than one layer of particles, the spheres roll and slide over the container base instead of sticking together.

Experimental Setup The experimental setup to analyze the particle bed's motion modes and energy dissipation under sinusoidal motion is shown in Fig. 5.1. It consists of a cuboid particle container mounted on a linear drive via a force

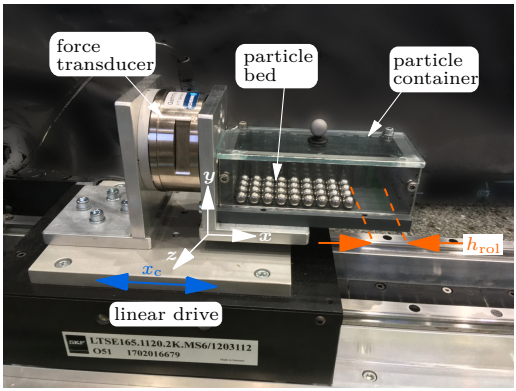

Figure 5.1: Experimental setup to analyze motion modes and effective fields of the driven particle bed for horizontal low intensity vibrations.

transducer. Thereby, the excitation force acting on the particle container can be measured. The particle container is made of polyvinyl chloride (PVC) and has a quadratic cross section with an inner edge width W and height H of 40 mm and a length L of 120 mm in excitation direction. The container is filled with steel (S235) spheres of $r = 5$ mm radius throughout this chapter. As these spheres are also used for ball bearings in the hardened form, they have a high degree of roundness. To reduce friction, the particles are lubricated with a small amount of oil. Between particle container and linear drive the force transducer *Gamma–SI–32–2.5* from the company SCHUNK is mounted to measure the excitation force. The linear drive *LTSE 165* is manufactured by SKF and SIEMENS. Its position is measured by the incremental encoder *LIA20* of NUMERIC JENA with a resolution of 20 µm. The control of the linear drive is performed by the motion controller *Simotion D435–2* of SIEMENS and the *Sinamics variable-speed drive* with a sampling frequency of 8 kHz. Thus, this setting ensures accurate control and fast reaction to safety issues. For further details see [MorlockEtAl18, MorlockEtAl21]. The measured results, namely the container motion and the driving force acting on the container, are saved with a sampling frequency of 1 kHz for later post-processing.
In the experiments, the linear drive excites the particle container sinusoidally, see Eq. (3.8)–Eq. (3.10). To analyze different effects and influence parameters on the particle bed, the excitation amplitude varies between $X = 0.5$ mm till $X = 50$ mm using 40 sample points and a logarithmic distribution. The excitation frequency is exemplary set to $f = 2$ Hz. It turns out that a lower and upper limit for the excitation frequency exists, which is discussed later. Each sample point is measured for 20 vibration cycles. After that, the linear drive pauses so the particles can come to rest. As only the stationary state of the system shall be analyzed, the first two vibration cycles are cut off during post-processing to remove the irregular movement of the particles through their initial state.

Numerical Model For numerical analyses, the DEM is utilized, see also Chap. 2. The standard settings and algorithms defined in Sect. 2.8 are utilized for the following simulations. The cuboid container is modeled using six planes, see Sect. 2.2.2. The same excitation and post-processing parameters as in the experiments are applied. The used material and contact data are listed in Tab. 5.1. Even though the experimental testbed is set up very precisely, little manufacturing and mounting inaccuracies cannot be precluded. Especially, the container width is slightly higher than previously stated with a value of about 40.4 mm. Additionally, little tilts around the container axes are observed using a spirit level. To account for these small inaccuracies, a rotation of 0.1° around all container axes is used for the simulations. It should be noted that these adjustments seem to be of minor importance. However, neglecting these inaccuracies can lead to abnormal or unrealistic behavior in the simulations as discussed later in detail. The particles' initial conditions are loaded from previously performed drop-down simulations.

Table 5.1: Material parameters of spheres and particle container.

	Sphere	Container
Material	S235	PVC
Young's Modulus E [GPa]	208	3
Poisson's Ratio ν [–]	0.3	0.38
Density ρ [$^{\mathrm{kg}}/_{\mathrm{m}^3}$]	7900	1400
Friction Coefficient μ [–]	0.1 for all contacts	
Coefficient of Restitution ε [–]	velocity dependent, see Chap. 4	
Dimensions [mm]	$r = 5$	$L, W, H = 120, 40.4, 40.0$

5.1.2 Experimental and Numerical Results

For the experiments, the particle container is filled with $n_\mathrm{p} = 36$ and $n_\mathrm{p} = 44$ particles, respectively. The maximum particle number necessary to cover the container base with one layer of particles is $n_\mathrm{p}^\mathrm{max} = 48$. The clearance h_rol, i. e. the distance between particle bed and opposite container wall with all particles lying on one side of the container's base, see also Fig. 5.1, is calculated as

$$h_\mathrm{rol} = L\left(1 - \frac{n_\mathrm{p}}{n_\mathrm{p}^\mathrm{max}}\right). \tag{5.1}$$

Hence, the clearance is calculated for 36 particles to $h_\mathrm{rol} = 30\,\mathrm{mm}$ and for 44 particles to $h_\mathrm{rol} = 10\,\mathrm{mm}$.
During all experiments, the particle bed does not fully take-off the container base. Only in rare cases, single particles leave the container base. This happens especially for higher container amplitudes. However, after a few vibration cycles, these flying particles usually integrate themselves into the particle bed again. This behavior is seen as the container's acceleration amplitude stays below the gravitational constant, i. e. $A = X\,\Omega^2 < g$. Hence, the gravitational constant is the upper bound for the container acceleration amplitude and thus for the container stroke and excitation frequency. Increasing the container acceleration amplitude for the analyzed systems above the gravitational constant, the particle bed, first of all, enters a motion mode of *fluidization* and finally turns into the bouncing collect-and-collide motion mode. However, these analyses are beyond the scope of this chapter and are dealt with in Chap. 6. Similar observations can be found e. g. in [YinEtAl17, ZhangEtAl17].

Motion Modes During the conducted experiments, two different motion modes of the particle bed are observed, i. e. the scattered motion mode and the rolling collect-and-collide motion mode. Snapshots of these motion modes are shown in Fig. 5.2 for different container positions. The resulting particle trajectories obtained from DEM simulations are shown in Fig. 5.3. For low-excitation amplitudes, the system is in the so-called scattering motion mode. Due to friction

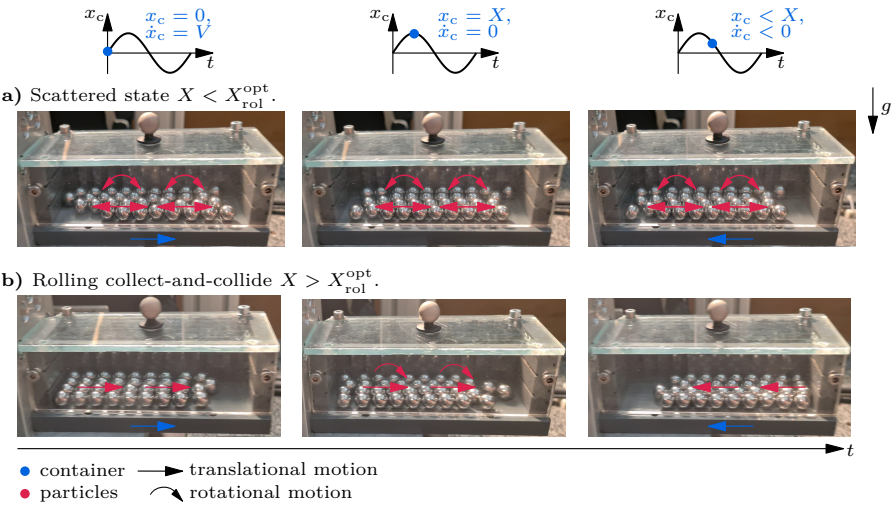

Figure 5.2: Observed motion modes at different container strokes for low-excitation horizontal vibrations.

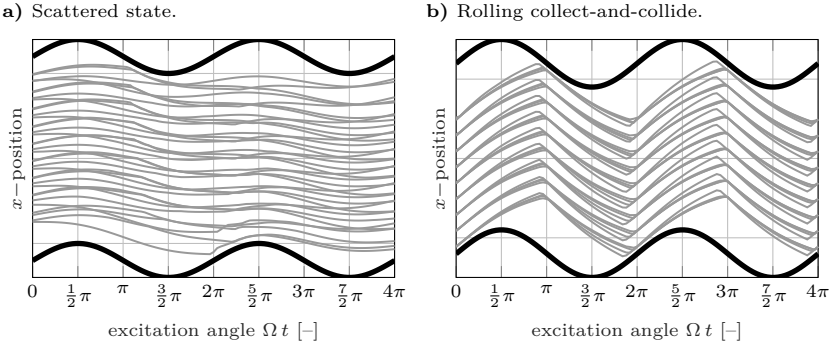

Figure 5.3: Particle trajectories obtained from DEM simulations for motion modes shown in Fig. 5.2. The bold black lines indicate the left and right container walls.

between particles and container base, only little particle movement with few collisions to the container walls is seen. Hence, no regular or synchronous motion of the particles is obtained, i. e. each particle moves in a different way.
When the container amplitude reaches a certain threshold amplitude X_{rol}^{opt} the system turns suddenly into the rolling collect-and-collide motion mode. Here, the particle bed stays together as one particle block and ideally rolls over the container base. However, the case of ideal rolling might not always hold and thus

additional slip occurs. During the impact of the particle bed with the container walls, multiple inter-particle and particle–wall impacts occur. Although, during every single impact, only a small amount of energy is dissipated, in sum a perfectly *inelastic collision* of the complete particle bed with the container wall is achieved, i. e. the particle bed adopts the velocity of the container instantaneously, see [SanchezEtAl12, McnamaraYoung92, BannermanEtAl11] for further discussions on the inelastic collision property. Hence, a synchronous particle motion with the container is achieved. However, for both particle numbers, i. e. for 36 and 44 particles, the container stroke for which the particle system switches its motion mode differs with $X_{\mathrm{rol}}^{\mathrm{opt}}(n_{\mathrm{p}} = 36) = 12\,\mathrm{mm}$ and $X_{\mathrm{rol}}^{\mathrm{opt}}(n_{\mathrm{p}} = 44) = 4\,\mathrm{mm}$, respectively.
It should be noted that this inelastic collision behavior partly vanishes within the DEM simulations when the container is modeled with no tilt and an ideal width of 40 mm. Instead, the particle bed rebounds from the container wall, which is not observed within the experiments. This happens as the particle rows behave like four single particle chains with no interactions between them. Hence, a lot fewer particle collisions occur, which are mandatory for the inelastic collision behavior.

Effective Loss Factor In the following, the *effective loss factors* $\bar{\eta}$ of the conducted experiments and numerical analyses is discussed. The effective loss factor is an efficiency factor, which correlates the dissipated energy of the particle bed to the kinetic energy of the particle bed, see also Eq. (3.15). The experimental and numerical results are shown in Fig. 5.4. The legend entry "ana. formulas" will be explained and discussed later in Sect. 5.1.3.

First, the experimental results are discussed. For small excitation amplitudes $X <$

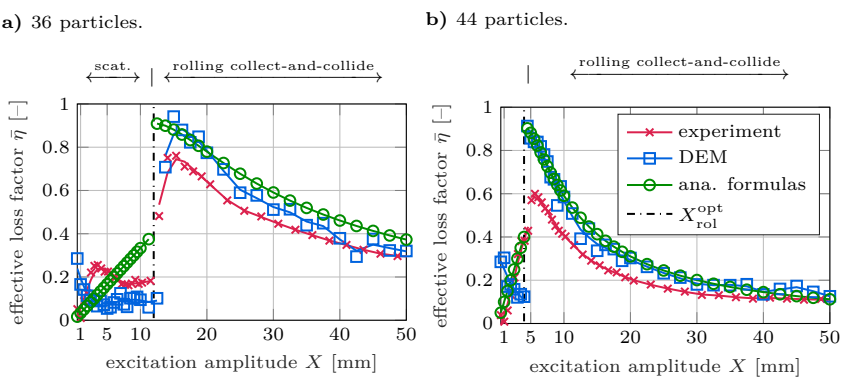

Figure 5.4: Effective loss factor of low-excitation horizontal vibrations. The threshold amplitude $X_{\mathrm{rol}}^{\mathrm{opt}}$ refers to Eq. (5.13).

$X_{\mathrm{rol}}^{\mathrm{opt}}$ both particle systems are in the scattered motion mode. Here, only small effective loss factor values $\bar{\eta} < 0.43$ are obtained. At $X \approx X_{\mathrm{rol}}^{\mathrm{opt}}$ both systems switch to the rolling collect-and-collide motion mode. At the optimal stroke, the highest effective loss factors are seen, with $\bar{\eta}_{\mathrm{rol}}^{\mathrm{max}} = 0.75$ for 36 particles and $\bar{\eta}_{\mathrm{rol}}^{\mathrm{max}} = 0.6$ for 44 particles. The shape of the effective loss factor curve is quite similar for the different particle numbers for the rolling collect-and-collide motion mode. It starts at the respective maximum values and decreases slowly with increasing excitation amplitudes. However, as $X_{\mathrm{rol}}^{\mathrm{opt}}$ is different for both particle settings, shifted excitation amplitudes are observed at the respective optimal stokes.
From these observations, it can be deduced that the rolling collect-and-collide motion mode is of much higher interest for the damper design with an underlying structure, because a higher damper efficiency is achieved. Especially, an operation within the maximum effective loss factors should be targeted. Thus, the rolling collect-and-collide motion mode and its influence parameters are of major interest in the following.

The numerical DEM results for the effective loss factor are also pictured in Fig. 5.4. For the scattered motion mode, i. e. $X < X_{\mathrm{rol}}^{\mathrm{opt}}$, the results are on the same scale as the experimental results. However, neither a qualitative nor quantitative agreement of the observed curves is achieved for this area. The energy dissipation can be expressed by Eq. (3.15), i. e. $\widetilde{E}_{\mathrm{diss}} = \frac{1}{2}\, m_{\mathrm{bed}}\, V^2 \bar{\eta}$, with m_{bed} being the mass of all particles. As the effective loss factor $\bar{\eta}$ and the container's velocity amplitude $V = X\,\Omega$ are low for the scattered motion mode, low energy dissipation is achieved for this regime as well. Hence, the energy dissipation could be very sensitive to certain properties, such as an additional container tilt. This will be further analyzed in Sect. 5.1.4.
For the rolling collect-and-collide motion mode, i. e. $X > X_{\mathrm{rol}}^{\mathrm{opt}}$, a good qualitative agreement with the experiments is observed. Monitoring strokes around the optimal one, i. e. $X \approx X_{\mathrm{rol}}^{\mathrm{opt}}$, the DEM yields higher effective loss factor values compared to the experiments. For the 36 and 44 particle settings differences up to 0.2 and 0.3, respectively, are obtained. Looking at strokes significantly above the optimal stroke, experimental and numerical results converge against each other for both particle numbers.

Effective Particle Mass The *effective particle mass* $\bar{m}_{\mathrm{bed}}$ describes to what extent the mass of the particle bed is coupled to the container movement, see Eq. (3.17). In Fig. 5.5 the experimental and numerical results for the ratio of the effective particle mass to the mass of the particle bed are depicted.
Within the experimental measurements, for very low container amplitudes, i. e. $X \ll X_{\mathrm{rol}}^{\mathrm{opt}}$ – the scattered motion mode, for both particle numbers the ratio of the effective particle mass to the mass of the particle bed is high. It even reaches values above one. Getting closer to the optimal stroke, the effective particle mass decreases dramatically and increases again around the optimal stroke. For the

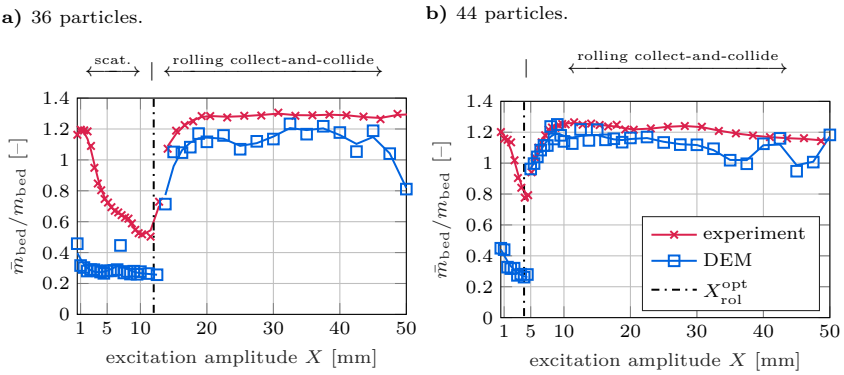

Figure 5.5: Ratio of effective particle mass to mass of the particle bed. The threshold amplitude $X_{\mathrm{rol}}^{\mathrm{opt}}$ refers to Eq. (5.13).

rolling collect-and-collide regime, i. e. $X > X_{\mathrm{rol}}^{\mathrm{opt}}$, the effective particle mass stays high at around a ratio of 1.2. Within the rolling collect-and-collide regime, the numerical DEM simulations show a good qualitative fit with only little quantitative differences. For the scattered regime, however, the effective mass ratio is highly underestimated by DEM.

5.1.3 Analytical Description

As seen in Fig. 5.4 the effective loss factor and thus the energy dissipation of the particle bed are strongly related to the scattered and rolling collect-and-collide motion modes. While for the scattered motion mode rather low values are obtained, the rolling collect-and-collide motion mode leads to high effective loss factor values, especially in the area of $X_{\mathrm{rol}}^{\mathrm{opt}}$. For both motion modes, an analytical equation shall be found in the following to describe the energy dissipation of the particle bed.

Scattered Motion Mode

This motion mode is characterized by its non-regular movement. It is similar to the gas-like motion mode observed by [SackEtAl13] under the condition of weightlessness. Thus, it can be assumed that the dissipated energy is proportional to the number of particle–wall collisions. This collision number depends on the volume pushed by the container. As the particles hit the container walls at random phases, a higher container stroke X leads to more collisions while a higher clearance h_{rol} leads to fewer collisions. Furthermore, the dissipated energy is assumed to scale with the particle's kinetic energy. Using an empirical approach

to derive an analytical equation for the energy dissipation considering the above mentioned observations, finally results in

$$E_{\mathrm{diss}} = \frac{X}{h_{\mathrm{rol}}} E_{\mathrm{kin}} = \frac{m_{\mathrm{bed}}\, X\, V^2}{2\, h_{\mathrm{rol}}}, \tag{5.2}$$

with m_{bed} being the mass of all particles. For this energy dissipation, the effective loss factor is hence

$$\bar{\eta} = \frac{E_{\mathrm{diss}}}{E_{\mathrm{kin}}} = \frac{X}{h_{\mathrm{rol}}}, \tag{5.3}$$

yielding a linear dependency on the excitation amplitude. Besides the excitation amplitude, Eq. (5.3) is only further dependent on the clearance and thus on the damper's filling ratio.
This analytical solution is shown in Fig. 5.4 for $X < X_{\mathrm{rol}}^{\mathrm{opt}}$, i. e. the scattering motion mode. For the 36 particle setting, see Fig. 5.4a, only a rough approximation is achieved. First, the analytical formula underestimates the effective loss factor and later on overestimates it. Whereas for the 44 particle setting, a good quantitative agreement is seen for the whole scattering motion mode, see Fig. 5.4b. These different matches of experiments and analytical formulas can be explained as the Eqs. (5.2) and (5.3) are derived empirically and not by formulas describing the physical behavior of motion of the particles. It should also be kept in mind that for the scattered motion mode the effective loss factor, as well as the dissipated energy of the particle system, are low. Thus, this regime should be avoided for practical applications and an accurate description of the energy dissipation is not of equally high practical importance as for the rolling collect-and-collide motion mode.

Rolling Collect-and-Collide Motion Mode

From the experiments, it is observed that in the rolling collect-and-collide motion mode, i. e. for $X > X_{\mathrm{rol}}^{\mathrm{opt}}$, the particles moves as one single particle block, see Fig. 5.2 and Fig. 5.3. Therefore, the translational and rotational velocities of every single particle are assumed to be identical. It is observed that the particle bed is first of all pushed by the container wall. At the container's maximum velocity $\dot{x}_{\mathrm{c}} = \pm V$, i. e. at $\Omega\, t = n\, \pi$ with $n \in \mathbb{N}$, see also Eq. (3.8)–Eq. (3.10) for the container motion, the particle bed leaves the pushing container wall, i. e. at $x_{\mathrm{c}} = 0$. As the particle bed is pushed by the container until it leaves the container wall, almost no rotational movement is seen up to this point in time and the particles' rotational velocity $\dot{\varphi}$ can be assumed to be zero. After leaving the container wall, the particles begin to roll due to friction between the particles and the container base. A perfect instantaneous transition from sliding to rolling is assumed and energy conservation is presumed until the particle bed impacts the opposite container wall. The conservation of energy balance for a

single particle before and after leaving the pushing container wall follows to

$$\underbrace{\frac{1}{2}\,m_\mathrm{p}\,V^2}_{\substack{\text{end of}\\ \text{pushing phase}}} = \underbrace{\frac{1}{2}\,m_\mathrm{p}\,\dot{x}_\mathrm{p}^2 + \frac{1}{2}\,I\,\dot{\varphi}^2}_{\text{rolling phase}}, \tag{5.4}$$

with $\dot{x}_\mathrm{p}$ being the particle's absolute translational velocity, m_p and I being the mass and moment of inertia of a single spherical particle and $\dot{\varphi}$ being the particle's angular velocity. At this point, $\dot{x}_\mathrm{p}$ and $\dot{\varphi}$ are assumed to be identical for all particles. To solve for the particle's absolute translational velocity $\dot{x}_\mathrm{p}$, the angular particle's velocity $\dot{\varphi}$ has to be expressed by it. Hence, the rolling condition of a single particle is used, reading here

$$\dot{\varphi} = \frac{1}{r}\left(\dot{x}_\mathrm{p} - \dot{x}_\mathrm{c}\right), \tag{5.5}$$

with r being the particle radius and $\dot{x}_\mathrm{c}$ being the container motion, see Eq. (3.9). Inserting Eq. (5.5) into Eq. (5.4), the particle's translational velocity during the rolling phase results in

$$\dot{x}_\mathrm{p} = \frac{1}{7}\,V\left(2\cos\left(\Omega\,t\right) + \sqrt{25 + 10\sin^2\left(\Omega\,t\right)}\right). \tag{5.6}$$

The relative velocity between particle bed and container during the rolling phase $\Delta\dot{x}_\mathrm{cp} = \dot{x}_\mathrm{p} - \dot{x}_\mathrm{c}$, given by Eq. (3.9) and Eq. (5.6), follows to

$$\Delta\dot{x}_\mathrm{cp} = \frac{1}{7}\,V\left(\sqrt{25 + 10\sin^2\left(\Omega\,t\right)} - 5\cos(\Omega\,t)\right). \tag{5.7}$$

It is noteworthy that Eqs. (5.6) and (5.7) only depend on the container's velocity amplitude V and the excitation angle $\Omega\,t$, but are independent of the particles' properties, like mass or radius.

Next, the particle bed collides with velocity $\dot{x}_\mathrm{p}^-(t_\mathrm{imp})$ inelastically with the opposite container wall at the impact time point t_imp. The impact time point is limited by $\Omega\,t_\mathrm{imp} = \pi$. For this point in time, the container is once again located at $x_\mathrm{c} = 0$ but moves in the other direction, i. e. $\dot{x}_\mathrm{c} = \mp V$. If the particle bed hits the container at a later instance of time, which is equivalent to container strokes below the optimal stroke, the aforementioned observation that the particle bed leaves the container wall at $x_\mathrm{c} = 0$ would be violated for the following vibration cycle. In the experiments, the scattering motion mode is observed instead.

In Fig. 5.6a the position of the particle bed during its rolling phase is shown to give an impression of the particle movement. The positions of the pushing (lower blue line) and impacting (upper blue line) container walls normalized by the container's amplitude X are shown as well. As the distance between both container walls depends on the clearance h_rol, see Fig. 5.1, the position of the impacting container wall (upper blue line) merely indicates one possible configuration. It

a) Position of particle bed, pushing container wall (lower blue line) and impacting container wall (upper blue line) normalized by the container's amplitude X.

b) Absolute and relative velocities of the particles and container normalized by the container velocity amplitude V.

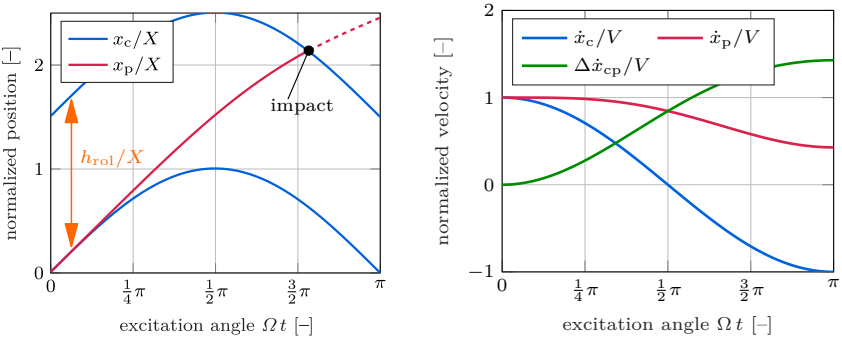

Figure 5.6: Positions and velocities of particle bed and container.

should be noted that for the rolling collect-and-collide motion mode, the particle impact could occur at any instance of time up to $\Omega\, t_{imp} = \pi$ depending on the clearance h_{rol}.
In Fig. 5.6b the absolute velocities of the particles $\dot{x}_p$, the absolute velocity of the container $\dot{x}_c$, and the relative velocity between particles and container $\Delta\dot{x}_{cp}$ normalized by the container's velocity amplitude V are shown. Due to the rolling condition, the particles' velocities decrease monotonically until impact with the opposite container wall. However, the relative velocity between particles and container is monotonically increasing. It should be noted that a higher container amplitude X and thus a higher container velocity amplitude V leads to an earlier impact of the particle bed with the opposite container wall, i. e. $\Omega\, t_{imp}$ decreases. Consequently, the normalized velocity ratio $\Delta\dot{x}_{cp}/V$ at particle impact decreases as the container amplitude X increases yielding a lower damper efficiency. This is in agreement with the effective loss factor, see Fig. 5.4.

To obtain the particles' impact velocity with the opposite container wall $\dot{x}_p^-(t_{imp})$, the impact time point t_{imp} is necessary. It describes the time the particle bed needs to travel from the pushing to the opposite container wall. It is achieved by solving

$$\underbrace{\int_0^{t_{imp}} \dot{x}_p(t)\,\mathrm{d}t}_{\text{particle motion}} = \underbrace{X\sin(\Omega\, t_{imp})}_{\text{container motion}} + \underbrace{h_{rol}}_{\text{clearance}} \,. \tag{5.8}$$

Using Eq. (5.6) for the particle velocity, Eq. (5.8) can be solved numerically for the impact time point t_{imp}.

During the impact of the particle bed with the container wall an inelastic collision occurs. Thus, the particle bed adopts the velocity of the container instantaneously, i. e. $\dot{x}_\mathrm{p}^+(t_\mathrm{imp}) = \dot{x}_\mathrm{c}^+(t_\mathrm{imp})$. During this impact, the rotational movement of the particles stops. In sum, two impacts (left container wall, right container wall) occur during one vibration cycle. Accordingly, the dissipated energy per cycle follows to

$$\widetilde{E}_\mathrm{diss} = 2\left(\frac{1}{2}\, m_\mathrm{bed}\, \Delta\dot{x}_\mathrm{cp}^2(t_\mathrm{imp}) + \frac{1}{2}\, I_\mathrm{bed}\, \dot{\varphi}^2(t_\mathrm{imp})\right), \tag{5.9}$$

with m_bed being the mass of all particles and I_bed being the sum of the particles' moment of inertia terms. Inserting the rolling condition, i. e. Eq. (5.5), and the relative velocity between particles and container, i. e. Eq. (5.7), into Eq. (5.9) yields the dissipated energy per cycle to

$$\widetilde{E}_\mathrm{diss} = \frac{1}{35}\, m_\mathrm{bed}\, V^2 \left(\sqrt{25 + 10\sin^2(\Omega\, t_\mathrm{imp})} - 5\cos\left(\Omega\, t_\mathrm{imp}\right)\right)^2. \tag{5.10}$$

The only unknown in this equation is the impact time point t_imp, which is solved for by Eq. (5.8). Finally, the effective loss factor $\bar{\eta}$ is obtained by Eq. (3.15).
As seen in Fig. 5.6b the highest relative velocity and thus the highest damping efficiency of the rolling collect-and-collide motion mode is achieved at an impact time point of $\Omega\, t_\mathrm{imp} = \pi$, i. e. at the switch point to the scattering motion mode. This has already been observed experimentally within the effective loss factor, see Fig. 5.4. By inserting this impact time point, i. e. $\Omega\, t_\mathrm{imp} = \pi$, into Eq. (5.10), the maximum dissipated energy per cycle $\widetilde{E}_\mathrm{diss}^\mathrm{max}$ and the maximum effective loss factor $\bar{\eta}_\mathrm{rol}^\mathrm{max}$ are obtained to

$$\widetilde{E}_\mathrm{diss}^\mathrm{max} = \frac{20}{7}\, m_\mathrm{bed}\, V^2, \tag{5.11}$$

$$\bar{\eta}_\mathrm{rol}^\mathrm{max} = \frac{\widetilde{E}_\mathrm{diss}^\mathrm{max}}{2\,\pi\, E_\mathrm{kin}} = \frac{20}{7\pi} \approx 0.91. \tag{5.12}$$

It is remarkable that the value of $\bar{\eta}_\mathrm{rol}^\mathrm{max}$, i. e. the damper's theoretical maximum efficiency, is neither dependent on the particle properties nor on the excitation conditions. Hence, this analytical optimal value of the effective loss factor can be used to judge different dampers and settings on their efficiency.
To obtain the container amplitude X for which $\Omega\, t_\mathrm{imp} = \pi$ holds, i. e. the stroke of maximum efficiency, Eq. (5.8) is solved with Eq. (5.6) numerically using this impact time point. This yields the optimal stroke as

$$X_\mathrm{rol}^\mathrm{opt} \approx 0.4\, h_\mathrm{rol}. \tag{5.13}$$

In agreement with the experimental results, see Fig. 5.4, this optimal stroke is only depending on the clearance h_rol. Remarkably, no dependency on the excitation frequency Ω or the particle properties exists again.

Validation To validate the analytical formula for the dissipated energy of the rolling collect-and-collide motion mode, i. e. Eq. (5.10), the effective loss factors and the optimal strokes are compared to the conducted experiments for 36 and 44 particles in Fig. 5.4 for $X > X_{\mathrm{rol}}^{\mathrm{opt}}$. The theoretical threshold $X_{\mathrm{rol}}^{\mathrm{opt}}$ only shows minor differences from the experimentally observed values. Moreover, the curves' progression of the effective loss factor concurs well with the experiments. However, the obtained values are above the experimentally measured ones for all excitation amplitudes. This starts at the optimal strokes with rather high differences of about 0.2 and 0.3 for the 36 and 44 particle settings, respectively. As the excitation amplitude increases, the differences decrease to 0.08 and 0.02, respectively. Although some quantitative differences between the analytical formula and experimental results exist, the qualitative validity of the derived formula is shown. Hence, the formula for the optimal stroke Eq. (5.13) and dissipated energy Eq. (5.10) provide a powerful tool to support the design of a particle damper for an underlying structure.
Interestingly, the DEM simulations are in much better agreement with the analytical formula than the experiments. This could be attributable to the fact that some influence parameters affecting the experiments are neither reproduced by the analytical formula Eq. (5.10) nor the DEM simulations. This will be further investigated in Sect. 5.1.4 by sensitivity analyses.

Effective Particle Mass

In contrast to the effective loss factor, it is hard to derive an analytical equation for the effective particle mass. In Fig. 5.5 it is observed that for the rolling collect-and-collide motion mode, a constant ratio of the effective particle mass to the mass of the particle bed, i. e. $\bar{m}_{\mathrm{bed}}/m_{\mathrm{bed}}$, exists. Sensitivity analyses in the next Sect. 5.1.4 show that this mass ratio depends on the container tilt among others. Within the **Structural Integrated Damper Level**, see Sect. 5.2, a mass ratio of one has been proven to be best for the rolling-collect-and-collide motion mode. For the scattered motion mode, however, no constant mass ratio is seen in Fig. 5.5. Regardless, here a constant ratio of 0.3 is taken as this approximates the effective particle mass around the optimal stroke best. The mass ratio is used in the following as

$$\bar{m}_{\mathrm{bed}} = \begin{cases} 1.0\, m_{\mathrm{bed}} & \text{for } X > X_{\mathrm{rol}}^{\mathrm{opt}} \text{ (rolling collect-and-collide),} \\ 0.3\, m_{\mathrm{bed}} & \text{for } X < X_{\mathrm{rol}}^{\mathrm{opt}} \text{ (scattered).} \end{cases} \tag{5.14}$$

5.1.4 Sensitivity Analyses

To obtain a deeper understanding of the influence parameters affecting the effective loss factor, sensitivity analyses are performed on selected parameters. Therefore, in this section, the experimental setup and the numerical DEM model are used. First, different particle properties are studied. Afterward, the influence of a container tilt is analyzed. Finally, the effect of the container's shape is investigated.

Particle Properties

Using both, experiments and DEM, the effect of single particle properties on the effective loss factor is investigated in the following. As only one property is varied at a time, independent results are obtained.

Young's Modulus: The Young's modulus of the particles is changed in the DEM to the values of PVC and tungsten, i. e. 3 GPa and 405 GPa compared to 210 GPa of steel. Indeed, only minor differences in the effective loss factor for 36 and 44 particles are obtained. A major reason for this is that the inelastic collision property of the particle bed stays conserved. Thus, the influence of the Young's modulus is negligible.

Density: As for the Young's modulus, the density values of PVC and tungsten are studied by DEM simulations, i. e. $1400\,\mathrm{kg/m^3}$ and $19250\,\mathrm{kg/m^3}$ compared to $7900\,\mathrm{kg/m^3}$ of steel. Again, only a negligible influence on the effective loss factor is obtained. However, it should be noted that the dissipated energy of the system is depending via Eq. (3.15) on the kinetic energy of the particles and thus on the particle mass as $E_{\mathrm{diss}} = \bar{\eta}\, E_{\mathrm{kin}} = \frac{1}{2}\,\bar{\eta}\, m_{\mathrm{bed}}\, V^2$. Thus, using the particles' density, the amount of dissipated energy can be adjusted.

Friction Coefficient: For the analysis of the sliding friction coefficient, values of $\mu = 0.01$ and $\mu = 1$ are additionally analyzed by DEM and compared to the baseline simulation of $\mu = 0.1$. The results are shown for 36 and 44 particles in Fig. 5.7. For both particle numbers, the same observations can be made. For low-excitation amplitudes $X < X_{\mathrm{rol}}^{\mathrm{opt}}$, i. e. the scattered motion mode, only a little dependency on the friction coefficient is seen, which is not of higher importance. At the optimal stroke of both particle settings, completely different results are obtained for the different friction coefficients. The higher the friction coefficient, the lower the maximum effective loss factor. Differences up to a factor of 1.7 are seen in the effective loss factor here, i. e. $\bar{\eta}_{\mathrm{rol}}^{\mathrm{max}} \approx 0.7$ for $\mu = 1$ to $\bar{\eta}_{\mathrm{rol}}^{\mathrm{max}} \approx 1.15$ for $\mu = 0.01$. Additionally, the optimal stroke is shifted to higher excitation strokes for a higher friction coefficient. For container strokes far higher than the optimal strokes, the results of the different friction coefficients converge against each other, showing only minor differences. Thus, in these areas, the friction

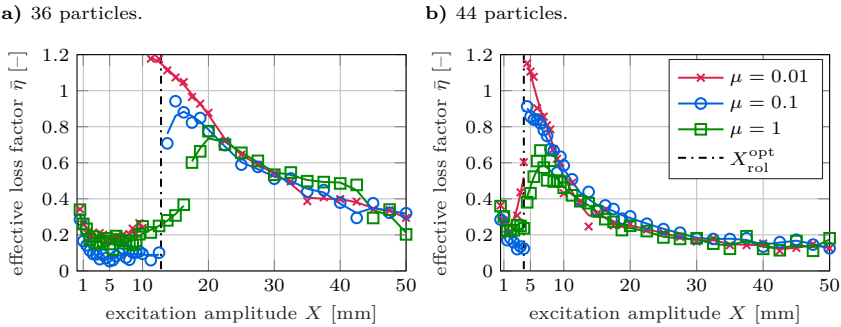

Figure 5.7: Effective loss factor for different friction coefficients analyzed by DEM.

coefficient is of minor influence.
The observed behavior around the optimal stroke can be explained, as a higher friction coefficient leads to more frictional energy dissipation. Hence, the particles' translational velocity during impact with the opposite container wall is lower. This reduces the total particle bed's energy dissipation, see Eq. (5.9), and, hence, a lower effective loss factor is achieved. In addition, due to the lower translational velocity of the particles, the impact time point with the opposite container wall occurs at a later instance of time. Hence, the optimal stroke is shifted to higher values. Vice versa, for low friction coefficients, less frictional losses occur. Moreover, a lower rolling movement is seen as more slip takes place, i. e. a higher translational velocity is obtained. This results in a higher impact velocity and, hence, higher energy dissipation and effective loss factor are determined. Consequently, due to the higher translational velocity, the impact time point with the opposite container wall occurs earlier. Therefore, the optimal stroke is shifted to lower values.

Using this knowledge, the differences in Fig. 5.4 between experimental results and DEM simulations with $\mu = 0.1$ might be explained. Especially, at the optimal strokes, the experiments lead to lower effective loss factors, while for excitation amplitudes above the optimal strokes a convergence is observed. This behavior can partially be explained by an underestimation of the friction coefficient in the simulations.

Coefficient of Restitution: To investigate the coefficient of restitution ε, instead of a velocity-dependent COR, see Chap. 4, three constant values of $\varepsilon = 0.8$, $\varepsilon = 0.9$ and $\varepsilon = 0.95$ are analyzed by DEM. One could expect a negative influence for high CORs, as instead of an inelastic collision particles might rebound from the impacting container wall for the rolling collect-and-collide motion mode. However, non of the values shows a major influence on the effective loss factor.
Within the **Single Particle** analyses, see Chap. 4, it is shown that for steel

contact partners the COR rises for repeated impacts onto the same spot, due to hardening of the contact zone. However, due to the low sensitivity of the effective loss factor on the COR, it is not expected that this influences the long-term behavior of the here utilized particle damper. Indeed, this requires further investigations.

Particle Number and Particle Radius: To analyze the effect of the particle number experimentally, it is incrementally reduced starting from 36 and 44 particles. With the use of a partition wall, the clearance is kept constant at $h_{\mathrm{rol}} = 30\,\mathrm{mm}$ and $h_{\mathrm{rol}} = 10\,\mathrm{mm}$, respectively. No major influence on the effective loss factor could be observed as long as more than three particles in the length and width direction of the container are used. Only for a lower number of particles in length or width direction, the inelastic collision behavior of the particles is negatively influenced, which results in a lower effective loss factor.

To examine the effect of the particle radius experimentally, spheres of 2.5 mm radius instead of 5 mm radius are investigated. The particle number to cover the container base with one layer of particles changes to $n_{\mathrm{p}}^{\mathrm{max}} = 192$. To keep the clearance at $h_{\mathrm{rol}} = 30\,\mathrm{mm}$ and $h_{\mathrm{rol}} = 10\,\mathrm{mm}$, 144 and 176 particles, respectively, are utilized. From the analytical Eq. (5.10) no dependency on the particle radius is obtained. However, in the experiments, a much lower particle movement is observed around the optimal strokes for the lower particle radius. This leads to significantly smaller effective loss factors in this area. The other areas of the effective loss factor are only minorly affected. An explanation for this could be the vastly increased surface area of the particles. Due to the strong influence of friction, as discussed earlier in this section, the lower particle movement may occur around the optimal stroke. Hence, bigger particles are in general beneficial. For high excitation amplitudes, it is observed that more particles take-off the container base. This movement could already be classified as *fluidization* mode. However, further studies on this are above the scope of this section and are discussed in detail in Chap. 6.

It should be noted that the mass of the particle bed and thus the amount of dissipated energy can also be influenced by the number of particles and the particle radius. Thus, particle radius, particle number and particle density need to be considered during the design phase of the particle damper.

Container Tilt

Now, an additional tilt around the three container axes, see Fig. 5.1, is analyzed. In Fig. 5.8 the effective loss factor is shown for an additional tilt α of 3° around the container's $x-$, $y-$ and $z-$axis, respectively. Thereby 36 and 44 particles are used in the DEM simulations. In each simulation, excitation acts in $x-$direction and gravity is acting in $y-$direction. The results are compared to the system with only a minor tilt of 0.1°, henceforth referred to as *baseline setting*.

a) 36 particles.

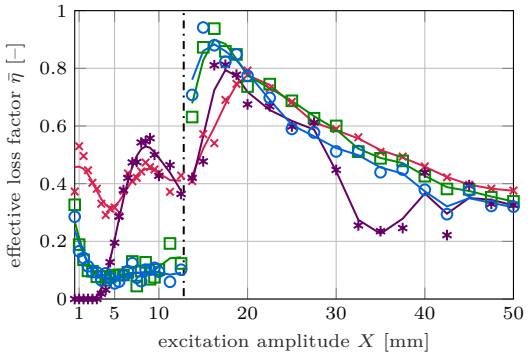

b) 44 particles.

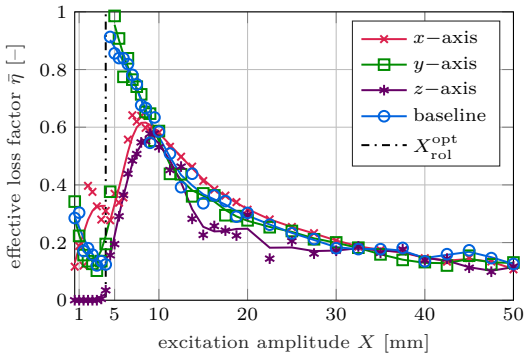

Figure 5.8: Effective loss factor for a container tilt of 3° around all its three axes by DEM simulations.

$y-$axis Tilt: A tilt around the containers $y-$axis (yaw), i. e. the direction of gravity, see Fig. 5.1, has only a minor influence on the effective loss factor for both particle settings. It can thus be considered negligible.

$z-$axis Tilt: A tilt around the container's $z-$axis (pitch), see Fig. 5.1, is showing a major influence. For the 36 particle setting and very low container strokes $X \ll X_{\mathrm{rol}}^{\mathrm{opt}} = 12\,\mathrm{mm}$ the effective loss factor is close to $\bar{\eta} \approx 0$ and thus even lower than the baseline setting. When the container stroke reaches $X = 4\,\mathrm{mm}$, the effective loss factor sharply increases and reaches values about $\bar{\eta} \approx 0.45$. Around the optimal stroke, i. e. $X \approx X_{\mathrm{rol}}^{\mathrm{opt}}$, no sharp transition between scattered motion mode and rolling collect-and-collide motion mode is seen. At this point, significantly lower values compared to the baseline setting are obtained, i. e. values

of about $\bar{\eta} \approx 0.4$ compared to $\bar{\eta} \approx 0.7$. At the highest effective loss factor, this difference decreases with values of about $\bar{\eta} \approx 0.8$ to $\bar{\eta} \approx 0.9$. For $X \gg X_{\mathrm{rol}}^{\mathrm{opt}}$ the envelope of the effective loss factor looks similar to the baseline setting.
For the 44 particles setting and low container strokes $X < X_{\mathrm{rol}}^{\mathrm{opt}} = 4\,\mathrm{mm}$ the effective loss factor is close to $\bar{\eta} \approx 0$. When the container stroke reaches $X = X_{\mathrm{rol}}^{\mathrm{opt}}$, the effective loss factor starts to increase up to $\bar{\eta} \approx 0.55$ at $X = 9\,\mathrm{mm}$. However, the baseline setting jumps at $X_{\mathrm{rol}}^{\mathrm{opt}}$ to high effective loss factors of about $\bar{\eta} \approx 0.9$. Hence, big differences to the baseline setting are seen around the optimal stroke. For strokes above $X > 9\,\mathrm{mm}$, the envelope of the effective loss factor is similar to the baseline setting.

To explain the observed behavior, the container's acceleration amplitude has to be considered. Due to the container's tilt, the particle bed will collect on the lower container wall for both motion modes. The particle bed can only leave the lower container wall if $A\cos(\alpha) > g\sin(\alpha)$ holds. Hence, one obtains $A > 0.51\,\mathrm{m/s^2}$ for $\alpha = 3°$. At the optimal strokes, the container accelerations for 36 particles follow to $A(X_{\mathrm{rol}}^{\mathrm{opt}} = 12\,\mathrm{mm}) = 1.9\,\mathrm{m/s^2}$ and for 44 particles to $A(X_{\mathrm{rol}}^{\mathrm{opt}} = 4\,\mathrm{mm}) = 0.63\,\mathrm{m/s^2}$. Therefore, for excitation amplitudes up to $X = 4\,\mathrm{mm}$ the particles barely take-off the lower container wall resulting in very low energy dissipation. Hence, only very low effective loss factor values are seen for both particle numbers up to this container stroke. For higher container strokes, a new motion mode is observed. The particles leave the lower container wall, but they do not reach the other container side. Instead, single-sided contacts with the lower container wall are obtained leading to effective loss factors of about $\bar{\eta} \approx 0.1 - 0.55$.
The rolling collect-and-collide motion mode occurs for $X > X_{\mathrm{rol}}^{\mathrm{opt}}$ and additionally if the container acceleration amplitude is high enough for the particle bed to be able to reach the other container side. However, the maximum effective loss factor is reduced in value and shifted to higher excitation strokes for both particle settings. It is observed that the higher the acceleration amplitude at the optimal stroke, the lower the influence due to the container's tilt. Hence, the effective loss factor of the 36 particles setting is not as affected as the one of the 44 particles setting. For container strokes above the maximum effective loss factor, the influence of the container's tilt becomes more and more negligible as the container's acceleration amplitude increases. Thus, baseline setting and $z-$axis tilt look similar in this regime.

In summary, to avoid a major influence of a container's $z-$axis tilt, it is necessary to ensure that $A\cos(\alpha) \gg g\sin(\alpha)$ holds at the point of operation of the particle damper. This condition is, hence, the lower bound for the container acceleration amplitude $A = X\,\Omega^2$ and thus for the container stroke and excitation frequency.

$x-$axis Tilt: The container's $x-$axis (roll) points in the direction of excitation, see Fig. 5.1. The envelope of the effective loss factor looks very similar for a container tilt around $x-$ and $z-$axis for both particle numbers, i. e. 36 and 44

particles, respectively. Only for very small excitation amplitudes up to $X = 4\,\mathrm{mm}$, major differences are seen. Here, effective loss factors between $\bar{\eta} \approx 0.1 - 0.5$ instead of $\bar{\eta} \approx 0$ are observed.
Even though the envelope of the effective loss factor looks similar for a container tilt around $x-$ and $z-$axis, different explanations are necessary. For a $x-$axis tilt, the particles also collect at the lower container wall. In this case, this is the sidewall though. Similar to the baseline setting, scattered and rolling collect-and-collide motion modes are observed. For the scattered motion mode, the $x-$axis tilt is advantageous compared to the baseline setting. As the particles get collected at the sidewall, more particle collisions occur, leading to higher energy dissipation. However, for the rolling collect-and-collide motion mode, the collection of particles hinders the particles' movement. This results in lower effective loss factors compared to the baseline setting. Only for high excitation amplitudes, the container's tilt influence becomes negligible, leading to similar effective loss factors as in the baseline setting.

Due to the high similarity between $x-$ and $z-$axis tilt, the same condition of $A\cos(\alpha) \gg g\sin(\alpha)$ should be considered during the damper's design phase. However, it is hard to derive this formula based on physical considerations for a container's $x-$axis tilt.

Comparing the simulation results for a tilt around the container's $x-$axis or $z-$axis of Fig. 5.8 with the experimental results shown in Fig. 5.4, one observes a higher agreement between the two tilted settings and the experiment compared to the baseline setting. Thus, besides an underestimation of the friction coefficient, a small tilt of the experimental setup around $x-$axis or $z-$axis could further explain the differences between experimental and numerical results in Fig. 5.4.

Container Shape

For the analyzed cuboid container, an excitation in the horizontal plane in the container's longitudinal direction is used. However, in some real technical applications, the excitation might occur in any direction in the horizontal plane, for instance for high-rise buildings or crane hooks. In this case, the clearance, the optimal stroke and the effective loss factor of a cuboid container would depend on the excitation direction, see Eqs. (5.1) and (5.13). To make the effective loss factor independent of the excitation direction in the horizontal plane, a cylindrical container shape is proposed. Thereby, its longitudinal axis points in the direction of gravity, i. e. in $y-$direction, see Fig. 5.9. This container is analyzed experimentally in the following. The cylinder has a radius of $R = 39\,\mathrm{mm}$. Thus, the same particle number of 48 is necessary to cover the container's base. Its height is slightly bigger than the particle's diameter with 11 mm. The clearance is approximated with Eq. (5.1) using $L = 2\,R$. To obtain the same clearances and thus the same optimal strokes as for the cuboid container the particle numbers are reduced from 36 to 30 and from 44 to 42, respectively.

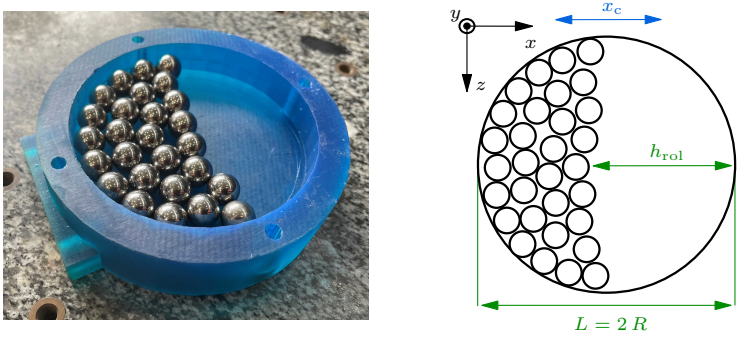

Figure 5.9: Analyzed cylinder with picture (*left*) and schematic representation (*right*).

In Fig. 5.10 the effective loss factors are compared between experimentally obtained results of the cuboid and cylinder shape. Between the experimental results of the cuboid and cylinder, just little differences occur in the effective loss factor for both motion modes. Only, for the rolling collect-and-collide motion mode of the 36 particle setting, slightly lower effective loss factors are obtained by the cylindrical container shape. In summary, the cylindrical container shape is well suited if the excitation direction in the horizontal plane is not well known.

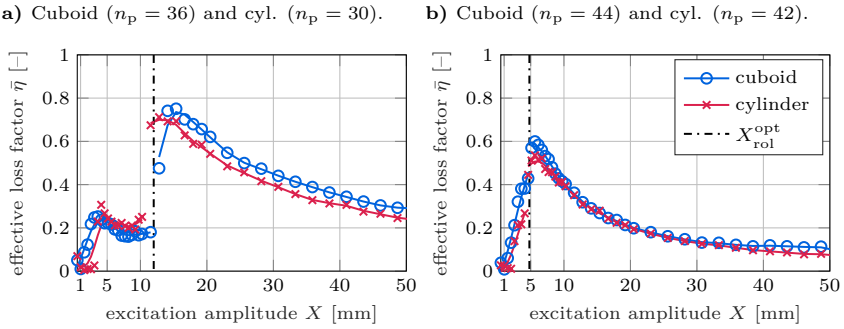

Figure 5.10: Effective loss factor for a cuboid and cylindrical container shape by experiments.

Effective Particle Mass

The influence of the previously analyzed parameters on the effective particle mass are studied as well. As the effective particle mass is not of such high importance, only a short summary is given here. While most studied parameters only have a small effect on the effective particle mass, it is shown by DEM simulations of the cuboid container that a container tilt around the $x-$ or $z-$axis has a major influence. Especially for the scattered motion mode significantly higher values are obtained as the particles have more contact with the container walls. The results are similar to the experimentally measured ones, shown in Fig. 5.5. Hence, such a container tilt is likely the reason for the discrepancies between experimental and DEM results of Fig. 5.5.

5.1.5 Summary

The attributes of particle dampers for low-excitation horizontal vibrations are analyzed on the **Single Damper Level**. Using a linear drive a cuboid particle container is subjected to a sinusoidal motion. For low-excitation amplitudes, a scattered motion mode of the spherical particles is observed. No regular movement is seen and the damper's efficiency is low. If the excitation amplitude exceeds a certain threshold amplitude, which only depends on the clearance of the particle bed to the opposite container wall, the system switches to the rolling collect-and-collide motion mode. In this, the particles slide and roll as one particle bed over the container's base and collide inelastically with the container's walls. At first, this synchronous motion leads to a high damper efficiency. With increasing container amplitude, the efficiency slightly decreases.
While for the scattered motion mode an empirical formula is found to describe the energy dissipation, for the rolling collect-and-collide motion mode an analytical expression based on physical equations describing the particle motion is derived. This expression is in good qualitative agreement with the experimental measurements with some quantitative differences. Moreover, an expression for the threshold amplitude separating both motion modes is derived, being also in good agreement with the measurements.

To obtain a deeper understanding of the dynamical processes inside the particle container, experimental and numerical sensitivity analyses are performed. The utilized discrete element model is validated by comparisons to the conducted experiments, showing a good agreement. Most of the particle properties, like Young's modulus, density, coefficient of restitution or particle number have a negligible influence on the damper's efficiency. However, it turns out that a low friction coefficient and a high particle radius are beneficial. In addition, a tilt around the damper's axes is studied. It turns out that a small tilt around the dampers yaw axis is showing only a slight influence on the damper's efficiency. However, a tilt around its roll or pitch axis can significantly decrease the efficiency

of the rolling collect-and-collide motion mode. Finally, the container shape is analyzed experimentally. The cuboid shape is replaced by a cylindrical shape with its longitudinal axis pointing in the direction of gravity. While the efficiency of the damper is only slightly reduced, this cylindrical shape shows the great advantage of being able to be applied to vibrations in all directions of the horizontal plane.

Overall, this new efficient damper design for low-intensity vibrations opens a completely new area of applications for particle dampers in mechanical and civil engineering such as crane hooks or high-rise buildings. This will be investigated at multiple examples in the next section on the **Structural Integrated Damper Level**.

5.2 Structural Integrated Damper

In this section, free and forced vibrations of structures with low first eigenfrequency shall be damped efficiently. For these vibrations, the particle container's acceleration amplitude is mostly below the gravitational constant. Hence, it is often reported that particles begin to stick and no relative motion between particles and container is obtained. Thus, only little amount of energy is dissipated and the structure is only slightly damped [LuEtAl16]. To face this problem, the rolling collect-and-collide motion mode of spherical particles is utilized, which is introduced in Sect. 5.1.
For the numerical analyses, the different particle damper **models 1–3**, i. e. DEM model, effective fields and analytical formulas, need to be coupled to the numerical models of the structures. See Sect. 3.3 for a detailed description of these coupling procedures. The DEM model has already been used on the **Single Damper Level**, see Sect. 5.1. The utilized effective fields and the results of the analytical formulas are shown exemplary in Fig. 5.4. For the structures within this section, only the first bending eigenmodes are considered. Hence, these systems are modeled according to Eq. (3.28) and Eq. (3.36), respectively.

At first, in Sect. 5.2.1, free vibrations of a simple beam-like structure and the so-called "Flexor", which is a lightweight manipulator, are studied. By comparison of the three different coupled damper **models 1–3** to the simple beam-like structure, these models are validated. To design an efficient particle damper, the analytical equation of the rolling collect-and-collide motion mode is studied in detail and a simple design guideline is derived. The idea of the design guideline is to separate the particle damper into multiple layers with different lengths. Hence, different vibration amplitudes can be damped efficiently, leading to high damping ratios on a large amplitude range. Alternatively, a numerical optimization procedure is presented based on the analytical equations. Both design approaches are validated experimentally.
Within the second section, see Sect. 5.2.2, forced vibrations of the same simple beam-like structure are studied. For this purpose, the beam-like structure is mounted on a linear drive and its base point is excited by a sinusoidal motion of variable frequency. By measuring the damper's velocity, the *frequency response function* (FRF) is obtained. Based on the analytical equations describing the damper's energy dissipation, a formula for an optimal damper design is derived and validated experimentally.
Finally, a summary is given in Sect. 5.2.3. The results of this section have been published in [MeyerEtAl21, MeyerSeifried21b].

5.2.1 Free Vibration Analyses

For free vibration analyses, the structures are subjected to a defined initial condition and their amplitude reduction is measured. The resulting damping ratio is extracted using the logarithmic decrement, which is evaluated between the maximum positive strokes of the particle container, see Eq. (3.41). For the coupling of the (experimentally) determined effective fields and the analytical formulas to the numerical models of the structures, see Sect. 5.1.2 and Sect. 5.1.3, some considerations have to be made:
The energy dissipation by the particles often occurs in a short period at discrete points in time. Especially for the rolling collect-and-collide motion mode, most energy dissipates at the impact time point t_{imp} of the particle bed with the container wall. In the optimal case, this is at an impact time point of $\bar{\omega}_1\, t_{\mathrm{imp}} = \pi$, with $\bar{\omega}_1$ being the *effective eigenfrequency* of the first bending eigenmode of the structure, see Eq. (3.37). This impact time point is thus at a damper position of $x_{\mathrm{pd}} = 0$. After the particle impact, the energy dissipation is close to zero until the next impact of the particle bed with the container. Consequently, a stationary state can be approximated for the system for a half-vibration cycle. In a stationary state, the viscous damping parameter $\bar{d}$ is calculated by the dissipated energy per cycle and the excitation conditions, see Eq. (3.39). The effective particle mass $\bar{m}_{\mathrm{bed}}$ follows directly from its corresponding field or from an analytical formula, see Fig. 5.5 and Eq. (3.38). Consequently, during the time integration of Eq. (3.36) the parameters $\bar{m}_{\mathrm{bed}}$ and $\bar{d}$ are updated here every half vibration cycle at the zero-crossing of the particle container, i. e. at $x_{\mathrm{pd}}(t_0) = 0$ with t_0 being the time points of the zero-crossing. The amplitude of the damper vibration is calculated via $X = V/\bar{\omega}_1 = \dot{x}_{\mathrm{pd}}(t_0)/\bar{\omega}_1$.

Simple Beam-Like Structure

At first, initial analyses are carried out using a simple beam-like structure setup, which is presented in the following.

Experimental Setup The experimental setup used first is shown in Fig. 5.11. It consists of a simple beam-like structure with the particle damper mounted at its tip, i. e. the end-effector. The elastic length of the steel beam is 512 mm with a rectangular profile of 80 mm × 2 mm and a Young's modulus of $E = 200$ GPa. The base point of the beam-like structure is fixed and the tip consists of an additional mass and the particle container with a total weight of 1.27 kg. The particle container has already been used for the **Single Damper** analyses in Sect. 5.1, i. e. it is made of polyvinyl chloride (PVC) and has a quadratic cross section with an inner edge width and height of 40 mm and a length L of 120 mm in excitation direction. The container can be separated into three horizontal layers with a height of 11 mm each, as shown in Fig. 5.11-*bottom*. Additionally, the length of each layer can be adjusted by separation walls. The

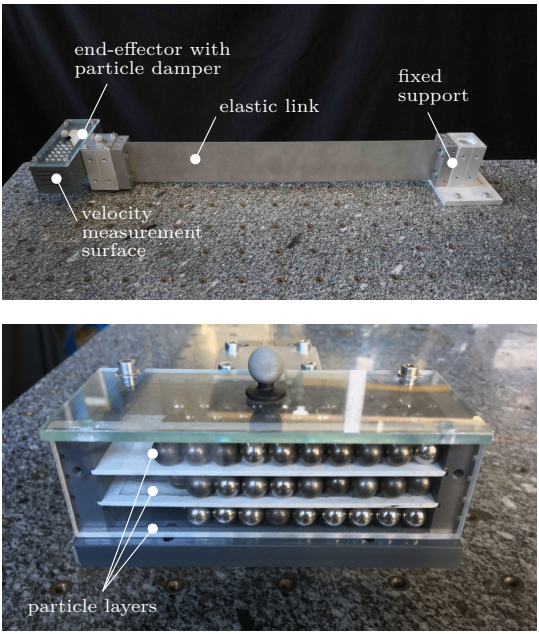

Figure 5.11: Simple beam-like structure setup with overview (*top*) and enlarged picture of its end-effector (*bottom*).

particle container's velocity is measured using a laser scanning vibrometer, the *PSV-500* from Polytec, with a sampling frequency of 250 kHz and integrated internally to obtain the container's output position. The measurement starts at the first zero crossing of the particle container.

Numerical Model For an efficient and accurate description of the beam-like structure, it is discretized with the finite element method (FEM), schematically illustrated in Fig. 5.12. The beam segment is discretized with 100 Timoshenko beam elements. As only 2D motion is considered, each beam node has three degrees of freedom. This results in 300 elastic degrees of freedom f_e. All other

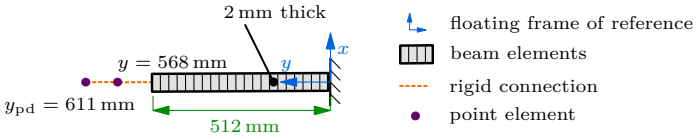

Figure 5.12: FEM model of simple beam-like structure.

components are modeled as rigid due to their high stiffness and are included as point elements with their corresponding mass. To take the boundary conditions into account, the reference system of the beam is chosen as a fixed frame [SchwertassekEtAl99], see also Fig. 5.12. By modal reduction of the FEM equation of motion, see Eq. (3.19), the mass and stiffness according to Eq. (3.36) follow to $M = 1.058\,\mathrm{kg}$ and $K = 143\,\mathrm{N/m}$, respectively. The eigenfrequency of the undamped system is $f_1 = \omega_1/(2\pi) = 1.85\,\mathrm{Hz}$. This numerically obtained eigenfrequency is very close to the experimentally measured one with only a difference of 0.02 Hz. The structural damping parameter D is obtained from measurements and is rather small with a value of $0.032\,\mathrm{kg/s}$.

Verification In a first step, the three numerical damper **models 1–3** are verified by comparison to an experiment using 36 spherical steel particles of 5 mm radius weighting 149 g in total. The end-effector of the simple beam-like structure is deflected to an initial amplitude of $X_0 = 63\,\mathrm{mm}$. The measurement starts at the first zero-crossing of the end-effector and last 10 s. The additional particle layers of the container, which are shown in Fig. 5.11, are not used for the experiment at first. The particle and container material data are listed in Tab. 5.1. The clearance and the optimal stroke are $h_{\mathrm{rol}} = 30\,\mathrm{mm}$ and $X_{\mathrm{rol}}^{\mathrm{opt}} = 12\,\mathrm{mm}$, see Eqs. (5.1) and (5.13). The corresponding effective loss factor for this setting is shown in Fig. 5.4a and the effective particle mass in Fig. 5.5a.

The four different results for the container movement, i. e. the experiment and the simulations with the **models 1–3**, are shown in Fig. 5.13a. Additionally, the damping ratios are depicted for all results in Fig. 5.13b. In both plots, the optimal stroke of the rolling collect-and-collide motion mode is indicated by $X_{\mathrm{rol}}^{\mathrm{opt}}$. Furthermore, for comparison, in Fig. 5.13a the envelope of the system with an empty particle container, i. e. only with structural damping, is shown. In the experiment medium damping ratios are achieved at the beginning. The damping is increasing as the container stroke decreases until the container stroke reaches 13 mm. Within the trajectory plot, this is visible in the first 4 s. Afterward, the damping ratio drops rapidly until it settles down to a low value. This damping behavior correlates to the effective loss factor, obtained on the **Single Damper Level**, see Fig. 5.4. Note, the $x-$axis is vice-verse in Fig. 5.13b compared to Fig. 5.4. This is chosen for a better correlation between Fig. 5.13a and Fig. 5.13b. The optimal container stroke of the rolling collect-and-collide motion mode, i. e. the stroke of the highest damper efficiency, is with an analytical value of $X_{\mathrm{rol}}^{\mathrm{opt}} = 12\,\mathrm{mm}$ very close to the highest measured damping ratio at 13 mm. Hence, Eq. (5.13) for the optimal strokes applies also for structural integrated particle dampers.
The DEM result is in great agreement with the experiment concerning amplitude and phase. The biggest differences occur around the optimal container stroke. At this point, the particle bed switches to the scattered motion mode, i. e. a state of much lower efficiency. Hence, the sensitivity of the energy dissipation is high

a) Trajectories of end-effector.

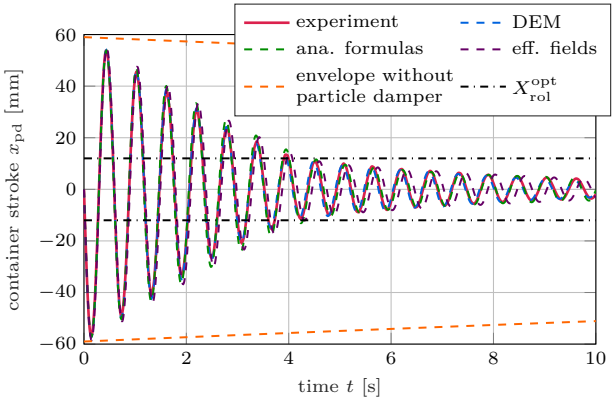

b) Damping ratios.

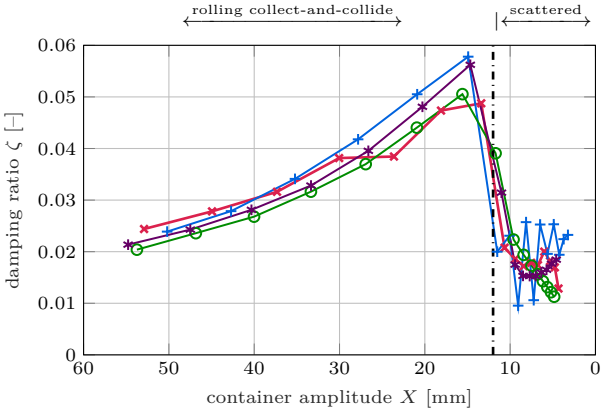

Figure 5.13: Experimental and numerical results of simple beam-like structure filled with 36 spherical steel particles of 5 mm radius.

in this area as little differences in the optimal stroke have a big effect on the damper's efficiency.

The result of the effective fields, i. e. energy dissipation and effective particle mass, shown in Fig. 5.4a and Fig. 5.5a, is capable of roughly capturing the motion of the particle container. The damping is first underestimated and later overestimated. For the rolling collect-and-collide motion mode, only a small phase shift is observed, which increases during the scattered motion mode. The observed behavior presents due to two main features. First of all, the effective damping parameter describing the particles' energy dissipation $\bar{d}$ is modeled as

viscous. Secondly, this effective damping parameter is only updated every half vibration cycle.
The result obtained by the analytical formulas describing the damper's energy dissipation and effective particle mass, i. e. Eqs. (5.2), (5.10) and (5.14), is also capable of roughly capturing the motion of the particle container for both motion modes. First, the damping is slightly underestimated and then overestimated, which compensates for each other. The phase is reproduced well.

The computational costs greatly differ for the different models. For the DEM model the computational costs are high, i. e. in the range of hours here, and depend strongly on the utilized particle number. To compute the effective fields the offline costs are high, as either preliminary experimental tests or numerical simulations need to be carried out. However, the costs for their application to a structure are low, i. e. within seconds. For the analytical formulas, the computational costs are low too, i. e. also in the range of seconds, and do not depend on the particle number. Thus, this is clearly the most efficient model if an accurate formula for the damper's energy dissipation is available.

By using Eq. (3.52) the efficiency of the particle damper can be assessed. The damping ratio at the optimal stroke is achieved in the ideal case to $\zeta(\bar{\eta}_{\mathrm{rol}}^{\max} = 0.91) = 0.056$. As seen in Fig. 5.13 this damping ratio is barely reached in the experiment. This is not surprising as $\bar{\eta}_{\mathrm{rol}}^{\max}$ is the analytical optimal value. Still, the question remains on how to design a particle damper to obtain a high efficiency on a large amplitude range. Hence, in the following section, a systematic design guideline for this task is presented.

Design Guideline The idea of the design guideline is to separate the particle damper into multiple layers with different clearances h_{rol}. Hence, different optimal strokes $X_{\mathrm{rol}}^{\mathrm{opt}} \approx 0.4\, h_{\mathrm{rol}}$ are obtained and thus different vibration amplitudes can be damped efficiently. This leads to high damping ratios on a large amplitude range. For the damper design, the analytical solution of the effective loss factor has to be considered. This one is shown again in Fig. 5.14. As the particle damper exhibits much higher effective loss factors during the rolling collect-and-collide motion mode, this motion mode should be realized during the operation of the damper. Likewise, any free vibration of a structure with an initial amplitude X_0 will decrease in amplitude over time. Hence, the particle layers should be designed such that $X_0 > X_{\mathrm{rol}}^{\mathrm{opt}}$ holds to ensure an operation within the rolling collect-and-collide motion mode. However, the question arises of how to design the individual particle layers, i. e. particle mass and clearance h_{rol} appropriately for the individual damper layers.

In the first step, the necessary particle mass needs to be determined. The particle mass can be calculated by the desired damping ratio of the structure ζ_{d} and by the effective loss factor utilizing Eq. (3.52). However, the effective loss factor of the damper is not known beforehand and changes over time/damper amplitude,

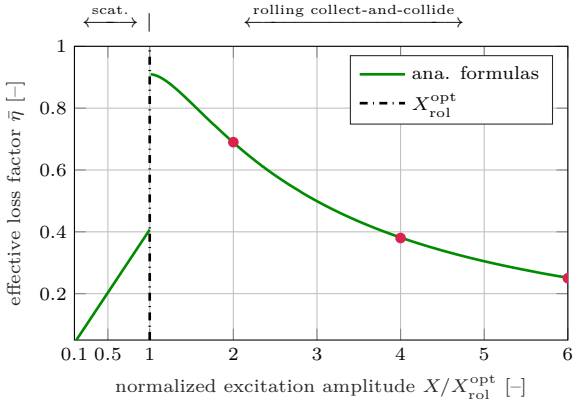

Figure 5.14: Analytical effective loss factor for scattered and rolling collect-and-collide motion mode by Eq. (5.3) and Eq. (5.10). The red dots ● indicate the initial effective loss factors $\bar{\eta}_0$ utilized by the design guideline.

see Fig. 5.14. Experimental measurements have shown that an appropriately designed particle damper exhibits an effective loss factor of about $\bar{\eta} = 0.5$ on a large amplitude range. This is a good starting value for design. The mass of the particle bed m_{bed} is obtained by rearranging Eq. (3.52) to

$$m_{\mathrm{bed}} \approx 2\,M\,\frac{\zeta_{\mathrm{d}}}{\bar{\eta}} = 4\,M\,\zeta_{\mathrm{d}}. \tag{5.15}$$

Many experimental measurements, see also [MeyerEtAl21], have shown that a separation of the particle container into at least three layers leads to good damping properties. To ensure high damping over a large vibration amplitude range, the damper's layers should be designed such that

$$\frac{X_0}{X_{\mathrm{rol}}^{\mathrm{opt}}} = \{2, 4, 6\}\,, \tag{5.16}$$

see also red dots in Fig. 5.14. Inserting Eq. (5.16) into Eq. (5.13) the clearances of the three damper layers are obtained to

$$h_{\mathrm{rol}} = \left\{\frac{5}{4}, \frac{5}{8}, \frac{5}{12}\right\} \cdot X_0. \tag{5.17}$$

Hence, starting from an initial vibration amplitude X_0, the effective loss factors are at the beginning $\bar{\eta}_0 = \{0.69, 0.38, 0.25\}$, see red dots in Fig. 5.14. These effective loss factors are increasing as the vibration amplitude decreases until the optimal strokes of the individual damper layers are reached. When the optimal stroke of a layer is reached, the particle bed within this layer switches to the

scattered motion mode, and the energy dissipation of this layer reduces drastically. The three optimal strokes are obtained by Eq. (5.16) to

$$X_{\mathrm{rol}}^{\mathrm{opt}} = \left\{ \frac{1}{2}, \frac{1}{4}, \frac{1}{6} \right\} \cdot X_0. \tag{5.18}$$

Hence, the minimum vibration amplitude of the system is about $X_{\mathrm{min}} \approx \frac{1}{6} X_0$ as for lower vibration amplitudes all three particle layers are in the scattered motion mode. Hence, only a small amplitude reduction is achieved from that moment. To ensure uniform damping, the particle mass should be distributed evenly over the damper layers. It should be noted that lower vibration amplitudes could be reached if additional damper layers are used with a higher ratio than $X_0/X_{\mathrm{rol}}^{\mathrm{opt}} = 6$. However, for very low vibration amplitudes, the effects of friction or little container tilts are becoming more and more dominant. Hence, additional damping could be difficult to realize for very low container amplitudes, see Sect. 5.1.4 for further details.

In the following, the presented design guideline shall be validated experimentally. Hence, the particle container of the simple beam-like structure is separated into three horizontal layers with a height of 11 mm each, as shown in Fig. 5.11-*right*. All three particle layers are filled with 16 steel spheres of 5 mm radius resulting in a total particle weight of 196 g. To verify Eq. (5.15) for the necessary particle mass, a damping ratio $\zeta_{\mathrm{d}} = 0.046$ should be measured with this particle mass on a large amplitude range. An initial amplitude of $X_0 = 63$ mm with clearances according to Eq. (5.17), i. e. $h_{\mathrm{rol}} \approx \{80, 40, 25\}$ mm, are utilized by the partition walls. The three resulting optimal strokes are $X_{\mathrm{rol}}^{\mathrm{opt}} = \{32, 16, 10\}$ mm. Figure 5.15a shows the trajectory of the system's end-effector, i. e. the particle damper, and the envelope of the undamped system. Additionally, the obtained damping ratios are depicted in Fig. 5.15b.
During the first vibration cycle, a damping ratio of $\zeta = 0.035$ is achieved, which increases as the container amplitude decreases. The damping ratio stays high with values around $\zeta \approx 0.046$, i. e. the desired damping ratio. Around the three optimal strokes, i. e. at container amplitudes of $X = \{32, 16, 10\}$ mm, a kink toward lower damping ratios are seen. This occurs due to the switch into the scattered motion mode of the corresponding particle layer, leading to a reduced energy dissipation. For container amplitudes below 11 mm, only very small damping ratios of about $\zeta \approx 0.02$ are achieved. This container amplitude is close to the theoretical minimal amplitude $X_{\mathrm{min}} = 10$ mm. The low damping ratios are achieved for strokes below 11 mm because all three particle layers are in the scattered motion mode from that moment. In summary, for this system, the design guideline has been proven to be very efficient.

Sensitivity Analysis: To prove that the design guideline also works efficiently for other systems, the beam-like structure is modified. The same initial amplitude, the same particle mass and the same clearances are used. For the modification, an additional mass of 942 g is mounted at the system's end-effector. The system's

mass according to Eq. (3.36) is hence $M = 2.0\,\mathrm{kg}$. The new eigenfrequency of this system results in $f_0 = 1.35\,\mathrm{Hz}$. Due to the higher system mass, the achievable damping ratio according to Eq. (5.15) reduces to $\zeta_\mathrm{d} = 0.025$. The experimental results of the container stroke and damping ratios are shown in Fig. 5.16. The results show the same qualitative behavior as for Fig. 5.15, but on a larger time scale, due to the lower damping ratio. The measured damping ratios are around $\zeta \approx 0.025$. Hence, the design guideline still works efficiently for this modified system.

Optimization In the last passage, the design guideline has efficiently been applied to design appropriate particle dampers for a simple beam-like structure under free vibrations. However, for large initial amplitudes or if a high damping ratio is required, large container dimensions are obtained by the design guideline. This is because a high clearance and a high particle mass are necessary for this. The utilization of a larger container, however, might not be realizable due to the limitations of available space for the particle damper. Hence, a different design approach is necessary for such systems.
As the analytical formulas are capable of capturing the movement of the particle container and are very efficient, see Fig. 5.13, they are used next to optimize the damping of the whole system for a given initial amplitude and given container dimensions. Once more, the particle container is separated into three horizontal layers. The objective of the optimization is to find the particle numbers of each container layer to minimize the container stroke at $t = 4\,\mathrm{s}$ for an initial amplitude of $X_0 = 63\,\mathrm{mm}$. The number of steel particles is varied by an increment of four for each layer. Due to the low number of design variables, the optimization is obtained by a simple brute force algorithm.

The particle numbers with the best damping performance are 36, 36 and 40 for layers one, two, and three, respectively, weighting in total 463 g. To validate this

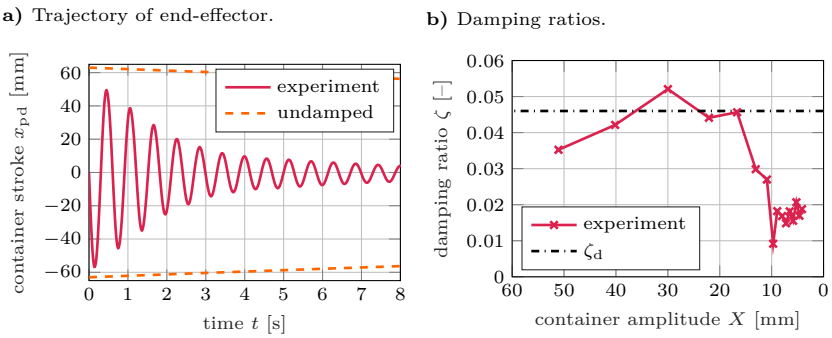

Figure 5.15: Damped simple beam-like structure utilizing three particle layers with 16 steel spheres of 5 mm radius each with clearances according to Eq. (5.17).

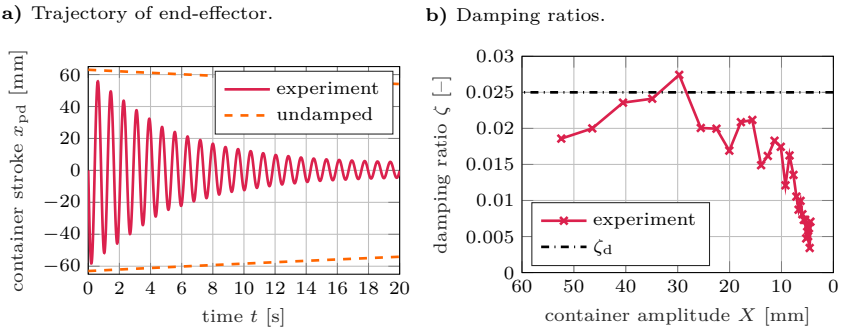

Figure 5.16: Damped simple beam-like structure with additional mass at the end-effector utilizing three particle layers with 16 steel spheres of 5 mm radius each with clearances according to Eq. (5.17).

result, the simulated container movement and damping ratios using the analytical formulas are compared to a conducted experiment with these particle numbers as shown in Fig. 5.17. Again, the envelope of the undamped system is shown for comparison.

A good agreement between trajectories of experiment and numerical optimization is achieved. The phase error increases slightly over time but stays small. The amplitude error is largest during the first vibration cycle and slightly decreases over time. The measured vibration amplitude of the system after 4 s is 3 mm and is, hence, much lower than the amplitude of the system designed with the analytical design guideline. There an amplitude of 10 mm at 4 s is obtained, see also Fig. 5.15. For the optimized system, the damping ratio in the experiment starts at 0.05 and is increasing up to 0.11. According to Eq. (5.15), the damper

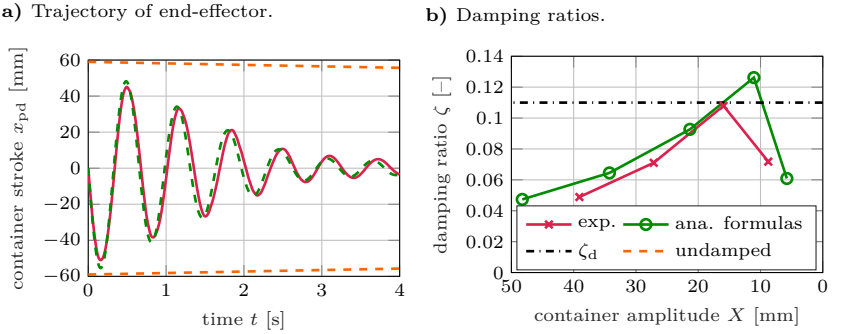

Figure 5.17: Damping optimized simple beam-like structure utilizing three particle layers with 36, 36 and 40 steel spheres of 5 mm radius each.

can be considered efficient for damping ratios above 0.11, however, this value is barely reached in the experiments. Despite the small difference between experiment and analytical formulas, a very good setting is found for the particle damper with limited container dimensions if a high damping ratio is necessary and the particle mass or efficiency of the individual particle layers is of minor importance.

Lightweight Manipulator - Flexor

As the rolling collect-and-collide motion mode was successfully applied to the simple beam-like structure, it shall now be applied to a more complex structure. For this, the lightweight manipulator "Flexor" is utilized.

Experimental Setup This system is a parallel lightweight manipulator with highly elastic links, see Fig. 5.18 and [MorlockEtAl18, MorlockEtAl21]. During its motion, harmonic vibrations are introduced in its links. The system consists of two linear motors set up in a "T–configuration". Elastic links, made of spring

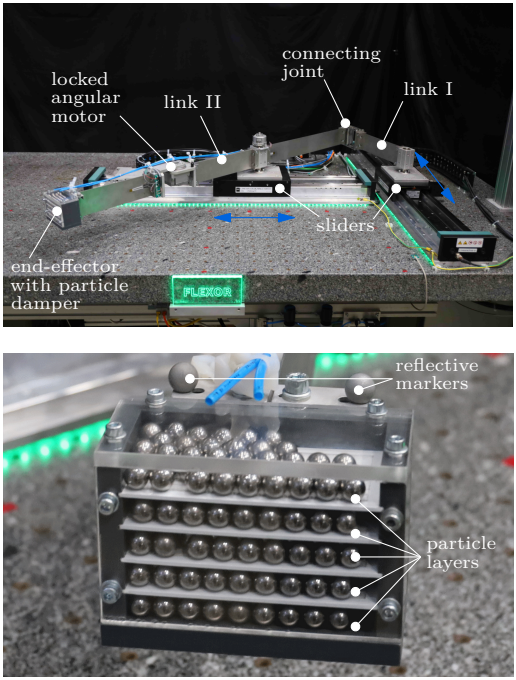

Figure 5.18: Lightweight manipulator "Flexor" with overview (*top*) and augmentation of its end-effector (*bottom*).

steel, are mounted via revolute joints on both sliders and are connected via a third revolute joint forming a parallel robot. Link II is also equipped with a rotary motor in-between. For the experiments conducted here the rotary motor is locked at a constant angle of 0 °. At the end of link II, the end-effector is mounted. The end-effector consists of the particle damper and two reflective markers at the top. With the help of these reflective markers, the end-effector's 2D position is tracked using an infrared camera. The large non-linear working motion of the system can be divided into a large rigid body motion and a linear-elastic deformation of the links. For that, the links are described in a floating frame of reference [SchwertassekEtAl99]. Due to its short length, link I can be modeled as rigid. The elastic deformation in link II is introduced via the rigid body motion, i. e. when the linear drives are moving, and is dominated by the first (bending) eigenmode.

Due to an increased effective mass of the lightweight manipulator compared to the simple beam-like structure, a new particle container is manufactured, see Fig. 5.18. However, due to safety and workspace restrictions, its inner length is reduced to 100 mm. The depth is the same as before with 40 mm and five layers of 11 mm height are used. The maximum particle number to fit in each layer is 40. To introduce a vibration, one of the sliders moves for 1.5 s so that the end-effector of a perfect rigid system would travel for 83 mm in the horizontal plane. The initial amplitude of the resulting vibration using an empty particle container is $X_0 = 78\,\text{mm}$. When particles are added the initial amplitude will increase, due to a higher mass of the end-effector. The initial amplitude is updated as

$$X_0 = X_0 \left(1 + \frac{m_{\text{bed}}}{M}\right). \tag{5.19}$$

This formula assumes that the maximum acceleration at the end-effector for the slider movement does not change when adding particles.

Numerical Model For an efficient and accurate description of the Flexor structure, it is discretized using the finite element method, schematically illustrated in Fig. 5.19. As with the simple beam-like structure, all beam segments are made up of 100 Timoshenko beam elements each with Young's modulus of $E = 180\,\text{GPa}$,

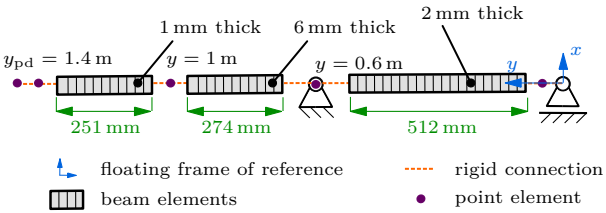

Figure 5.19: FEM model of link II of the lightweight manipulator "Flexor".

a Poison's ratio of $\nu = 0.3$ and a density of $\rho = 7900\,\mathrm{kg/m^3}$. As once again only 2D motion is considered, each beam node has three degrees of freedom. This results in 900 elastic degrees of freedom f_e. All other components are modeled as rigid, due to their high stiffness and are included as point elements with their corresponding mass. To take the boundary conditions into account, the reference system is chosen as a chord frame [SchwertassekEtAl99], see also Fig. 5.19. The effective mass and stiffness at the end-effector used for Eq. (3.36) follow from the modal reduced FEM model to $M = 1.69\,\mathrm{kg}$ and $K = 65\,\mathrm{N/m}$. The eigenfrequency of the undamped system is $f_1 = 0.99\,\mathrm{Hz}$ and close to the measured undamped eigenfrequency of 1.09 Hz. The experimental obtained structural damping parameter D is rather small with a value of $0.32\,\mathrm{kg/s}$.

Optimization The same brute force optimization procedure as for the simple beam-like structure, which is based on the analytical formulas describing the damper's energy dissipation, is applied. The optimization function is to find the particle number of each layer to minimize the container stroke at $t = 5\,\mathrm{s}$. The optimized particle numbers are once 24 and four times 28 weighting 563 g in total. To validate this result, the container movement is compared to a conducted experiment utilizing these particle numbers as shown in Fig. 5.20. To exclude the rigid body motion component of the end-effector trajectory, the measurement is shown from the first zero crossing of the resulting container vibration after the sliders have come to rest. The envelope of the undamped system is shown as well by using an added static mass equivalent to the mass of the particle bed.
The initial amplitude of the end-effector increases from 78 mm without particles to about 110 mm with particles. As the amplitude of the first vibration of the analytical result fits well with the experiment, the update scheme for the initial amplitude, i. e. Eq. (5.19), is accurate. The experimental result shows the same properties as already observed for the optimization of the simple beam-like

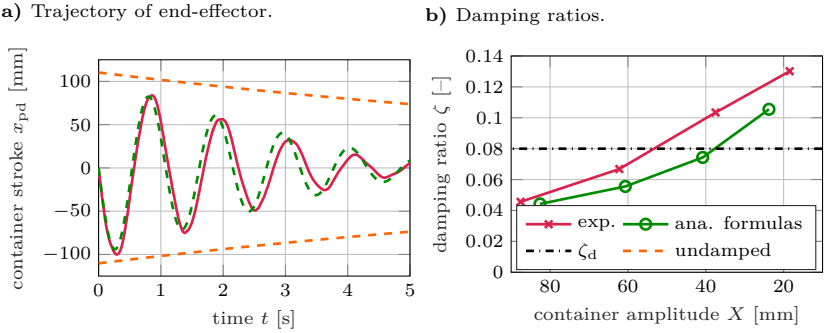

Figure 5.20: Damping optimized lightweight manipulator "Flexor" utilizing five particle layers with once 24 and four time 28 steel spheres of 5 mm radius each.

structure shown in Fig. 5.17. Even though little errors in the phase and amplitude occur again, the analytical formulas are capable of approximating the resulting end-effector trajectory. The measured vibration amplitude of the system after 5 s is less than 11 mm and is significantly lower than the amplitude of the undamped system with 72 mm. Hence, the optimization procedure is validated again.
However, according to Eq. (5.15), the damper can be considered efficient for damping ratios above 0.08. This is achieved for container amplitudes below 40 mm. This implies again that a quick amplitude reduction of the system is achieved, whereas the efficiency of the individual damper layers is not maximized.

5.2.2 Forced Vibration Analyses

In the following, forced vibrations are analyzed. For these analyses, the same simple beam-like structure as in the previous section is used, see Fig. 5.21. The beam's base point is subjected to a sinusoidal motion of variable frequency and the damper's velocity is measured. Thus, the *frequency response function* (FRF) is obtained, see also Eq. (3.42). These experimental results are compared to numerical results based on the analytical formulas describing the damper's energy dissipation coupled to the modal reduced model of the structure. See again Sect. 3.3.2 and Fig. 3.7 for a detailed discussion on the coupling procedure. The DEM model and the effective fields are not utilized within this section. First of all, the coupled numerical model, based on the analytical equations, is validated by comparison to multiple measurements. Afterward, a formula for an optimal damper design is derived.

Experimental and Numerical Setups

As the same beam-like structure as for the free vibration analyses is used, see Sect. 5.2.1, only differences to the setup of Sect. 5.2.1 are stated in the following.

Experimental Setup The experimental setup consists of the same simple beam-like structure used for the free vibration analyses of Sect. 5.2.1. The structure's base point is subjected to a sinusoidal motion of variable frequency using a linear drive, which has already been used for the **Single Damper** analyses of Sect. 5.1.1. The combined system is shown in Fig. 5.21 with undamped eigenfrequency of $f_1 = 1.87\,\text{Hz}$. The container's velocity is measured again using a laser scanning vibrometer, the *PSV-500* from Polytec. The measured results, i. e. velocity of the linear drive and particle damper, are saved with a sampling frequency of 1 kHz for later post-processing.
To obtain the system's FRF, a sine sweep excitation with linearly increasing excitation frequency Ω over time is applied to the linear drive ranging from 0.5 Hz to 4.5 Hz in 30 min. Hereby, a constant stroke amplitude U of the linear drive

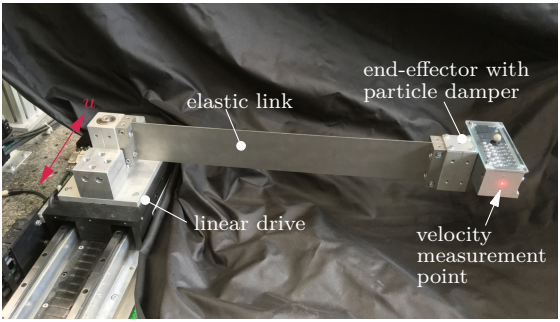

Figure 5.21: Simple beam-like structure setup excited by linear drive.

is utilized, i. e. $u = U\cos(\Omega(t)\,t)$. The system's FRF follows to $H^*(\Omega) = V^*(\Omega)/V_\mathrm{u}^*(\Omega)$ with V^* being the complex amplitude obtained by *fast Fourier transform* (FFT) of the particle container's velocity signal and V_u^* being the complex amplitude obtained by FFT of the linear drive's velocity signal. Note, that the FRF is obtained here by dividing the damper response V^* by the linear drive's velocity amplitude V_u^* and not by the excitation force as usual. For this definition of the FRF, $H^* = X^*/U^* = V^*/V_\mathrm{u}^* = A^*/A_\mathrm{u}^*$ is valid. Each setting is measured three times and the FRFs are then combined using the *complex mean* [Brandt11].

Numerical Setup From the modal reduction of the beam's FEM model, see also Fig. 5.12, the mass and stiffness at the end-effector, see Eq. (3.36), follow to $M = 1.058\,\mathrm{kg}$ and $K = 143\,\mathrm{N/m}$. The structural damping parameter D obtained from measurements is rather small with a value of $0.032\,\mathrm{kg/s}$. For such a base point excitation used here, the external force in Eq. (3.28) is expressed as $f_\mathrm{ex} = U\,K\,\cos(\Omega\,t) - V_\mathrm{u}\,D\,\sin(\Omega\,t)$. As the structural damping of the system D is small, the second term of the excitation force through the linear drive can be neglected yielding $f_\mathrm{ex} = U\,K\,\cos(\Omega\,t)$. Hence, for Eq. (3.36), the system's excitation force $R' = U\,K$ is employed.
To obtain the system's FRF numerically, the iteration scheme in Fig. 3.7 is used in conjunction with the analytical equations describing the damper's energy dissipation and effective particle mass, i. e. Eqs. (5.2), (5.10) and (5.14). Here, the frequency range between 0.5 Hz till 4.5 Hz is divided into 1000 sample points and every sampling point is solved successively. For the coupling of the analytical formulas to the modal reduced FEM model of the beam-like structure, it turns out that the jump in the effective loss factor between scattered and rolling collect-and-collide motion mode, see Fig. 5.22, leads to convergence problems of the iteration scheme. Thus, a smoothing function is used to avoid this problem, see "approximation" in Fig. 5.22. In the performed studies, the iteration scheme generally converges in five to ten iterations.

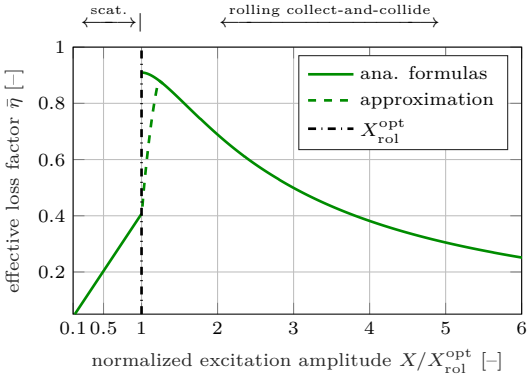

Figure 5.22: Analytical effective loss factor for scattered and rolling collect-and-collide motion mode by Eq. (5.3) and Eq. (5.10).

Experimental and Numerical Results

In the first step, the numerical iteration scheme to obtain the structure's FRF, shown in Fig. 3.7, shall be validated. In Fig. 5.23 numerical and experimental FRFs are compared for an excitation amplitude of $U = 0.25\,\mathrm{mm}$ using no particles. The numerical eigenfrequency of the undamped system is $f_1 = \omega_1/(2\pi) = 1.85\,\mathrm{Hz}$ and is very close to the experimentally measured one with only a difference of $0.02\,\mathrm{Hz}$. The envelope of the FRFs fit well. However, for frequencies above the eigenfrequency, the difference in the FRFs is slightly increasing. This is because the numerical model only considers the first eigenmode. However, in the

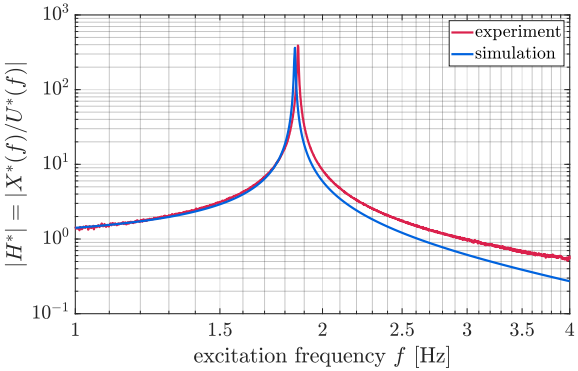

Figure 5.23: Comparison of numerical and experimental FRFs of undamped system for an excitation of $U = 0.25\,\mathrm{mm}$.

experiments, the second eigenmode of the system at about 22 Hz is also excited, leading to an increased amplitude.

As the accuracy of the numerical model without particles has been validated, in the next step 36 spherical steel particles of 5 mm radius weighting 147 g in total are filled in the particle container. The resulting clearance and optimal stroke are $h_{\mathrm{rol}} = 30\,\mathrm{mm}$ and $X_{\mathrm{rol}}^{\mathrm{opt}} = 12\,\mathrm{mm}$, respectively, see Eqs. (5.1) and (5.13). To check the proposed numerical calculation scheme for the FRF, i. e. Fig. 3.7, two numerical results are compared to experiments for excitation amplitudes of $U = 0.5\,\mathrm{mm}$ and $U = 2\,\mathrm{mm}$. The obtained FRFs are depicted in Fig. 5.24 and the corresponding damping ratios are summarized in Tab. 5.2. Additionally, in Fig. 5.24, the FRF of the undamped system is plotted and the value of the normalized optimal stroke $X_{\mathrm{rol}}^{\mathrm{opt}}/U$ for the corresponding excitation amplitude is depicted, i. e. the threshold value for which the particle bed switches from the scattered motion mode to the rolling collect-and-collide motion mode and exhibits the highest efficiency.
From both results, it is seen that the reduction of the system's eigenfrequency, due to the temporarily coupled particle mass, is numerically well approximated. In both cases, the eigenfrequency reduces from $f = 1.85\,\mathrm{Hz}$ to $f = 1.73\,\mathrm{Hz}$. For an excitation amplitude of $U = 0.5\,\mathrm{mm}$ the simulation's FRF peak agrees well with the experiment, see Fig. 5.24a. As the peak's amplitude is below the optimal stroke, the particle bed is still in the scattered motion mode. However, for excitation frequencies slightly above the damped eigenfrequency, somewhat bigger differences between experiment and simulation occur. While in the simulation the amplitude is reducing as expected, in the experiment the opposite happens. The vibration amplitude slightly increases and even reaches the threshold $X_{\mathrm{rol}}^{\mathrm{opt}}$. The damping ratio of simulation and experiment follow to $\zeta = 0.025$ and $\zeta = 0.017$, respectively. These values are on a similar scale and are much higher compared to the undamped case with $\zeta = 0.0013$.
For an excitation amplitude of $U = 2\,\mathrm{mm}$ the simulation's FRF peak agrees well with the experiment again, see Fig. 5.24b. The peaks of both FRFs are above the threshold amplitude $X_{\mathrm{rol}}^{\mathrm{opt}}/U$, i. e. the rolling collect-and-collide motion mode is seen here within the particle damper. In contrast to Fig. 5.24a, for excitation frequencies slightly above the eigenfrequency, somewhat smaller differences are obtained. This is attributable to the fact that the energy dissipation of the rolling collect-and-collide motion mode is more accurately described by the analytical

Table 5.2: Experimental and numerical obtained damping ratios of Fig. 5.24.

Damping Ratio ζ [–]		
	Excitation	
	$U = 0.5\,\mathrm{mm}$	$U = 2\,\mathrm{mm}$
Experiment	0.017	0.024
Simulation	0.025	0.029

a) $U = 0.5\,\mathrm{mm}$.

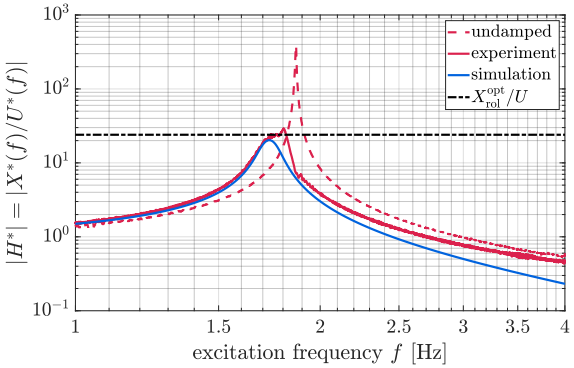

b) $U = 2\,\mathrm{mm}$.

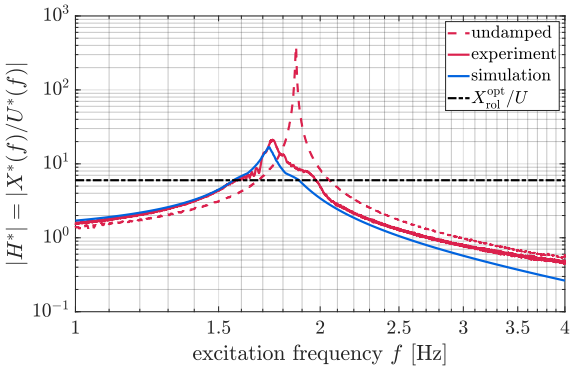

Figure 5.24: Comparison of numerical and experimental FRFs of damped system for different excitation amplitudes for 36 steel spheres of 5 mm radius.

formulas than the scattered motion mode, see also Fig. 5.4. The damping ratio of simulation and experiment follow to $\zeta = 0.029$ and $\zeta = 0.024$, respectively. These values are on a similar scale as for an excitation amplitude of $U = 0.5\,\mathrm{mm}$, see also Tab. 5.2. This might be unexpected because for the higher excitation the particle damper is in the efficient rolling collect-and-collide motion mode while for the lower excitation the particle damper is in the inefficient scattered motion mode. However, the resulting container's amplitude for an excitation amplitude of $U = 2\,\mathrm{mm}$ reaches about $X = 40\,\mathrm{mm}$ and is therefore far beyond the optimal stroke of $X_{\mathrm{rol}}^{\mathrm{opt}} = 12\,\mathrm{mm}$. For this high amplitude, the analytical effective loss factor is about $\bar{\eta} = 0.46$. At the optimal stroke, the effective loss factor is $\bar{\eta}_{\mathrm{rol}}^{\mathrm{max}} = 0.91$, see also Fig. 5.4. Hence, the effective loss factor is highly reduced compared to its optimal value for this large container stroke and on a

similar scale as within the scattered motion mode.

For both conducted experiments, the experimental damping ratio deviates from the numerical results due to not modeled dynamics of the particle damper and inaccuracies and imperfections in the experimental setup. These are among others, a small tilt around the container's axis, an additional rotation of the container through the bending of the beam, a torsional movement due to the low beam torsion constant and a non-perfect rolling movement of the particles. These parameters significantly influence the particle motion and thus the energy dissipation. Still, the proposed calculation scheme, shown in Fig. 3.7, is suitable for obtaining the system's FRF and a first good approximation of the resulting damping ratios.

Optimal Damper Design: In Fig. 5.24 and Tab. 5.2 it is seen that it is possible to damp the simple beam-like structure utilizing the scattered motion mode as well as utilizing the rolling collect-and-collide motion mode of the particle bed. However, in both cases, the efficiency of the particle damper is far below its optimum, as shown in the following. The damper's highest efficiency is reached at a container amplitude of $X_{\mathrm{rol}}^{\mathrm{opt}}$, see also Fig. 5.14. Hence, an operation of the particle damper with amplitude $X_{\mathrm{rol}}^{\mathrm{opt}}$ is favored. In this state, the energy dissipation is obtained by Eq. (5.11). Inserting Eq. (5.11) into Eq. (3.39) and further into Eq. (3.49), and neglecting the structural damping, the optimal damping ratio is obtained, i. e. an operation of the particle damper at $X_{\mathrm{rol}}^{\mathrm{opt}}$, for a given particle mass m_{bed} to

$$\zeta_{\mathrm{opt}} = \frac{10\, m_{\mathrm{bed}}}{7\,\pi\,(M + \bar{m}_{\mathrm{bed}})}. \tag{5.20}$$

As the effective particle mass $\bar{m}_{\mathrm{bed}}$ in Eq. (5.20) is unknown, it can be approximated by the mass of the particle bed, i. e. $\bar{m}_{\mathrm{bed}} = m_{\mathrm{bed}}$. This is justified as a high effective loss factor correlates with a high effective particle mass, see also Fig. 5.4 and Fig. 5.5. For the utilized system the optimal damping ratio results in $\zeta_{\mathrm{opt}} = 0.055$. This damping ratio is about twice as high as those obtained from Fig. 5.24, see Tab. 5.2. Thus, the question arises of how to design the particle damper, such that it is operated at its optimal operation point $X_{\mathrm{rol}}^{\mathrm{opt}}$. To answer this, Eq. (5.20) is inserted into Eq. (3.44) describing the system's vibration amplitude and an excitation in the system's effective eigenfrequency, i. e. $\Omega = \bar{\omega}_1$, is assumed. This yields for the particle damper's amplitude

$$X = \frac{7\,\pi R'\,(M + m_{\mathrm{bed}})}{20\, m_{\mathrm{bed}}\, K}, \tag{5.21}$$

with $R' = U\,K$ being the system's excitation force. Solving this equation for the necessary mass of the particle bed, one obtains after a few transformations

$$m_{\mathrm{bed}}^{\mathrm{opt}} = \frac{7\,\pi\,R'\,M}{20\,K\,X_{\mathrm{max}} - 7\,\pi\,R'}, \tag{5.22}$$

The desired maximum vibration amplitude during resonance $X_{\max}$ has to be chosen as desired. Using this desired maximum amplitude, the necessary clearance follows by Eq. (5.13) to $h_{\mathrm{rol}} = 2.5\, X_{\max}$. It should be kept in mind that these equations are only valid as long as the container's acceleration amplitude stays below the gravitational constant, i. e. $A_{\max} < g$, since otherwise the rolling condition of the spherical particles is violated.
To validate Eq. (5.22) for the necessary particle mass, it is applied to the simple beam-like structure. However, as the particle container is already manufactured, Eq. (5.21) is solved for the necessary excitation amplitude U_{opt} to excite the given system in its optimal state, i. e. such that a damper amplitude of $X_{\mathrm{rol}}^{\mathrm{opt}}$ is achieved. This results in

$$U_{\mathrm{opt}} = \frac{20\, m_{\mathrm{bed}}\, X_{\mathrm{rol}}^{\mathrm{opt}}}{7\,\pi\,(M + m_{\mathrm{bed}})}. \tag{5.23}$$

Applying Eq. (5.23) to the simple beam-like structure using 36 steel particles of 5 mm radius, results in $U_{\mathrm{opt}} = 1.34$ mm. The corresponding FRFs of simulation and experiment are shown in Fig. 5.25. The FRFs envelopes of simulation and experiment fit well. However, during resonance slightly higher amplitudes are seen in the experiment. Moreover, for excitation frequencies slightly above the eigenfrequency, almost no reduction in the vibration amplitude is observed. This happens due to the high sensitivity of the effective loss factor and effective particle mass around the optimal stroke, see Fig. 5.4 and Fig. 5.5. The damping ratios of simulation and experiment result in $\zeta = 0.048$ and $\zeta = 0.037$, respectively. These values are notably lower than the optimal damping ratio $\zeta_{\mathrm{opt}} = 0.055$ but significantly higher than the damping ratios obtained from Fig. 5.24 with values between $\zeta = 0.017 - 0.029$.

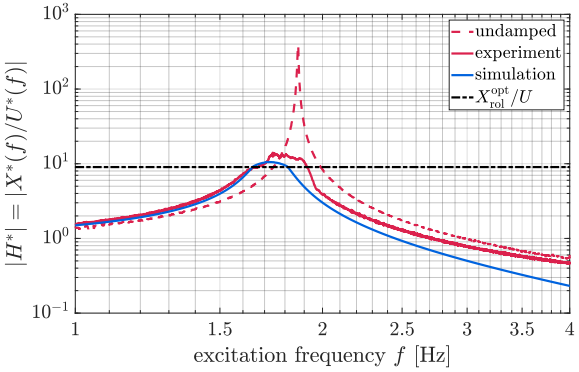

Figure 5.25: Comparison of numerical and experimental FRFs of simple beam-like structure under theoretical optimal excitation of $U_{\mathrm{opt}} = 1.34$ mm for 36 spherical steel particles of 5 mm radius.

Theoretically, in the optimal case during resonance, a container amplitude of $X = X_{\mathrm{rol}}^{\mathrm{opt}}$ is achieved. However, in Fig. 5.25 it is seen that even the simulation result crosses the $X_{\mathrm{rol}}^{\mathrm{opt}}/U$ threshold instead of touching it. This happens due to the approximation made for the effective loss factor between scattered and rolling collect-and-collide motion mode, see Fig. 5.22. This approximation is necessary for the iteration scheme to converge.
Due to inaccuracies occurring during the experiment, like a tilt of the container, the experimental damping ratio is lower than the numerical result. Reducing the effects of these influence parameters could significantly increase the measured damping and thus reduce the difference between simulation and experiment. With the utilized system, this is indeed not possible. Still, Eq. (5.22) enables a simple, accurate and quick design of particle dampers for horizontal, forced vibrations of low intensities. However, special care for precise manufacturing, mounting and operation are necessary.

5.2.3 Summary

In this section, the rolling attribute of spheres is used to damp low frequency horizontal free and forced vibrations of different structures. This rolling attribute has intensively been studied in the previous section and analytical formulas describing the energy dissipation have been derived. As test structures, a simple beam-like structure and a lightweight manipulator undergoing a large working motion are utilized. The particle dampers are mounted at the tips of the structures and can be separated into multiple layers for optimization purposes. Numerically, the structures are discretized via FEM and reduced in size by modal reduction. The numerical structures' models are coupled to the analytical formulas describing the dampers' energy dissipation to obtain the systems movement for free and forced vibrations.

First, a systematic design guideline for the development of layered particle dampers for free vibrations is presented. The particle damper is separated into multiple particle layers and filled with steel spheres. Via the design guideline, the necessary particle mass for the desired damping ratio is determined only based on the structure's mass. A simple analytical equation is given to design the clearances of the different particle layers, i. e. the distances between the particle bed and opposite container walls. The efficiency of the design guideline is verified experimentally by the simple beam-like structure setup. The structure is subjected to an initial deflection and the damping ratio of the free vibration is measured. The damping ratios are close to the designed values. Performed sensitivity analyses by adding mass to the structure's end-effector show that the good damping performance is conserved.
For structures with limited container space under free vibrations, a numerical optimization procedure is presented. For a given particle container with multiple

layers, the particle numbers for each layer causing the highest damping are determined. This optimization procedure is validated by experimental measurements using a simple beam-like structure and a lightweight manipulator.

Finally, forced vibrations are analyzed. The base point of the simple beam-like structure used for free vibration analyses is subjected to a sinusoidal motion of variable frequency via a linear drive. The numerically obtained FRFs are validated experimentally. Finally, the numerical model is used to calculate the design parameter of the particle damper to operate it at its maximum efficiency. A simple analytical expression is obtained. Its accuracy is proven experimentally. However, due to inaccuracies within the experimental setup, numerical and experimental results are not in perfect agreement. Still, the formula provides a powerful tool to design particle dampers for applications of low acceleration intensity under forced vibrations.

Medium-Excitation Horizontal Vibration Analyses

Vibrations at medium-excitation intensities are going to be classified as vibration frequencies $f \approx 5\,\mathrm{Hz}$ and acceleration amplitudes of the particle damper below and above the gravitational constant. Especially, at a particle damper acceleration amplitude around the gravitational constant, the particle dynamics completely change. This ranges for horizontal vibrations from a rolling state at low accelerations to a bouncing state at high accelerations. In between the particle bed is fluidized. These different *motion modes* and the corresponding *energy dissipation* are studied in detail in this chapter as well as how to apply these to damp an underlying structure.
The rolling state of the particle bed within the particle damper is also called *rolling collect-and-collide* motion mode and is discussed in detail in Chap. 5. The bouncing state, called *bouncing collect-and-collide* motion mode, was first described by [BannermanEtAl11] and [SackEtAl13] under the condition of weightlessness, i. e. in absence of gravity. Both bouncing and rolling collect-and-collide motion modes can accurately be described by analytical formulas and are based on the completely inelastic bouncing ball motion mode [MehtaLuck90]. The *fluidization* mode, which connects bouncing and rolling collect-and-collide motion modes, has been observed by multiple authors for very different excitation conditions [AnsariAlam13, SaluenaEtAl98, YinEtAl17, ZhangEtAl17]. However, this motion mode is hard to analytically describe and depends on various parameters.

At first, in Sect. 6.1, numerical studies of the **Single Damper Level** of the presented *toolchain*, see Fig. 3.1, are performed. The *discrete element method* (DEM) model of the particle damper investigated in previous Chap. 5 is utilized for this task. The same cuboid particle container as in Chap. 5 is subjected to a horizontal sinusoidal motion and occurring motion modes and energy dissipation within the damper are analyzed. In the following Sect. 6.2, **Structural Integrated Damper** analyses are performed. The damping behavior of free vibrations of a simple beam-like structure are studied experimentally. The same design guideline as for horizontal low-excitation vibrations is utilized and validated experimentally. The following results have been published in [MeyerEtAl21, MeyerSeifried22].

6.1 Single Damper

For the analyses of the **Single Damper Level** experimental as well as numerical studies can be performed. However, the experimental testbed used in Chap. 5, i. e. the linear drive, is not suited for the high analyzed frequencies. Likewise, the experimental shaker setup later used in Chap. 8 is not suited for such high container strokes. In both cases, different devices, i. e. linear drive and shaker, would be necessary for the requirements here. Hence, on this level purely numerical DEM studies are performed for the damper analyses. See Chap. 2 for further information on the DEM and Sect. 2.8 for the chosen DEM algorithms. The analyzed particle container will be later used for experimental measurements on the **Structural Integrated Damper Level** in Sect. 6.2.
In the performed simulations, the particle container is moved sinusoidally by a rheonomic constraint of amplitude X and angular excitation frequency $\Omega = 2\,\pi\,f$ as $x_\mathrm{c} = X\sin(\Omega\,t)$, see Eq. (3.8). The container's velocity and acceleration amplitudes follow as $V = X\,\Omega$ and $A = X\,\Omega^2$, respectively, see Eqs. (3.9) and (3.10). To analyze the different effects and influence parameters onto the particle bed, the excitation amplitude varies between $X = 1\,\mathrm{mm} - 200\,\mathrm{mm}$ and the excitation frequency varies between $f = 1\,\mathrm{Hz} - 10\,\mathrm{Hz}$ using 462 sample points and a logarithmic distribution. Each sample point is simulated for ten vibration cycles. The DEM results are the applied container motion and the driving force acting on the container. These are saved for later post-processing with a sampling frequency between 1 kHz–10 kHz depending on the excitation frequency. As only the stationary state of the system shall be analyzed, during post-processing the first two vibration cycles are cut off to remove the irregular movement of the particles thru their initial state.
On this level, the same particle container as in Chap. 5 is studied, i. e. a cuboid container. Hence, only a short description of its numerical model is given here. The cuboid container is modeled using six bounding geometry planes, see Sect. 2.2.2. The container is made of polyvinyl chloride (PVC) and has a quadratic cross section with an inner edge width W and height H of 40 mm and a length L of 120 mm in excitation direction. Steel (S235) spheres of $r = 5\,\mathrm{mm}$ radius are used throughout this chapter. The used material and contact data are listed in Tab. 6.1, which is identical to Tab. 5.1 of the previous chapter. As discussed in Sect. 5.1.1, the container width should be modeled slightly higher, here with a value of 40.4 mm. Additionally, little tilts around the container axes of 0.1° are used. It should be noted that these adjustments seem to be of minor importance. However, neglecting these imperfections can lead to abnormal or unrealistic behavior in the simulations. The particle initial conditions are loaded from previously performed drop-down simulations.

Table 6.1: Material parameters of spheres and particle container.

	Sphere	Container
Material	S235	PVC
Young's Modulus E [GPa]	208	3
Poisson's Ratio ν [–]	0.3	0.38
Density ρ [$^{\mathrm{kg}}/_{\mathrm{m}^3}$]	7900	1400
Friction Coefficient μ [–]	0.1 for all contacts	
Coefficient of Restitution ε [–]	velocity dependent, see Chap. 4	
Dimensions [mm]	$r = 5$	$L, W, H = 120, 40.4, 40.0$

6.1.1 Numerical Results

In the first step, the rheological behavior of the vibrating granular matter shall be analyzed. As the particle dynamics are highly nonlinear, it is kind of arbitrary which particle setup is chosen first. Here, $n_{\mathrm{p}} = 44$ steel particles are taken as all motion modes within this chapter are visible for this setup. After discussing the motion modes, the *effective loss factor* and the *effective particle mass* for this system are analyzed.

Motion Modes

In this chapter, three different motion modes are observed within the DEM simulations. These are shown in Fig. 6.1 for three different time steps. The first time instance is at a container position of $x_{\mathrm{c}} = 0$, i.e. at its maximum velocity of $\dot{x}_{\mathrm{c}} = \pm V$. The second time instance is at the maximum container stroke, i.e. at $x_{\mathrm{c}} = \pm X$ and $\dot{x}_{\mathrm{c}} = 0$. The last time instance shows the particle bed impact onto the container wall at the impact time point t_{imp}.
The first motion mode, shown in Fig. 6.1a, is the rolling collect-and-collide motion mode discussed in detail in Chap. 5. It is characterized by the fact that the whole particle bed stays together at the container base and slides and rolls over it. The second motion mode is the fluidization mode, as pictured in Fig. 6.1b. Particles start to take-off the container's ground and the whole particle bed acts as a fluid. The last motion mode, see Fig. 6.1c, is the bouncing collect-and-collide motion mode [BannermanEtAl11, SackEtAl13]. Here, the whole particle bed behaves like a single bouncing body with only little contact with the container base. The rolling and bouncing collect-and-collide motion modes are further subdivided into repetitive and scattered behavior. The repetitive behavior is shown in Fig. 6.1 and is meant with the rolling and bouncing collect-and-collide motion modes. The scattered behavior is not shown as no regular or synchronous motion of the particles is obtained, i. e. each particle moves differently. See also the discussion of the scattered motion mode of the rolling collect-and-collide motion mode in Chap. 5.

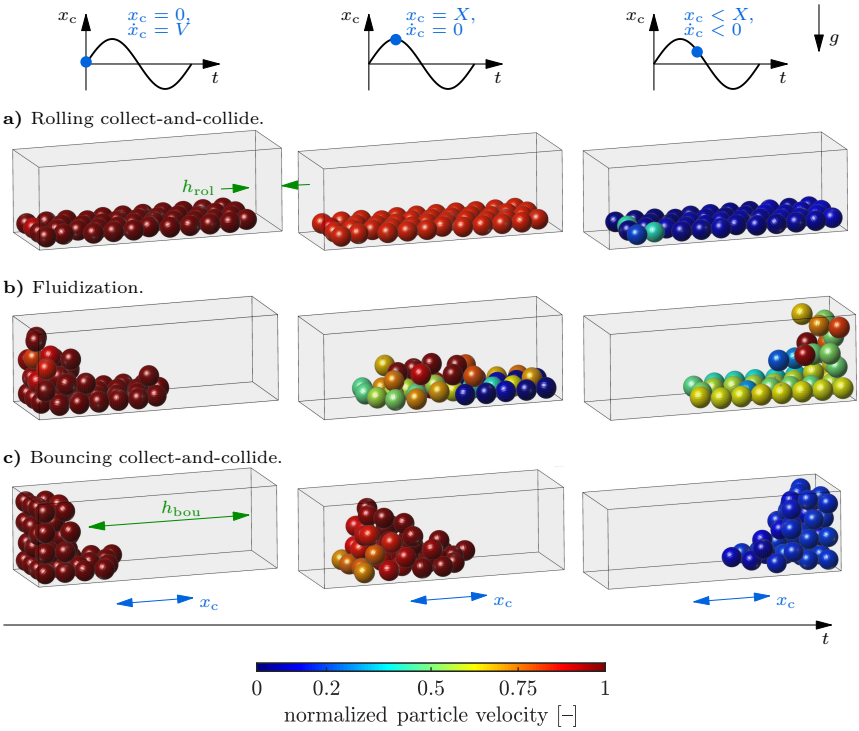

Figure 6.1: Observed motion modes at different container strokes for horizontal medium-excitation vibrations. The colors show the magnitude of the particle velocity normalized by the container velocity amplitude V from low (*blue*) to high (*red*).

For the rolling and bouncing collect-and-collide motion mode, different clearances h are obtained, see Fig. 6.1. While for the rolling collect-and collide motion mode the particles stay on the container's base, for the bouncing collect-and collide motion mode the particles are distributed along the pushing container wall. Hence, the two different clearances are given by

$$h_{\mathrm{rol}} = L\left(1 - \frac{n_{\mathrm{p}}}{n_{\mathrm{p}}^{\mathrm{rol}}}\right) \quad \text{and} \quad h_{\mathrm{bou}} = L\left(1 - \frac{n_{\mathrm{p}}}{n_{\mathrm{p}}^{\mathrm{bou}}}\right). \tag{6.1}$$

Here, $n_{\mathrm{p}}^{\mathrm{rol}}$ describes the number of particles necessary to cover the container's base with one layer of particles. The whole number of particles to fit in the container is given by $n_{\mathrm{p}}^{\mathrm{bou}}$. As these numbers vary to $n_{\mathrm{p}}^{\mathrm{rol}} = 48$ and $n_{\mathrm{p}}^{\mathrm{bou}} = 192$, the clearances obtained for the 44 particle setting are $h_{\mathrm{rol}} = 10\,\mathrm{mm}$ and $h_{\mathrm{bou}} = 92.5\,\mathrm{mm}$, see also Fig. 6.1.

Effective Loss Factor

In the following, the *effective loss factor* of the conducted numerical analyses is discussed. The effective loss factor is an efficiency factor, which correlates the dissipated energy of the particle bed to the kinetic energy of the particle bed, see also Eq. (3.15). The effective loss factor and the motion modes for 44 steel particles of 5 mm radius are shown in Fig. 6.2a and Fig. 6.2b. Figure 6.2c and Fig. 6.2d are discussed later in this section. To not overload the picture of the motion modes, not all excitation amplitudes are classified here. A yellow color indicates an effective loss factor of one or higher. A dark blue color indicates an effective loss factor of 0.1 or less.

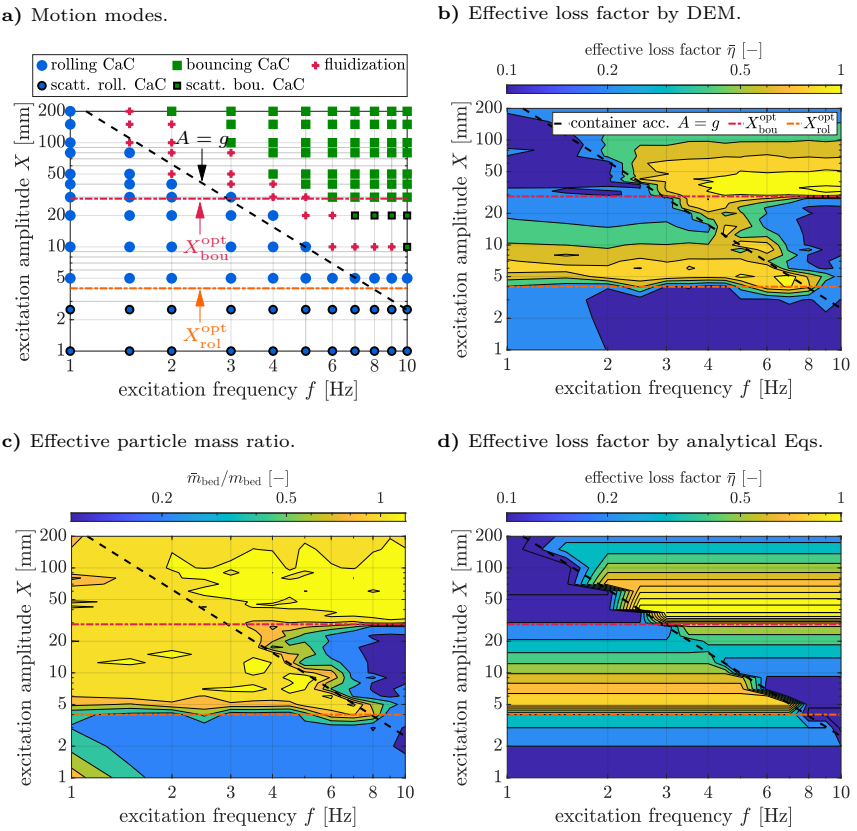

Figure 6.2: Effective fields: Numerical and analytical results of 44 steel particles with 5 mm radius. The threshold amplitudes $X^{\text{opt}}_{\text{rol}}$ and $X^{\text{opt}}_{\text{bou}}$ refer to Eqs. (5.13) and (6.11). CaC: collect-and-collide

Different motion modes can be observed, depending on both the excitation frequency and excitation amplitude. The rolling collect-and-collide motion mode is observed almost only for container acceleration amplitudes below the gravitational constant, i. e. $A < g$, see also black dashed line in Fig. 6.2. Here, in the rolling collect-and-collide motion mode, high effective loss factor values occur near the optimal container stroke of $X_{\mathrm{rol}}^{\mathrm{opt}} \approx 0.4\, h_{\mathrm{rol}} = 4\,\mathrm{mm}$, see Eq. (5.13) and orange dashed-dotted line in Fig. 6.2, with values up to $\bar{\eta} \approx 0.8$. Only for high excitation frequencies ($f > 7\,\mathrm{Hz}$), i. e. when the container acceleration amplitude reaches the gravitational constant, the effective loss factor reduces dramatically at this container stroke. For container strokes above the optimal stroke, i. e. $X > 4\,\mathrm{mm}$ the effective loss factor reduces with a small gradient. For container strokes below the optimal stroke, i. e. X < 4 mm, the system switches to the scattered rolling collect-and-collide motion mode. Here, a high gradient towards lower values in the effective loss factor is seen. For a detailed discussion on the rolling collect-and-collide motion mode, it is further referred to Sect. 5.1.
At container acceleration amplitudes around the gravitational constant, i. e. $A \approx g$, the particle bed moves to the fluidization mode. The effective loss factor is then a combination of the rolling and bouncing collect-and-collide motion modes with values ranging from low to high.
For container acceleration amplitudes above the gravitational constant, i. e. $A > g$, the system is in the bouncing collect-and-collide motion mode. Here, high effective loss factor values up to $\bar{\eta} \approx 1.1$ occur at an optimal container stroke of $X_{\mathrm{bou}}^{\mathrm{opt}} = h_{\mathrm{bou}}/\pi = 29\,\mathrm{mm}$, see red dashed-dotted line in Fig. 6.2. This formula will be derived later in this section, see Eq. (6.11). At this stroke but for low excitation frequencies, i. e. $f < 2\,\mathrm{Hz} - 3\,\mathrm{Hz}$, the effective loss factor starts to decrease, as here the container acceleration amplitude reaches the gravitational constant. Likewise, to the rolling state, the effective loss factor reduces with a small gradient for container amplitudes above the optimal stroke, i. e. for $X > 29\,\mathrm{mm}$. For container amplitudes below the optimal stroke, i. e. $X < 29\,\mathrm{mm}$, the system switches to the scattered bouncing collect-and-collide motion mode. Hence, only small effective loss factors are achieved in this area.
Although, both equations for the optimal stroke of the rolling and bouncing collect-and-collide motion modes, i. e. Eqs. (5.13) and (6.11), are very similar, the optimal strokes $X_{\mathrm{rol}}^{\mathrm{opt}} = 4\,\mathrm{mm}$ and $X_{\mathrm{bou}}^{\mathrm{opt}} = 29\,\mathrm{mm}$ are not. This is because the clearances h_{rol} and h_{bou} are significantly different, see also Fig. 6.1.

Effective Particle Mass

Next, the effective particle mass of the system is analyzed, i. e. it describes how much the mass of the particle bed is coupled to the container movement, see also Eq. (3.17). In Fig. 6.2c the ratio of the effective particle mass $\bar{m}_{\mathrm{bed}}$ to the mass of the particle bed m_{bed} is shown. The mass ratio is about one for container strokes slightly above the optimal container strokes of the bouncing

and rolling collect-and-collide motion modes, i. e. slightly above $X_{\mathrm{rol}}^{\mathrm{opt}} = 4\,\mathrm{mm}$ and $X_{\mathrm{bou}}^{\mathrm{opt}} = 29\,\mathrm{mm}$. For even higher container strokes, the mass ratio is above one. Mostly, with only minor higher values. For lower container strokes as the optimal strokes, the mass ratio is reduced. This implies that a high effective loss factor and thus a high energy dissipation also leads to a strong mass coupling. These observations match those made by [SanchezPugnaloni11]. However, vice versa is not generally true, see for instance the very high excitation amplitudes at $X = 200\,\mathrm{mm}$. It seems like that a high effective particle mass is either caused by a long contact duration of the particle bed with the container or by high contact forces exerting during impact between them. However, these analyses need further investigations, which are out of the scope of this work.

6.1.2 Analytical Description

As seen in Fig. 6.2a and Fig. 6.2b the effective loss factor and thus the energy dissipation of the particle bed are strongly related to the different motion modes. While for the (scattered) rolling collect-and-collide motion mode analytical descriptions are derived in Sect. 5.1.3, descriptions of the (scattered) bouncing collect-and-collide motion mode are still missing here. These motion modes have accurately been described by [BannermanEtAl11] and [SackEtAl13] and are shortly recaptured at this point.

Scattered Motion Mode

The scattered bouncing collect-and-collide motion mode is similar to the scattered rolling collect-and-collide motion mode. However, instead of randomly rolling over the container's base, the particles show a gas-like behavior. It can be assumed that the dissipated energy is proportional to the number of particle–wall collisions. This collision number depends on the volume swept by the container. As the particles hit the container walls at random phases, a higher container amplitude X leads to more collisions while a higher clearance h_{bou} to fewer collisions. Furthermore, the dissipated energy is assumed to scale with the particles' kinetic energy. Hence, [SackEtAl13] obtains

$$E_{\mathrm{diss}} = \frac{2\,X}{h_{\mathrm{bou}}} E_{\mathrm{kin}} = \frac{m_{\mathrm{bed}}\,X\,V^2}{h_{\mathrm{rol}}}. \tag{6.2}$$

For this energy dissipation, the effective loss factor is achieved to

$$\bar{\eta} = \frac{E_{\mathrm{diss}}}{E_{\mathrm{kin}}} = \frac{2\,X}{h_{\mathrm{bou}}}, \tag{6.3}$$

yielding a linear dependency on the container amplitude. Besides the excitation amplitude, Eq. (6.3) is only further dependent on the clearance of the bouncing collect-and-collide motion mode and thus on the damper's filling ratio.

Bouncing Collect-and-Collide Motion Mode

[SackEtAl13] observed within experimental measurements performed in microgravity during parabolic flights, i. e. $g \approx 0$, that in the bouncing collect-and-collide motion mode, i. e. for $X > X_{\mathrm{bou}}^{\mathrm{opt}}$, the particles are flying as one single particle block though the container with only little contact to the container sides, see also Fig. 6.1. This is also observed within DEM simulations here for container acceleration amplitudes sufficiently larger as the gravity constant. Thus, the translational velocities of every single particle are assumed to be identical while almost no rotational movement occurs. It is also observed that the particle bed is first pushed by the container wall. Then the particle bed leaves the pushing container wall at the container's maximum velocity $\dot{x}_{\mathrm{c}} = \pm V$ at $x_{\mathrm{c}} = 0$, i. e. at $\Omega\, t = n\, \pi$ with $n \in \mathbb{N}$, see also Eq. (3.8)–Eq. (3.10) for the container motion. After leaving the container wall, the particles begin to fly, in the ideal case with constant velocity

$$\dot{x}_{\mathrm{p}} = V, \tag{6.4}$$

until the impact with the opposite container side occurs. This is different to the rolling collect-and-collide motion mode, as for this one the particles' velocity decrease, due to the rolling condition, see also Eq. (5.6). The relative velocity between particles' and container $\Delta\dot{x}_{\mathrm{cp}} = \dot{x}_{\mathrm{p}} - \dot{x}_{\mathrm{c}}$ during the particles' flying phase follows to

$$\Delta\dot{x}_{\mathrm{cp}} = V\,(1 - \cos(\Omega\, t))\,. \tag{6.5}$$

Next, the particle bed collides with velocity $\dot{x}_{\mathrm{p}}^{-}(t_{\mathrm{imp}}) = V$ inelastically with the opposite container wall at the impact time point t_{imp}. Likewise, to the rolling collect-and-collide motion mode, the impact time point is limited by $\Omega\, t_{\mathrm{imp}} = \pi$. For this time point the container is again located at $x_{\mathrm{c}} = 0$ but moves in the other direction, i. e. $\dot{x}_{\mathrm{c}} = \mp V$. If the particle bed hits the container at a later instant of time, which is equivalent to container strokes below the optimal stroke, the observation that the particle bed leaves the container wall at $x_{\mathrm{c}} = 0$ would be violated for the next vibration cycle. In the simulations and by [BannermanEtAl11] and [SackEtAl13], the scattering motion mode is observed instead if this condition is violated.

To give an impression of the particle movement, in Fig. 6.3a the position of the particle bed during the flying phase and the positions of the pushing (lower blue line) and impacting (upper blue line) container walls normalized by the container's amplitude X are shown. As the distance between both container walls depends on the clearance h_{bou}, the position of the impacting container wall (upper blue line) indicates just one possible configuration. It should be noted that for the bouncing collect-and-collide motion mode the particle impact could occur at any instance of time up to $\Omega\, t_{\mathrm{imp}} = \pi$ depending on the clearance h_{bou}.

In Fig. 6.3b the absolute velocity of the particles $\dot{x}_{\mathrm{p}}$, the container velocity $\dot{x}_{\mathrm{c}}$ and the relative velocity between particles and container $\Delta\dot{x}_{\mathrm{cp}}$ normalized by the

a) Position of particle bed, pushing container wall (lower blue line) and impacting container wall (upper blue line) normalized by the container's amplitude X.

b) Absolute and relative velocities of the particles and container normalized by the container velocity amplitude V.

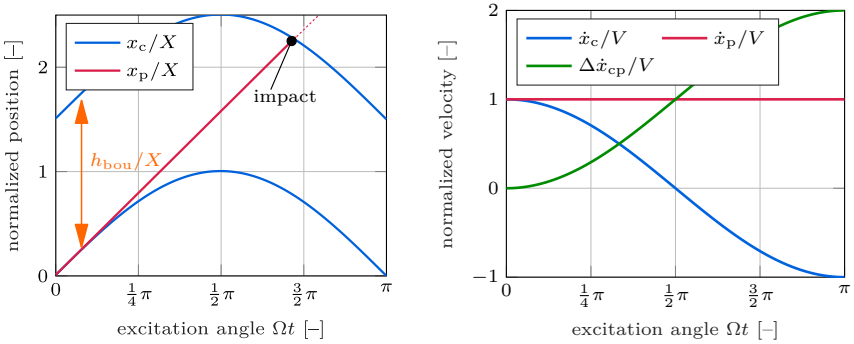

Figure 6.3: Positions and velocities of particle bed and container motion of the bouncing collect-and-collide motion mode.

container's velocity amplitude V are shown. Compare both graph also with the rolling collect-and-collide graphs, see Fig. 5.6.

For the bouncing collect-and-collide motion mode, the particles' velocity stays constant until impact with the opposite container wall. However, the relative velocity between particles and container is monotonically increasing as the container decelerates. It should be noted that a higher container amplitude X and thus a higher container velocity amplitude V leads to an earlier impact of the particle bed with the opposite container wall, i. e. $\Omega\, t_{\mathrm{imp}}$ decreases. Consequently, the normalized velocity ratio $\Delta\dot{x}_{\mathrm{cp}}/V$ at particle impact decreases as X increases.

To obtain the relative particle impact velocity with the opposite container wall $\Delta\dot{x}_{\mathrm{cp}}(t_{\mathrm{imp}})$, the impact time point t_{imp} is necessary. It describes the time the particle bed needs to travel from the pushing to the opposite container wall. It is achieved by solving

$$\underbrace{\int_0^{t_{\mathrm{imp}}} \dot{x}_{\mathrm{p}}(t)\,\mathrm{d}t}_{\text{particle motion}} = \underbrace{X\sin(\Omega\, t_{\mathrm{imp}})}_{\text{container motion}} + \underbrace{h_{\mathrm{bou}}}_{\text{clearance}}\,, \tag{6.6}$$

and is hence equivalent to Eq. (5.8) of the rolling collect-and-collide motion mode. However, for bouncing and rolling collect-and-collide motion modes, the clearances and the particles' velocity $\dot{x}_{\mathrm{p}}(t)$ differ as in the latter case particles begin to roll, see Eq. (6.1) and compare Eqs. (5.6) and (6.4). Using Eq. (6.4) for the particles' velocity, the Eq. (6.6) can be solved numerically for the impact time point t_{imp}.

During the impact of the particle bed with the container wall an inelastic collision

occurs. Thus, the particle bed adopts the velocity of the container, i. e. $\dot{x}_\mathrm{p}^+(t_\mathrm{imp}) = \dot{x}_\mathrm{c}^+(t_\mathrm{imp})$. In sum, two impacts (left container wall, right container wall) occur during one vibration cycle. Accordingly, the dissipated energy per cycle follows to

$$\widetilde{E}_\mathrm{diss} = 2\left(\frac{1}{2}\, m_\mathrm{bed}\, \Delta\dot{x}_\mathrm{cp}^2(t_\mathrm{imp})\right). \tag{6.7}$$

Inserting Eq. (6.5) into Eq. (6.7) yields the dissipated energy per cycle to

$$\widetilde{E}_\mathrm{diss} = m_\mathrm{bed}\, V^2\, (1 - \cos(\Omega\, t_\mathrm{imp}))^2\,. \tag{6.8}$$

Finally, the effective loss factor $\bar{\eta}$ is obtained by Eq. (3.15).
As seen in Fig. 6.3b the highest relative velocity of $2\,V$ and thus the highest damper's efficiency of the bouncing collect-and-collide motion mode is achieved at an impact time point of $\Omega\, t_\mathrm{imp} = \pi$, i. e. at the switch point to the scattering motion mode. This is likewise to the rolling collect-and-collide motion mode. By inserting $\Omega\, t_\mathrm{imp} = \pi$ into Eq. (6.8), the maximum dissipated energy per cycle $\widetilde{E}_\mathrm{diss}^\mathrm{max}$ and the maximum effective loss factor $\bar{\eta}_\mathrm{bou}^\mathrm{max}$ are obtained to

$$\widetilde{E}_\mathrm{diss}^\mathrm{max} = 4\, m_\mathrm{bed}\, V^2, \tag{6.9}$$

$$\bar{\eta}_\mathrm{bou}^\mathrm{max} = \frac{\widetilde{E}_\mathrm{diss}^\mathrm{max}}{2\,\pi\, E_\mathrm{kin}} = \frac{4}{\pi} \approx 1.27. \tag{6.10}$$

To obtain the container amplitude X for which $\Omega\, t_\mathrm{imp} = \pi$ holds, i. e. the stroke of maximum efficiency, Eq. (6.6) is solved with Eq. (6.4) analytically using this impact time point. This yields the optimal stroke as

$$X_\mathrm{bou}^\mathrm{opt} = \frac{h_\mathrm{bou}}{\pi} \approx 0.32\, h_\mathrm{bou}. \tag{6.11}$$

Likewise, to the rolling collect-and-collide motion mode, this optimal stroke is only depending on its clearance h_bou, but there exists no dependency on the excitation frequency Ω or the particle properties. This holds as long as the container acceleration amplitude is sufficiently above the gravitational constant, i. e. $A = X\,\Omega^2 > g$. Hence, for a constant container stroke X, there exists a lower threshold value for the excitation frequency. This can also be seen in Fig. 6.2.

Comparison: Bouncing–Rolling Collect-and-Collide At this point, the rolling and bouncing collect-and-collide motion modes shall be compared. For this purpose, Fig. 6.4 shows the analytical effective loss factors of both motion modes normalized by the corresponding optimal strokes $X_\mathrm{bou}^\mathrm{opt}$ and $X_\mathrm{rol}^\mathrm{opt}$, respectively, see Sect. 5.1.3 and Sect. 6.1.2. Within the scattered states, both motion modes start at very low effective loss factors for very small excitation amplitudes, i. e. for $X \ll X_\mathrm{rol/bou}^\mathrm{opt}$. The bouncing state is then increasing faster as the rolling state with values of the effective loss factor up to 0.64 compared to 0.4. At the optimal strokes both motion modes jump to higher effective loss factor values, i. e. 1.27

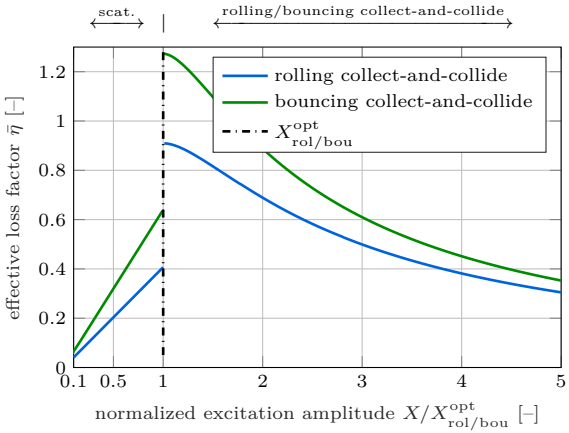

Figure 6.4: Analytical effective loss factor for rolling and bouncing collect-and-collide motion modes.

and 0.91, respectively. Hence, the bouncing state is here 1.4-times more efficient than the rolling state. From the optimal strokes, the effective loss factor of both motion modes reduces slowly towards higher amplitudes. Finally, both curves converge on each other for very high amplitudes. It should be noted that the lower effective loss factors of the rolling state are not a disadvantage, as both motion modes occur at completely different system dynamics, i. e. above and below a container acceleration amplitude of $A = g$.

Validation To distinguish between the rolling and bouncing collect-and-collide motion modes only the amplitude X and acceleration amplitude A of the particle container are considered for the analytical equations as

$$\widetilde{E}_{\mathrm{diss}} = \begin{cases} \text{Eq. (5.2)} & \text{for } A < g \wedge X \leq X^{\mathrm{opt}}_{\mathrm{rol}} \text{ (scattered)}, \\ \text{Eq. (5.10)} & \text{for } A < g \wedge X > X^{\mathrm{opt}}_{\mathrm{rol}} \text{ (rolling collect-and-collide)}, \\ \\ \text{Eq. (6.2)} & \text{for } A \geq g \wedge X \leq X^{\mathrm{opt}}_{\mathrm{bou}} \text{ (scattered)}, \\ \text{Eq. (6.8)} & \text{for } A \geq g \wedge X > X^{\mathrm{opt}}_{\mathrm{bou}} \text{ (bouncing collect-and-collide)}. \end{cases} \tag{6.12}$$

For validation and verification purposes, the analytical equations of the rolling and bouncing collect-and-collide motion mode are compared to the DEM analyses of 44 steel particles of 5 mm radius in Fig. 6.2b and Fig. 6.2d. The identified motion modes for this setting are depicted in Fig. 6.2a. For container strokes below the optimal strokes, i. e. below $X^{\mathrm{opt}}_{\mathrm{rol}} = 4\,\mathrm{mm}$ and $X^{\mathrm{opt}}_{\mathrm{bou}} = 29\,\mathrm{mm}$, the particle system

scatters. This results in a very low energy dissipation, which is only described by empirically derived formulas. This results in high differences in the effective loss factor with ratios up to five and higher. However, as the dissipated energy is low in these regimes, differences are of minor importance for later particle damper applications. Above the optimal strokes, i. e. above $X_{\mathrm{rol}}^{\mathrm{opt}} = 4\,\mathrm{mm}$ and $X_{\mathrm{bou}}^{\mathrm{opt}} = 29\,\mathrm{mm}$, the results fit qualitatively well with some quantitative discrepancies. The effective loss factor is here described by equations describing the physical behavior of the particle bed. Along the fluidization line, i. e. $A \approx g$, differences up to three occur in the energy dissipation, as no accurate description of this state is possible so far.

Overall, the analytical formulas given in Eq. (6.12) are very well suited to calculate the optimal strokes and the occurring energy dissipation at and above the optimal strokes of the rolling and bouncing collect-and-collide motion modes. For smaller strokes than the optimal strokes, i. e. the scattered motion modes, and for the fluidization mode, the analytical formulas are not well suited.

6.1.3 Sensitivity Analyses

Intensive sensitivity analyses on the rolling collect-and-collide motion mode are presented in Sect. 5.1.4 and not repeated here. As rolling and bouncing collect-and-collide motion modes are both based on the inelastic collision property of the particle bed, the sensitivity of the effective loss factor is very similar. DEM simulations show that most container and particle properties, like particle radius, Young's modulus, coefficient of restitution or friction coefficient, are of minor importance for the effective loss factor of the bouncing collect-and-collide motion mode. Compared to the rolling collect-and-collide motion mode, in the bouncing collect-and-collide motion mode, the particle radius and friction coefficient have a much lower sensitivity. This is because particles are flying through the container for the bouncing state. Hence, much lower frictional losses occur.
Likewise, to the rolling collect-and-collide motion mode, for the bouncing collect-and-collide motion mode, the minimum particle number in each container direction should be three. This ensures that the inelastic collision of the particle bed takes place. Furthermore, particle number, particle radius and particle density determine the total particle mass and thus the amount of dissipated energy. Interestingly, the particle number in combination with the container dimensions have a huge impact on the shape of the effective loss factor as will be shown in the following. This is because the clearances h_{rol} and h_{bou} are differently affected, see Eq. (6.1). For the rolling collect-and-collide motion mode, the clearance depends on the particle number to cover the container's base with one layer of particles. The clearance of the bouncing collect-and-collide motion mode depends on the particle number to fill the complete container. To demonstrate these different dependencies in Fig. 6.5 the effective loss factors of four different

particle numbers, i. e. $n_\mathrm{p} = 24, 44, 48$ and 96, are shown. The resulting clearances and optimal strokes for these particle numbers obtained by Eqs. (5.13), (6.1) and (6.11) are summarized in Tab. 6.2.
As for the 48 and 96 particles the whole container base is filled with one layer of particles, the clearances of the rolling collect-and-collide motion mode are zero, i. e. not existing. Hence, this motion mode is not seen for these particle numbers, resulting in very low effective loss factor values, see Fig. 6.5c and Fig. 6.5d. By comparing the analytical optimal strokes of Tab. 6.2 with the numerical obtained high effective loss factors, see Fig. 6.5, a good agreement is seen for all particle numbers. For the 44 particle setting, the clearances and thus the optimal strokes of the rolling and bouncing collect-and-collide motion mode differ with a factor of 7.5, i. e. $X_\mathrm{rol}^\mathrm{opt} = 4\,\mathrm{mm}$ to $X_\mathrm{bou}^\mathrm{opt} = 30\,\mathrm{mm}$. Hence, two decoupled regimes are seen in the effective loss factor plot, connected by the fluidization mode, see Fig. 6.5b. For the 24 particle setting, the ratio between rolling and bouncing optimal stroke is 1.4, i. e. $X_\mathrm{rol}^\mathrm{opt} = 24\,\mathrm{mm}$ to $X_\mathrm{bou}^\mathrm{opt} = 34\,\mathrm{mm}$. Hence, for this particle setting, the regimes in the effective loss factor are coupled to each other, see also Fig. 6.5a. Interestingly, even for the 96 particle setting the optimal stroke of the bouncing collect-and-collide motion mode is on a similar scale as for the 24 particle setting, i. e. $X_\mathrm{bou}^\mathrm{opt}(n_\mathrm{p} = 96) = 19\,\mathrm{mm}$ to $X_\mathrm{bou}^\mathrm{opt}(n_\mathrm{p} = 24) = 34\,\mathrm{mm}$.
These findings imply that it is possible to adjust rolling and bouncing collect-and-collide motion modes at a time using the particle number and container dimensions in a desired way. Depending on the vibration conditions, i. e. frequency and amplitude, a particle damper for an underlying structure could exploit both motion modes for different excitation conditions.

While the rolling and bouncing collect-and-collide motion modes are easily analyzed, the fluidization mode seems to be highly sensitive. In a perfect flat container with no imperfections, there would be no momentum such that the particles take-off. Still, they do so in the simulations. One reason is the little-used container tilt of 0.1°. Another reason is that the particles penetrate in the simulations the container's base and have hence slightly different heights. Also, the initial conditions affect the fluidization mode, i. e. how much motion is present at the beginning. At last, experimental measurements using the linear

Table 6.2: Clearances and optimal strokes of the rolling and bouncing collect-and-collide motion modes for different particle numbers obtained by Eqs. (5.13), (6.1) and (6.11).

	particle number n_p [–]			
	24	44	48	96
h_rol[mm]	60	10	0	0
$X_\mathrm{rol}^\mathrm{opt}$[mm]	24	4	–	–
h_bou[mm]	105	92.5	90	60
$X_\mathrm{bou}^\mathrm{opt}$[mm]	34	29	29	19

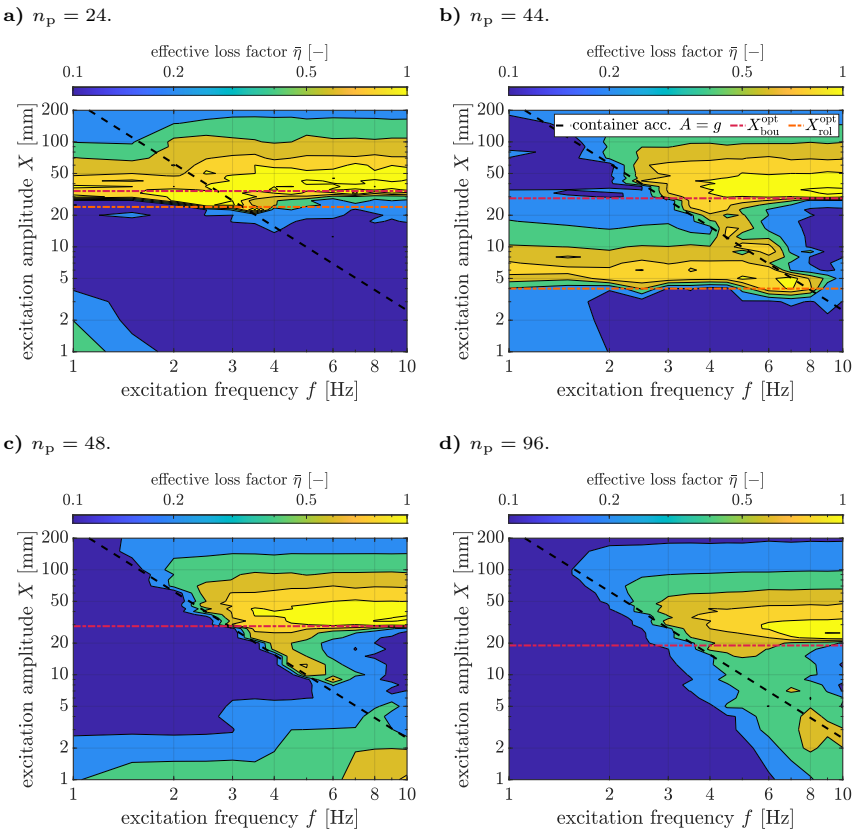

Figure 6.5: Effective loss factor fields of steel particles with 5 mm radius by DEM simulations for different particle numbers.

drive depicted in Fig. 5.1, have shown that smaller particles tend to fluidize at lower container amplitudes. This could be caused by the fact that the disorder of these systems is higher. Still, the process from rolling to fluidization to bouncing is not fully understood jet and, hence, an interesting topic for further studies.

6.2 Structural Integrated Damper

Within this level of the toolchain, see Fig. 3.1, the damping of free and forced vibrations of an underlying structure are studied. For the rolling collect-and-collide motion mode, intensive studies are presented on both vibration kinds in Sect. 5.2. The bouncing collect-and-collide motion mode is applied to forced vibrations in Sect. 8.2. So in this section, free vibrations and the transition from bouncing to rolling shall be considered.
For this task, a modification of the simple beam-like structure setup of Sect. 5.2 is utilized, see Fig. 5.11 and Eq. (3.28) for its numerical description. However, now a different beam is used. This steel beam has the same length of 512 mm as the previous one but with a rectangular profile of 80 mm × 3 mm instead of 80 mm × 2 mm. This significantly changes the system's stiffness to $K = 484\,\mathrm{N/m}$ compared to $K = 143\,\mathrm{N/m}$ previously. The system's total mass is only a little affected, i. e. $M = 1.108\,\mathrm{kg}$. The system's eigenfrequency follows to $f_0 = 3.33\,\mathrm{Hz}$ compared to $f_0 = 1.85\,\mathrm{Hz}$ previously. Due to the increased eigenfrequency of the system, the acceleration amplitude at the initial stroke $X_0 = 63\,\mathrm{mm}$ increases to $|A_0| = 28\,\mathrm{m/s^2} > g$. Theoretically, this causes the particle system to be in the bouncing collect-and-collide motion mode first. Hence, the particles should fly through the container instead of rolling.

Experimental measurements show that it is hard to obtain a reproducible trajectory of the particle container as the particle dynamics are highly sensitive. Little changes in the initial conditions of the container can cause a significantly different particle motion. Particles eventually take-off the container's base, i. e. fluidize and turn into the bouncing collect-an-collide motion mode. However, eventually, particles stay on the container's base and remain in the rolling collect-and-collide motion mode. This changes the particle forces onto the container walls and, hence, also the container's trajectory. Thus, no repetitive container trajectory is obtained within the experiments and it is challenging to accurately simulate the container's motion using DEM or utilizing the analytical equations.
To still obtain a sophisticated design approach for the particle damper, the design guideline of Sect. 5.2.1 is considered. Likewise, to Fig. 5.11, the particle damper is separated into multiple layers. As only one layer of particles fits into a container layer, the fluidization mode disappears, see [MeyerSeifried21c]. For container acceleration amplitudes above the gravitational constant, i. e. $A > g$, it is expected that a hybrid motion mode between rolling and bouncing collect-and-collide occurs. The lower bound of the effective loss factor is the rolling collect-and-collide motion mode, see also Fig. 6.4. For the damper design of the different particle layers Eq. (5.15)–Eq. (5.18) are utilized, i. e. as used previously for the rolling collect-and-collide motion mode in Sect. 5.2.1. All three particle layers are filled with 16 steel spheres of 5 mm radius resulting in a total particle weight of 196 g. The obtained clearances by the design guideline, i. e. Eq. (5.15)–Eq. (5.18), are adjusted by separation walls to $h_{\mathrm{rol}} = \{80, 40, 25\}$ mm and thus

$X_{\mathrm{rol}}^{\mathrm{opt}} = \{32, 16, 10\}$ mm.
In Fig. 6.6 the trajectory of the system's end-effector, i. e. the particle container, and the measured damping ratios are depicted. The results show similar qualitative behavior as for Fig. 5.15, i. e. the pure rolling case. Although the theoretical maximum effective loss factor of the bouncing state is higher compared to the rolling state, i. e. $\bar{\eta}_{\mathrm{bou}}^{\mathrm{max}} = 1.27$ to $\bar{\eta}_{\mathrm{rol}}^{\mathrm{max}} = 0.91$, the damping ratios here are very similar compared to Fig. 5.15. Probably, the container layers hinder the deployment of a purely flying particle state. Indeed, this requires further investigations. Concerning Eq. (5.15) the damper can be considered as efficient, if damping ratios of $\zeta_{\mathrm{d}} = 0.044$ are achieved. As this is the case, see Fig. 6.6b, the design guideline even works well for container acceleration amplitudes above the gravitational constant.

a) Trajectory of end-effector.

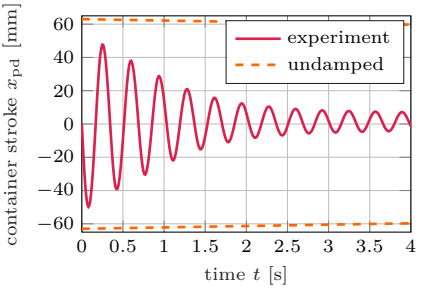

b) Damping ratios.

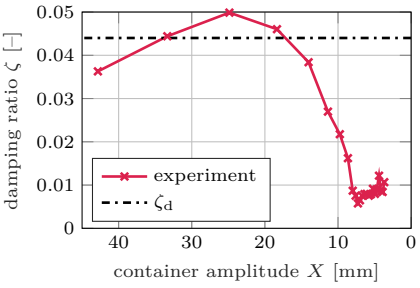

Figure 6.6: Results of damped simple beam-like structure shown in Fig. 5.11 with stiffer beam.

6.3 Summary

Horizontal vibrations of medium intensities are studied in this chapter. On the **Single Damper Level**, three different motion modes of the particle bed are identified numerically using DEM. For container acceleration amplitudes below the gravitational constant, the particle damper is in the rolling collect-and-collide motion mode. The spherical particles roll over the container base, enabling a high energy dissipation for container amplitudes above a certain threshold value. The second motion mode is the bouncing collect-and-collide motion mode. It occurs for container acceleration amplitudes above the gravitational constant.

Again, high energy dissipation is possible for container amplitudes above a certain threshold value, which is different from the rolling collect-and-collide motion mode. Both motion mode regimes are connected by the fluidization mode. While an analytical formula is derived for the rolling collect-and-collide motion mode in the previous chapter, for the bouncing collect-and-collide motion mode this formula is reproduced from [BannermanEtAl11] and [SackEtAl13]. These analytical descriptions are in good qualitative agreement with numerical DEM results with some quantitative differences. Also, formulations for the optimal strokes, i. e. the threshold values, of the rolling and bouncing collect-and-collide motion modes are derived. These strokes are only depending on the clearance between the particle bed and the opposite container wall.
For validation purposes, on the **Structural Integrated Damper Level**, a simple beam-like structure under free vibration is utilized. However, due to the high sensitivity of the fluidization mode, it is challenging to obtain a reproducible damper behavior. Hence, the particle container is separated into multiple layers. The same design guideline as for low-intensity horizontal vibrations is successfully applied.

Medium-Excitation Vertical Vibration Analyses

Again, medium-excitation vibrations are going to be classified as a vibration range with frequencies $f \approx 5\,\mathrm{Hz}$ and acceleration amplitudes of the particle damper below and above the gravitational constant. However, now vibrations in the vertical direction, i. e. in direction of gravity, are considered. Early studies on vertical free vibrations go back to [FriendKinra00]. They studied the vibration suppression of a simple beam-like structure and derived analytical equations to describe the damping of the particle damper. However, these analytical equations are tuned by the coefficient of restitution (COR). The work of [MasmoudiEtAl16] studies a vertically driven particle container. A good agreement between the experimental measurements and their derived analytical equations is obtained. Indeed, only single-sided particle contacts with the container base are considered. By [SanchezEtAl12] it is shown that the *bouncing collect-and-collide* motion mode can also be obtained in vertical driven particle containers. This motion mode has been described by [BannermanEtAl11] and [SackEtAl13] for applications in microgravity and is based on the inelastic bouncing ball motion mode [MehtaLuck90]. However, by [SanchezEtAl12], no analytical equations are derived to describe the energy dissipation of this motion mode in detail. For vertical vibrations of high excitation frequencies some more motion modes have been observed, like the local fluidization, global fluidization, undulation, convection, Leidenfrost effect and Buoyancy convection [AnsariAlam13, EshuisEtAl06, SaluenaEtAl98, YinEtAl17, ZhangEtAl17]. However, these motion modes are sensitive to excitation conditions and often yield no high energy dissipation. Hence, these motion modes are not further considered in this chapter.

Overall, no comprehensive study for medium-excitation vertical vibrations exists so far. Hence, on the **Single Damper Level**, see Sect. 7.1, the *effective fields*, i. e. *motion modes, energy dissipation* and *effective particle mass*, of a vertically driven particle container are studied in detail using the *discrete element method* (DEM). Different motion modes are observed, namely the *solid-like* state, *scattered* state and *bouncing collect-and-collide* motion mode. The latter is further subdivided into *single sided* and *double sided* contacts. For all motion modes analytical equations describing their energy dissipation are derived.
Afterward, on the **Structural Integrated Damper Level**, see Sect. 7.2, a particle damper is integrated into a simple beam-like structure under free vertical

vibration to obtain its overall damping effect. In the first step, the different particle damper models, i. e. DEM model, effective fields and analytical formulations, are coupled to a model of the simple beam-like structure. A good agreement between experiments and all utilized models is achieved for an initial deflection of the system and the following free vibration. Finally, the coupled model based on the analytical formulations is used for a damper optimization of the previously used initial deflection and the following free vibration. The efficiency of the optimized damper design is proven experimentally.
The following results have been published in [MeyerSeifried23b].

7.1 Single Damper

The considered particle container used for the later structural integration, see Sect. 7.2, is the same as already used in Chap. 5 and Chap. 6. It is a cuboid container made of polyvinyl chloride (PVC) and has a quadratic cross section with an inner edge width of 40 mm and a length (L) of 120 mm in the excitation direction, i. e. here in the direction of gravity. Steel particles of 5 mm radius are used throughout this chapter. See Tab. 7.1 for details on the damper and particle properties. This particle damper is subjected to a sinusoidally vertical motion using DEM of amplitude X and angular excitation frequency $\Omega = 2\,\pi\,f$ as $x_\mathrm{c} = X\sin(\Omega\,t)$, see Eq. (3.8). The container's velocity amplitude and acceleration amplitudes follow to $V = X\,\Omega$ and $A = X\,\Omega^2$, respectively, see Eqs. (3.9) and (3.10). The excitation frequency varies between $f = 2\,\mathrm{Hz} - 20\,\mathrm{Hz}$ and the excitation stroke varies between $X = 1\,\mathrm{mm} - 200\,\mathrm{mm}$. For this studied excitation regime all relevant motion modes for the later damper integration into a structure are clearly visible.
The resulting motion modes obtained by DEM simulations are depicted in Fig. 7.1.

Table 7.1: Material parameters of spheres and particle container.

	Sphere	Container
Material	S235	PVC
Young's Modulus E [GPa]	208	3
Poisson's Ratio ν [–]	0.3	0.38
Density ρ [$\mathrm{kg/m^3}$]	7900	1400
Friction Coefficient μ [–]	0.1 for all contacts	
Coefficient of Restitution ε [–]	velocity dependent, see Chap. 4	
Dimensions [mm]	$r = 5$	$L, W, H = 120, 40.4, 40.0$

Within the analyzed particle settings, the *solid-like* state and the *bouncing collect-and-collide* motion modes are observed here. Within the solid-like state, the particles remain on the container base. Only very little relative motion between

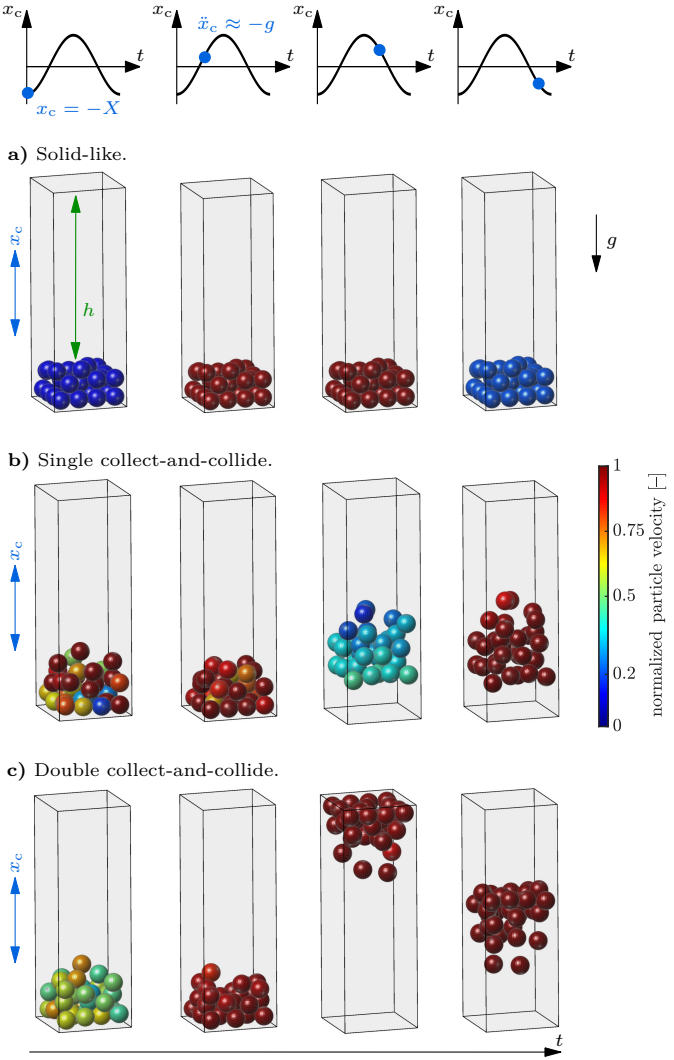

Figure 7.1: Observed motion modes for medium-excitation vertical vibrations at different time steps. The colors show the magnitude of the particles' velocity normalized by the container velocity amplitude V from low (*blue*) to high (*red*).

the particles is seen. Within the bouncing collect-and-collide state, the particles take-off the container's base and move up and down as one particle block. This particle bed collides inelastically with the container's walls, i. e. after impact the particle bed has adopted the container's velocity and does not rebound from it. This happens due to multiple inter-particle collisions during impact. For further discussions see [BannermanEtAl11, SanchezEtAl12]. Hence, a synchronous particle motion with the container is achieved. This state is further subdivided into *single collect-and-collide* and *double collect-and-collide*. Within the single collect-and-collide motion mode, the particle bed does not reach the upper container wall, but only collides with the container bottom. Within the double collect-and-collide motion mode, the particle bed reaches the upper container wall. Hence, a collision with the lower and upper container walls is achieved. Under certain conditions, as will be discussed later, a *scattered* motion mode is observed. In this state, the particle system begins to scatter and no regular motion is seen anymore. As this motion mode evolves from the bouncing collect-and-collide motion mode and exhibits no repetitive movement, it is not shown in Fig. 7.1.

7.1.1 Analytical Description

[SackEtAl13] and [BannermanEtAl11] derived an analytical formula for the energy dissipation of the double collect-and-collide motion mode under the assumption of zero gravity and achieved good agreement with experimental measurements under micro gravity, i. e. $g \approx 0$ with g being the gravitational constant. In this section, a similar analytical description shall be derived for vertical vibrating granular matter under the effect of gravity. Afterward, the analytical results are compared and validated via DEM analyses. The derived analytical descriptions are numerically much more efficient than the DEM simulations and are later used for designing a damper for an underlying structure. Some experimental results for **Structural Integrated Damper** analyses are given later in Sect. 7.2.

Derivation of Analytical Formulations

To set up the analytical equations for the energy dissipation of the particle bed, some assumptions on the particle motion have to be made. These are based on insights of the DEM simulations and can also be observed from the motion modes depicted in Fig. 7.1. As detected in Fig. 7.1, the particles stay together and move as one particle block for the considered motion modes. This means that the translational velocities of the particles are the same. The particle rotations are only of minor magnitude and are thus neglected. Initially, the particle bed is located at the container bottom, i. e. at $x_\mathrm{c} = -X$. When the container moves upwards, the particle bed will take-off the container bottom if $\ddot{x}_\mathrm{c} \leq -g$ holds. The particle bed collides in the following either with the lower or upper container wall. This depends on the excitation conditions and the clearance h, i. e. the distance

from the particle bed to the upper container wall, see also Fig. 7.1. When the particle bed collides with either container wall, an inelastic collision occurs, i. e. the particle bed instantaneous adopts the velocity of the container. The inelastic nature of the collision is justified in [BannermanEtAl11, SanchezEtAl12] and occurs due to multiple inter particle–particle and particle–wall impacts. Even though only a small amount of energy is dissipated in every single collision, an inelastic collision is achieved due to the combined energy dissipation.
Using these assumptions and insights from DEM simulations different trajectories of the particle bed are obtained as displayed in Fig. 7.2. The trajectories are shown until the first impact of the particle bed with the container bottom occurs. If a trajectory ends at the upper container wall, it implies that this trajectory does not lead to a repetitive particle motion. Instead, the scattering motion mode is seen in DEM simulations. In Fig. 7.2 the same motion modes as in Fig. 7.1 are visible, i. e. solid-like state, single collect-and-collide and double collect-and-collide. However, these motion modes can further be subdivided into harmonic and subharmonic particle impact with the container, see numbering in Fig. 7.2. The motion modes are obtained to:

1. **Solid-Like State**
2. **Single Collect-and-Collide**
   i) Harmonic impact with container bottom
   ii) Subharmonic impact with container bottom
3. **Double Collect-and-Collide**
   i) Harmonic impact with container top and bottom
   ii) Harmonic impact with container top and subharmonic impact with container bottom (conditionally repetitive particle trajectory)
   iii) Subharmonic impact with container top (no repetitive particle trajectory)

Distinction of Cases At first, for a given excitation, the motion mode of the particle bed has to be determined. The particle bed is in the solid-like state as long as the container acceleration amplitude is below the gravitational constant, i. e. $A < g$. For higher container acceleration amplitudes the particle bed will take-off the container bottom. Then, the system is either in the single collect-and-collide or double collect-and-collide motion mode. The time when the particle bed takes-off the container bottom $t_{\mathrm{off}}^{\mathrm{bot}}$, also referred to as *take-off time*, is obtained by numerically solving the take-off condition

$$A \sin\left(\Omega\, t_{\mathrm{off}}^{\mathrm{bot}}\right) = g, \tag{7.1}$$

with the condition $0 < \Omega\, t_{\mathrm{off}}^{\mathrm{bot}} < \frac{1}{2}\pi$. Next, it has to be determined whether the particle bed impacts the container top or not. If so, the double collect-and-collide

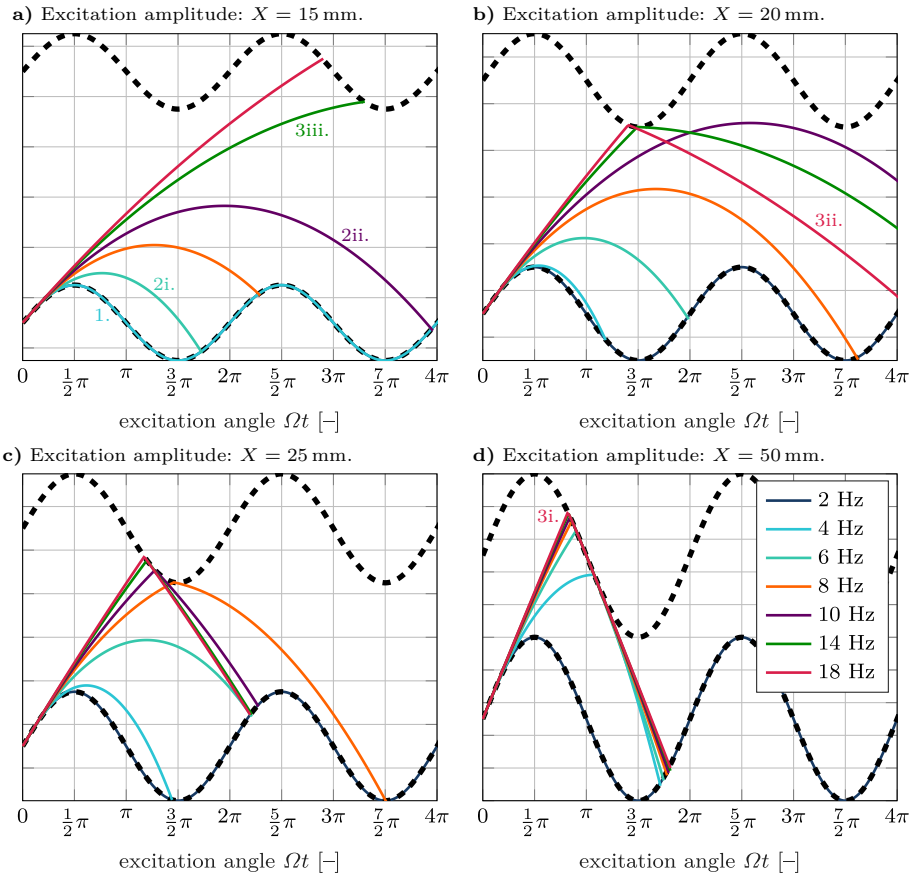

Figure 7.2: Trajectories of particle bed for vertical vibrations for different excitation frequencies and amplitudes with $h = 0.1\,\mathrm{m}$. The black dashed lines indicate the motion of the top and bottom container walls. The numbers indicate examples of the different motion modes.

motion mode is achieved. Otherwise, the single collect-and-collide motion mode is obtained. After the particle bed takes-off the container bottom, a parabolic flight occurs. In the following, the particle bed's take-off position $x_{\mathrm{off}}^{\mathrm{bot}} = x_{\mathrm{c}}(t_{\mathrm{off}}^{\mathrm{bot}})$ and the particle bed's take-off velocity $\dot{x}_{\mathrm{off}}^{\mathrm{bot}} = \dot{x}_{\mathrm{c}}(t_{\mathrm{off}}^{\mathrm{bot}})$ are used. Introducing, the impact time point with the upper container wall $t_{\mathrm{imp}}^{\mathrm{st}}$, i. e. the first impact (index st) of the particle bed, and introducing the flight duration of the particle bed $\Delta t_{\mathrm{st}} = t_{\mathrm{imp}}^{\mathrm{st}} - t_{\mathrm{off}}^{\mathrm{bot}}$, it can be checked if an impact with the upper container wall occurs. This is the case, if a numerical solution of $t_{\mathrm{imp}}^{\mathrm{st}}$ to the following impact condition

exists

$$x_{\mathrm{off}}^{\mathrm{bot}} + \int_{t_{\mathrm{off}}^{\mathrm{bot}}}^{t_{\mathrm{imp}}^{\mathrm{st}}} \left(\dot{x}_{\mathrm{off}}^{\mathrm{bot}} - g \ \left(t - t_{\mathrm{off}}^{\mathrm{bot}} \right) \right) \mathrm{d}t = X \sin(\Omega \, t_{\mathrm{imp}}^{\mathrm{st}}) + h, \tag{7.2}$$

$$\Rightarrow \underbrace{x_{\mathrm{off}}^{\mathrm{bot}} + \dot{x}_{\mathrm{off}}^{\mathrm{bot}} \, \Delta t_{\mathrm{st}} - \frac{1}{2} \, g \, \Delta t_{\mathrm{st}}^2}_{\text{particle motion}} = \underbrace{X \sin(\Omega \, t_{\mathrm{imp}}^{\mathrm{st}})}_{\text{container motion}} + \underbrace{h}_{\text{clearance}} . \tag{7.3}$$

If no solution to Eq. (7.3) exists, the particle bed is in the single collect-and-collide motion mode. The clearance between particle bed and upper container wall h is shown in Fig. 7.1 and can be calculated by

$$h = L \left(1 - \frac{n_{\mathrm{p}}}{n_{\mathrm{p}}^{\mathrm{max}}} \right), \tag{7.4}$$

with $n_{\mathrm{p}}^{\mathrm{max}}$ being the maximum possible particle number to fit in the container and n_{p} being the actual particle number in the container. Note that compared to previous chapters the index "bou" is dropped here, as no differentiation to other motion modes is necessary.
Now it is possible to distinguish between the different motion modes by evaluating Eqs. (7.1) and (7.3). In the next step, analytical equations for the dissipated energy for every motion mode are derived.

Solid-Like State In the solid-like state, i. e. for $A < g$, the particles do not take-off the container bottom. As a result, only very little relative motion between the particles occurs. An accurate analytical description is therefore not possible. The dissipated energy per cycle is roughly approximated by comparisons to DEM results to 0.1% of the particles' kinetic energy as

$$\widetilde{E}_{\mathrm{diss}} = \frac{2 \, \pi}{1000} \, E_{\mathrm{kin}} = \frac{\pi}{1000} \, m_{\mathrm{bed}} \, V^2, \tag{7.5}$$

with m_{bed} being the mass of all particles.

Single Collect-and-Collide Motion Mode The particle system is in the single collect-and-collide state, if a solution to Eq. (7.1) exists but not to Eq. (7.3), i. e. the particle bed takes-off the container bottom but does not collide with the container top. Instead, the particle bed collides with the container bottom again. The impact time point with the container bottom $t_{\mathrm{imp}}^{\mathrm{st}}$, i. e. the first and only impact, is obtained by solving

$$\underbrace{x_{\mathrm{off}}^{\mathrm{bot}} + \dot{x}_{\mathrm{off}}^{\mathrm{bot}} \, \Delta t_{\mathrm{st}} - \frac{1}{2} \, g \, \Delta t_{\mathrm{st}}^2}_{\text{particle motion}} = \underbrace{X \sin(\Omega \, t_{\mathrm{imp}}^{\mathrm{st}})}_{\text{container motion}}, \tag{7.6}$$

with the flight duration of the particle bed $\Delta t_{\mathrm{st}} = t_{\mathrm{imp}}^{\mathrm{st}} - t_{\mathrm{off}}^{\mathrm{bot}}$. Note, except for the clearance h, Eq. (7.6) is identical to Eq. (7.3).
For a harmonic impact with the container bottom, this motion mode results in one inelastic collision per vibration cycle. Thus, the dissipated energy per cycle follows to

$$\widetilde{E}_{\mathrm{diss}} = \kappa \, \frac{1}{2} \, m_{\mathrm{bed}} \, \Delta v_{\mathrm{st}}^2, \tag{7.7}$$

$$\Delta v_{\mathrm{st}} = \underbrace{\dot{x}_{\mathrm{off}}^{\mathrm{bot}} - g \, \Delta t_{\mathrm{st}}}_{\text{particle velocity}} - \underbrace{\dot{x}_{\mathrm{imp}}^{\mathrm{st}}}_{\substack{\text{container} \\ \text{velocity}}} , \tag{7.8}$$

with Δv_{st} being the relative velocity between particle bed and container at impact. The velocity of the container at the time of impact is $\dot{x}_{\mathrm{imp}}^{\mathrm{st}} = \dot{x}_{\mathrm{c}}(t_{\mathrm{imp}}^{\mathrm{st}})$. The variable κ is a scaling of the dissipated energy for subharmonic particle impacts with the container bottom, see e. g. Fig. 7.2-2ii. In contrast to horizontal vibrations [Kollmer14], these subharmonic impacts lead to repetitive particle trajectories, as shown by DEM simulations. The variable κ follows to $\kappa = 1/(1 + n_{\mathrm{imp}})$, with $n_{\mathrm{imp}} \in \mathbb{N}_0$ being the number of container vibrations till the particle bed impact. The number of the container vibration till the particle bed impact n_{imp} follows from the impact time point as

$$\frac{5}{2}\,\pi + 2\,\pi \;\; (n_{\mathrm{imp}} - 1) < \Omega \, t_{\mathrm{imp}}^{\mathrm{st}} < \frac{5}{2}\,\pi + 2\,\pi \, n_{\mathrm{imp}}, \tag{7.9}$$

see also Fig. 7.2. It is noted that a vibration cycle is considered from $\frac{1}{2}\pi$ till $\frac{5}{2}\pi$. Their exist a small range for the impact time point for which the particle's take-off condition is violated, i. e. for $2\pi + \Omega \, t_{\mathrm{off}}^{\mathrm{bot}} < \Omega \, t_{\mathrm{imp}}^{\mathrm{st}} < \frac{5}{2}\pi$. This means that the particle bed impacts the container bottom when the container's acceleration is already below g, i. e. the time point when the particle normally takes off. If this happens, it is observed from DEM simulations that a repetitive particle trajectory is still achieved. By impact, the particles rebound from the container base, which is hard to analytically describe. Still, Eq. (7.7) can be used as a rough approximation for the energy dissipation as will be shown later.

Double Collect-and-Collide Motion Mode: The double collect-and-collide motion mode occurs if a solution to Eqs. (7.1) and (7.3) exists, i. e. the particles take-off the container bottom and an impact with the container top occurs. The particle bed will "take-off" the container top when the container acceleration raises above the negative gravitational constant, i. e. for $\ddot{x}_{\mathrm{c}} \geq -g$. This time point can be expressed by using the take-off time from the container bottom, i. e. the solution to Eq. (7.1). If the collision with the container top occurs at a container acceleration above the negative gravitational constant, i. e. for $\ddot{x}_{\mathrm{c}} > -g$, the particle bed directly rebounds from the container top. The "take-off" time from

the container top $t_{\mathrm{off}}^{\mathrm{top}}$ is

$$t_{\mathrm{off}}^{\mathrm{top}} = \max\Big(\underbrace{t_{\mathrm{imp}}^{\mathrm{st}}}_{\text{rebound}} \, , \, \underbrace{\frac{\pi}{\Omega} - t_{\mathrm{off}}^{\mathrm{bot}}}_{\ddot{x}_{\mathrm{c}}=-g} \Big). \tag{7.10}$$

In this equation, a subharmonic impact with the container top is not considered, see e. g. Fig. 7.2-3iii. This is because DEM simulations have shown that these subharmonic impacts do not lead to a repetitive particle trajectory, i. e. a scattering of the particle system occurs instead. In these cases, Eq. (7.5) is used to approximate the energy dissipation of the particle bed.
After the particle bed takes-off the container top, a parabolic flight occurs until the impact with the container bottom. Defining the take-off position from the container's top $x_{\mathrm{off}}^{\mathrm{top}} = x_{\mathrm{c}}(t_{\mathrm{off}}^{\mathrm{top}})$ and the take-off velocity from the container's top $\dot{x}_{\mathrm{off}}^{\mathrm{top}} = \dot{x}_{\mathrm{c}}(t_{\mathrm{off}}^{\mathrm{top}})$, the time of impact $t_{\mathrm{imp}}^{\mathrm{nd}}$ with the container bottom, i. e. the second particle impact (index nd), follows by solving

$$\underbrace{x_{\mathrm{off}}^{\mathrm{top}} + \dot{x}_{\mathrm{off}}^{\mathrm{top}} \, \Delta t_{\mathrm{nd}} - \frac{1}{2} \, g \, \Delta t_{\mathrm{nd}}^2}_{\text{particle motion}} = \underbrace{X \sin(\Omega \, t_{\mathrm{imp}}^{\mathrm{nd}})}_{\text{container motion}} - \underbrace{h}_{\text{clearance}} \, . \tag{7.11}$$

Thereby, $\Delta t_{\mathrm{nd}} = t_{\mathrm{imp}}^{\mathrm{nd}} - t_{\mathrm{off}}^{\mathrm{top}}$ being the flight duration of the particle bed from the container's top to bottom.
In conclusion, for the double collect-and-collide motion mode, two impacts of the particle bed with the container walls (top wall, bottom wall) occur during one vibration cycle. Hence, the dissipated energy per cycle follows for this motion mode to

$$\widetilde{E}_{\mathrm{diss}} = \kappa \, \frac{1}{2} \, m_{\mathrm{bed}} \left(\Delta v_{\mathrm{st}}^2 + \Delta v_{\mathrm{nd}}^2 \right), \tag{7.12}$$

$$\Delta v_{\mathrm{st}} = \dot{x}_{\mathrm{off}}^{\mathrm{bot}} - g \, \Delta t_{\mathrm{st}} - \dot{x}_{\mathrm{imp}}^{\mathrm{st}}, \tag{7.13}$$

$$\Delta v_{\mathrm{nd}} = \underbrace{\dot{x}_{\mathrm{off}}^{\mathrm{top}} - g \, \Delta t_{\mathrm{nd}}}_{\text{particle velocity}} - \underbrace{\dot{x}_{\mathrm{imp}}^{\mathrm{nd}}}_{\substack{\text{container} \\ \text{velocity}}} \, , \tag{7.14}$$

with Δv_{st} and Δv_{nd} being the relative velocities between particle bed and container at impact with the container's top and bottom, respectively. The variable $\dot{x}_{\mathrm{imp}}^{\mathrm{nd}} = \dot{x}_{\mathrm{c}}(t_{\mathrm{imp}}^{\mathrm{nd}})$ denotes the velocity of the container at the time of particle impact with the container bottom. The variable κ is again a scaling for subharmonic impacts onto the container bottom and is defined analogously as for the single collect-and-collide motion mode, i. e. $\kappa = 1/(1 + n_{\mathrm{imp}})$ with $n_{\mathrm{imp}} \in \mathbb{N}_0$ being the number of the container vibration till particle impact. Here, the latter follows to

$$\frac{5}{2} \, \pi + 2 \, \pi \; (n_{\mathrm{imp}} - 1) < \Omega \, t_{\mathrm{imp}}^{\mathrm{nd}} < \Omega \, t_{\mathrm{off}}^{\mathrm{bot}} + 2 \, \pi \, n_{\mathrm{imp}}, \tag{7.15}$$

see also Fig. 7.2. This means that for a harmonic impact with the container bottom, i. e. $n_{\mathrm{imp}} = 0$, the particle bed has to impact the container bottom before the take-off time of the next vibration cycle. From DEM simulations it is observed that a particle impact after the take-off time of the next vibration cycle but before the container's maximum stroke, i. e. an impact time point of $\Omega\, t_{\mathrm{off}}^{\mathrm{bot}} + 2\,\pi\, n_{\mathrm{imp}} < \Omega\, t_{\mathrm{imp}}^{\mathrm{nd}} < \frac{5}{2}\pi + 2\,\pi\, n_{\mathrm{imp}}$, leads to a scattering of the particle bed and no repetitive particle trajectory. In this case, Eq. (7.5) is applied to approximate the energy dissipation of the particle system.
For very high container acceleration amplitudes $A \gg g$ the influence of gravity becomes negligible. This is in analogy to a zero-gravity environment. Hence, during one vibration cycle, two identical impacts with the container walls occur. By [BannermanEtAl11] and [SackEtAl13] it is shown that for zero-gravity environments the optimal impact time point is at $\Omega\, t_{\mathrm{imp}}^{\mathrm{st}} = \pi$. At this point, the maximum relative velocity between the particle bed and container is achieved. See Sect. 6.1.2 for a detailed discussion on this motion mode. Furthermore, [BannermanEtAl11] and [SackEtAl13] derived an analytical equation for the optimal container stroke for this impact time point. It reads

$$X_{\mathrm{opt}} = \frac{h}{\pi}. \tag{7.16}$$

The resulting energy dissipation follows in this case to

$$\widetilde{E}_{\mathrm{diss}}^{\mathrm{max}} = 4\, m_{\mathrm{bed}}\, V^2. \tag{7.17}$$

This is the highest possible energy dissipation for the double collect-and-collide motion mode. The maximum effective loss factor $\bar{\eta}_{\mathrm{max}}$ is obtained by inserting Eq. (7.17) into Eq. (3.15) to

$$\bar{\eta}_{\mathrm{max}} = \frac{4}{\pi} \approx 1.27. \tag{7.18}$$

Hence, $\bar{\eta}_{\mathrm{max}}$ is used to judge the efficiency of the different motion modes and damper designs.

Validation of Analytical Formulations

In the next step, the derived analytical equations for the energy dissipation of the particle bed shall be validated. This is done by comparing the results of the analytical equations to DEM simulations. For the DEM simulation, the standard settings and algorithms defined in Sect. 2.8 are utilized. The container and particle settings are listed in Tab. 7.1 and shown in Fig. 7.1, i. e. 32 steel particles of 5 mm radius with clearance $h = 0.1$ m are used. This container setting will be integrated later into a structure in Sect. 7.2. Using the DEM model, 14 excitation frequencies and 24 excitation amplitudes are analyzed within the frequency range of $f = 2\,\mathrm{Hz} - 20\,\mathrm{Hz}$ and the excitation range of $X = 1\,\mathrm{mm} - 200\,\mathrm{mm}$. Every configuration is simulated for a duration of ten vibration cycles, whereas the

first two cycles are cut off to remove the irregular particle movement introduced through the initial conditions. In Fig. 7.3 the results of the analytical equations and DEM simulations are depicted.

In Fig. 7.3a the predicted motion modes obtained by the analytical equations are shown. The transitions between the different motion modes can also be observed by the particle bed's trajectories in Fig. 7.2. For container acceleration amplitudes of $A < g$ the solid-like state is seen. When the container acceleration amplitude reaches the gravitational constant, i. e. the black dashed line in Fig. 7.3, the harmonic single collect-and-collide motion mode occurs first. From this state, transitions in different motion modes are possible, depending on the excitation amplitude X, excitation frequency f and clearance h. However, the

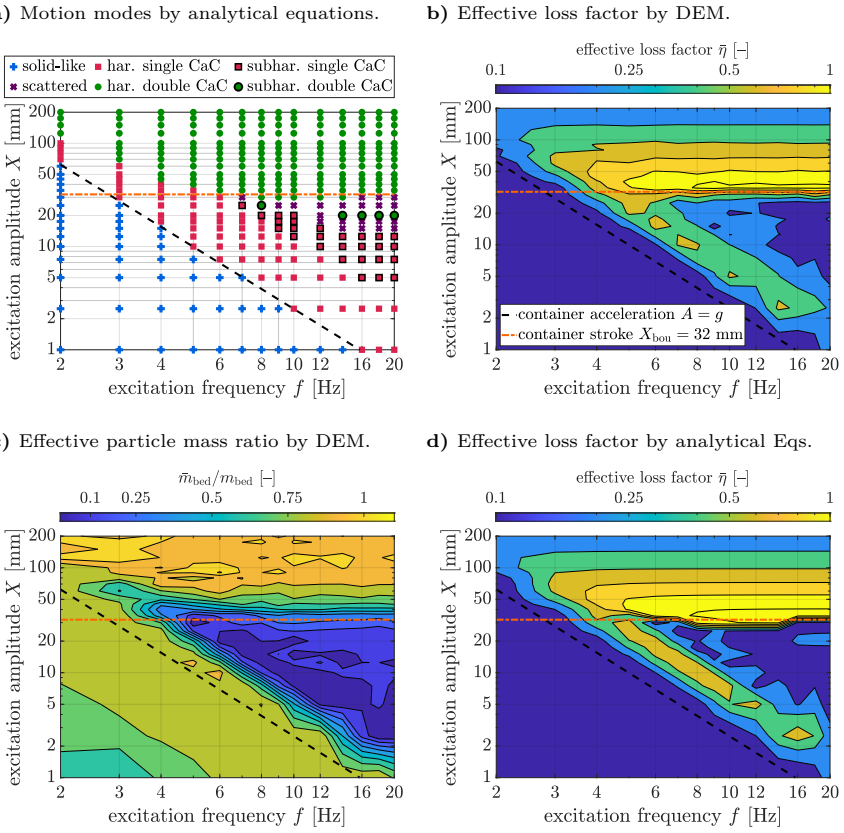

Figure 7.3: Effective fields: Numerical and analytical results of 32 steel particles of 5 mm radius with $h = 0.1$ m. CaC: collect-and-collide.

influence of the clearance is not further discussed here. For excitation frequencies up to $f = 6\,\mathrm{Hz}$ the system directly switches to the harmonic double collect-and-collide motion mode. For higher excitation frequencies, the system first of all changes into the subharmonic single collect-and-collide motion mode. From this state transitions into the scattered motion mode or subharmonic double collect-and-collide motion mode occur. Especially, at high excitation frequencies $f > 12\,\mathrm{Hz}$, the motion modes are very sensitive to the container stroke and change quickly. In any case, the system reaches the harmonic double collect-and-collide motion mode when the container stroke gets high enough, i. e. such that $A \gg g \wedge X > X_{\mathrm{opt}}$ holds, see orange dashed-dotted line in Fig. 7.3.

In Fig. 7.3b the effective loss factor obtained from DEM simulations is shown. The effective loss factor is an efficiency factor, which correlates the dissipated energy of the particle bed to the kinetic energy of the particle bed, see also Eq. (3.15). A yellow color indicates an effective loss factor of one or higher. A dark blue color indicates an effective loss factor of 0.1 or less. For the solid-like state, only very low values are achieved, i. e. $\bar{\eta} \ll 0.1$. This is reasonable, as there is only very little relative motion between the particles.
By crossing over to the harmonic single collect-and-collide motion mode much higher effective loss factors up to $\bar{\eta} = 0.7$ are reached. Turning into the subharmonic single collect-and-collide, subharmonic double collect-and-collide or scattering motion modes, a strong reduction within the effective loss factor is observed with values between $0.1 < \bar{\eta} < 0.3$. In the last motion mode, the harmonic double collect-and-collide, a very wide range of effective loss factor values are observed with $0.25 < \bar{\eta} < 1.25$. Using Eq. (7.16) the optimal stroke under zero gravity is calculated analytically to $X_{\mathrm{opt}} = 32\,\mathrm{mm}$. This value is depicted in Fig. 7.3 as a dash-dotted orange line and is in good agreement with the high effective loss factor values. In the DEM simulations, the optimal stroke occurs at slightly higher values. This is probably due to the influence of gravity. The maximum obtained effective loss factor by DEM simulations of $\bar{\eta} = 1.25$ is very close to the theoretical optimal one of $\bar{\eta}_{\mathrm{max}} = 1.27$, see Eq. (7.18). Only for excitation frequencies $f < 5\,\mathrm{Hz}$, i. e. when the container acceleration amplitude A becomes close to the gravitational constant, the effective loss factor decreases rapidly.
Another important property of the harmonic double collect-and-collide motion mode can be observed starting from the optimal stroke. A high gradient in the effective loss factor is seen for lower container strokes as the optimal one, i. e. $X < X_{\mathrm{opt}}$. Here, the system quickly turns into the single collect-and-collide or scattering motion mode. For higher container strokes as the optimal one, i. e. $X > X_{\mathrm{opt}}$, only a small gradient in the effective loss factor is observed. Here, the system is still in the harmonic double collect-and-collide motion mode, but the relative impact velocity between particles and container reduces. For further explanations see [SackEtAl13] and Sect. 6.1.2.

In Fig. 7.3d the effective loss factor obtained from the analytical equations is

depicted. For all motion modes, a good qualitative approximation of the energy dissipation to the DEM simulations is achieved. Especially in the harmonic single collect-and-collide and harmonic double collect-and-collide motion modes, the values are in good agreement. However, few local areas of higher discrepancies occur for the other motion modes, i. e. the subharmonic and scattering motion modes. This is not surprising as the transition between these modes is sharp and little differences between the DEM model and analytical equations, which are based on model predictions, can lead to an entirely different particle motion and energy dissipation. The differences, among others, are the size of the clearance or a not completely inelastic collision between the particle bed and container wall. For the scattering motion mode no accurate analytical description exists either and the dissipated energy is merely approximated. Note, this can not be seen in Fig. 7.3, as DEM and analytical formulas lead to effective loss factors below 0.1 and hence to a dark blue color. This difference is of minor importance for a later damper design as this motion mode can not be influenced in a targeted manner anyways.

In Fig. 7.3c the ratio of effective particle mass to the mass of the particle bed obtained by DEM simulations is shown. It describes to what extent the mass of the particle bed is coupled to the container movement, see Eq. (3.17). For the solid-like and harmonic double collect-and-collide motion modes rather high ratios of $0.5\,m_{\mathrm{bed}} < \bar{m}_{\mathrm{bed}}$ are achieved. This implies that the dissipated energy and effective particle mass are not coupled to each other as for these two motion modes completely different effective loss factors are obtained, see Fig. 7.3b. For the harmonic single collect-and-collide motion mode medium effective mass ratios of about $0.5\,m_{\mathrm{bed}} < \bar{m}_{\mathrm{bed}} < 0.75\,m_{\mathrm{bed}}$ are obtained. For the other motion modes, i. e. scattering and subharmonic impact, low ratios are seen $\bar{m}_{\mathrm{bed}} < 0.5\,m_{\mathrm{bed}}$. It seems like a shorter contact time with the container results in a lower effective particle mass. However, an analytical description for the effective particle mass is hard to derive. Therefore, for the structural integration of the particle damper in Sect. 7.2, the effective particle mass will be approximated as follows:

$$\bar{m}_{\mathrm{bed}} = \begin{cases} 0.75\,m_{\mathrm{bed}} & \text{for solid-like \& harmonic double collect-and-collide,} \\ 0.65\,m_{\mathrm{bed}} & \text{for harmonic single collect-and-collide,} \\ 0.2\,m_{\mathrm{bed}} & \text{for subharmonic single/double collect-and-collide,} \\ 0.1\,m_{\mathrm{bed}} & \text{for scattered.} \end{cases} \tag{7.19}$$

7.2 Structural Integrated Damper

In the following, the particle damper analyzed on the **Single Damper Level**, see Sect. 7.1, is integrated into a simple beam-like structure under free vertical vibration to obtain its overall damping effect. First, in Sect. 7.2.1 the experimental and numerical setups are presented. The numerical models are validated in Sect. 7.2.2. Finally, in Sect. 7.2.3 a damper optimization procedure is presented.

7.2.1 Experimental and Numerical Setups

The setups used here are similar to the simple beam-like structure of Sect. 5.2.1. However, as vertical free vibrations of medium intensities are studied, some adjustments to the system are necessary.

Experimental Setup

The utilized simple beam-like structure setup is shown in Fig. 7.4. It consist of a 680 mm long elastic beam with rectangular profile of 80 mm × 6 mm and an Young's modulus of $E = 200\,\mathrm{GPa}$. The beam has a fixed support on one side. On the other side, the particle damper including an additional mass is mounted. The system's total weight is 1.27 kg. The inner measurements of the cuboid PVC particle damper are 120 mm × 40 mm × 40 mm. This damper has already been analyzed in Sect. 7.1 on the **Single Damper Level** of the toolchain. The whole system is deflected using a counterweight of 11 kg yielding an initial displacement of $X_0 = -58\,\mathrm{mm}$. As the later used particle mass is

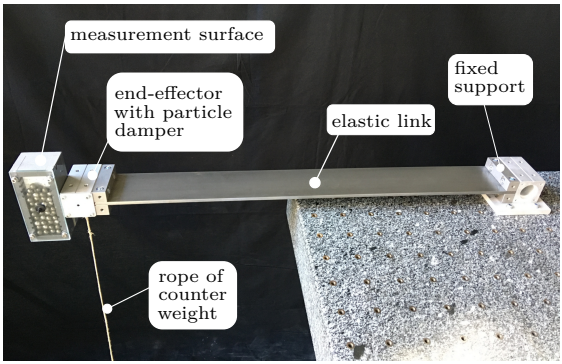

Figure 7.4: Composition of simple beam-like structure setup for vertical free vibration analyses.

much lower than the counterweight, an additional deflection of the beam due to the particles can be neglected. The system is released by cutting the rope of the counterweight. After release, the velocity of the end-effector is measured using a laser vibrometer, the *PSV-500* from POLYTEC pointing on the top side of the end-effector. The data acquisition is accomplished using the frontend of the *PSV-500* with a sampling frequency of 250 kHz. The measured velocity is internally integrated to the container's position. To remove the initial offset, the initial deflection of the particle damper is added to the measurements.

Numerical Setup

To calculate the movement of the simple beam-like structure, different particle damper models, i. e. DEM model, effective fields and analytical formulas, are coupled to a modal reduced model of the structure. This is discussed extensively in Sect. 3.3. In the first step, the simple beam-like structure is discretized using the *finite element method* (FEM), see Fig. 7.5. The flexible beam is discretized using 100 Timoshenko beam elements. All other components are modeled as rigid bodies and are included as point elements with the corresponding mass. Then, the linear equations of motion are set up. The structural damping is neglected and is added later based on measurements. Using modal reduction the system is reduced in size. Only the first bending vibration mode is considered as it is dominant for the free vibration considered later on. Finally, the parameters of the beam's equation of motion, i. e. Eq. (3.36), follow to mass $M = 1.139\,\mathrm{kg}$, stiffness $K = 1848\,\mathrm{N/m}$ and measured structural damping $D = 0.55\,\mathrm{kg/s}$. The eigenfrequency of the undamped beam-like structure follows from the numerical model to $f_0 = 5.56\,\mathrm{Hz}$ and fits very well with the experimental measured one of $f_0 = 5.56\,\mathrm{Hz}$ with only a very small deviation for different measurements.
For the effective fields and the analytical formulas, the effective particle mass $\bar{m}_{\mathrm{bed}}$ and the *effective viscous damping parameter* $\bar{d}$ are used, see Eq. (3.36). The effective viscous damping parameter depends on the energy dissipation of the particle damper according to Eq. (3.39). However, effective particle mass and effective viscous damping parameter are not constant and change as the damper's amplitude changes, see Fig. 7.3. Hence, both parameters are updated at the negative container peaks in each vibration cycle. This is justified as all motion modes last for at least one vibration cycle, see also Sect. 7.1.

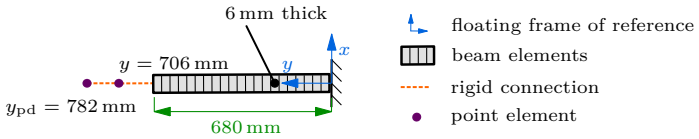

Figure 7.5: FEM model of simple beam-like structure.

7.2.2 Verification

In the first step, the coupling procedure of the different damper models with the beam's equation of motion is validated by comparison to a conducted experiment. Therefore, the particle container is filled with 32 of 192 possible steel particles of 5 mm radius weighting 131 g. The system is then released from the initial deflection. For DEM simulation the material data of Tab. 6.1 is used. The corresponding effective fields are shown for this setup in Fig. 7.3 and the analytical equations are given in Sect. 7.1.1.

In Fig. 7.6 the different trajectories and damping ratios are compared between experiment and coupled damper models. To give an impression of the additional damping by the particles in Fig. 7.6 the envelope of the system without particles, i. e. only the structural damping, is also shown. After release from the initial deflection, the system is first in the double collect-and-collide motion mode. The damping ratio in the experiment starts with a value of about $\zeta = 0.035$ for $X = 53\,\text{mm}$ and is increasing while the container amplitude decreases. This occurs up to a damping ratio of $\zeta = 0.05$ at $X = 41\,\text{mm}$. At the next sampling point, the system is already in the single collect-and-collide motion mode. The theoretical value of the optimal stroke for this setting, see Eq. (7.16), is $X_{\text{opt}} = 32\,\text{mm}$ and thus close to the measured high damping ratios and close to the switching point to the single collect-and-collide motion mode, see vertical dashed line in Fig. 7.6b.
During the single collect-and-collide motion mode, the damping ratio decreases (almost linearly) with decreasing container amplitude. Finally, the system reaches the solid-like state at $t = 1.66\,\text{s}$. In this state, hardly any damping by the particles occurs resulting in an almost constant container amplitude. This nearly constant container amplitude is approximated by the theoretical transition to the solid-like state by $X_{\text{min}} = g/\omega_{\text{bed}}^2 = 8.8\,\text{mm}$ with ω_{bed} being the eigenfrequency of the system including particles as static mass, see Eq. (3.35). From Fig. 7.6 it is seen that the system does not reach this minimum amplitude. This happens as the particle bed is already in the solid-like state for slightly higher values than X_{min}. Compared to the undamped system, a very good damping behavior is achieved. The undamped system shows damping ratios of about $\zeta = 0.005$ and an amplitude of about 40 mm after 2 s.

A very good agreement is achieved when comparing the trajectories of the different numerical models to the experiment. The DEM result fits best with the experiment. The trajectories of the effective fields and analytical formulas slightly differ from the experimental result at the maximum positive container strokes. This happens as the effective viscous damping parameter $\bar{d}$ is only updated once per vibration cycle at the negative container peaks. Thus, the nonlinear behavior of the particle damper at particle impact with the container is not reproduced. However, over one complete vibration cycle, the reproduction of the damping behavior is given. For the analytical formulas, an additional shift

a) Trajectories of end-effector.

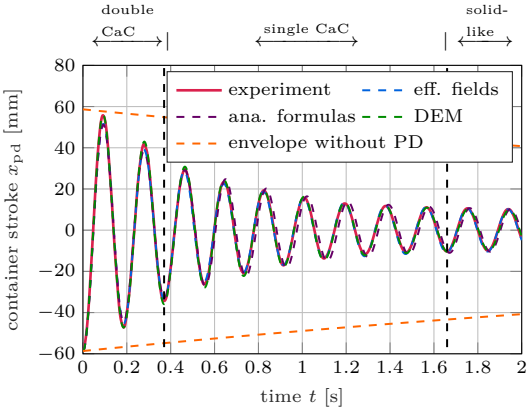

b) Damping ratios.

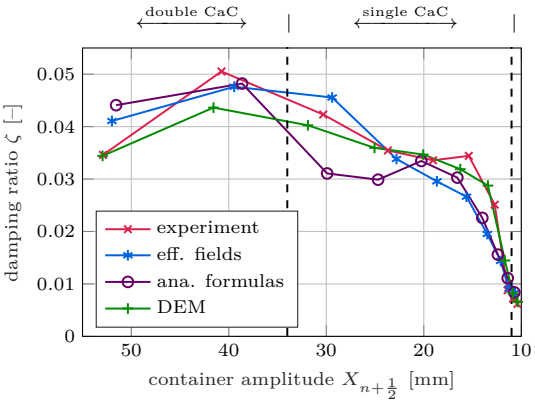

Figure 7.6: Experimental and numerical results of simple beam-like structure filled with 32 steel particles of 5 mm radius. The vertical dashed lines indicate the transitions between the different motion modes obtained by DEM simulation. CaC: collect-and-collide

in phase is visible. This phase shift occurs during the single collect-and-collide motion mode and happens because the effective particle mass is only roughly approximated by Eq. (7.19). In consequence, the effective eigenfrequency differs between experiment and analytical formulas, resulting in the observed phase shift.

As the obtained trajectories fit very well, the same is true for the damping ratios.

Only for the analytical formulas, two values are slightly off, having a negligible effect on the container's trajectory. Although all three numerical models perform very well, their computational costs are again very different. The DEM has high online costs, i. e. in the range of hours to days. The analytical formulas and effective fields, however, have very low online costs, i. e. in the range of seconds, but the effective fields have high offline costs similar to DEM. This is because these fields have to be pre-computed using DEM for every particle number. Thus, the analytical formulas are computationally most efficient in their application.

7.2.3 Optimization

Due to the high numerical efficiency of the analytical formulas, they are used for damper optimization next. The objective is to find the filling ratio of the damper to achieve the system's smallest container amplitude after 0.8 s. Therefore, the particle number is varied by an increment of 16, i. e. by one layer of particles. Note, the more particles are used, the more energy can theoretically dissipate. However, the higher the used particle number, the smaller the clearance and thus the smaller the optimal stroke. Due to the low number of settings, a simple brute-force algorithm is used to find the optimal configuration. The resulting particle number is 64 weighting 265 g in total with clearance $h = 80\,\text{mm}$.
To check this analytical result, it is compared to an equivalent conducted experiment as shown in Fig. 7.7. In the experiment, great damping behavior is achieved. After 0.75 s the system has almost reached its minimum stroke $X_{\text{min}} = 10\,\text{mm}$. At this time point, the system shown in Fig. 7.6 is at 19 mm amplitude and the undamped system at 51 mm amplitude. The analytical formulas are in good

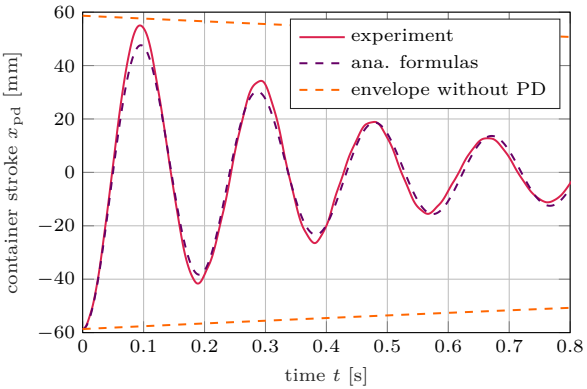

Figure 7.7: Comparison of container trajectory for optimized particle number between experiment and analytical result.

agreement with the experiment with only little quantitative differences. The phase difference between the experiment and the analytical result is small. Hence, a good damping setting is found using this optimization procedure.

Similar to Sect. 5.2.1, a systematic design guideline could be developed for vertical free vibrations. However, for this design optimization further investigations into the influence of the clearance h are necessary in the future to obtain a deeper understanding of this parameter.

7.3 Summary

Vertical vibrations of medium intensities have been studied in this chapter. On the **Single Damper Level**, multiple motion modes are observed for a vertically driven particle damper, namely, the solid-like, single collect-and-collide, double collect-and-collide and scattering motion modes. For the single collect-and-collide and double collect-and-collide motion modes analytical equations based on the physical behavior of the particle bed have been derived to describe the energy dissipation. These equations are in good agreement with numerical DEM simulations. For both motion modes, harmonic and subharmonic impacts of the particle bed with the container walls can occur. While the harmonic particle impacts lead to a repetitive particle behavior and high energy dissipation rates, the subharmonic impacts often do not. The solid-like and scattered states are only roughly approximated analytically. Moreover, the effective particle mass is determined by DEM simulations and approximated analytically. Especially, the solid-like and double collect-and-collide motion modes yield a high particle mass coupling.
Then, on the **Structural Integrated Damper Level** of the toolchain, the particle damper is applied to damp a simple beam-like structure under vertical free vibration. The different numerical models of the particle damper, i. e. DEM model, effective fields and analytical formulas, are coupled to a modal reduced model of the structure. A good agreement between simulations and experiments is observed for all models. Lastly, a damper optimization is performed using the analytical equations and its efficiency is validated experimentally.

High-Excitation Vibration Analyses

High-excitation vibrations are categorized in this work as horizontal and vertical vibrations with frequencies $f \gg 5\,\mathrm{Hz}$ and acceleration amplitudes of the particle damper general significantly above the gravitational constant, i. e. $A \gg g$. Due to these significantly changed excitation conditions, compared to the previous chapters 5–7, different experimental setups are necessary for the particle damper analyses. Often, smaller particle radii but higher particle numbers are utilized, making *discrete element method* (DEM) simulations burdensome or even impossible. Hence, for sensitivity analyses, either time-consuming experimental measurements or simplified numerical simulations are carried out, as discussed in detail in the following sections.

In Sect. 8.1 the **Single Damper Level** of the toolchain, see Fig. 3.1, is considered. Different shaker driven particle containers are analyzed concerning their *effective fields*, i. e. *motion modes, energy dissipation* and *effective particle mass*. The influence of various particle and container properties on the damper's efficiency are studied numerically and experimentally. However, it turns out that their effects are limited. Hence, more complex design approaches, like *inner structures* and *coated container walls*, are investigated. These show a great potential to increase the damper's efficiency. Finally, some generally applicable design rules are stated.

In the following Sect. 8.2, the **Structural Integrated Damper Level** of the toolchain is discussed. A shaker excited beam-like structure with free-free boundary conditions is utilized here. The damping of multiple eigenmodes is determined using a sine sweep excitation. Different excitation forces and particle damper positions are analyzed experimentally. For numerical analyses, a full DEM model and the damper's effective fields are coupled to a modal reduced model of the beam structure. These coupling procedures are analyzed concerning efficiency and accuracy. Big differences are obtained for both approaches. Finally, some concluding design rules are presented.

8.1 Single Damper

Early studies including high-excitation vibrations go back to [SaluenaEtAl98]. They studied the motion modes of the rheology behavior of vibrating granular material and compared those to the loss factor of the system. In [SaluenaEtAl98], three different regimes are determined, namely the *solid, convective* and *gas-like* ones. By [ZhangEtAl15] this classification is refined into seven different motion modes to *solid-like, local-fluidization, global-fluidization, convection, Leidenfrost effect, bouncing collect-and-collide* and *buoyancy convection*. Also, [YinEtAl17] studied those regimes and found a correlation to the damper's loss factor. In all cases, no parameter analyses were performed and only a small excitation range was analyzed. Furthermore, some of these motion modes only occur for very specific excitation conditions and are, hence, uninteresting for the application in particle dampers.

In the following, an intensive study about the correlation of particle motion modes and energy dissipation is presented for a wide excitation frequency range interval and excitation amplitude range interval. It is analyzed how particle properties, container properties and micro-mechanical contact behavior influence the efficiency of the different motion modes. However, the efficiency of some motion modes can not be targeted in a desired manner by the studied influence parameters. In literature, various approaches are presented to increase the damper's efficiency at specific excitation conditions, partly by creating new motion modes. Indeed, [HollkampGordon98] experimentally found only little effect of the particle shape. Numerical studies by [PourtavakoliEtAl16] came to the same conclusion. On the other hand, complex container shapes could have a significant influence [WongEtAl09a]. An interesting approach is presented by Gnanasambandham [GnanasambandhamEtAl19] who uses liquid-filled particle dampers to damp low frequency vibrations and achieved a good damping behavior. Another design is presented by [YaoChen15]. They equipped the particle dampers with loose spoilers to increase the damping performance at small vibration amplitudes. This approach is adopted by [GnanasambandhamEtAl20] to fixed inner structures. Thereby, an increased damping performance at a single frequency is obtained. In [LuEtAl12] and [LiDarby08] coated particle dampers for application in civil engineering are investigated, i. e. for low-frequency applications. These dampers show significantly lower force peaks caused by the particles and could increase the damping performance.
Although many promising approaches exist to increase the damping performance and excitation robustness of particle dampers for high vibration intensities, accurate design guidelines are still missing. This is because the investigations are often restricted to numerical analyses or a single excitation frequency. Hence, the overall picture is not obtained and general statements are difficult to derive. Another aim of this section is to close this gap by presenting extensive numerical and experimental studies and by deriving general design guidelines for the design

of robust particle dampers at high-excitation vibrations. Especially, coated container walls and fixed inner structures within the particle container are used to fulfill this task.

First, in Sect. 8.1.1 the newly developed experimental test bed is presented, enabling damper analyses on a large excitation range. The validity and accuracy of the experimental testbed and of the numerical model are shown in Sect. 8.1.2. Afterward, in Sect. 8.1.3 sensitivity analyses on different particle and container properties are presented. To increase the damper's efficiency, more robust designs are proposed in the following Sect. 8.1.4 and Sect. 8.1.5. Finally, in Sect. 8.1.6 the summary is given. This section has been partly published in [MeyerSeifried19a, MeyerSeifried19b, MeyerSeifried21c, MeyerSeifried23a].

8.1.1 Experimental and Numerical Setups

The experimental and numerical setups to analyze particle dampers for high-excitation vibrations are presented in the following. The particle container is subjected hereby to a sinusoidally motion of amplitude X and angular excitation frequency $\Omega = 2\,\pi\,f$ as $x_\mathrm{c} = X\sin(\Omega\,t)$, see Eq. (3.8). The container's velocity and acceleration amplitudes follow to $V = X\,\Omega$ and $A = X\,\Omega^2$, respectively, see Eqs. (3.9) and (3.10). The damper's energy dissipation, effective loss factor and effective particle mass are extracted by the *complex power method*, see Sect. 3.2.2 for a detailed description.

Experimental Setup

For the analyses within this section, a corresponding shaker testbed is set up as shown in Fig. 8.1. To realize the rheonomic constraint of the container movement, see Eq. (3.8)–Eq. (3.10), the particle container is connected via a load cell to the shaker and is excited by a controlled harmonic force perpendicular to gravity. The shaker's excitation force is controlled in order for the frequency and acceleration magnitude of the particle container to stay constant. Load cell (*Type 8230-002*), accelerometers (*Type 4534-B*), control system (*LDS Comet*) and shaker (*LDS V455*) are from Brüel & Kjaer. Two accelerometers are used. The first is for the controller and the second is to trigger the measurement. Due to the impacting particles on the container walls, the acceleration signal is very noisy. In order to use this acceleration signal for the control of the excitation, this accelerometer is connected via a plastic tube with Young's modulus of $86\,{}^{\mathrm{N}}/_{\mathrm{mm}^2}$ to the shaker. The accelerometer and plastic tube form a spring–mass system and act, hence, as a low-pass filter. The plastic tube is designed in a way that the cut-off frequency is at 2.5 kHz. Hence, single particle impacts on the container walls are filtered efficiently, as their contact frequency is normally significantly above 5 kHz, see e. g. Fig. 4.21 for the impact duration of metallic particles. Simultaneously,

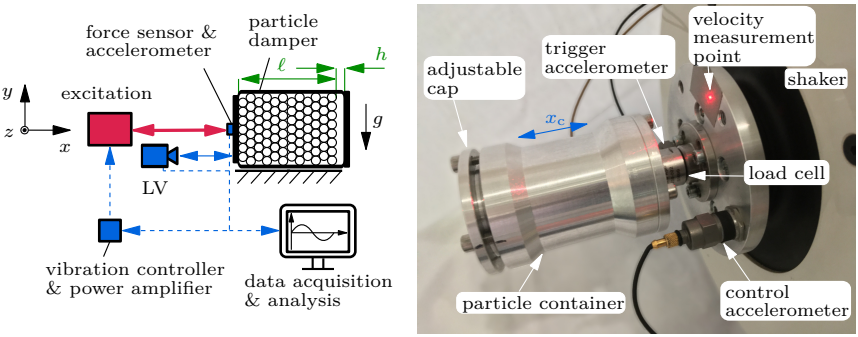

Figure 8.1: Testbed for determination of effective fields of cylindrical particle damper for high-excitation vibrations with schematic representation (*left*) and picture (*right*).

low frequencies up to the excitation range of 1 kHz are only little influenced. The velocity of the particle container is measured via a laser vibrometer (LV), the *PSV-500* from POLYTEC. The data acquisition of the velocity and force signals is accomplished by the frontend of the *PSV-500* with a sampling frequency of 40 kHz.
The feasible measurement range of the experimental setup lies between excitation frequencies of $40\,\mathrm{Hz} \leq f \leq 1\,\mathrm{kHz}$ and accelerations amplitudes within the range of $1 \leq \Gamma = A/g \leq 40$. Hereby, the *excitation intensity* Γ is defined as the acceleration amplitude A normalized by the gravitational constant g. The measurement range is divided up into a logarithmic grid of 108 points. Twelve frequencies and nine acceleration values are used and each combination is measured for a duration of 5 s, when the shaker has reached its steady state. Two different particle container shapes are utilized in the following for the measurements:

Cubical Container Shape One of the particle container is an aluminum cube with an inner edge length of $L_{\mathrm{cub}} = 40\,\mathrm{mm}$ and a container weight of $m_{\mathrm{con}} = 165\,\mathrm{g}$. Particles are filled into the container from its top and the container's top cover plate is secured via four screws. One of the container's sides is mounted centric to the load cell such that the container's cover plate is perpendicular to gravity. For this container shape, the clearance h, see Fig. 8.1, is calculated as

$$h = L_{\mathrm{cub}} \left(1 - \frac{n_{\mathrm{p}}}{n_{\mathrm{p}}^{\mathrm{max}}}\right), \tag{8.1}$$

with n_{p} being the number of particles in the container and $n_{\mathrm{p}}^{\mathrm{max}}$ being the maximum number of particles to fit in the container. However, the determination of $n_{\mathrm{p}}^{\mathrm{max}}$ is not unambiguous and can vary a little for different filling procedures

as particles distribute differently within the container. Especially for bigger particles, the clearance by Eq. (8.1) is hence not precisely determined.

Cylindrical Container Shape The second container is an aluminum cylinder with an inner radius R_{cyl} of 20 mm and an adjustable length L_{cyl} of 50 ± 5 mm. This container is shown in Fig. 8.1. To realize the adjustable container length, the container and the cap of the container are equipped with a fine thread. The mass of this container is $m_{\mathrm{con}} = 200$ g. This adjustable length of the cylinder is used to set up the clearance h between particle bed and container cap precisely, see Fig. 8.1. Experimental tests performed here have shown that the minimum clearance is limited by the particle radius as $h_{\mathrm{min}} \approx r$. This limitation could be due to the irregular surface of the particle bed. Hence, the fine-tuning of the clearance is performed by experimental tests, as the clearance can also be extracted from the measurement results. This is discussed later in detail.
For the filling procedure, the longitudinal axis of the container points against gravity. Particles are poured up to a marking at about $\ell = 50$ mm, see Fig. 8.1. Then the container cap is adjusted. For the experiments, the container is turned by 90 °, so that the longitudinal axis of the cylinder is perpendicular to gravity, i. e. points in the direction of excitation.

Numerical Model

For the numerical analyses, the DEM is utilized, see also Chap. 2. The standard settings and algorithms defined in Sect. 2.8 are utilized. The same excitation and post-processing parameters as in the experiments are chosen. The used material and contact data are listed in Tab. 8.1. The cubical particle container is modeled using six bounding geometry planes, see Sect. 2.2.2. The cylindrical particle container is modeled using an infinite bounding geometry cylinder with its surfaces modeled by bounding geometry planes. To obtain the high filling ratios of the later utilized dampers, previously particle drop-down simulations are performed. The initial conditions are then loaded from these results.

Table 8.1: Material parameters of spheres and particle container.

	Sphere	Container
Material	S235	Al6060
Young's Modulus E [GPa]	208	70
Poisson's Ratio ν [–]	0.3	0.33
Density ρ [$\mathrm{kg/m^3}$]	7900	2700
Friction Coefficient μ [–]	0.1 for all contacts	
Coefficient of Restitution ε [–]	velocity dependent, see Chap. 4	
Dimensions [mm]	$r = 0.3 - 5$	$L_{\mathrm{cub/cyl}} = 40/50, R_{\mathrm{cyl}} = 20$

8.1.2 Experimental and Numerical Results

For the experimental and numerical analyses, the cylindrical particle container is filled first with 4500 steel spheres of 1.25 mm radius weighting 291 g. Hence, a sufficient amount of particles exist in all container dimensions and numerical analyses using DEM are still affordable. The adjustable cap of the cylindrical container is used to set up roughly a clearance of $h = \pi$ mm. With this clearance all motion modes are clearly visible, as discussed later. This setting is also referred to as *baseline setting* in the following. Later on, the effect of different particle and container properties are studied, like particle radius, particle number or inner structures. Consequently, this changes the total amount and weight of particles inside the damper. However, for comparison of these different settings, the *effective loss factor* is used, see Eq. (3.15). This is an efficiency factor correlating the dissipated energy by the particles to the kinetic energy of the particles. Hence, the effective loss factor is independent of the container mass and particle mass and the obtained results are comparable. Furthermore, the *effective particle mass* is studied. It describes how much the mass of the particle bed is coupled to the container movement.

Motion Modes

For the utilized particle setting five different *motion modes* are observed. The velocity fields of these motion modes obtained by DEM are shown in Fig. 8.2 for the in-plane particle velocity in the direction of excitation and gravity. All velocity fields are taken at a container position of $x_c = X$, i. e. at the maximum container stroke and zero container velocity.
The *solid-like* state, see Fig. 8.2a, is characterized by almost no relative motion between particles and container. This causes the granular matter to look like an added block, staying at the container base and moving with the same velocity as the container. Here, this motion mode is seen at low excitation intensities up to $\Gamma \approx 1$.
For excitation intensities $\Gamma \geq 1$ the granular systems first enters a state of *local-fluidization*, see Fig. 8.2b. Particles located at the top layers become fluidized, i. e. irregular relative motion between these particles, while particles at the container bottom still behave like a solid. When the excitation intensity is further increased the whole particle system gets fluidized, called *global-fluidization*, as shown in Fig. 8.2c. It should be noted that the global-fluidization is very similar for certain excitation conditions to the scattered bouncing collect-and-collide motion mode of Chap. 6. However, this state occurs here on a large excitation range and due to its evolution from local-fluidization it is named differently.
From the global-fluidization motion mode, the particle system can migrate in different motion modes, like *bouncing collect-and-collide, decoupled, convection* or *Leidenfrost effect*. This depends on the excitation conditions. For the investigated particle dampers here, only the bouncing collect-and-collide and decoupled

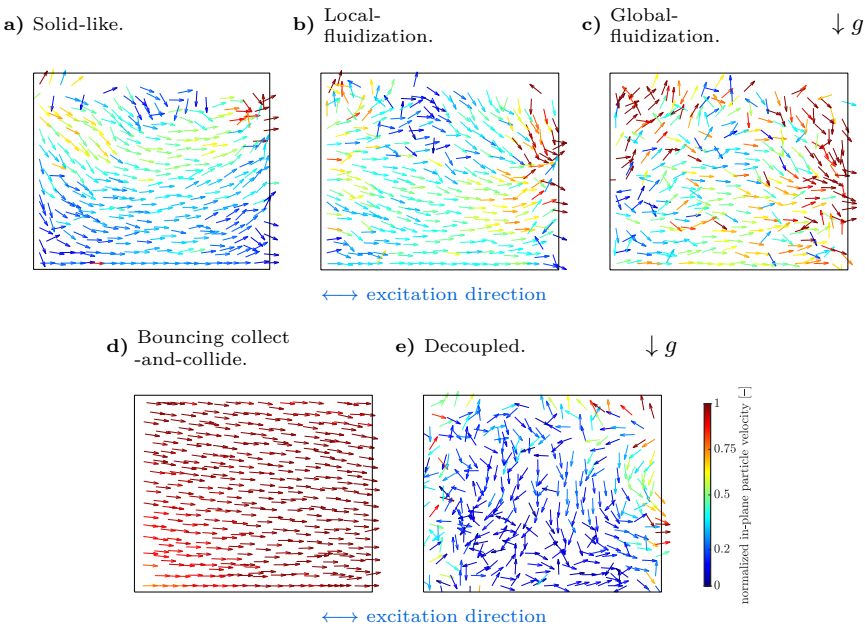

Figure 8.2: Velocity fields of motion modes for high-excitation vibrations at $x_c = X$. The colors show the magnitude of the in-plane particle velocity normalized by the container velocity amplitude V from low (*blue*) to high (*red*).

motion modes are observed. In the bouncing collect-and-collide motion mode, see Fig. 8.2d, the particles move as one single particle block synchronously with the driven container and collide inelastically with the damper walls. A detailed discussion on this motion mode is given in Sect. 6.1.2. The decoupled motion mode is shown in Fig. 8.2e. This motion mode also migrates from the global-fluidization motion mode. It is characterized by a very small absolute particle velocity compared to the velocity of the driven container. Thus, the granular matter appears to be decoupled from the container.

Effective Loss Factor and Effective Particle Mass

In Fig. 8.3 motion modes, effective loss factor $\bar{\eta}$ and effective particle mass $\bar{m}_{\mathrm{bed}}$ for the previously introduced setting are shown. The motion modes are determined from DEM animations, DEM velocity fields and from the experimentally measured effective loss factor. The latter is possible due to the strong correlation between effective loss factor and motion modes, see [MeyerSeifried21c] and further discussion in this section. For the effective loss factor, the experimental as well as DEM results, are shown. Hereby, a dark blue color indicates a value of 0.1 or

less, a yellow color indicates a value of one or higher. The effective particle mass is extracted from the experimental measurements.

At first, motion modes and experimentally obtained effective loss factor are discussed. The solid-like state is only seen at the lowest acceleration intensity $\Gamma = 1$ and low excitation frequencies $f \leq 100\,\mathrm{Hz}$. The solid-like state, see also Fig. 8.2a, is classified by almost no relative motion between the particles and the container. This results in a low energy dissipation and causes the effective loss factor to be low, i. e. $\bar{\eta} < 0.1$.
From the solid-like state, the system turns into the local-fluidization mode, see also Fig. 8.2b. The local-fluidization mode is seen for low acceleration inten-

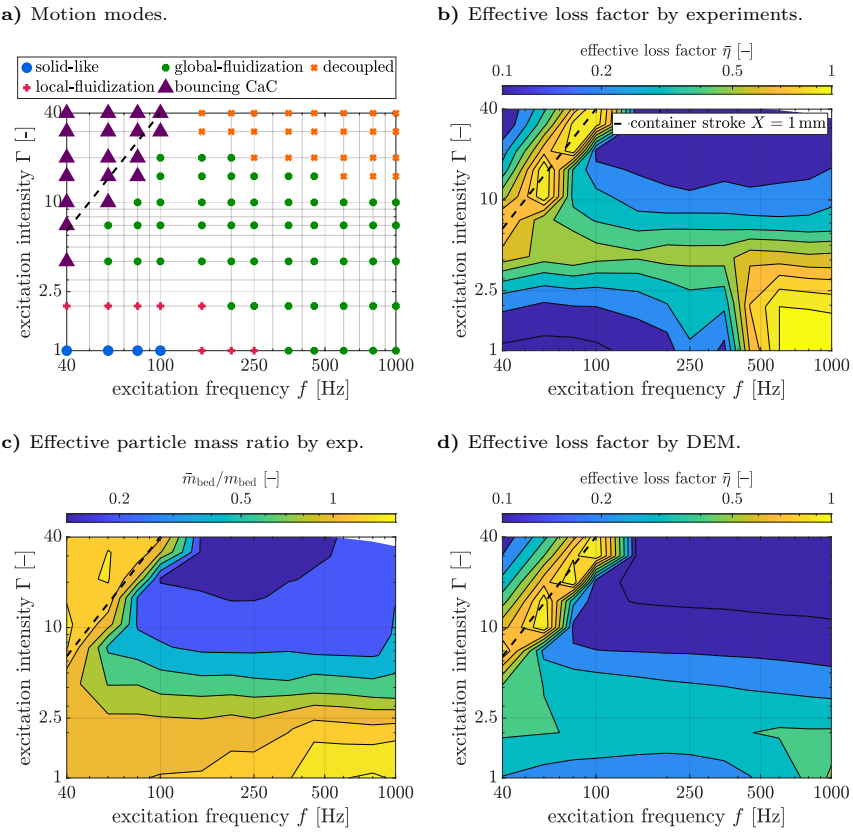

Figure 8.3: Effective fields: Experimental and numerical results of 4500 steel spheres of 1.25 mm radius with clearance $h = \pi$ mm inside cylindrical container. CaC: collect-and-collide.

sities $\Gamma \leq 2$ and low to medium excitation frequencies $f = 40\,\text{Hz} - 250\,\text{Hz}$. As most of the particles still behave like a solid and only the top particle layers show some relative motion, the effective loss factor is still comparatively low, i. e. $\bar{\eta} = 0.2 - 0.3$.

From the local-fluidization motion mode, the system switches to global-fluidization, see Fig. 8.2c. The global-fluidization mode can be observed on a large excitation range with low to high effective loss factor values, i. e. $\bar{\eta} = 0.2 - 1.6$. Medium effective loss factor values occur at the transition from local- to global-fluidization, i. e. at acceleration intensities of $\Gamma \approx 3$ for this particle setting. This behavior can be explained by the transition to global-fluidization. Even though there is a substantial amount of relative motion between the particles, the total kinetic energy is still comparatively low. This results in medium effective loss factor values. Accelerating the container further leads to an increase in relative motion and an even higher increase of kinetic energy, resulting in a reduction of the effective loss factor. However, at high excitation frequencies $f > 500\,\text{Hz}$ and low excitation intensities $\Gamma < 3$ effective loss factor values up to $\bar{\eta} = 1.6$ are seen. In this regime, the kinetic energy of the particle bed is very low, because the container velocity amplitude V is low, see Eq. (3.9). However, the reason for the high measured effective loss factor values is not conclusively clarified but might occur due to air resistance, cohesive forces or a little varying particle size. This is still under investigation.

The bouncing collect-and-collide and decoupled motion modes, see Fig. 8.2d and Fig. 8.2e, develop from the global-fluidization mode at high acceleration intensities $\Gamma \geq 10$. The decoupled motion mode occurs at medium to high excitation frequencies $f \geq 150\,\text{Hz}$ and is characterized by a small effective loss factor $\bar{\eta} = 0.05 - 0.15$. This is reasonable as the motion of the particle bed is decoupled from the container. Hence, only little energy is transferred to the particle bed, resulting in low energy dissipation.

The bouncing collect-and-collide motion mode appears instead at low excitation frequencies $f < 150\,\text{Hz}$. The effective loss factor range is very large with $\bar{\eta} = 0.1 - 1.0$. This motion mode is intensively discussed in Sect. 6.1.2 and here only shortly repeated. In the bouncing collect-and-collide motion mode, the particle bed forms a packed layer that takes-off the container base, see Fig. 8.2d. This packed particle layer moves synchronously with the driven container. At impact with the container walls, an *inelastic collision* occurs, i. e. the particle bed adopts the container's velocity instantaneously. This happens as multiple inter-particle and particle–wall impacts occur. Although, during every single impact, only a small amount of energy is dissipated, in sum an inelastic collision of the particle bed with the container wall is achieved, see [SanchezEtAl12, BannermanEtAl11] for further details. It is seen in Fig. 8.3 that the contour lines of the effective loss factor for this motion mode agree very well with the lines of constant container strokes, as indicated for $X = 1\,\text{mm}$ by the black dashed line. Thus, the effective loss factor of this motion mode is very sensitive to the container stroke. [BannermanEtAl11] and [SackEtAl13]

derived a formula to calculate the container stroke at maximum effective loss factor, i. e. the *optimal stroke*, of the bouncing collect-and-collide motion mode to

$$X_{\mathrm{opt}} = \frac{h}{\pi}. \tag{8.2}$$

Thereby, h is the clearance of the particle bed to the opposite container wall as indicated in Fig. 8.1. Note that compared to previous chapters 5–6 the index "bou" is dropped here, as no differentiation to other motion modes, e. g. the rolling collect-and-collide motion mode, is necessary. For container strokes higher than the optimal stroke of $X_{\mathrm{opt}} = 1\,\mathrm{mm}$ (above the dashed line in Fig. 8.3), the effective loss factor slowly decreases. However, for container strokes lower than the optimal stroke (below the dashed line in Fig. 8.3), the effective loss factor quickly decreases. This happens due to the transition into a different motion mode. By using the experimentally measured optimal stroke and Eq. (8.2) the clearance h can be extracted from measurements and tuned in a targeted manner for the cylindrical particle container.

The effective loss factor obtained by DEM simulations is shown in Fig. 8.3d. The simulation meets the qualitative characteristics of the energy dissipation well, with some quantitative differences in its magnitude. Especially, the values within the bouncing collect-and-collide motion mode agree well. The transition from local- to global-fluidization, i. e. at $\Gamma \approx 3$, is roughly approximated. For high excitation frequencies $f > 500\,\mathrm{Hz}$ and low excitation intensities $\Gamma < 3$, the effective loss factor is, however, highly underestimated. The reason for this discrepancy is not finally clarified.
This good match between DEM and experiment on a large measurement range is also observed for the cubical particle container, other particle numbers and other particle radii, see [MeyerSeifried19a, MeyerSeifried21c]. However, for the cubical container or bigger particles somewhat higher differences are obtained. Especially the optimal stroke of experiments and DEM differ. Inaccuracies in the container dimensions and the irregular surface of the particle bed might be the reason for this. At this point, it should be pointed out that using a velocity-dependent coefficient of restitution (COR) for the DEM simulations, which is determined in Chap. 4, and the typical value for the friction coefficient of steel $\mu = 0.1$ means that no tuning at all is performed for the conducted DEM simulations. This is remarkable as the excitation range in terms of frequency and acceleration amplitude is over almost two decimal powers. However, besides the quantitative discrepancies the simulations are very useful to give qualitative insights into the complex dynamics inside the particle containers.

The experimentally obtained effective particle mass is shown in Fig. 8.3c. The effective particle mass is high, i. e. $\bar{m}_{\mathrm{bed}} \geq m_{\mathrm{bed}}$, for acceleration intensities $\Gamma \leq 3$ for all excitation frequencies. In this regime, the particle bed has a lot of contact with the container walls. Also, for the bouncing collect-and-collide motion mode, i. e. $X > 1\,\mathrm{mm}$, the effective particle mass is high. Likely, due to the

inelastic collisions of the particle bed with the container walls. By approaching the decoupled motion mode, i. e. at high acceleration intensities $\Gamma \geq 10$ and medium to high excitation frequencies $f \geq 150\,\mathrm{Hz}$, the effective particle mass decreases drastically. This is because the particle bed has only little contact with the container walls. This implies that a high effective loss factor also leads to a strong mass coupling. However, vice versa is not generally true.

8.1.3 Sensitivity Analyses

By the following sensitivity analyses, the influence of different particle and container properties are determined. These analyses are performed with the cubical as well as the cylindrical particle container. For this, experimental and numerical studies are conducted in the following.

Particle Radius and Particle Number

At first, the influence of particle number and particle radius is determined. For this purpose, the cylindrical particle container is analyzed experimentally. Compared to the baseline setting, once a smaller particle radius and once a bigger particle radius are used. The first set is a steel powder of about 0.3 mm radius and a total particle weight of 270 g. The second set are 550 steel spheres of 2.5 mm radius. In both cases, a clearance of $h = \pi\,\mathrm{mm}$ is utilized. The resulting effective loss factors are shown in Fig. 8.4.
It is seen that the effective loss factor of most motion modes is only slightly affected. Especially, the bouncing collect-and-collide motion mode seems to be

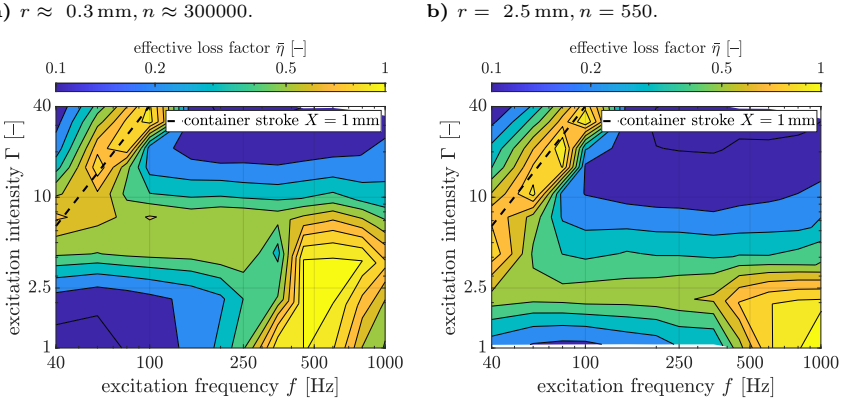

Figure 8.4: Experimentally determined effective loss factor fields for two different steel particle radii in cylindrical particle container with clearance $h = \pi\,\mathrm{mm}$.

unaffected for $\Gamma > 10$. Indeed, for the steel powder, the transition from local- to global-fluidization is shifted to higher excitation intensities, i. e. to $\Gamma \approx 5$, compared to $\Gamma \approx 2$, see green effective loss factor areas in Fig. 8.4. This could be due to an increased number of particle layers and, hence, an increased necessary container acceleration amplitude to fluidize all particle layers.
The biggest differences are seen at high frequencies $f > 250\,\mathrm{Hz}$ and low to medium excitation intensities $\Gamma < 10$. In this area, the particle powder is much more efficient. Hence, an increased number of particle layers seems to be highly favorable for this regime. Similar observations are made in [MeyerSeifried21c] using a larger particle radius of $r = 5\,\mathrm{mm}$ and different particle numbers. Again, the more particle layers are used, the higher the efficiency in this excitation regime. Unfortunately, the DEM does not match well for this excitation area as shown in Fig. 8.3. An explanation of the observed behavior is consequently only hardly possible. As the system is in the global-fluidization motion mode here, an increased number of particle layers could cause more collisions between the particles and hence higher efficiency. Indeed, this requires further investigations in future work.

Container Shape

Within this section, the influence of the container shape is studied experimentally in more detail. The cubical container's effective loss factor is compared to the cylindrical container's effective loss factor in Fig. 8.5. In both cases, steel spheres of 2.5 mm radius are used. The clearance of the cylindrical container is adjusted for the 550 utilized particles to $h = \pi\,\mathrm{mm}$ and hence $X_{\mathrm{opt}} = 1\,\mathrm{mm}$. For the cubical container, the clearance and thus the optimal stroke of the 520 utilized particles are calculated via Eqs. (8.1) and (8.2) to $X_{\mathrm{opt}} = 1.2\,\mathrm{mm}$ with $n_{\mathrm{p}}^{\mathrm{max}} = 573$. This optimal stroke should be sufficiently similar to the cylindrical container's optimal stroke for comparison reasons. However, for the cubical particle container, it is seen in Fig. 8.5a that the optimal stroke slightly differs from the experimentally measured one. This is because Eq. (8.1) is an approximation that does not account for the irregular surface of the particle bed. Also, the determination of $n_{\mathrm{p}}^{\mathrm{max}}$ can be inaccurate.
Otherwise, the effective loss factor has a very similar shape for both particle containers. Furthermore, the same motion modes are observed using DEM simulations, see [MeyerSeifried21c]. Only within the bouncing collect-and-collide motion mode, see Fig. 8.3a, the cuboid container leads to little reduced maximum values. However, this could be attributable to the fact that a different clearance is realized here. Overall, this implies that simple different container shapes seem to be of little importance for the effective loss factor.

a) Cubical container. **b)** Cylindrical container.

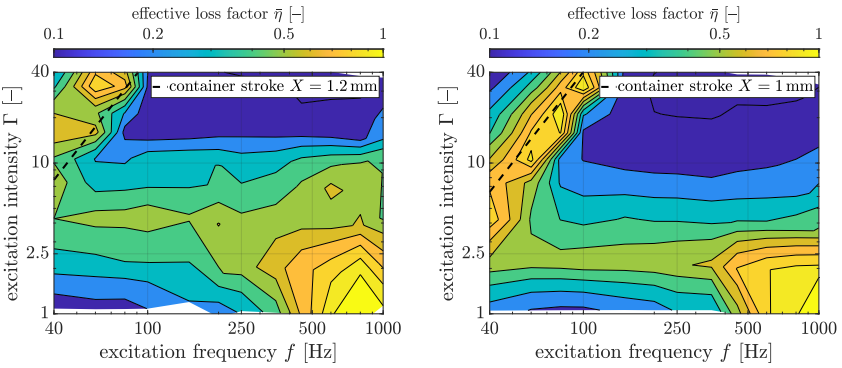

Figure 8.5: Experimentally determined effective loss factor fields for cubical and cylindrical particle container filled with steel spheres of 2.5 mm radius and similar utilized clearance of $h = 1.2\,\pi$ mm and $h = \pi$ mm.

Particle Material

Three different particle materials, namely, steel, tungsten and polypropylene, are tested experimentally to analyze their influence on the effective loss factor. The material parameters are summarized in Tab. 8.2. Tungsten has about twice the density, stiffness and tensile strength of steel. The density and tensile strength of polypropylene is about one decimal power lower than those of steel and its stiffness is about two decimal power lower. This means, that especially polypropylene exhibits a completely different material behavior. For the comparison of the different materials 58 particles of 5 mm radius are used within the cubical particle container. The obtained effective loss factors are shown in Fig. 8.6. The clearance and the optimal stroke for this particle setting are calculated via Eqs. (8.1) and (8.2) to $X_{\mathrm{opt}} = 1.4\,\mathrm{mm}$ with $n_{\mathrm{p}}^{\mathrm{max}} = 65$ as indicated in Fig. 8.6. Again, for the cuboid container shape, the experimental determined optimal stroke is a little bit off its analytical value.
Even though completely different particle materials are used, only small quantitative differences in the effective loss factor can be observed, see Fig. 8.6. Only polypropylene's effective loss factor is slightly different for excitation intensi-

Table 8.2: Material parameters of tested particles.

Material	Steel	Tungsten	Polypropylene
Young's Modulus E [GPa]	208	406	1.45
Density ρ [kg/m^3]	7900	19250	900
Yield Stress σ_{y} [MPa]	230	520	32

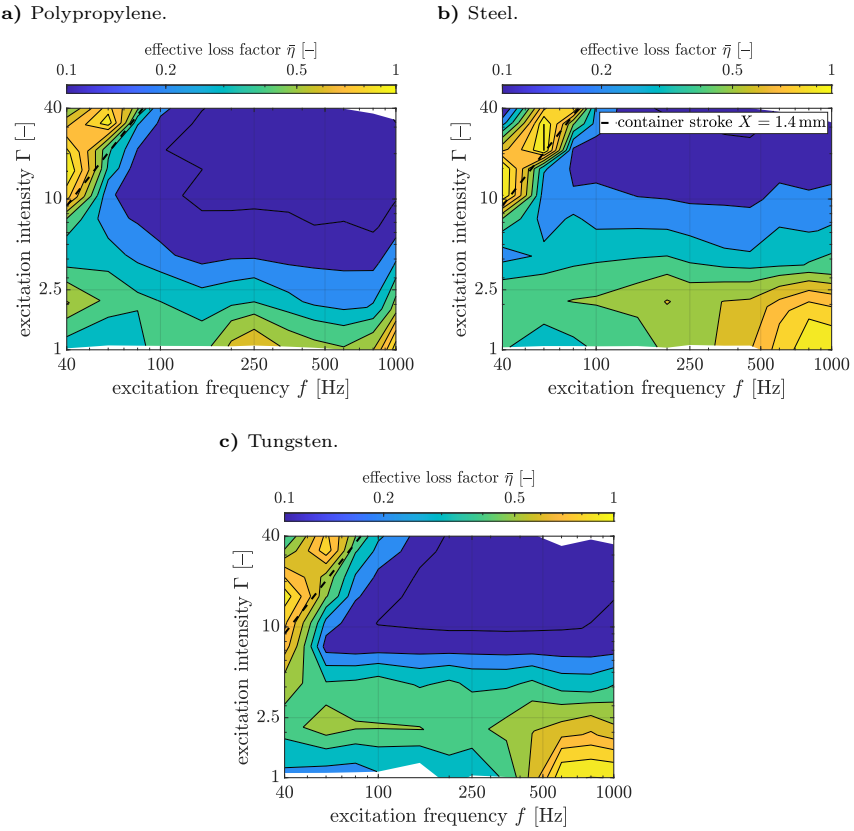

Figure 8.6: Experimentally determined effective loss factor fields of 58 particles of 5 mm radius of different materials in cubical particle container.

ties $\Gamma < 5$. There it shows lower reduced loss factors than the other two materials. However, it should be noted that the total particle weight is extremely low for this material. In conclusion, this means that the effective loss factor is only weakly coupled to the particle material for all observed motion modes, i. e. the dampers efficiency does not depend on the particle weight. It also implies that the energy dissipation of the damper can be tuned by the particle material with only little changes to its efficiency. It should be noted that for smaller particles higher differences might be observed, e. g. at high vibration frequencies. Indeed, this requires further investigations in the future.

Excitation Direction

So far, the excitation occurred perpendicular to gravity. Next, the influence of excitation in the direction of gravity and under zero gravity is analyzed numerically by DEM for the cubical particle container. In Fig. 8.7 the effective loss factor is shown for 58 steel particles of 5 mm radius for these two excitation conditions and compared to a horizontal excitation. The optimal stroke of this setting by Eqs. (8.1) and (8.2) is $X_{\mathrm{opt}} = 1.4\,\mathrm{mm}$.
For both additional settings, i. e. vertical excitation and zero gravity, the optimal stroke of the bouncing collect-and-collide motion mode is shifted to slightly higher values compared to the horizontal excitation, but the effective loss factor is not affected in magnitude. This shift happens as the clearance is increasing. The

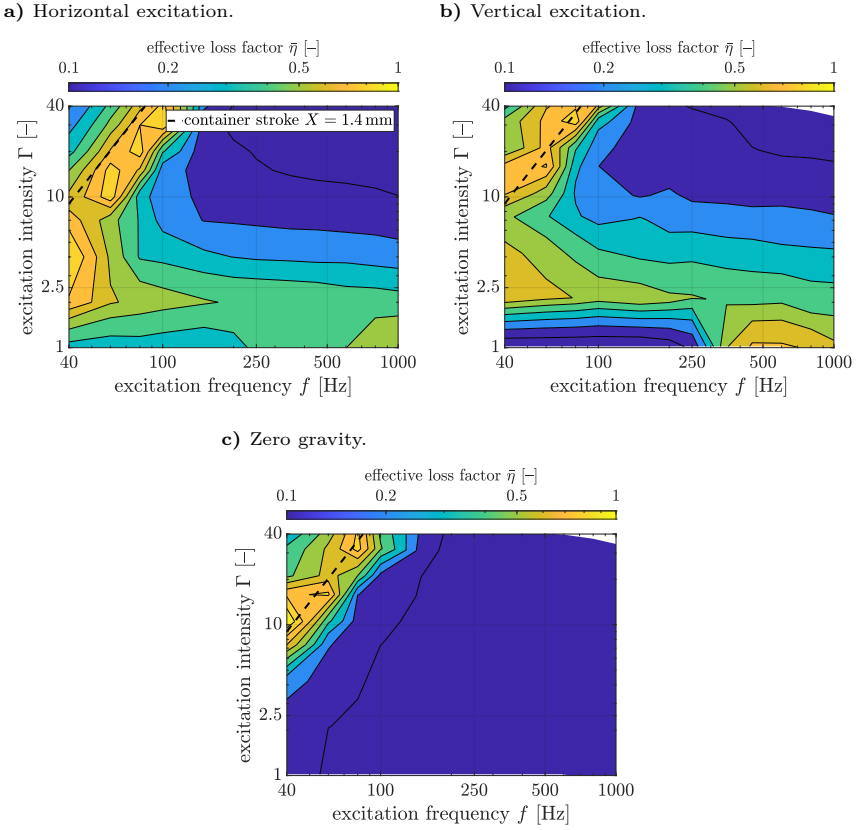

Figure 8.7: Numerically determined effective loss factor fields of 58 steel particles of 5 mm radius in cubical particle container for different excitation directions.

clearance increases because the particles are better distributed along the container wall in the corresponding excitation direction.
For the vertical excitation with $\Gamma = 1$ and $f < 350\,\mathrm{Hz}$ the effective loss factor decreases dramatically. This happens as no relative motion between particles occurs anymore. For zero gravity the fluidization modes at $\Gamma \leq 5$, are not visible at all anymore, as the relative motion between the particle layers is significantly reduced. This results in very low effective loss factors in this area and could also be classified as the decoupled state. Hence, for zero gravity, the particle damper only shows a high efficiency for the optimal stroke of the bouncing collect-and-collide motion mode.

Microscopic Effects

Previously in this section, it was found experimentally that the effective loss factor is only a little affected by the used particle material. Using DEM, the effect of some microscopic contact parameters is investigated next. Partially opposite statements exist about the influence and dominance of certain contact parameters, namely the coefficient of restitution ε and friction coefficient μ, see for instance [WongEtAl09b, LuEtAl11, BannermanEtAl11]. The main reasons are presumably different areas of application and the values of the chosen coefficients. Recently, it was also reported that the magnitude of the coefficients could be of minor importance for the energy dissipation [GagnonEtAl19].
To obtain insights into the influence of the contact coefficients for the here applied excitation conditions, the energy dissipation of 58 steel particles of 5 mm radius is analyzed using DEM simulations within the cubical particle container. The ratio of the energy dissipation of normal contacts to frictional contacts is shown in Fig. 8.8, i. e. $E^{\mathrm{n}}_{\mathrm{diss}}/E^{\mathrm{t}}_{\mathrm{diss}}$ with n and t being the indices for normal and tangential contact. A value above one means a higher dissipation by normal contacts. Vice versa for values below one. Three major regions can be observed. At first, the energy dissipation is dominated by normal contacts. Second, by frictional effects or third is on the same scale. For low acceleration intensities $\Gamma < 4$ or high frequencies $f > 500\,\mathrm{Hz}$ the dissipation is dominated by frictional effects by a factor up to two. This is the area of local- or global-fluidization and a lot of relative motion between the particles occurs. Around the optimal stroke of the bouncing collect-and-collide motion mode, i. e. at $X \approx X_{\mathrm{opt}}$, normal contacts dominate the energy dissipation up to a factor of two. In between both dissipation effects are on a similar scale.

Next, it is analyzed how the effective loss factor and the ratio of normal losses to frictional losses change when the COR and friction coefficient are varied. For this, these two coefficients are changed within the range of $0.5 < \varepsilon < 0.99$ and $0.1 < \mu < 0.5$. In Fig. 8.9 the effective loss factor is shown for four simulated settings. The corresponding ratios of the energy dissipation of normal to frictional losses are shown in Fig. 8.10. The first setting, indicated by a blue color, is the standard setting with $\mu = 0.1$ and a velocity-dependent COR obtained by FEM

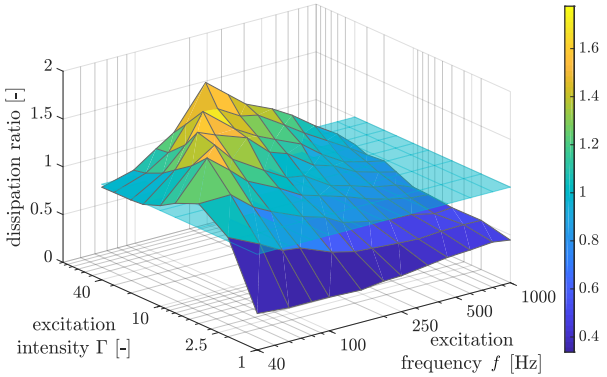

Figure 8.8: Ratio of dissipated energy of normal contacts to frictional contacts for 58 steel particles of 5 mm radius with $\mu = 0.1$ and velocity dependent COR.

simulations in Chap. 4. This velocity-dependent COR is labeled by "FEM".
The second setting is simulated with a COR of $\varepsilon = 0.5$, which is a rather low value already, and $\mu = 0.1$. The optimal stroke of the bouncing collect-and-collide mode shifts to higher strokes at very high excitation intensities $\Gamma > 20$. The energy dissipation is completely dominated by normal impacts, but the effective loss factor is otherwise only little influenced.
The third setting is simulated with a COR of $\varepsilon = 0.99$ and $\mu = 0.1$. It could be expected that the bouncing collect-and-collide motion mode is negatively influenced, as the inelastic collision behavior of the particle bed might vanish, i. e. particles rebound from the impacting container wall. However, this is not the case and only little reduced effective loss factors around the optimal container

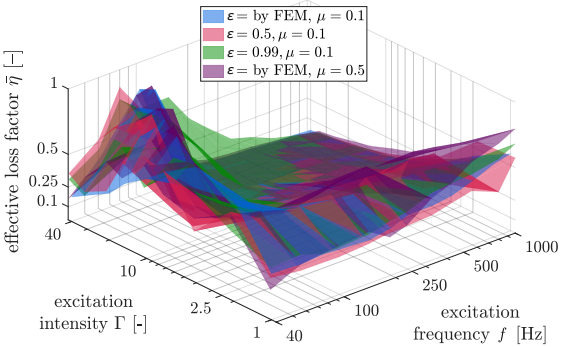

Figure 8.9: Effective loss factor of 58 steel particles of 5 mm radius for different contact parameters by DEM.

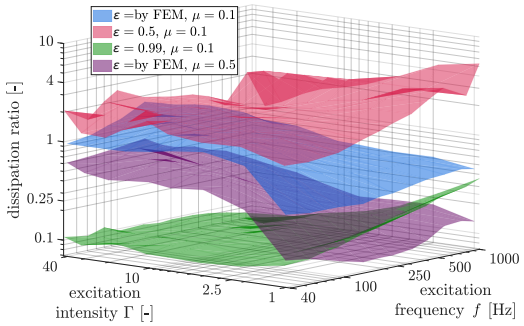

Figure 8.10: Ratio of dissipated energy of normal contacts to frictional contacts of 58 steel particles of 5 mm radius for different contact parameters by DEM.

stroke X_{opt} are obtained. However, much higher effective loss factor values are observed below the optimal stroke, i. e. for $X < X_{\text{opt}}$. Within this area, the particle bed remains in the bouncing collect-and-collide motion mode instead of switching to the global-fluidization mode. Even though the larger excitation range is a useful attribute, the realization of CORs of this high magnitude in real applications might not be possible. All other areas of the effective loss factor are only slightly influenced. The energy dissipation is totally dominated by frictional losses for this setting.
The fourth setting is simulated with a friction coefficient of $\mu = 0.5$ and the velocity-dependent COR. The bouncing collect-and-collide motion mode stays unchanged, but for the local- and global-fluidization motion modes slightly higher effective loss factors are achieved. The energy dissipation is dominated by frictional losses again.

This leads to the conclusion that even if the ratio of impact losses to frictional losses completely changes, due to the chosen contact parameters, the total amount of dissipated energy is rather independent of the contact parameters. The insignificant effect of the contact parameters on the bouncing collect-and-collide motion mode can be explained by the inelastic collision property of the particle bed with the container wall. For example, as the energy dissipation per contact reduces, the number of contacts is increasing and thus leading to a similar energy dissipation, i. e. the inelastic collision behavior stays conserved. The local and global-fluidization modes are characterized by the observed relative motion between particles. Hence, the explanation is presumably similar to the bouncing collect-and-collide motion mode, i. e. less dissipation per contact leads to more particle collisions. Only a very high friction coefficient could have a positive effect on the energy dissipation at high frequencies.
These observations can also explain the partly opposite statements found in the literature. First, the energy dissipation can be dominated by normal impacts

or frictional effects based on the analyzed excitation conditions. Second, the contact parameters have a big influence on the dissipation ratio of normal to frictional dissipation, although the total energy dissipation is only slightly affected. Hence, different contact parameters lead to very similar energy dissipation from a global perspective. From a local perspective, i. e. for a specific motion mode under certain excitation conditions, the difference in energy dissipation might be bigger for different contact parameters. However, these special cases are rather unimportant for the particle damper design.

8.1.4 Robust Damper Design by Fixed Inner Structures

In the previous Sect. 8.1.3 many different particle and container properties are studied and their effect on the effective loss factor are examined. However, none of these properties is appropriate to increase the damper's energy dissipation above a certain amount. Consequently, these damper designs still show a large dependency on excitation conditions, which is not desired.
In the following, three different fixed inner structures are analyzed to reduce the damper's dependency on excitation conditions for the cylindrical particle container. These structures are printed by the stereolithography 3D printer *Form3* by FORMLABS using the *Tough 2000 Resin* and a printing resolution of 100 µm. In order for the structures to withstand the high impact forces applied by the particles, this especially strong and durable resin is chosen. Figure 8.11 shows the three different inner structures analyzed here. The structures are printed with an included base plate for the cylindrical container and are attached to it by four screws. All arms of the structures have a cross-section of 5 mm × 5 mm. The first structure, see Fig. 8.11a, is a single cross positioned in the middle of the cylinder. The second structure, shown in Fig. 8.11b, is a triple cross with three evenly distributed crosses connected to each other. Likewise, the last structure depicted in Fig. 8.11c is a triple star with uniform intervals between the stars.

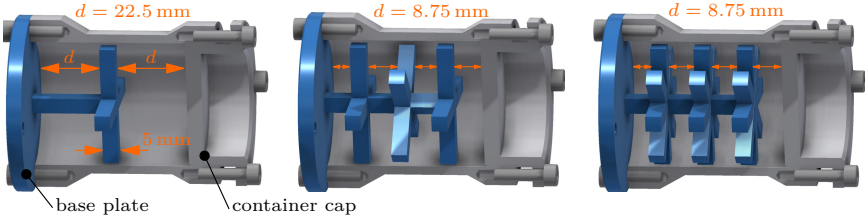

Figure 8.11: CAD sketches of inner structures inside cylindrical particle container.

Experimental Results

The experimental results of the effective loss factor for these three structures filled with steel spheres of 1.25 mm radius and a clearance of $h = \pi$ mm are shown in Fig. 8.12. For the triple star setting the particle mass reduces from 291 g of the baseline setting to 220 g, which results still in a particle number of about 3400 instead of 4500. This is still sufficiently enough for all motion modes to appear. As the effective loss factor is independent of the particle mass, all results are comparable. To further enhance comparability, the result of the baseline setting of Fig. 8.3b, i. e. without inner structure, is displayed as well. A strong influence of the inner structures on the effective loss factor is visible. The use of more structural elements results in a greater impact on the damping characteristics. At

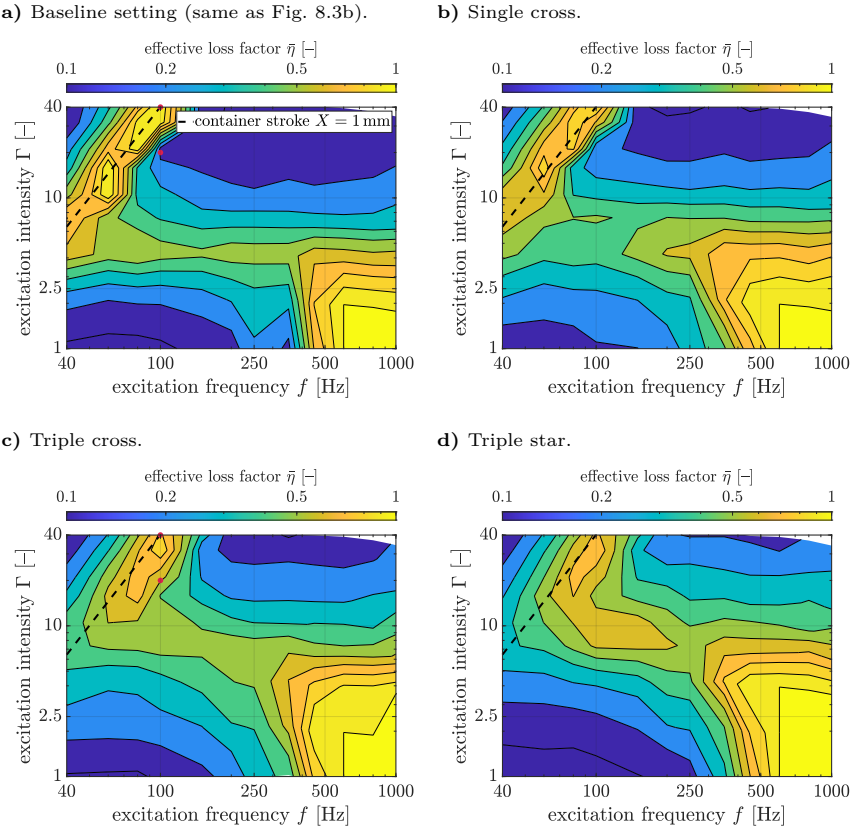

Figure 8.12: Experimental effective loss factor fields of particle dampers with inner structures filled with steel particles of 1.25 mm radius and clearance $h = \pi$ mm.

the optimal stroke of the bouncing collect-and-collide motion mode, the effective loss factor decreases with an increasing number of used inner structures. Starting at $\bar{\eta} = 1.0$ for the baseline setting and reducing to $\bar{\eta} = 0.8$ for the triple star setting. On the other hand, the gradient of the effective loss factor towards lower container strokes as the optimal one, i. e. for $X < X_{\mathrm{opt}}$ (below the dashed line), strongly decreases with more inner structures being used. Thus, the particle damper becomes more robust in this excitation area. Note, this is only true for excitation intensities $\Gamma > 7$. Simultaneously, the effective loss factor increases faster at high excitation frequencies $f >$ 500 Hz the more inner structures are used. Especially at low excitation intensities $\Gamma < 4$, high effective loss factor values up to $\bar{\eta} = 2.0$ are achieved for the triple star structure.

For the next analyses, steel powder of 0.3 mm radius is utilized. In Fig. 8.13 the experimentally obtained effective loss factor is compared for a particle radius of 0.3 mm with and without the triple star inner structure and same clearance $h =$ π mm. It is seen that a smaller particle radius increases the influence of the inner structure, compare to Fig. 8.12d. While in the bouncing collect-and-collide motion mode the maximum effective loss factor further decreases to $\bar{\eta} = 0.6$, at high excitation frequencies a very large efficient area is seen. It ranges from excitation frequencies $f >$ 400 Hz and excitation intensities $\Gamma \leq 10$. From these experiments, the aforementioned observations can be summarized with three simple rules of thumb:

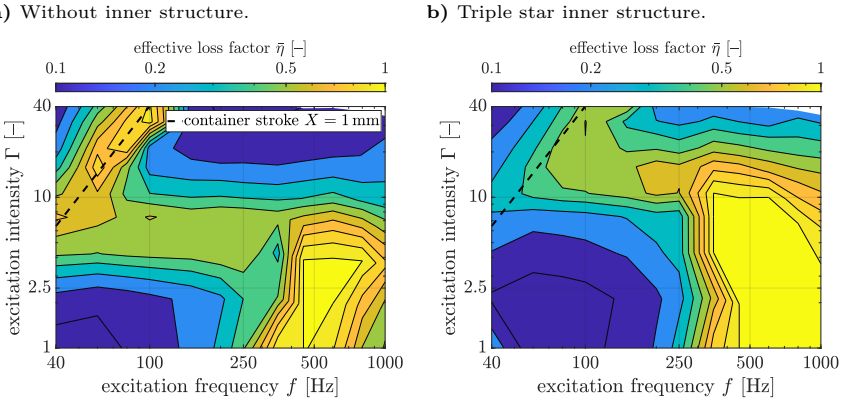

Figure 8.13: Experimental comparison of effective loss factor fields for a steel powder of 0.3 mm radius for container with and without triple star inner structure and clearance $h =$ π mm.

– Inner structures lead to lower effective loss factors within the bouncing collect-and-collide motion mode, but to a more robust (less sensitive) behavior in this excitation area.

– Inner structures lead to higher effective loss factors at high frequencies.

– The more inner structures are used and the smaller the particle radius, the stronger the influence on the effective loss factor, whereby positive and negative effects occur.

Numerical Insights

To obtain more insights into the effect of the inner structures, these are also analyzed numerically by DEM for the triple cross setting and a particle radius of 1.25 mm. The inner structures are modeled by triangular surface meshes exported from CAD, see Sect. 2.2.2. At first, the effect on the bouncing collect-and-collide motion mode is discussed. The velocity fields of the baseline setting and the triple cross setting at an excitation frequency of $f = 100\,\mathrm{Hz}$ and an excitation intensity of $\Gamma = 20$ and $\Gamma = 40$ are examined. These excitation conditions are marked as red points in Fig. 8.12a and Fig. 8.12c, respectively. These points mark the transition from low to high effective loss factor values of the bouncing collect-and-collide motion mode. The corresponding experimental and numerical effective loss factors are summarized in Tab. 8.3.
The effective loss factor values of experiment and simulation fit well for the considered excitation conditions. Only for the triple cross and $\Gamma = 20$, a significant difference can be observed. From the analyses in the previous chapters, it is nevertheless assumed that the numerical model captures the qualitative dynamical behavior of the particles for all settings.

The obtained velocity fields, shown in Fig. 8.14, display the in-plane particle velocity in the direction of excitation and gravity, i. e. the $x-y$ plane, see Fig. 8.1. The analyzed plane has an offset in $z-$direction of 3 mm to reduce the visibility of the inner structure, which can be seen as empty boxes in the velocity fields. Comparing the velocity field of the baseline setting with the triple cross setting at $\Gamma = 40$, see Fig. 8.14b, only small differences are seen. In the baseline setting, the particles are unobstructed in their movement, resulting in a high particle

Table 8.3: Effective loss factor values of red dots marked in Fig. 8.12 for baseline setting and triple cross setting.

Effective Loss Factor $\bar{\eta}\,[-]$				
	Baseline		Triple Cross	
	$\Gamma = 20$	$\Gamma = 40$	$\Gamma = 20$	$\Gamma = 40$
Experiment	0.17	1.0	0.64	0.81
Simulation	0.13	0.98	0.43	0.74

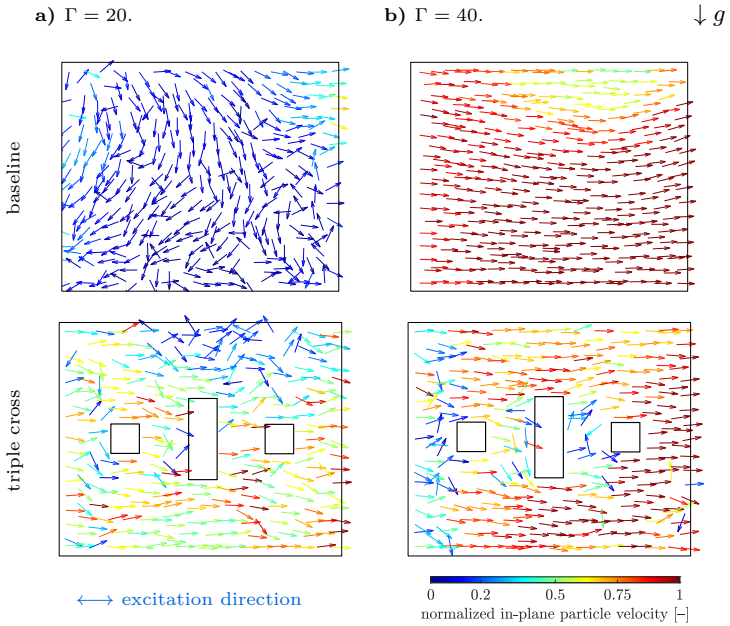

Figure 8.14: Numerical velocity fields of absolute particle velocity at $x_c = X$ of baseline setting and triple cross setting marked as red dots in Fig. 8.12. The colors show the magnitude of the in-plane particle velocity normalized by the container velocity amplitude V from low (*blue*) to high (*red*).

velocity. Whereas for the triple cross setting, the mean particle velocity decreases slightly. Additionally, around the inner structure and on the left side of the particle bed much lower velocities are achieved. This lowers the effective loss factor from $\bar{\eta} = 1.0$ to $\bar{\eta} = 0.81$.

In contrast to that, at $\Gamma = 20$ the baseline setting shows only very little particle movement resulting in a low effective loss factor of $\bar{\eta} = 0.17$, see Fig. 8.14a. This happens because the clearance h is too big and therefore no synchronized movement between the particle bed and the container is achieved, see [SackEtAl13] and Sect. 6.1.2 for further discussion on this topic. By using an inner structure, the classical definition of the clearance during testing vanishes, as some particles get hindered by the structure. This leads to the effect that the bouncing collect-and-collide motion mode stays active even for container strokes of $X < X_{\text{opt}}$. However, the particle velocity is reduced compared to the optimal stroke, which results in a decrease of the effective loss factor from $\bar{\eta} = 0.81$ to $\bar{\eta} = 0.64$. However, this value is still much bigger than the baseline setting with an effective loss factor of $\bar{\eta} = 0.17$.

An accurate numerical analysis at high excitation frequencies $f >$ 500 Hz is

not possible as the utilized numerical model is rather inaccurate in that area as discussed before in Sect. 8.1.2. As the kinetic energy of the particle bed is very low in that area, resulting in only little absolute motion of the particles, this gives cause to conclude that the inner structures might lead to a higher energy transition onto the particles, which can then dissipate. Thus, more inner structures yield higher energy dissipation. However, this assumption needs further investigations to be validated.

8.1.5 Robust Damper Design by Coated Container Walls

Using inner structures within the particle container, it is possible to tune the effective loss factor in a targeted manner, see Sect. 8.1.4. However, at low to medium vibration frequencies $f < 250\,\mathrm{Hz}$ and low to medium vibration intensities $\Gamma < 5$, still low effective loss factor values are obtained, see Fig. 8.12. As seen in Fig. 8.3, the particle bed is in the local-fluidization or global-fluidization mode here. Therefore, especially the lower particles show only little relative motion, which can be seen in Fig. 8.2b. As demonstrated in the last section, even inner structures are not able to increase the relative motion for this excitation range. Hence, a different approach is necessary to increase the efficiency.
The idea is to equip the container walls in the longitudinal direction, i. e. in direction of excitation, with a *coating material*, to achieve a similar motion as in the bouncing collect-and-collide motion mode. Within the bouncing collect-and-collide motion mode, the particles takes-off the container's base and move through the container as one particle block. Now, the particles stay on the container's base and penetrate the coated wall as one particle block, see Fig. 8.15. By completely compressing this material, an inelastic collision with the container wall occurs and the relative velocity between particles and the container wall vanishes. When the container moves in the other direction, this procedure is repeated. This new

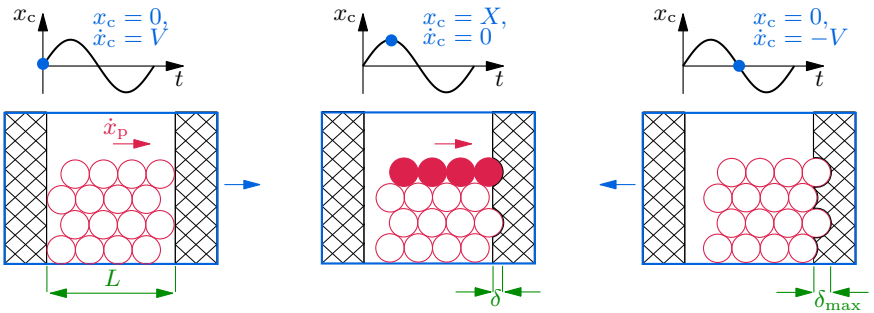

Figure 8.15: Particle movement for the compression collect-and-collide motion mode at high effective loss factor values. • one particle chain.

particle motion is referred to as *compression collect-and-collide*.
Various measurements have shown that a high effective loss factor is achieved at low excitation intensities utilizing a wall thicknesses of 3 mm. This behavior is shown by example in Fig. 8.16 for experimental measurements of steel particles of 1.25 mm radius, coated wall Young's moduli of both 1.4 MPa and 55 MPa, and a clearance of $h = \pi$ mm. The coated wall materials are the previously in Chap. 4 analyzed T2 and SAA. See Sect. 4.3.2 for further information on these polymers. Compare Fig. 8.16 also to the baseline setting of Fig. 8.3. For the weaker wall Young's modulus of 1.4 MPa, high effective loss factor values are obtained around an excitation frequency of $f = 100$ Hz and $\Gamma \leq 2.5$ with a decrease in excitation frequency towards higher excitation intensities. For the stronger wall Young's modulus of 55 MPa, additional high effective loss factor values around an excitation frequency of $f = 500$ Hz and $\Gamma \leq 2.5$ are seen. Hence, the frequency at high effective loss factors and low excitation intensities $\Gamma \leq 2.5$ is strongly dependent on the coating wall material.

a) Wall Young's modulus of 1.4 MPa. **b)** Wall Young's modulus of 55 MPa.

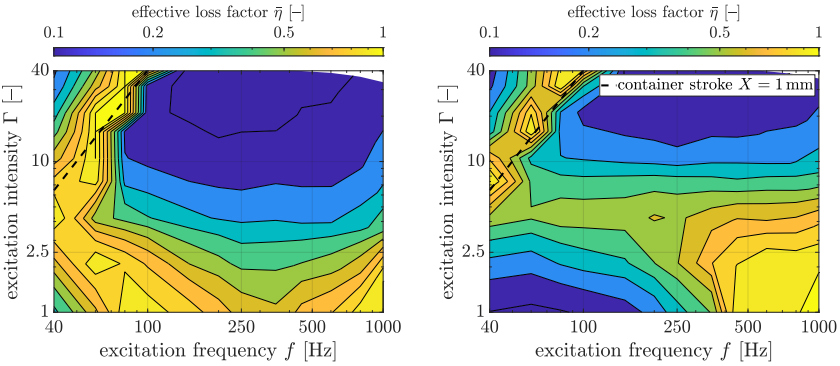

Figure 8.16: Experimental effective loss factor fields for coated wall systems with different wall Young's moduli, steel particles of 1.25 mm radius and clearance $h = \pi$ mm.

Analytical Design Formula

The following objective is to find a systematic analytical formula to efficiently design the coating container wall material. The focus lies on the excitation region which showed the most effects in the experiments when coating the container walls, i. e. for excitation intensities of $\Gamma \leq 2.5$. By Fig. 8.16 it is found that the compression collect-and-collide motion mode depends on the material stiffness and thus on the compression depth of the coated material. Hence, a semi-empirical formula based on Hertz impact theory [Hertz82] shall be derived to design the coating wall material. Hertz's theory assumes that both contact partners, i. e. particle and (coated) wall, are touching at a single point and all elastic deformation is limited to this contact point. From Hertz's theory the maximum penetration depth $\delta_{\max}$, as indicated in Fig. 8.15, follows to

$$\delta_{\max} = \left(\frac{5\,\bar{M}\,\dot{\delta}_0^2}{4\,k_\mathrm{n}} \right)^{2/5}, \tag{8.3}$$

with $\dot{\delta}_0$ being the initial collision velocity in normal direction. See [Barber18] for a detailed description. For reasons of simplification it is assumed that the initial collision velocity is $\dot{\delta}_0 = V$, i. e. the relative velocity at the impact point corresponds to the maximum container velocity. The contact stiffness k_n can be expressed as

$$k_\mathrm{n} = \frac{4}{3}\,\bar{E}\sqrt{\bar{R}}. \tag{8.4}$$

The effective Young's modulus $\bar{E}$ is given by

$$\frac{1}{\bar{E}} = \frac{1-\nu_\mathrm{p}^2}{E_\mathrm{p}} + \frac{1-\nu_\mathrm{w}^2}{E_\mathrm{w}}, \tag{8.5}$$

with Young's modulus $E_{\mathrm{p/w}}$ and Poison's ratio $\nu_{\mathrm{p/w}}$ of particle and wall, respectively. The effective radius $\bar{R}$ is obtained by

$$\frac{1}{\bar{R}} = \frac{1}{r_\mathrm{p}} + \frac{1}{r_\mathrm{w}}, \tag{8.6}$$

with radius $r_{\mathrm{p/w}}$ of a particle and wall. As the wall radius is infinite it follows $\bar{R} = r_\mathrm{p}$. The effective mass $\bar{M}$ is given by

$$\frac{1}{\bar{M}} = \frac{1}{m_\mathrm{p}} + \frac{1}{m_\mathrm{w}}, \tag{8.7}$$

with mass $m_{\mathrm{p/w}}$ of a particle and wall, respectively. As the container wall is driven by the shaker, its mass can be assumed to be infinitely large. Additionally, instead of a single particle a whole particle chain "impacts" the coated wall, see solid particle line in Fig. 8.15. Hence, the particle mass is adjusted by the number of particles in one line $n_\mathrm{p}^\mathrm{line}$. Thus, $\bar{M} = n_\mathrm{p}^\mathrm{line}\,m_\mathrm{p}$ is obtained.

Within the bouncing collect-and-collide motion mode there can be derived a direct correlation between optimal container stroke X_{opt} and clearance h, i. e. $X_{\mathrm{opt}} = h/\pi$, see Eq. (8.2). A similar correlation is found empirically for the compression collect-and-collide motion mode. Indeed, here the clearance h is represented by the maximum compression of the coating wall material δ_{max}, see also Fig. 8.15. Empirically from the experiments, the correlation

$$X = \delta_{\mathrm{max}}. \tag{8.8}$$

is found at the high effective loss factor values. This formula matches with the high effective loss factors in Fig. 8.16 for the compression collect-and-collide motion mode. Hence, Eq. (8.8) can be solved conjointly with Eq. (8.3) in order to obtain the necessary effective Young's modulus to

$$\bar{E} = \frac{15\,\bar{M}\,V^2}{16\,\sqrt{\bar{R}}\,X^{5/2}}. \tag{8.9}$$

By inserting $X = A\,\Omega^2$ for the container amplitude and $V = A\,\Omega$ for the container velocity amplitude, the equation for the effective Young's modulus follows to

$$\bar{E} = \frac{15\,\bar{M}\,\Omega^3}{16\,\sqrt{A\,\bar{R}}}. \tag{8.10}$$

Lastly, from the experiments presented in Fig. 8.16 a high efficiency of the compression collect-and-collide is observed at an excitation intensity $\Gamma = 1$ which implies a container acceleration amplitude of $A = g$. This finally results in

$$\bar{E} = \frac{15\,n_{\mathrm{p}}^{\mathrm{line}}\,m_{\mathrm{p}}\,\Omega_{\mathrm{d}}^3}{16\,\sqrt{g\,r_{\mathrm{p}}}}, \tag{8.11}$$

with $\Omega_{\mathrm{d}} = 2\,\pi\,f_{\mathrm{d}}$ being the desired vibration frequency of high effective loss factor values at $\Gamma = 1$. From the effective Young's modulus by Eq. (8.11), the coating wall Young's modulus by Eq. (8.5) can be solved. Within the experiments, it turns out that Young's moduli values in the range of polymers are obtained. For such low Young's moduli values the impact theory of Hertz is losing accuracy, as large deformations in the contact zone occur and thus the assumption of contact at a single point is not fulfilled anymore. Additionally, polymers generally behave in a visco-elastic manner instead of purely elastic. Therefore, Eq. (8.11) can only be seen as a rough estimation for the necessary Young's modulus of the coating wall material. This is likewise true as Eq. (8.11) is based on Eq. (8.8), which is based on empirical experimental observations.
Even though the necessary Young's modulus of the coated wall can be obtained now, the particle damper can not be considered as robust, see Fig. 8.16. This is because the high effective loss factor values of the compression collect-and-collide and bouncing collect-and-collide motion modes do not occur at the same vibration frequency. The goal is to adjust the effective loss factor of the bouncing

collect-and-collide motion mode in such a manner that it fits the desired vibration frequency f_d of the compression collect-and-collide motion mode. Measurements have shown that a good match is achieved if the clearance of the bouncing collect-and-collide motion mode is adjusted to match an excitation intensity at $\Gamma = 15$ at the desired excitation frequency Ω_d. Hence, the clearance follows from Eq. (8.2) to

$$h = \pi\, X_\mathrm{opt} = \pi\, \frac{A_\mathrm{opt}}{\Omega_\mathrm{d}^2} = \pi\, \frac{15\, g}{\Omega_\mathrm{d}^2}. \tag{8.12}$$

Validation

To validate experimentally the presented semi-empirical design approach, it is applied to design a particle damper utilizing steel spheres of 1.25 mm radius for excitation frequencies of $f_\mathrm{d} =$ 50 Hz, 60 Hz and 80 Hz, respectively. The calculated and used parameters for these experimental tests are summarized in Tab. 8.4 and the results are shown in Fig. 8.17. All utilized polymers are cold vulcanizing silicone rubber manufactured by Zhermack SpA (Badia Polesine, Italy) distributed through Troll Factory Rainer Habekost e.K. (Riede, Germany).

For each configuration, a very robust behavior of the effective loss factor concerning the excitation intensity at the desired excitation frequency is achieved. This range of excitation intensities almost extends over the whole measurement range of $\Gamma = 1 - 40$. For excitation frequencies below and above the desired frequency, a medium reduction in the effective loss factor is seen. However, at medium to high excitation frequencies $f >$ 200 Hz, no improvement in comparison to the baseline setting is achieved. First measurements at even higher excitation frequencies $f >$ 1000 Hz indicate very high effective loss factors in this regime. This tendency can already be seen in Fig. 8.17 but needs further investigations in future work.

Table 8.4: Settings of coated wall experiments.

Design Frequency f [Hz]	50	60	80
Clearance h [mm]	4.7	3.3	1.9
Optimal Stroke X_opt [mm]	1.5	1.1	0.6
E_w [MPa] (by Eq. (8.11))	0.25	0.44	1.0
E_w [MPa] (used)	0.27	0.72	1.4
Material	TFC Type 13	TFC Type 1	TFC Type 2

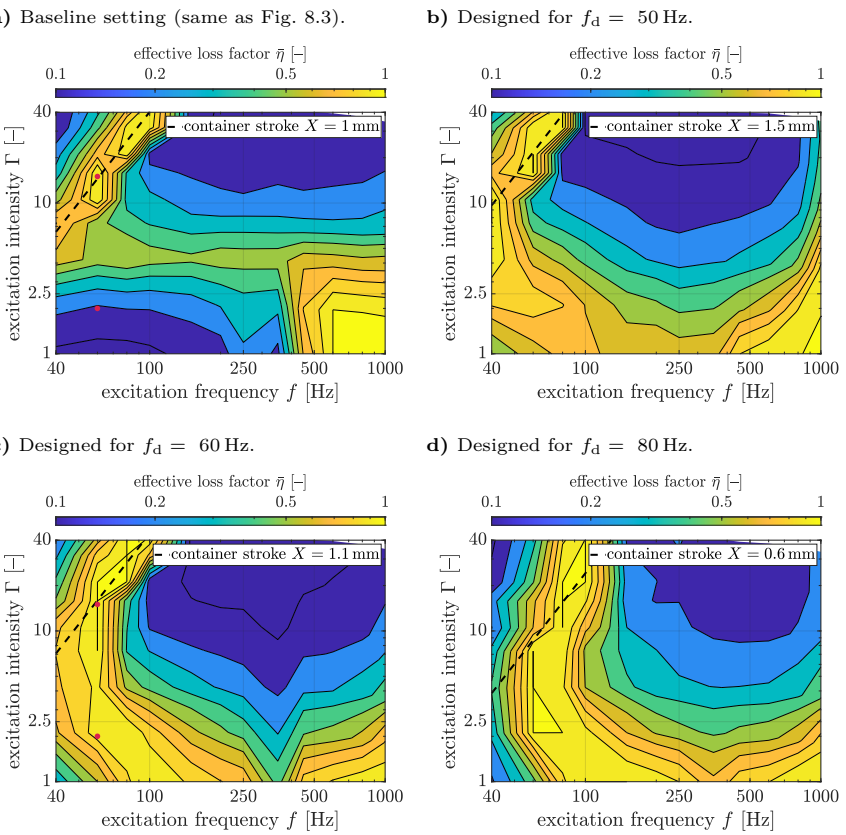

Figure 8.17: Experimentally obtained effective loss factor fields for particle dampers with coated walls designed for steel particles of 1.25 mm radius and different excitation frequencies. The design parameters are summarized in Tab. 8.4.

Numerical Insights

To obtain deeper insights into the particle motion using coated walls, numerical studies using DEM are performed for the setting shown in Fig. 8.17c, i. e. designed for $f = 60$ Hz, and are compared to the baseline setting. Hereby, the bouncing collect-and-collide and compression collect-and-collide motion modes for an excitation frequency of $f = 60$ Hz and excitation intensities of $\Gamma = 2$ and $\Gamma = 15$ are studied, see also red marks in Fig. 8.17. The effective loss factors obtained from simulations and experiments are summarized in Tab. 8.5. Experimental and numerical values are in the same range, showing the qualitative agreement. However, quantitatively there is some mismatch for low excitation

Table 8.5: Effective loss factor values of red dots shown in Fig. 8.17.

Effective Loss Factor $\bar{\eta}\,[-]$				
	Baseline		Coated Wall ($f_\mathrm{d} = 60\,\mathrm{Hz}$)	
	$\Gamma = 2$	$\Gamma = 15$	$\Gamma = 2$	$\Gamma = 15$
Experiment	0.20	1.0	0.97	1.4
Simulation	0.41	0.96	0.64	1.1

intensities. Despite this, it can be assumed that the overall dynamical behavior of the particles is reproduced by simulation. The corresponding velocity fields extracted from simulations are displayed in Fig. 8.18.
The baseline setting is in the local-fluidization mode for $\Gamma = 2$. While the upper particles move at a high velocity, particles in the middle and at the bottom are comparably slow. This results in a low effective loss factor of $\bar{\eta} = 0.2$. In the coated wall system, the upper particles also show high velocities. However, the middle and bottom particles move as one particle block with an even higher velocity. This particle system does not take-off the container's base. Though, as

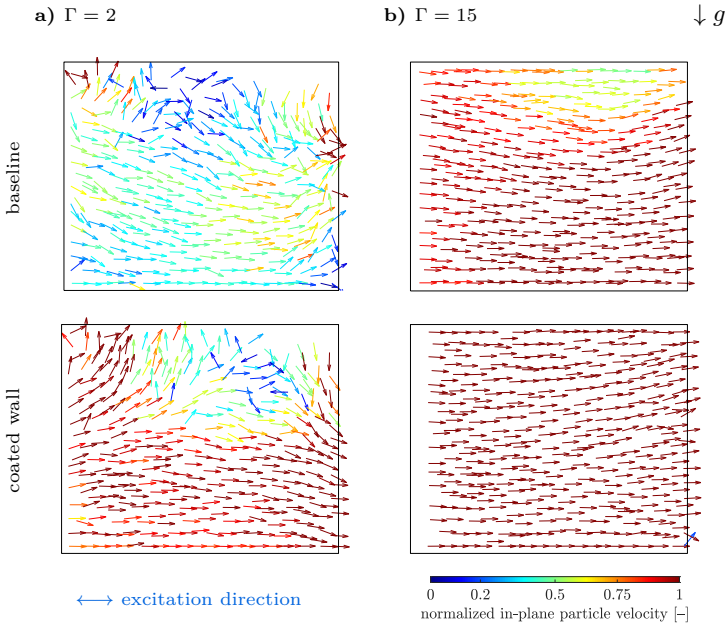

Figure 8.18: Velocity fields of absolute particle velocity of baseline setting and coated wall setting at $x_\mathrm{c} = X$ of red dots in Fig. 8.17. The colors show the magnitude of the in-plane particle velocity normalized by the container velocity amplitude V from low (*blue*) to high (*red*).

the container's wall gets compressed, a relative motion between the container and particle bed is possible. Hence, a high effective loss factor of $\bar{\eta} = 0.97$ is achieved in the experiment. At $\Gamma = 15$ the bouncing collect-and-collide motion mode is observed for both settings, i. e. baseline setting and coated wall setting. Here, the particles take-off the container's base and move with a high velocity as one particle block. In both cases, this results in high effective loss factors. Interestingly, the coated wall system reaches even higher particle velocities than the baseline setting. Consequently, its experimental and numerical obtained effective loss factor value are higher than the ones obtained without coating, i. e. $\bar{\eta} = 1.4$ to $\bar{\eta} = 1.0$ and $\bar{\eta} = 1.1$ to $\bar{\eta} = 0.96$ for $\Gamma = 15$. This means that the bouncing collect-and-collide motion mode is more efficient for the coated wall setting than for the baseline setting.

8.1.6 Summary

To analyze particle dampers at high-intensity vibrations on the **Single Damper Level**, a controlled shaker setup is realized and the results are compared to numerical DEM simulations. Multiple different motion modes of the particle bed are observed within experiments and simulations for classical particle systems. Especially the bouncing collect-and-collide motion mode and the global-fluidization at high excitation frequencies lead to high effective loss factor values.
While the bouncing collect-and-collide motion mode can be adjusted by the clearance in a targeted manner, for the global-fluidization motion mode a high filling ratio of the particle container and a small particle size are advantageous. However, the global-fluidization motion mode is not observed if a sufficient number of particle layers do not exist or in the absence of gravity. As the bouncing collect-and-collide motion mode depends mainly on the clearance between the particle bed and the opposite container wall, it depends also on the filling ratio and the container size. The clearance controls at which container stroke the maximum effective loss factor occurs. Particle properties, container properties and contact parameters are of minor importance for the efficiency of this motion mode. However, with a smaller particle radius the estimation of the optimal container stroke gets more accurate. With the particle material, number and radius, the amount of dissipated energy can be adjusted in a targeted manner.
This concludes that the efficiency of classical particle dampers is sensitive to the excitation frequency and excitation amplitude. Thus, during the design process of these dampers, the excitation conditions have to be known quite accurately, which is rarely feasible for real industrial applications.

To obtain a robust particle damper, two different design approaches are further discussed. The first design approach uses inner structures inside the particle container. The inner structures are manufactured using a stereolithography 3D printer and consist of different numbers of beams placed perpendicularly to the

container motion. These inner structures yield lower effective loss factors of the bouncing collect-and-collide motion mode, but also a more robust behavior. At high excitation frequencies, higher effective loss factors are achieved. These effects can even be increased by using more inner structures or a smaller particle radius. It is concluded that inner structures are especially suitable when damping on a large excitation range or at high vibration frequencies is necessary.
The second design approach uses coated container walls to increase the damping performance. A new motion mode, called compression collect-and-collide, is observed within this setting. In traditional particle dampers at low excitation frequencies and low excitation intensities, only little relative motion between the particle bed and container is seen. In the coated wall container instead, the wall material gets compressed, resulting in a high relative motion and thus energy dissipation. An analytical formula based on Hertz's contact theory is derived to design the wall material. Its accuracy is proven experimentally. By adjusting the bouncing collect-and-collide motion mode to fit the compression collect-and-collide motion mode, a very robust damper at low excitation frequencies is achieved. Additionally, the efficiency of the bouncing collect-and-collide motion mode is increased. However, the damper's efficiency at medium and high excitation frequencies is not affected.

8.2 Structural Integrated Damper

In this section, the damping behavior of a beam-like structure with free–free boundary conditions under forced vibrations is studied. The coupling results of a reduced model of the beam to the particle damper **models 1–2**, i. e. DEM model and effective fields, are discussed and compared to measurements. However, analytical formulas describing the damper's energy dissipation are not utilized for this vibration regime. This is due to the fact that it is not possible to describe the energy dissipation within the damper accurately on a large excitation range, see also the **Single Damper Level** in Sect. 8.1.
At first, the experimental testbed and numerical models are presented in Sect. 8.2.1. Then, in Sect. 8.2.2 the simulation coupling results from the DEM–structural coupling are presented. In the following Sect. 8.2.3, the experimentally obtained effective fields are used for damping prediction of the structure. Finally, in Sect. 8.2.4, a summary is given. The following results have partly been published in [MeyerSeifried20, MeyerSeifried21a].

8.2.1 Experimental and Numerical Setups

Experimental Setup A picture and a schematic representation of the utilized beam-like structure are shown in Fig. 8.19. The testbed consists of a flexible aluminum beam with a hollow profile supported by three soft cables, thus free–free boundary conditions can be assumed. For testing, two different beams have been utilized. The beam parameters are listed in Tab. 8.6. The total weights of the 1.8 m long beams and their mountings are 3.6 kg and 6.6 kg, respectively. The first beam has a symmetric profile and was only used for some preliminary analyses. The second beam has a rectangular profile, i. e. twice the height of the first beam, and is used in general.
The particle container can be placed at any desired position on the beam. For the investigated analyses, the container is mostly placed at the free, not excited end at $y_{\mathrm{pd}} = 1.765\,\mathrm{m}$, as shown in Fig. 8.19. The beam is exited in the transverse direction with a variable force by a shaker at its free end at $y = 40\,\mathrm{mm}$. A sine sweep excitation is used with logarithmic frequency change and frequencies between 15 Hz and 600 Hz in 300 s. Thus, for this slow frequency change, a

Table 8.6: Parameters of flexible beams utilized for testbed in Fig. 8.19.

No.	Cross-sectional Area [mm^2]	Young's Modulus [GPa]	Density [$\mathrm{kg/m}^3$]	Poisson's Ratio [–]	Second Moment of Area [mm^4]
1	1138	68	2700	0.34	166 000
2	646	68	2700	0.34	90 000

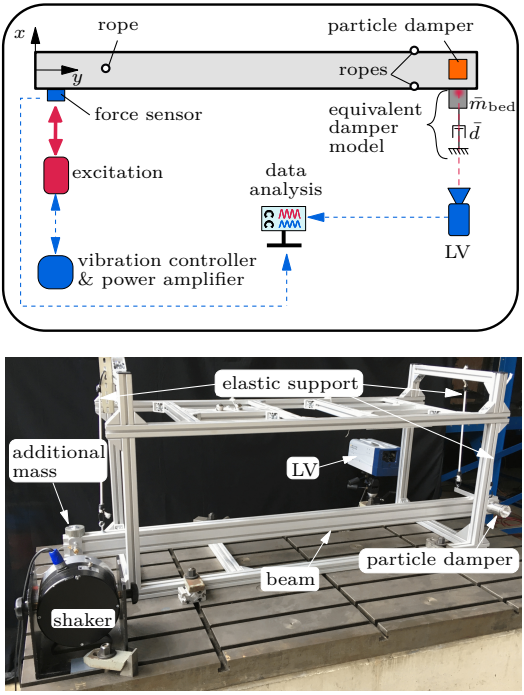

Figure 8.19: Testbed to determine the overall damping behavior of particle dampers coupled to a beam-like structure for high vibration intensities with schematic representation (*top*) and picture (*bottom*).

stationary state of the system can be assumed for every instant of time. The measurement is windowed using a *hanning window*. The windows are combined using a *peak hold algorithm*. The sampling frequency is 12.8 kHz. The shaker and its power amplifier are from Brüel & Kjaer, namely the Modal Exciter *Type 4824* and Power Amplifier *Type 2719*. As only the input current to the shaker is controlled and not the input force, 1 kg of additional weight is placed at the excitation position. This reduces the values of the shape functions at the excitation point and thus the force distortion. The excitation force is measured by the force transducer *8230-001* by Brüel & Kjaer and the velocity profile of the beam is measured by the laser vibrometer *PSV-500* from Polytec and analyzed with the software *BK Connect*.

Numerical Setup For an efficient and accurate description of the beam-like structure, it is discretized with the *finite element method* (FEM), schematically illustrated in Fig. 8.20. The beam is discretized with 90 Timoshenko beam

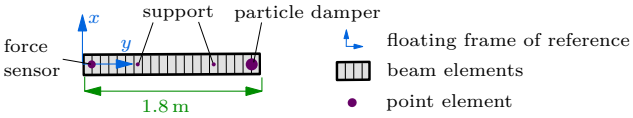

Figure 8.20: FEM model of the beam-like structure with free–free boundary condition.

elements. The screws of the support, the force sensor and its mounting, and the particle container are included as point masses. A free-free support is chosen as the boundary condition. Solving Eq. (3.20) the eigenfrequencies and shape functions of the reduced model are obtained, see Eq. (3.21). The first two eigenmodes are the translational and rotational rigid body modes. The first four flexible shape functions $\Phi^{(k)}$, see Eq. (3.21), are shown in Fig. 8.21 for the second beam and are analyzed within this section. It should be noted that the eigenfrequencies and shape functions of both utilized beams are very similar. This is because the differences in cross-sectional area and second moment of area cancel each other out. Especially, at the initial particle damper position of $y_{\mathrm{pd}} = 1.765\,\mathrm{m}$, high shape function amplitudes are achieved. This is important, as the resulting higher container acceleration normally also leads to a higher energy dissipation of the particle damper. At the shaker excitation position of $y = 40\,\mathrm{mm}$, comparable low shape function amplitudes are observed. This reduces the force distortion within the experiments, as mentioned before.
The very small material damping of the structure is modeled with Rayleigh damping [Strutt77]. The necessary parameters are obtained from measurements. A least-squared-error algorithm [SchwarzRichardson13] is used to obtain a good

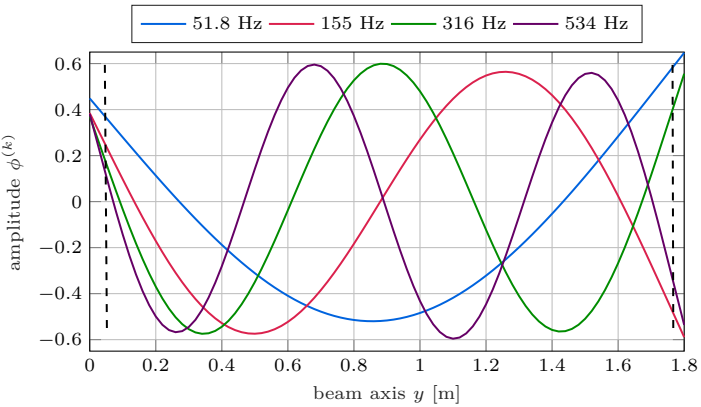

Figure 8.21: Mode shapes of beam-like structure for the second beam. The black dashed lines indicate the position of the shaker (*left*) and the initial particle damper position (*right*).

approximation for the utilized parameters over all considered eigenfrequencies.

Validation At first, the numerical model of both utilized beams is validated, i. e. Eq. (3.21). The numerically obtained eigenfrequencies of the system with an empty particle damper and the corresponding *frequency response function* (FRF), see Eq. (3.42), are compared to measurements for the second beam. The system's response used for FRF calculation is measured at the particle container position, i. e. at $y_{\mathrm{pd}} = 1.765\,\mathrm{m}$. As the velocity of the beam at this position is measured, the FRF's mobility is plotted. For the excited frequency range four eigenmodes are determined between 51.7 Hz and 513 Hz. The results are shown in Tab. 8.7 and Fig. 8.22.
The numerical and measured eigenfrequencies fit very well. The biggest difference occurs for the fourth mode, i. e. at 513 Hz, with a difference of 4.1 %. A good agreement is also observed within the FRF. All modes are well recognizable and only slightly damped, thus the additional damping by the particle damper will be observed easily.

Table 8.7: Eigenfrequencies of undamped beam-like structure for the second beam.

Eigenfrequencies f_k				
	Eigenmode			
	1	2	3	4
Experiment [Hz]	51.7	153	309	513
Numeric [Hz]	51.8	155	316	534
Difference [%]	0.2	1.3	2.2	4.1

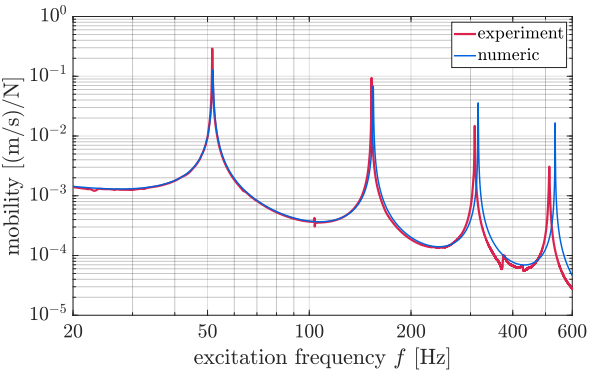

Figure 8.22: Experimental and numerical frequency response function of undamped beam-like structure for the second beam.

8.2.2 Damping Prediction by DEM–Structure Coupling

For the damping prediction by DEM, two different approaches are utilized in the following, i. e. the *time domain* approach and the *frequency domain* approach. Both approaches are discussed in detail in Sect. 3.3.2. In both cases, the damper's DEM model is coupled to a modal reduced model of the structure. Within the time domain approach, it is simulated over a small area around the eigenfrequencies of the structure. The resulting time domain results are analyzed using the analytical solution of Eq. (3.32). The damping ratio is extracted by Eq. (3.47) and the maximum amplitude of the beam. Within the frequency domain approach, the structure's FRF is calculated by simulation. Here, a sine sweep excitation over all considered eigenfrequencies is utilized. The frequency range is divided up into multiple overlapping segments and calculated simultaneously. The modal parameters are extracted from the combined FRFs.

However, it turned out that both simulation approaches are very time consuming. Consequently, they have only been used at an early stage for verification purposes. At this, the first beam is utilized. For these preliminary experiments, the cubical particle container is used and filled with 40 steel spheres of 5 mm radius and placed in the middle of the beam. The total weight of the particles is 166 g, which is about 5 % of the structure's mass.
In Fig. 8.23, the damping ratios for the experiment of the undamped, i. e. without particles, and damped system excited by a force amplitude of 4 N are shown. Also, the damping ratios of the simulation calculated from time domain and frequency domain are displayed. A high increase of the damping for odd modes, i. e. mode 1 and 3, is achieved when particles are added. For the first mode, the damping

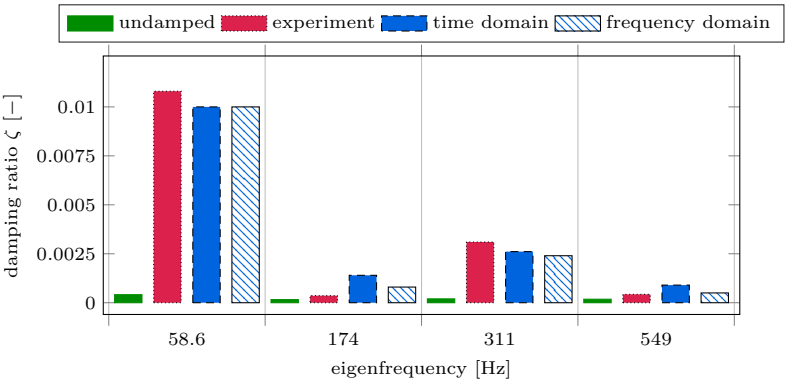

Figure 8.23: Damping ratios of modes 1 – 4 of beam-like structure with cubical particle container filled with 40 steel spheres of 5 mm radius placed in the beam's middle.

increases from $\zeta = 0.0004$ to $\zeta = 0.011$. Only a slight increase in the damping is recognizable in the even modes, i. e. mode 2 and 4. This behavior can be explained by the position of the particle container. At the position in the middle of the beam, the odd modes exhibit extrema, as seen in Fig. 8.21, resulting in a high translational movement of the particle damper. The even modes, in turn, exhibit a root at this position and thus resulting only in a rotational movement of the particle container. By this rotational movement, only little momentum is transferred to the particles causing small energy dissipation.
For the odd modes, i. e. 1 and 3, the damping ratios of both computational methods, i. e. time domain and frequency domain approach, agree well with the experiment. However, some differences occur for the even modes. This is due to the fact that damping is very small here. Computationally, the calculation of the damping ratio is much more efficient from the time domain approach compared to the frequency domain approach. For the time domain approach, four simulations with a simulation time between 2 s–7 s for the different modes are necessary. For the calculation of the frequency domain results, 33 simulations of 12 s are needed. In turn of computation time, the time domain approach can be performed in the range of hours, while the frequency domain approach, i. e. the complete FRF, is in the range of days.

By using Eq. (3.51) the efficiency of the particle damper can be evaluated. Eq. (3.51) correlates the mass of the particle bed and the particle damper's effective loss factor, i. e. its efficiency, to the damping ratio ζ of the structure. If the particle damper exhibits an effective loss factor of $\bar{\eta} = 1$, the resulting damping ratio of the structure would be $\zeta = 0.026$ for the first mode. For this value, the damper can be considered efficient. However, this value is way above the determined damping ratio of the first mode with an experimental determined value of $\zeta = 0.011$. Hence, the efficiency of this mode is low. For all other modes, the efficiency is even less. This behavior is due to two facts. First, the particle damper's filling ratio and clearance, respectively, are not well designed in these experiments and simulations. Second, the big particles used here are not suited to damp vibrations of higher frequencies. See Sect. 8.1 for a detailed discussion. Hence, much smaller particles need to be utilized. For these smaller particles much higher particle numbers are necessary to obtain the same particle weight. As the simulation time increases at least linearly with the particle number, the coupling of the DEM model would be very time-consuming or even impossible. Consequently, the utilization of the experimentally obtained effective fields to obtain the beam's damping ratio is a much more promising approach for such particle systems. This is presented in the next section.

8.2.3 Damping Prediction by Effective Fields–Structure Coupling

To show the accuracy and efficiency of the coupling by the effective fields, 350 g of steel powder of 0.3 mm radius is utilized within the cylindrical particle container. Now, the second beam is used. Thus, the particle mass is again about 5 % of the total system's mass. For this particle setting a clearance of $h = 1\,\text{mm}$ is adjusted. Hence, an optimal stroke of $X_{\text{opt}} = 0.32\,\text{mm}$ is achieved, see Eq. (8.2). The corresponding experimentally obtained effective fields of the **Single Damper Level** are shown in Fig. 8.24. Such fields are intensively discussed in Sect. 8.1 and only shortly recapped here.

Within the effective loss factor, two regions can be observed showing high values $\bar{\eta} \geq 1$. The first region is at excitation frequencies between 100 Hz and 200 Hz and high acceleration intensities $\Gamma > 10$. In this regime, the particle motion is classified as bouncing collect-and-collide. The particle bed moves together as a quasi-single body and collides inelastically with the container walls. The second regime of high effective loss factor values up to $\bar{\eta} = 1.8$ is at high excitation frequencies $400\,\text{Hz} < f < 800\,\text{Hz}$ and low to medium excitation intensities $\Gamma < 5$. The particle system is in a state of global-fluidization in this regime. In the area of medium acceleration intensities $\Gamma \approx 5$ and medium excitation frequencies $100\,\text{Hz} < f < 500\,\text{Hz}$, medium effective loss factor values are obtained $0.5 < \bar{\eta} < 1$. This regime connects the two areas of high effective loss factor values. In all other regimes, rather low effective loss factor values are achieved $\bar{\eta} < 0.5$.

For the later use of the particle damper connected to the beam-like structure,

a) Effective loss factor. **b)** Ratio of effective particle mass.

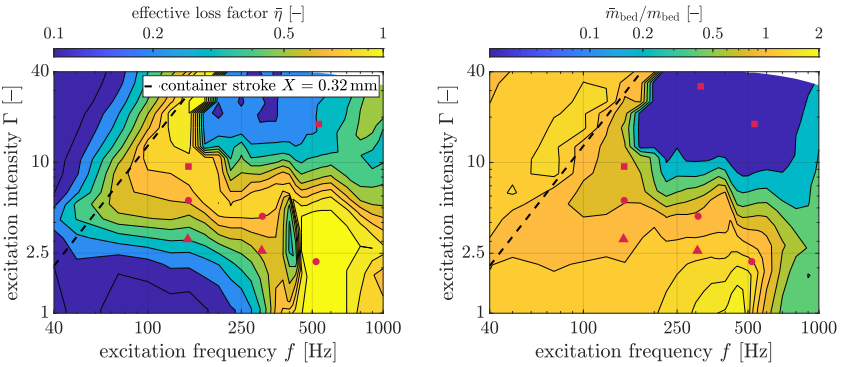

Figure 8.24: Experimental obtained effective loss factor and effective particle mass of 350 g steel powder inside cylindrical particle container with clearance $h = 1\,\text{mm}$. ●,▲,■: Equilibrium points obtained from structure coupling.

an operation in the areas of high effective loss factor values should be aimed. This depends on the characteristics of the particle damper as well as on the dynamics of the underlying structure. Using knowledge of previous Sect. 8.1 the characteristics of particle dampers can be influenced in a targeted manner, e. g. by the clearance, coated container walls or inner structures. However, here, the accuracy of the coupling procedure is of most interest and not an efficient design of the particle damper to match the dynamics of the underlying structure.
The ratio of the effective particle mass to the mass of the particle bed is shown in Fig. 8.24b. For excitation frequencies of $f < 175\,\mathrm{Hz}$ and all excitation intensities the effective particle mass is high with values of $0.8\,m_{\mathrm{bed}} < \bar{m}_{\mathrm{bed}} < 1.2\,m_{\mathrm{bed}}$. The effective loss factor ranges from very low to very high values for this area. For excitation frequencies $f > 175\,\mathrm{Hz}$ and high acceleration intensities $\Gamma > 10$ the effective particle mass is very low. In this area, the effective loss factor is also low and can be characterized by a decoupling of the particle bed from the container. For excitation frequencies $f > 175\,\mathrm{Hz}$ and low excitation intensities $\Gamma < 2.5$ a very high effective particle mass up to $\bar{m}_{\mathrm{bed}} = 2\,m_{\mathrm{bed}}$ is obtained. The corresponding effective loss factor is also high in this regime. Thus, a high effective loss factor causes the mass ratio to be high, but vice versa is not necessarily true.

Validation of Coupling Procedure

The reduced FEM model of the beam-like structure is now coupled with the effective fields of the particle damper as described in Sect. 3.3.2. For this coupling, the iterative scheme shown in Fig. 3.7 is used. The particle damper's effective fields are shown in Fig. 8.24. The damper is mounted at the free, not excited end of the beam. The beam-like structure is excited first by the shaker with a force amplitude of about $f_{\mathrm{ex}} = 26\,\mathrm{N}$. The obtained damping ratios are shown in Fig. 8.25. The legend entry "undamped" corresponds to the experimentally obtained damping without particles, while the entry "experiment" the actual measured damping by the particle damper denotes. The damping prediction by the coupling of the effective fields is labeled with "eff. fields". The solution of Eq. (3.51) is denoted by $\zeta(\bar{\eta} = 1)$ and describes the damping ratio in case of a damper with an assumed effective loss factor of one. In addition, in the effective fields of Fig. 8.24 the equilibrium points by the iteration scheme of the particle damper are marked by •. Furthermore, in Tab. 8.8 the reduction of the eigenfrequencies of the structure is listed, which occurs due to the effective particle mass.
The experimental damping ratio of the beam's first eigenmode increases from the undamped case $\zeta = 0.000\,45$ to $\zeta = 0.0028$. Although this damping is six times higher, the absolute damping ratio is still small. Its value is only a fraction of $\zeta(\bar{\eta} = 1) = 0.053$, i. e. in the case the particle damper exhibits a reduced loss factor of one, and thus far away from being considered efficient. In Fig. 8.24 no equilibrium points are marked, as the resulting acceleration amplitude of the particle container is outside the measurement range. The damping prediction by the

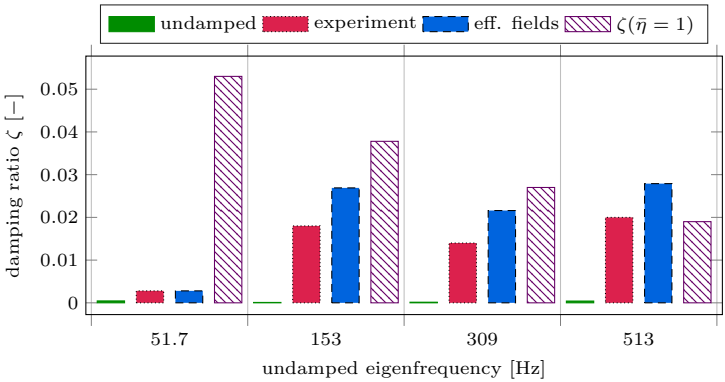

Figure 8.25: Damping ratios of modes $1-4$ of beam-like structure excited by an excitation force amplitude of $f_{\text{ex}} = 26\,\text{N}$ with particle damper coupled to the beam's free end. The damper's effective fields are shown in Fig. 8.24.

Table 8.8: Relative reduction of eigenfrequencies of undamped to damped system. The corresponding particle damper's effective fields are shown in Fig. 8.24 and the damping ratios in Fig. 8.25.

Reduction of Eigenfrequencies

	Eigenmode			
	1	2	3	4
Exp. Eigenfrequency [Hz]	51.7	153	309	513
Experiment [%]	4.6	2.6	3.6	5.7
Eff. Fields [%]	3.7	3.9	2.8	3.7

effective fields is still good, as outside the measurement range linear interpolated values are taken. Although the dissipated energy is low, the effective particle mass is high. Using Eq. (3.33) and the measured effective eigenfrequency, the experimentally determined effective particle mass follows to $\bar{m}_{\text{bed}} = 0.85\,m_{\text{bed}}$. As result, the eigenfrequency reduces about 4.6 % in the experiment. Similarly, this reduction of the eigenfrequency is approximated numerically by the iterative scheme with 3.7 %.

The second and third beam's eigenmodes show a very similar damping behavior. The experimental damping ratios are greatly increased compared to the undamped case. Damping ratios up to $\zeta = 0.018$ are achieved in the experiments. The damping prediction by the effective fields is, however, about 35 % off and could be considered only acceptable for qualitative assessment. The equilibrium points within Fig. 8.24 lie in the measurement range. The experimental damping values reach about 50 % of $\zeta(\bar{\eta} = 1)$. Thus, the damping could already be considered as close to efficient. The reduction of the eigenfrequencies are 2.6 % and 3.6 %, respectively. These differ with 1.3 % and 0.8 % between experimental

and numerical results. Consequently, the effective eigenfrequencies are only roughly approximated.
The fourth mode shows the strongest damping with a damping ratio of $\zeta = 0.02$ within the experiment. The damping ratio is slightly above $\zeta(\bar{\eta} = 1)$ and the damper can be considered efficient. The damping prediction by the effective fields is 28 % higher compared to the experiment. The equilibrium point in Fig. 8.24 is in the area of the highest effective loss factor values. The eigenfrequency reduces 5.7 % in the experiment and thus the most of all modes. The calculation of the effective eigenfrequency by the effective fields is a little bit off with a difference of 2 % to the experimental result.
Overall, a first good approximation of the damping ratios and effective eigenfrequencies are accomplished. The evaluation of the iterative scheme is done within seconds and no need for computational inefficient modal reduced FEM-DEM simulations are necessary. It is shown that it is possible to damp with a single damper multiple different eigenfrequencies at an almost constant efficient level. Damping ratios up to $\zeta = 0.02$ are achieved with a particle mass of 5 % of the system's mass.

Influence of Excitation Force

In the next step, the robustness of the iterative scheme is of interest. Therefore, the excitation force amplitude is varied. In Fig. 8.26 the damping ratios for $f_{\mathrm{ex}} = 13\,\mathrm{N}$ and $f_{\mathrm{ex}} = 52\,\mathrm{N}$ are shown and compared to $f_{\mathrm{ex}} = 26\,\mathrm{N}$, which was used previously. In Fig. 8.24 the equilibrium points of the iteration scheme are marked for $f_{\mathrm{ex}} = 13\,\mathrm{N}$ (▲) and $f_{\mathrm{ex}} = 52\,\mathrm{N}$ (■).
For all modes and excitations, except for one case, a first good approximation of

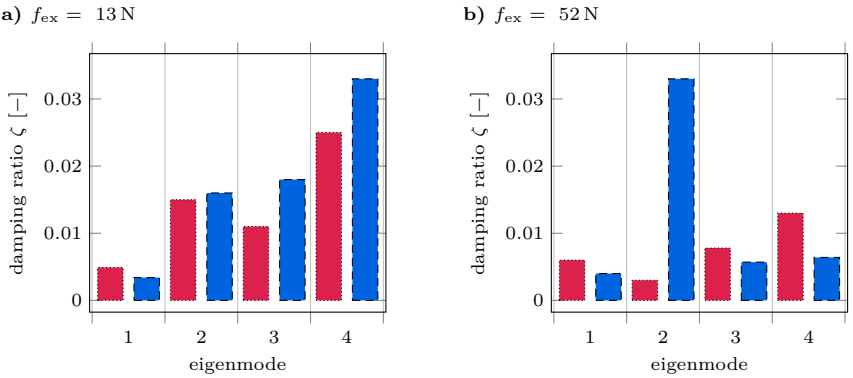

Figure 8.26: Damping ratios of beam-like structure coupled to particle damper for different excitation intensities for the experiment (*red*) and effective fields (*blue*). The damper's effective fields are shown in Fig. 8.24.

the damping ratio is achieved again using the iterative scheme. Especially, for the lower excitation level, see Fig. 8.26a, high damping ratios up to $\zeta = 0.025$ are obtained. For the higher excitation, see Fig. 8.26b, the damping ratios are lower with values around $\zeta = 0.01$. This is reasonable as the equilibrium points in Fig. 8.24 for the higher excitation lie in areas of low effective loss factor values. This can especially be observed for modes 3 and 4.
For the second mode at high excitation level, a very high damping ratio is calculated by the iterative scheme of $\zeta = 0.033$, although in the experiment a small value is measured i. e. $\zeta = 0.003$. As seen in Fig. 8.24, the calculated equilibrium point by the iterative scheme reaches the state of bouncing collect-and-collide, i. e. is close to X_{opt} and the effective loss factor is high with $\bar{\eta} = 0.81$. However, the particle container performs an additional rotation in the experiments. This is due to the form of the shape function of the beam-like structure, see Fig. 8.21. This is not represented by the effective field, which is obtained from shaker experiments on the **Single Damper Level**. Hence, it is assumed that this additional rotational movement of the particle container destroys the bouncing collect-and-collide motion mode. This results in much lower energy dissipation. Consequently, the damping ratio decreases as well in the real system.

Influence of Particle Damper Position

As an additional rotation of the particle container seems to have a big influence on the damping ratio and damping prediction, it is analyzed next what happens if no container rotation occurs. Thus, the particle damper is placed for every eigenmode at a corresponding extrema of the shape function with zero slope, e. g. at $y_{\mathrm{pd}} = 0.9\,\mathrm{m}$ for eigenmode 1 and 3, see Fig. 8.21. The so determined damping ratios are shown in Fig. 8.27 for excitations amplitudes of $f_{\mathrm{ex}} = 13\,\mathrm{N}$, $26\,\mathrm{N}$ and $52\,\mathrm{N}$, respectively. From these results, two major aspects can be seen. First, the differences between experimental results and damping prediction by the iteration scheme are reasonably small for almost every excitation case and eigenmode. The damping approximation can be considered as good except for mode 3 and 4 of the high excitation case, see Fig. 8.27c. This is reasonable, as the particle damper performs only a translational movement as supposed within the iterative scheme. Even eigenmode 2 at high excitation force amplitude, which resulted before in a low damping ratio, is greatly damped, see Fig. 8.27c compared to Fig. 8.26b. This also proves the above assumption that the additional container rotation vanishes the bouncing collect-and-collide motion mode.
Second, even higher damping ratios are achieved compared to the particle damper position where the shape functions exhibits an additional rotation, compare Fig. 8.27 to Fig. 8.25 and Fig. 8.26. This can be explained by the fact that the particle damper is now mounted directly at an extremum of the corresponding shape functions. At the position before, lower shape function values were realized. On the other hand, if the particle damper is placed at an extremum with zero

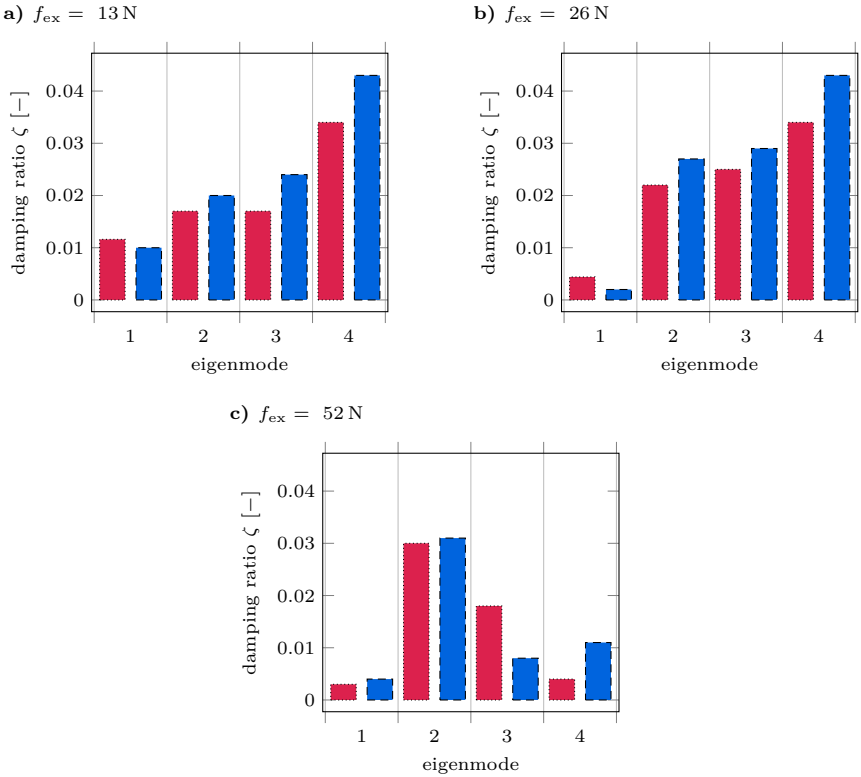

Figure 8.27: Damping ratios of beam-like structure coupled to particle damper placed at individual extrema of the shape functions with zero slope for different excitation intensities for experiment (*red*) and effective fields (*blue*). The damper's effective fields are shown in Fig. 8.24.

slope, the other shape functions might exhibit a node or a very low value at this position. This leads to extremely low damping ratios for these eigenmodes as discussed previously for Fig. 8.23.

In consequence, the position of the particle damper has to be chosen carefully. It depends on a variety of parameters. The magnitude of the shape function plays an important role. A higher value leads normally to higher damping. Placing the particle damper at a position where multiple shape functions have a high value, enables the efficient damping of multiple eigenmodes. Though, additional rotation of the particle container can reduce the energy dissipation significantly. Also, the damping prediction by the iterative scheme gets worse since it does not include container rotations. This trade-off has to be done for every application individually. As particle dampers are rather simple devices, also a placement

of multiple units at different locations should be considered or the utilization of more robust damper designs, like inner structures or coated container walls, as presented in Sect. 8.1.4 and Sect. 8.1.5. However, this is still part of ongoing research.

8.2.4 Summary

Within this section, different particle dampers are coupled to an underlying structure under forced vibration by a shaker. By measuring the structure's velocity response using a laser scanning vibrometer, the system's frequency response function is obtained. In doing so, the damping ratio is extracted. To obtain the damping ratio numerically, the structure is modeled using the finite element method and reduced in size via modal reduction. For the numerical coupling of the particle damper, two approaches are used.
For the first approach, the DEM model of the **Single Damper Level** is coupled to the reduced model of the structure. A qualitative good agreement between experiment and simulation is observed. Also, the quantitative behavior is within reasonable bounds. However, already for the utilized particle number of 40 particles, high numerical costs are obtained. Consequently, this approach is not suited for arbitrarily high particle numbers, e. g. in the case of a particle powder. Hence, for the second coupling approach, the damper's effective fields, i. e. the energy dissipation and effective particle mass obtained on the **Single Damper Level**, are coupled to the reduced model of the structure. This yields an iterative process that can be evaluated quickly. Based on this coupled model various investigations are conducted to show its qualitative accuracy and efficiency. While a perfect quantitative fit is not obtained, the qualitative results provide useful guidelines during the particle damper design process. The position of the particle damper plays an important role. Placing the particle damper at an extremum with zero slope of the shape function of the underlying structure results in good agreement between damping prediction and the experimental result. By placing the damper at a position where the shape function exhibits an additional rotation, the damping prediction is mostly still acceptable. Although, in some cases this greatly reduces the energy dissipation of the damper, e. g. for the bouncing collect-and-collide motion mode. Even multiple eigenmodes can be damped efficiently if the particle damper is placed at a position, where these modes have a high shape function value and the damper's effective field is in an efficient state.
The utilization of more robust damper designs, like inner structures or coated container walls, and the adjustment of the damper properties to match the dynamics of the underlying structure is still part of ongoing work.

Conclusion

One of the very promising tools to reduce undesired vibrations is the deployment of particle dampers. These are a derivative of impact dampers, i. e. instead of using only one impact object, multiple particles within a closed geometry are used. The structural vibrations are transmitted onto the particles via the container geometry. Interactions between particles among themselves and between particles and the container walls cause energy to dissipate due to inelastic impacts and frictional phenomena. This energy dissipation reduces the undesired structural vibration.

Until now, particle dampers have mostly been developed and designed using time-consuming experiment-based trial-and-error strategies for very specific applications. By this means the adaption to other systems is extremely limited. An explanation for this design approach derives from the highly nonlinear characteristics of particle dampers. This commences with the micro-mechanical effects during single inelastic particle impacts and sliding contacts, continues with the energy dissipation inside the vibrating particle container and ends at the interaction of the damper with the vibrating structure. These different effects cause the particle damper to depend on a variety of influence parameters, like the friction coefficient or the vibration amplitude. Due to the lack of understanding of these influence parameters and processes within the dampers, their application has been very limited so far. Additionally, the comparison of different design approaches and results is still a challenging task, due to different investigated excitation ranges and utilized quantifying factors.

To enhance the comprehension of the influence of different parameters and, therefore, also target a systematical approach to the design of particle dampers, investigations on the dampers' different scales or levels, respectively, are necessary. In this work, a new design methodology in form of a *toolchain* for the efficient development and application of particle dampers for passive vibration attenuation is developed. By the use of simulations, that are verified by experiments, during this process a deeper understanding of the micro-mechanical occurrences in the dampers is obtained. This deeper knowledge is a crucial step in the systematic design of particle dampers. Using this developed design methodology, which is in parts independent of the specific application, it is possible to extend particle dampers to a variety of very different applications, which is shown for multiple examples.

The developed design toolchain is separated into three serial levels. Insights made on one level can be used on the next level to better understand the dynamical properties and expedite the overall design process of particle dampers. On all levels, numerical models as well as experimental tests can be used for analyses. The appropriate choice depends on the specific requirements at each level.
The first level, called **Single Particle Level**, analyzes single particle–particle and particle–wall interactions. A particle collides in a defined manner with its collision partner. At this, the energy dissipation during the impacts is of major interest and is described by the *coefficient of restitution*, which can be used on the second level of the toolchain for *discrete element method* simulations. The investigated metal–metal impacts show a high dependency on the impact velocity and a significant rise of the coefficient of restitution for repeated impacts on the same spot. This occurs due to the *elastic-viscoplastic* material behavior of steel, which leads to a hardening of the contact zone. In contrast, the analyzed metal–polymer contacts show only little dependency on the impact velocity and no history-dependent behavior takes place. This happens as the *visco-elastic* material of polymers fully recovers after impact.
The second level of the toolchain, called **Single Damper Level**, represents investigations of an isolated particle damper subjected to a defined horizontal or vertical sinusoidal motion. The resulting particle movement is called *motion mode*. Using the *complex power method*, the *energy dissipation*, the *effective loss factor* and the *effective particle mass* of the particle damper are determined for the desired excitation range. These results are also referred to as *effective fields*, which can be correlated to the damper's motion modes. The calculated effective fields can be used on the third level of the toolchain for the integration process of particle dampers mounted to a vibrating structure. If applicable, the effective fields are approximated by analytical formulas, which can also be integrated into the next design level. All these aspects help to shorten the design phase on the last level.
The third level of the toolchain, called **Structural Integrated Damper Level**, represents the integration of particle dampers in a vibrating structure to evaluate their overall damping effect. For numerical investigations, three different strategies are developed. For the first approach, the complete discrete element model from the **Single Damper Level** is coupled with a dynamical model of the structure. The flexible structures are described by modal reduced finite element models. While this approach is very accurate and useful for verification purposes, it is also computationally expensive. Alternatively, the flexible structure models can be coupled with either the effective fields or the analytical formulas found in the **Single Damper Level**. This coupling leads to accurate results and short computation times. If an analytical formula is present, it can even be used for a first damper optimization.

Within this work, the toolchain is applied to four major vibration regimes for the design of particle dampers. The first vibration regime considers horizon-

tal vibrations of low excitation amplitudes and frequencies, i. e. the particle damper acceleration amplitude stays below the gravitational constant. For these applications, usually only small energy dissipation rates are obtained, due to sticking of particles. In this work, the rolling effect of spherical particles on flat container bases is used to significantly increase the damper's energy dissipation, i. e. the so-called *rolling collect-and-collide* motion mode is utilized. On the **Single Damper Level**, an analytical equation is derived to describe this rolling effect and the resulting energy dissipation. Hereby, the analytical formulas are in good agreement with experimental measurements utilizing a linear drive. Sensitivity analyses show that a low friction coefficient and a high particle radius are beneficial for obtaining a high damper efficiency. A container tilt, however, should be avoided.
Based on the analytical equation describing the rolling effect, a systematic damper design approach is developed for free and forced vibrations of the underlying structure. Simple analytical equations for an efficient damper design are derived. Their validity is proven by experimental measurements on a simple beam-like structure and a lightweight manipulator. The application of the design approaches to more complex structures, like high-rise buildings, overhead cranes or crane hooks, is a promising field for further research. This also includes the analysis of more complex excitations, like real earthquake displacements or wind excitation forces.

Within the second vibration regime, medium-excitation horizontal vibrations are studied. Here, the particle damper acceleration amplitude is below and above the gravitational constant. Besides the already analyzed rolling state of particles, a bouncing state, named *bouncing collect-and-collide*, is numerically observed at higher excitation rates on the **Single Damper Level**. Between the rolling and the bouncing state of the particle bed, a *fluidization* mode is observed. Similar to the rolling state, the energy dissipation within the bouncing state can be accurately described using analytical formulas.
The systematic damper design approach for low-excitation horizontal vibrations is adopted to design particle dampers for structural free vibrations of medium intensities. The validity of this design approach is again proven experimentally on a simple beam-like structure setup. The expansion to more complex systems and the analysis of forced vibrations is still an open field here.

The third vibration regime considers medium-excitation vibrations in the vertical direction. For these vibrations, particle dampers show multiple different motion modes on the **Single Damper Level**. For container acceleration amplitudes below the gravitational constant, the damper's efficiency is low. For container acceleration amplitudes above the gravitational constant, multiple motion modes are observed which are very sensitive to the excitation conditions and the container dimensions. This ranges from single-sided contacts with the container bottom, over double-sided contacts with both container walls to a completely scattered movement. Analytical equations for all motion modes are derived

describing their energy dissipation accurately.
For the damper coupling with an underlying free vibrating structure, an optimization procedure based on the analytical equations is used. This optimization procedure is successfully applied to a beam like-structure setup and validated experimentally. Especially the low energy dissipation rates for container acceleration amplitudes below the gravitational constant are still a big challenge and could stimulate further research. Moreover, forced vibrations should be considered in future studies.

The last investigated vibration regime consists of high-excitation vibrations, i. e. vibrations with acceleration amplitudes significantly above the gravitational constant. Hence, the difference between horizontal and vertical vibrations often vanishes. On the **Single Damper Level**, the particle damper is driven by an experimental shaker setup. At rather low vibration frequencies the bouncing collect-and-collide particle state can be efficiently used and adjusted in a targeted manner. However, this bouncing state is highly sensitive to the container stroke. To reduce this sensitivity, inner structures within the particle container or coated container walls can be utilized, as shown by experimental measurements. Simple design guidelines for both approaches are derived. For higher excitation frequencies the particle system is in a state of *global-fluidization*. It turns out that a small particle radius is beneficial. The efficiency in this excitation regime can be further increased by utilizing the aforementioned inner structures.
Experimental measurements on a forced vibrating beam-like structure with free–free boundary conditions show the applicability of particle dampers to these vibration conditions. The prediction of the damping ratio is hereby accurately possible using numerical simulations. While the use of the discrete element method coupled with a structural model in simulations can be burdensome, the effective fields obtained on the **Single Damper Level**, can be evaluated quickly in conjunction with a structural model. The extension to more complex structures for real-life applications is a very promising field for further studies. Additionally, improvements of single particle damper units to increase the damper's energy dissipation and robustness still have tremendous potential.

BIBLIOGRAPHY

[AbbasEtAl14] Abbas, H.; Hai, H.; Rongong, J.; Xing, Y.: Damping performance of metal swarfs in a horizontal hollow structure. *Journal of Mechanical Science and Technology*, Vol. 28, No. 1, pp. 9–13, 2014. DOI:10.1007/s12206-013-0980-3.

[AhmadEtAl16] Ahmad, N.; Ranganath, R.; Ghosal, A.: Modeling and experimental study of a honeycomb beam filled with damping particles. *Journal of Sound and Vibration*, Vol. 391, 2016. DOI:10.1016/j.jsv.2016.11.011.

[AnderssonEtAl07] Andersson, S.; Söderberg, A.; Björklund, S.: Friction models for sliding dry, boundary and mixed lubricated contacts. *Tribology International*, Vol. 40, No. 4, pp. 580–587, 2007. DOI:10.1016/j.triboint.2005.11.014.

[AnsariAlam13] Ansari, I.H.; Alam, M.: Patterns and velocity field in vertically vibrated granular materials. *AIP Conference Proceedings*, Vol. 1542, No. 1, pp. 775–778, 2013. DOI:10.1063/1.4812046.

[ArakiEtAl83] Araki, Y.; Yokomichi, I.; Inoue, J.: Impact damper with granular materials : Single side impact in a vertical oscillating system. *Transactions of the Japan Society of Mechanical Engineers Series C*, Vol. 49, No. 442, pp. 945–951, 1983. DOI:10.1299/kikaic.49.945.

[ArakiEtAl85] Araki, Y.; Yokomichi, I.; Inoue, J.: Impact damper with granular materials: 2nd report, both sides impacts in a vertical oscillating system. *Bulletin of Japan Society of Mechanical Engineers*, Vol. 28, No. 241, pp. 1466–1472, 1985. DOI:10.1299/jsme1958.28.1466.

[AryaeiEtAl10] Aryaei, A.; Hashemnia, K.; Jafarpur, K.: Experimental and numerical study of ball size effect on restitution coefficient in low velocity impacts. *International Journal of Impact Engineering*, Vol. 37, No. 10, pp. 1037–1044, 2010. DOI:10.1016/j.ijimpeng.2010.04.005.

[BaiEtAl09] Bai, X.M.; Shah, B.; Keer, L.M.; Wang, Q.J.; Snurr, R.Q.: Particle dynamics simulations of a piston-based particle damper. *Powder Technology*, Vol. 189, No. 1, pp. 115–125, 2009. DOI:10.1016/j.powtec.2008.06.016.

[BajkowskiEtAl15] Bajkowski, J.M.; Dyniewicz, B.; Bajer, C.I.: Damping properties of a beam with vacuum-packed granular damper. *Journal of Sound and Vibration*, Vol. 341, pp. 74–85, 2015. DOI:10.1016/J.JSV.2014.12.036.

[BandeiraZohdi18] Bandeira, A.A.; Zohdi, T.: 3D numerical simulations of granular materials using DEM models considering rolling phenomena. *Computational Particle Mechanics*, Vol. 6, pp. 97–131, 2018. DOI:10.1007/S40571-018-0200-0.

[BannermanEtAl11] Bannerman, M.N.; Kollmer, J.E.; Sack, A.; Heckel, M.; Mueller, P.; Pöschel, T.: Movers and shakers: Granular damping in microgravity. *Physical Review E*, Vol. 84, 2011. DOI:10.1103/PHYSREVE.84.011301.

[Barber18] Barber, J.R.: *Contact Mechanics*. Solid Mechanics and Its Applications. Cham: Springer, 2018. DOI:10.1007/978-3-319-70939-0.

[Bergström15] Bergström, J.: *Mechanics of Solid Polymers: Theory and Computational Modeling*. Plastics Design Library. Amsterdam: Elsevier, 1. Edn., 2015. DOI:10.1016/C2013-0-15493-1.

[BoonEtAl13] Boon, C.W.; Houlsby, G.T.; Utili, S.: A new contact detection algorithm for three-dimensional non-spherical particles. *Powder Technology*, Vol. 248, pp. 94–102, 2013. DOI:10.1016/J.POWTEC.2012.12.040.

[Brandt11] Brandt, A.: *Noise and Vibration Analysis: Signal Analysis and Experimental Procedures*. Chichester: John Wiley and Sons, 2011. DOI:10.1002/9780470978160.

[BrendelDippel98] Brendel, L.; Dippel, S.: Lasting contacts in molecular dynamics simulations. *In: Herrmann, H.J., Hovi, JP., Luding, S. (Eds). Physics of Dry Granular Media. NATO ASI Series*, Vol. 350. Springer, Dordrecht, 1998. DOI:10.1007/978-94-017-2653-5_22.

[BrinsonBrinson08] Brinson, H.F.; Brinson, L.C.: *Polymer Engineering Science and Viscoelasticity*. New York: Springer, 2008. DOI:10.1007/978-0-387-73861-1.

[BustamanteEtAl16] Bustamante, M.; Gerges, S.; Vergara, E.; Arenas, J.: High damping characteristics of an elastomer particle damper. *International Journal of Acoustics and Vibrations*, Vol. 21, pp. 112–121, 2016. DOI:10.20855/IJAV.2016.21.1401.

[ChanEtAl16] Chan, K.W.; Liao, W.H.; Wang, M.Y.; Choy, P.K.: Experimental studies for particle damping on a bond arm. *Journal of Vibration and Control*, Vol. 12, No. 3, pp. 297–312, 2016. DOI:10.1177/1077546306063257.

[ChaudryEtAl22] Chaudry, M.A.; Woitzik, C.; Düster, A.; Wriggers, P.: A multiscale DEM-FEM coupled approach for the investigation of granules

as crash-absorber in ship building. *Computational Particle Mechanics*, Vol. 9, No. 1, pp. 179–197, 2022. DOI:10.1007/S40571-021-00401-5.

[ChenEtAl01] Chen, T.; Mao, K.; Huang, X.; Wang, M.: Dissipation mechanisms of nonobstructive particle damping using discrete element method. *Proceedings of SPIE - The International Society for Optical Engineering*, Vol. 4331, pp. 294–301, 2001. DOI:10.1117/12.432713.

[ChenGeorgakis13] Chen, J.; Georgakis, C.T.: Tuned rolling-ball dampers for vibration control in wind turbines. *Journal of Sound and Vibration*, Vol. 332, No. 21, pp. 5271–5282, 2013. DOI:10.1016/J.JSV.2013.05.019.

[Christensen82] Christensen, R.M.: *Theory of Viscoelasticity: An Introduction.* New York: Academic Press, 2. Edn., 1982. DOI:10.1016/B978-0-12-174252-2.X5001-7.

[CioccaWang11] Ciocca, M.; Wang, J.: Watching and listening to the coefficient of restitution. *Journal of the Kentucky Academy of Science*, Vol. 72, No. 2, pp. 100–104, 2011. DOI:10.1119/1.4758161.

[CundallStrack79] Cundall, P.A.; Strack, O.D.L.: A discrete numerical model for granular assemblies. *International Journal of Rock Mechanics and Mining Sciences and Geomechanics*, Vol. 16, No. 4, pp. 47–65, 1979. DOI:10.1680/GEOT.1979.29.1.47.

[DarabiRongong12] Darabi, B.; Rongong, J.A.: Polymeric particle dampers under steady-state vertical vibrations. *Journal of Sound and Vibration*, Vol. 331, No. 14, pp. 3304–3316, 2012. DOI:10.1016/J.JSV.2012.03.005.

[Di RenzoDi Maio05] Di Renzo, A.; Di Maio, F.P.: An improved integral non-linear model for the contact of particles in distinct element simulations. *Chemical Engineering Science*, Vol. 60, No. 5, pp. 1303–1312, 2005. DOI:10.1016/J.CES.2004.10.004.

[DuanChen10] Duan, Y.; Chen, Q.: Simulation and experimental investigation on dissipative properties of particle dampers. *Journal of Vibration and Control*, Vol. 17, No. 5, pp. 777–788, 2010. DOI:10.1177/1077546309356183.

[DuEtAl08] Du, Y.; Shulin, W.; Yan, Z.; Laiqiang, L.; Guangqiang, H.: Performance of a new fine particle impact damper. *Advances in Acoustics and Vibration*, Vol. 2008, 2008. DOI:10.1155/2008/140894.

[EshuisEtAl06] Eshuis, P.; Weele, K.; Meer, D.; Lohse, D.: Granular leidenfrost effect: Experiment and theory of floating particle clusters. *Physical Review Letters*, Vol. 95, p. 258001, 2006. DOI:10.1103/PHYSREVLETT.95.258001.

[EshuisEtAl07] Eshuis, P.; van der Weele, K.; van der Meer, D.; Bos, R.; Lohse, D.: Phase diagram of vertically shaken granular matter. *Physics of Fluids*, Vol. 19, No. 12, p. 123301, 2007. DOI:10.1063/1.2815745.

[FangTang06a] Fang, X.; Tang, J.: A direct simulation monte carlo approach for the analysis of granular damping. *Journal of Computational and Nonlinear Dynamics*, Vol. 2, No. 2, pp. 180–189, 2006. DOI:10.1115/1.2447502.

[FangTang06b] Fang, X.; Tang, J.: Granular damping in forced vibration: Qualitative and quantitative analyses. *Journal of Vibration and Acoustics*, Vol. 128, No. 4, pp. 489–500, 2006. DOI:10.1115/1.2203339.

[FerreyraEtAl21] Ferreyra, M.V.; Gómez-Paccapelo, J.M.; Suarez, R.; Pugnaloni, L.A.: Avoiding chaos in granular dampers. *The European Physical Journal Conferences*, Vol. 249, p. 15003, 2021. DOI:10.1051/EPJCONF/202124915003.

[Fleissner10] Fleissner, F.: *Parallel Object Oriented Simulation with Lagrangian Particle Methods*. Schriften aus dem Institut für Technische und Numerische Mechanik der Universität Stuttgart (Ph.D. Thesis). Düren: Shaker, 2010.

[FleissnerEtAl07] Fleissner, F.; Gaugele, T.; Eberhard, P.: Applications of the discrete element method in mechanical engineering. *Multibody System Dynamics*, Vol. 18, No. 1, pp. 81–94, 2007. DOI:10.1007/S11044-007-9066-2.

[FriendKinra00] Friend, R.D.; Kinra, V.K.: Particle impact damping. *Journal of Sound and Vibration*, Vol. 233, No. 1, pp. 93–118, 2000. DOI:10.1006/JSVI.1999.2795.

[GagnonEtAl19] Gagnon, L.; Morandini, M.; Ghiringhelli, G.L.: A review of particle damping modeling and testing. *Journal of Sound and Vibration*, Vol. 459, p. 114865, 2019. DOI:10.1016/J.JSV.2019.114865.

[GamaEtAl04] Gama, B.A.; Lopatnikov, S.L.; Gillespie, J.W.: Hopkinson bar experimental technique: A critical review. *Applied Mechanics Reviews*, Vol. 57, No. 4, pp. 223–250, 2004. DOI:10.1115/1.1704626.

[Gear67] Gear, C.W.: The numerical integration of ordinary differential equations of various orders. *Mathematics of Computation*, Vol. 21, No. 98, p. 146, 1967. DOI:10.2307/2004155.

[GharibKarkoub15] Gharib, M.; Karkoub, M.: Shock-based experimental investigation of the linear particle chain impact damper. *Journal of Vibration and Acoustics*, Vol. 137, 2015. DOI:10.1115/1.4031406.

[GlothSinapius05] Gloth, G.; Sinapius, M.: Analysis of swept-sine runs during modal survey and qualification tests. *Proceedings of the European Conference on Spacecraft Structures, Materials and Mechanical Testing 2005*, Vol. 581, pp. 579–590, 2005.

[GnanasambandhamEtAl19] Gnanasambandham, C.; Stender, M.; Hoffmann, N.; Eberhard, P.: Multi-scale dynamics of particle dampers using wavelets: Extracting particle activity metrics from ring down experiments. *Journal of Sound and Vibration*, Vol. 454, pp. 1–13, 2019. DOI:10.1016/J.JSV.2019.04.009.

[GnanasambandhamEtAl20] Gnanasambandham, C.; Fleissner, F.; Eberhard, P.: Enhancing the dissipative properties of particle dampers using rigid obstacle-grids. *Journal of Sound and Vibration*, Vol. 484, p. 115522, 2020. DOI:10.1016/J.JSV.2020.115522.

[Goldsmith60] Goldsmith, W.: *Impact: The Theory and Physical Behavior of Colliding Solids*. London: Edward Arnold Publishers, 1960. DOI:10.1115/1.3641808.

[GonthierEtAl04] Gonthier, Y.; McPhee, J.; Lange, C.; Piedbœuf, J.C.: A regularized contact model with asymmetric damping and dwell-time dependent friction. *Multibody System Dynamics*, Vol. 11, No. 3, pp. 209–233, 2004. DOI:10.1023/B:MUBO.0000029392.21648.BC.

[HairerEtAl08] Hairer, E.; Wanner, G.; Nørsett, S.P.: *Solving Ordinary Differential Equations I: Nonstiff Problems*. Berlin and Heidelberg: Springer, 2. Edn., 2008. DOI:10.1007/978-3-540-78862-1.

[HeckelEtAl12] Heckel, M.; Sack, A.; Kollmer, J.; Pöschel, T.: Granular dampers for the reduction of vibrations of an oscillatory saw. *Physica A: Statistical Mechanics and its Applications*, Vol. 391, pp. 4442–4447, 2012. DOI:10.1016/J.PHYSA.2012.04.007.

[Hertz82] Hertz, H.: Über die Berührung fester elastischer Körper (On the contact of stiff elastic solids). *Journal für die Reine und Angewandte Mathematik*, Vol. 92, pp. 156–171 (in german), 1882. DOI:10.1515/CRLL.1882.92.156.

[HollkampGordon98] Hollkamp, J.J.; Gordon, R.W.: Experiments with particle damping. *Proceedings Volume 3327, Smart Structures and Materials 1998: Passive Damping and Isolation*, 1998. DOI:10.1117/12.310675.

[HuangEtAl21] Huang, X.h.; Xu, W.b.; Wang, J.; Yan, W.m.; Chen, Y.j.: Equivalent model of a multi–particle damper considering particle rolling and its analytical solution. *Structural Control and Health Monitoring*, Vol. 28, No. 6, 2021. DOI:10.1002/STC.2718.

[HuEtAl13] Hu, L.; Hu, G.M.; Fang, Z.Q.; Zhang, Y.: A new algorithm for contact detection between spherical particle and triangulated mesh boundary in discrete element method simulations. *International Journal for Numerical Methods in Engineering*, Vol. 94, No. 8, pp. 787–804, 2013. DOI:10.1002/NME.4487.

[Ibrahim09] Ibrahim, R.A.: *Vibro-Impact Dynamics: Modeling, Mapping and Applications*. Berlin and Heidelberg: Springer, 1. Edn., 2009. DOI:10.1007/978-3-642-00275-5.

[JadhavAwasare16] Jadhav, T.A.; Awasare, P.J.: Enhancement of particle damping effectiveness using multiple cell enclosure. *Journal of Vibration and Control*, Vol. 22, No. 6, pp. 1516–1525, 2016. DOI:10.1177/1077546314543725.

[Johnson95] Johnson, C.D.: Design of passive damping systems. *Journal of Mechanical Design*, Vol. 117, No. B, pp. 171–176, 1995. DOI:10.1115/1.2838659.

[Johnson03] Johnson, K.L.: *Contact Mechanics*. Cambridge: Cambridge University Press, 9. Edn., 2003. DOI:10.1017/CBO9781139171731.

[Jones90] Jones, N.: *Structural Impact*. Cambridge: Cambridge University Press, 1990. DOI:10.1017/CBO9780511624285.

[Kollmer14] Kollmer, J.: Probing the validity of an effective-one-particle description of granular dampers in microgravity. *Granular Matter*, Vol. 17, 2014. DOI:10.1007/s10035-014-0539-8.

[KremmerFavier01] Kremmer, M.; Favier, J.F.: A method for representing boundaries in discrete element modelling: Part I - geometry and contact detection. *International Journal for Numerical Methods in Engineering*, Vol. 51, No. 12, pp. 1407–1421, 2001. DOI:10.1002/NME.184.

[Kruggel-EmdenEtAl07] Kruggel-Emden, H.; Simsek, E.; Rickelt, S.; Wirtz, S.; Scherer, V.: Review and extension of normal force models for the discrete element method. *Powder Technology*, Vol. 171, No. 3, pp. 157–173, 2007. DOI:10.1016/J.POWTEC.2006.10.004.

[Kuphal65] Kuphal, K.: Über die Beeinflussung von Schwingungen durch einen Stoßkörper I (About the influence of vibrations by an impactor). *Zeitschrift für Angewandte Mathematik und Mechanik*, Vol. 45, pp. 73–86 (in german), 1965. DOI:10.1002/ZAMM.19650450202.

[LankaraniNikravesh90] Lankarani, H.M.; Nikravesh, P.E.: A contact force model with hysteresis damping for impact analysis of multibody systems. *Journal of Mechanical Design*, Vol. 112, No. 3, pp. 369–376, 1990. DOI:10.1115/1.2912617.

[LiDarby08] Li, K.; Darby, A.P.: A buffered impact damper for multi-degree-of-freedom structural control. *Earthquake Engineering & Structural Dynamics*, Vol. 37, No. 13, pp. 1491–1510, 2008. DOI:10.1002/EQE.823.

[LieberJensen45] Lieber, P.; Jensen, D.P.: An acceleration damper: Development, design and some applications. *Transactions of the American Society of Mechanical Engineers*, Vol. 67, No. 10, pp. 523–530, 1945.

[Luding08a] Luding, S.: Cohesive, frictional powders: Contact models for tension. *Granular Matter*, Vol. 10, No. 4, p. 235, 2008. DOI:10.1007/s10035-008-0099-x.

[Luding08b] Luding, S.: Introduction to discrete element methods: Basic of contact force models and how to perform the micro-macro transition to continuum theory. *European Journal of Environmental and Civil Engineering*, Vol. 12, No. 7-8, pp. 785–826, 2008. DOI:10.1080/19648189.2008.9693050.

[LuEtAl10] Lu, Z.; Lu, X.; Masri, S.: Studies of the performance of particle dampers under dynamic loads. *Journal of Sound and Vibration*, Vol. 329, pp. 5415–5433, 2010. DOI:10.1016/J.JSV.2010.06.027.

[LuEtAl11] Lu, Z.; Masri, S.; Lu, X.: Studies of the performance of particle dampers attached to a two-degree-of-freedom system under random excitation. *Journal of Vibration and Control*, Vol. 17, pp. 1454–1471, 2011. DOI:10.1177/1077546310370687.

[LuEtAl12] Lu, Z.; Lu, X.; Lu, W.; Masri, S.: Experimental studies of the effects of buffered particle dampers attached to a multi-degree-of-freedom system under dynamic loads. *Journal of Sound and Vibration*, Vol. 331, pp. 2007–2022, 2012. DOI:10.1016/J.JSV.2011.12.022.

[LuEtAl15] Lu, G.; Third, J.R.; Müller, C.R.: Discrete element models for non-spherical particle systems: From theoretical developments to applications. *Chemical Engineering Science*, Vol. 127, pp. 425–465, 2015. DOI:10.1016/J.CES.2014.11.050.

[LuEtAl16] Lu, Z.; Wang, D.; Masri, S.; Lu, X.: An experimental study of vibration control of wind-excited high-rise buildings using particle tuned mass dampers. *Smart Structures and Systems*, Vol. 18, pp. 93–115, 2016. DOI:10.12989/SSS.2016.18.1.093.

[LuEtAl17] Lu, Z.; Wang, Z.; Masri, S.F.; Lu, X.: Particle impact dampers: Past, present, and future. *Structural Control and Health Monitoring*, Vol. 25, No. 1, p. e2058, 2017. DOI:10.1002/STC.2058.

[MaoEtAl04] Mao, K.; Wang, M.Y.; Xu, Z.; Chen, T.: DEM simulation of particle damping. *Powder Technology*, Vol. 142, No. 2-3, pp. 154–165, 2004. DOI:10.1016/J.POWTEC.2004.04.031.

[MarhadiKinra05] Marhadi, K.; Kinra, V.K.: Particle impact damping: Effect of mass ratio, material, and shape. *Journal of Sound and Vibration*, Vol. 283, pp. 433–448, 2005. DOI:10.1016/J.JSV.2004.04.013.

[MasmoudiEtAl16] Masmoudi, M.; Job, S.; Abbes, M.S.; Tawfiq, I.; Haddar, M.: Experimental and numerical investigations of dissipation mechanisms in particle dampers. *Granular Matter*, Vol. 18, No. 3, p. 71, 2016. DOI:10.1007/s10035-016-0667-4.

[Masri69] Masri, S.F.: Analytical and experimental studies of multiple–unit impact dampers. *The Journal of the Acoustical Society of America*, Vol. 45, No. 5, pp. 1111–1117, 1969. DOI:10.1121/1.1911581.

[MatchettEtAl00] Matchett, A.J.; Yanagida, T.; Okudaira, Y.; Kobayashi, S.: Vibrating powder beds: A comparison of experimental and distinct element method simulated data. *Powder Technology*, Vol. 107, No. 1, pp. 13–30, 2000. DOI:10.1016/S0032-5910(99)00080-7.

[Matuttis14] Matuttis, H.G.: *Understanding the Discrete Element Method: Simulation of Non-Spherical Particles for Granular and Multi-Body Systems*. Singapore: Wiley, 2014. DOI:10.1002/9781118567210.

[McnamaraYoung92] Mcnamara, S.; Young, W.R.: Inelastic collapse and clumping in a one–dimensional granular medium. *Physics of Fluids A: Fluid Dynamics*, Vol. 4, No. 3, pp. 496–504, 1992. DOI:10.1063/1.858323.

[MehtaLuck90] Mehta, A.; Luck, J.M.: Novel temporal behavior of a nonlinear dynamical system: The completely inelastic bouncing ball. *Physical Review Letters*, Vol. 65, No. 4, pp. 393–396, 1990. DOI:10.1103/PhysRevLett.65.393.

[MeyerEtAl21] Meyer, N.; Schwartz, C.; Morlock, M.; Seifried, R.: Systematic design of particle dampers for horizontal vibrations with application to a lightweight manipulator. *Journal of Sound and Vibration*, Vol. 510, p. 116319, 2021. DOI:10.1016/j.jsv.2021.116319.

[MeyerEtAl22] Meyer, N.; Wagemann, E.L.; Jackstadt, A.; Seifried, R.: Material and particle size sensitivity analysis on coefficient of restitution in low-velocity normal impacts. *Computational Particle Mechanics*, Vol. 9, No. 6, pp. 1293–1308, 2022. DOI:10.1007/s40571-022-00471-z.

[MeyerSeifried19a] Meyer, N.; Seifried, R.: Experimental and numerical investigations on parameters influencing energy dissipation in particle dampers. *VI International Conference on Particle-based Methods - Fundamentals and Applications*, pp. 260–271, 2019.

[MeyerSeifried19b] Meyer, N.; Seifried, R.: An experimental model for the analysis of energy dissipation in particle dampers. *Proceedings in Applied Mathematics and Mechanics*, Vol. 19, No. 1, 2019. DOI:10.1002/pamm.201900171.

[MeyerSeifried20] Meyer, N.; Seifried, R.: Numerical and experimental investigations in the damping behavior of particle dampers attached to a

vibrating structure. *Computers & Structures*, Vol. 238, p. 106281, 2020. DOI:10.1016/J.COMPSTRUC.2020.106281.

[MeyerSeifried21a] Meyer, N.; Seifried, R.: Damping prediction of particle dampers for structures under forced vibration using effective fields. *Granular Matter*, Vol. 23, No. 3, p. 64, 2021. DOI:10.1007/S10035-021-01128-Z.

[MeyerSeifried21b] Meyer, N.; Seifried, R.: Optimal design of particle dampers for structures with low first eigenfrequency under forced vibration. *7th edition of the International Conference on Particle-based Methods*, 2021. DOI:10.23967/PARTICLES.2021.022.

[MeyerSeifried21c] Meyer, N.; Seifried, R.: Toward a design methodology for particle dampers by analyzing their energy dissipation. *Computational Particle Mechanics*, Vol. 8, No. 4, pp. 681–699, 2021. DOI:10.1007/S40571-020-00363-0.

[MeyerSeifried22] Meyer, N.; Seifried, R.: Energy dissipation in horizontally driven particle dampers of low acceleration intensities. *Nonlinear Dynamics*, Vol. 108, No. 4, pp. 3009–3024, 2022. DOI:10.1007/S11071-022-07348-Z.

[MeyerSeifried23a] Meyer, N.; Seifried, R.: Design of robust particle dampers using inner structures and coated container walls. *Granular Matter*, Vol. 25, No. 1, 2023. DOI:10.1007/S10035-022-01298-4.

[MeyerSeifried23b] Meyer, N.; Seifried, R.: Systematic design of particle dampers for transient vertical vibrations. *Granular Matter*, Vol. 25, No. 1, p. 580, 2023. DOI:10.1007/S10035-022-01290-Y.

[MichonEtAl13] Michon, G.; Almajid, A.; Aridon, G.: Soft hollow particle damping identification in honeycomb structures. *Journal of Sound and Vibration*, Vol. 332, No. 3, pp. 536–544, 2013. DOI:10.1016/J.JSV.2012.09.024.

[MinamotoEtAl11] Minamoto, H.; Seifried, R.; Eberhard, P.; Kawamura, S.: Analysis of repeated impacts on a steel rod with visco-plastic material behavior. *European Journal of Mechanics - A/Solids*, Vol. 30, No. 3, pp. 336–344, 2011. DOI:10.1016/J.EUROMECHSOL.2010.12.002.

[MooreEtAl95] Moore, J.J.; Palazzolo, A.B.; Gadangi, R.; Nale, T.A.; Klusman, S.A.; Brown, G.V.; Kascak, A.F.: A forced response analysis and application of impact dampers to rotordynamic vibration suppression in a cryogenic environment. *Journal of Vibration and Acoustics*, Vol. 117, No. 3A, pp. 300–310, 1995. DOI:10.1115/1.2874452.

[MorlockEtAl18] Morlock, M.; Meyer, N.; Pick, M.A.; Seifried, R.: Modeling and trajectory tracking control of a new parallel flexible link robot. *Proceedings of the 2018 IEEE/RSJ International Conference on Intelligent Robots and Systems*, 2018. DOI:10.1109/IROS.2018.8594008.

[MorlockEtAl21] Morlock, M.; Meyer, N.; Pick, M.A.; Seifried, R.: Real-time trajectory tracking control of a parallel robot with flexible links. *Mechanism and Machine Theory*, Vol. 158, p. 104220, 2021. DOI:10.1016/J.MECHMACHTHEORY.2020.104220.

[NetoWriggers21] Neto, A.; Wriggers, P.: Discrete element model for general polyhedra. *Computational Particle Mechanics*, Vol. 9, pp. 353–380, 2021. DOI:10.1007/S40571-021-00415-Z.

[NorouziEtAl16] Norouzi, H.R.; Zarghami, R.; Sotudeh-Gharebagh, R.; Mostoufi, N.: *Coupled CFD-DEM Modeling: Formulation, Implementation and Application to Multiphase Flows*. Chichester: Wiley, 2016. DOI:10.1002/9781119005315.

[NowakowskiEtAl12] Nowakowski, C.; Fehr, J.; Fischer, M.; Eberhard, P.: Model order reduction in elastic multibody systems using the floating frame of reference formulation. *IFAC Proceedings Volumes*, Vol. 45, No. 2, pp. 40–48, 2012. DOI:10.3182/20120215-3-AT-3016.00007.

[OltmannEtAl18] Oltmann, J.; Hartwich, T.; Krause, D.: A systematic approach for vibration reduction of lightweight structures with particle damping. *Symposium Lightweight Design in Product Development 2018*, 2018.

[OppenheimSchafer75] Oppenheim, A.V.; Schafer, R.W.: *Digital Signal Processing*. New Jersey: Prentice-Hall, 1975.

[O'SullivanBray04] O'Sullivan, C.; Bray, J.D.: Selecting a suitable time step for discrete element simulations that use the central difference time integration scheme. *Engineering Computations*, Vol. 21, No. 2/3/4, pp. 278–303, 2004. DOI:10.1108/02644400410519794.

[Paget37] Paget, A.L.: Vibration in steam turbine buckets and damping by impacts. *Engineering*, Vol. 143, pp. 305–307, 1937.

[Panossian92] Panossian, H.: Structural damping enhancement via non-obstructive particle damping technique. *Journal of Vibration and Acoustics*, Vol. 105, No. 114, pp. 101–105, 1992. DOI:10.1115/1.2930221.

[Panossian02] Panossian, H.: Non-obstructive particle damping experience and capabilities. *Proceedings of SPIE - The International Society for Optical Engineering*, Vol. 4753, pp. 936–941, 2002. DOI:10.2514/6.2008-2102.

[Panossian06] Panossian, H.: Optimized non-obstructive particle damping treatment for composite honeycomb structures. *47th AIAA/ASME/ASCE/AHS/ASC Structures, Structural Dynamics, and Materials Conference*, 2006. DOI:10.2514/6.2006-2210.

[PatilHiggs17] Patil, D.; Higgs, F.C.: Experimental investigations on the coefficient of restitution for sphere–thin plate elastoplastic impact.

Journal of Tribology, Vol. 140, No. 1, pp. 011406–011406–13, 2017. DOI:10.1115/1.4037212.

[Perzyna66] Perzyna, P.: Fundamental problems in viscoplasticity. *Advances in Applied Mechanics*, Vol. 9, pp. 243–377, 1966. DOI:10.1016/S0065-2156(08)70009-7.

[PopplewellSemercigil89] Popplewell, N.; Semercigil, S.E.: Performance of the bean bag impact damper for a sinusoidal external force. *Journal of Sound and Vibration*, Vol. 133, No. 2, pp. 193–223, 1989. DOI:10.1016/0022-460X(89)90922-X.

[Pöschel05] Pöschel, T.: *Computational Granular Dynamics: Models and Algorithms*. Berlin: Springer, 2005. DOI:10.1007/3-540-27720-X.

[PöschelBrilliantov01] Pöschel, T.; Brilliantov, N.V.: Extremal collision sequences of particles on a line: Optimal transmission of kinetic energy. *Physical Review E*, Vol. 63, No. 2, pp. 1–9, 2001. DOI:10.1103/PhysRevE.63.021505.

[PourtavakoliEtAl16] Pourtavakoli, H.; Parteli, E.J.R.; Pöschel, T.: Granular dampers: Does particle shape matter? *New Journal of Physics*, Vol. 18, No. 7, p. 073049, 2016. DOI:10.1088/1367-2630/18/7/073049.

[ProakisManolakis92] Proakis, J.G.; Manolakis, D.G.: *Digital Signal Processing: Principles, Algorithms, and Applications*. New York: Macmillan, 2. Edn., 1992.

[RomdhaneEtAl13] Romdhane, M.; Bouhaddi, N.; Trigui, M.; Foltête, E.; Haddar, M.: The loss factor experimental characterisation of the non-obstructive particles damping approach. *Mechanical Systems and Signal Processing*, Vol. 38, pp. 585–600, 2013. DOI:10.1016/j.ymssp.2013.02.006.

[RougierEtAl04] Rougier, E.; Munjiza, A.; John, N.W.M.: Numerical comparison of some explicit time integration schemes used in DEM, FEM/DEM and molecular dynamics. *International Journal for Numerical Methods in Engineering*, Vol. 61, No. 6, pp. 856–879, 2004. DOI:10.1002/nme.1092.

[SackEtAl13] Sack, A.; Heckel, M.; Kollmer, J.; Zimber, F.; Pöschel, T.: Energy dissipation in driven granular matter in the absence of gravity. *Physical Review Letters*, Vol. 111, 2013. DOI:10.1103/PhysRevLett.111.018001.

[SackEtAl15] Sack, A.; Heckel, M.; Kollmer, J.E.; Pöschel, T.: Probing the validity of an effective-one-particle description of granular dampers in microgravity. *Granular Matter*, Vol. 17, pp. 73–82, 2015. DOI:10.1007/s10035-014-0539-8.

[Saeki02] Saeki, M.: Impact damping with granular materials in a horizontally vibrating system. *Journal of Sound and Vibration*, Vol. 251, No. 1, pp. 153–161, 2002. DOI:10.1006/JSVI.2001.3985.

[SaluenaEtAl98] Saluena, C.; Esipov, S.E.; Poeschel, T.; Simonian, S.S.: Dissipative properties of granular ensembles. *Proceedings of SPIE Volume 3327, Smart Structures and Materials 1998: Passive Damping and Isolation*, pp. 23–29, 1998. DOI:10.1117/12.310696.

[SanchezCarlevaro11] Sanchez, M.; Carlevaro, M.: Nonlinear dynamic analysis of an optimal particle damper. *Journal of Sound and Vibration*, Vol. 332, 2011. DOI:10.1016/J.JSV.2012.09.042.

[SanchezEtAl12] Sanchez, M.; Rosenthal, G.; Pugnaloni, L.: Universal response of optimal granular damping devices. *Journal of Sound and Vibration*, Vol. 331, No. 20, pp. 4389–4394, 2012. DOI:10.1016/J.JSV.2012.05.001.

[SanchezEtAl14] Sanchez, M.; Carlevaro, C.M.; Pugnaloni, L.: Effect of particle shape and fragmentation on the response of particle dampers. *Journal of Vibration and Control*, Vol. 20, No. 12, pp. 1846–1854, 2014. DOI:10.1177/1077546313480544.

[SanchezPugnaloni11] Sanchez, M.; Pugnaloni, L.: Effective mass overshoot in single degree of freedom mechanical systems with a particle damper. *Journal of Sound and Vibration*, Vol. 330, 2011. DOI:10.1016/J.JSV.2011.07.016.

[SchiehlenEtAl06] Schiehlen, W.; Seifried, R.; Eberhard, P.: Elastoplastic phenomena in multibody impact dynamics. *Computer Methods in Applied Mechanics and Engineering*, Vol. 195, No. 50, pp. 6874–6890, 2006. DOI:10.1016/J.CMA.2005.08.011.

[SchönleEtAl22] Schönle, A.; Gnanasambandham, C.; Eberhard, P.: Broadband damping properties of particle dampers mounted to dynamic structures. *Experimental Mechanics*, 2022. DOI:10.1007/S11340-022-00882-2.

[SchwarzRichardson13] Schwarz, B.; Richardson, M.: Proportional damping from experimental data. *Sound and Vibration*, Vol. 47, No. 6, pp. 14–17, 2013.

[SchwertassekEtAl99] Schwertassek, R.; Wallrapp, O.; Shabana, A.: Flexible multibody simulation and choice of shape functions. *Nonlinear Dynamics*, Vol. 20, No. 4, pp. 361–380, 1999. DOI:10.1023/A:1008314826838.

[Seifried14] Seifried, R.: *Dynamics of Underactuated Multibody Systems: Modeling, Control and Optimal Design*. Cham: Springer, 2014. DOI:10.1007/978-3-319-01228-5.

[SeifriedEtAl10] Seifried, R.; Minamoto, H.; Eberhard, P.: Viscoplastic effects occurring in impacts of aluminum and steel bodies and their influence on

the coefficient of restitution. *Journal of Applied Mechanics*, Vol. 77, No. 4, 2010. DOI:10.1115/1.4000912.

[SemercigilEtAl92] Semercigil, S.E.; Lammers, D.; Ying, Z.: A new tuned vibration absorber for wide-band excitations. *Journal of Sound and Vibration*, Vol. 156, No. 3, pp. 445–459, 1992. DOI:10.1016/0022-460X(92)90738-J.

[SessnerEtAl19] Sessner, V.; Jackstadt, A.; Liebig, W.; Kärger, L.; Weidenmann, K.: Damping characterization of hybrid carbon fiber elastomer metal laminates using experimental and numerical dynamic mechanical analysis. *Journal of Composites Science*, Vol. 3, No. 1, p. 3, 2019. DOI:10.3390/JCS3010003.

[Shabana13] Shabana, A.A.: *Dynamics of Multibody Systems*. Cambridge: Cambridge University Press, 4. Edn., 2013. DOI:10.1017/CBO9781107337213.

[Shabana19] Shabana, A.A.: *Theory of Vibration: An Introduction*. New York: Springer, 3. Edn., 2019. DOI:10.1007/978-1-4612-3976-5.

[ShahEtAl09] Shah, B.; Pillet, D.; Bai, X.M.; Keer, L.; Wang, Q.; Snurr, R.: Construction and characterization of a particle-based thrust damping system. *Journal of Sound and Vibration*, Vol. 326, pp. 489–502, 2009. DOI:10.1016/J.JSV.2009.06.007.

[Simonian95] Simonian, S.S.: Particle beam damper. *Proceedings of SPIE Volume 2445, Smart Structures and Materials 1995: Passive Damping*, pp. 149–160, 1995. DOI:10.1117/12.208884.

[Simonian04] Simonian, S.: Particle damping applications. *Proceedings of 45th AIAA/ASME/ASCE/AHS/ASC Structures, Structural Dynamics & Materials Conference*, 2004. DOI:10.2514/6.2004-1906.

[SkiporBain80] Skipor, E.; Bain, L.J.: Application of impact damping to rotary printing equipment. *Journal of Mechanical Design*, Vol. 102, No. 2, pp. 338–343, 1980. DOI:10.1115/1.3254749.

[SoongCostantinou94] Soong, T.T.; Costantinou, M.C.: *Passive and Active Structural Vibration Control in Civil Engineering*. Vienna: Springer, 1994. DOI:10.1007/978-3-7091-3012-4.

[Souza NetoEtAl08] de Souza Neto, E.A.; Peri, D.; Owen, D.R.J.: *Computational Methods for Plasticity*. Chichester: John Wiley & Sons, 2008. DOI:10.1002/9780470694626.

[Stronge18] Stronge, W.J.: *Impact Mechanics*. Cambridge: Cambridge University Press, 2. Edn., 2018. DOI:10.1017/9781139050227.

[Strutt77] Strutt, J.W.: *The Theory of Sound*. New York: Cambridge University Press, 1877. DOI:10.1017/CBO9781139058087.

[TangEtAl15] Tang, N.; Rongong, J.A.; Tomlinson, G.R.: Nonlinear behaviour of tangled metal wire particle dampers. *International Conference on Structural Engineering Dynamics 2015 (ICEDYN2015)*, 2015.

[TataraMoriwaki82] Tatara, Y.; Moriwaki, N.: Study on impact of equivalent two bodies: Coefficients of restitution of spheres of brass, lead, glass, porcelain and agate, and the material properties. *Bulletin of the Japan Society of Mechanical Engineers*, Vol. 25, No. 202, pp. 631–637, 1982. DOI:10.1299/JSME1958.25.631.

[TerziogluEtAl20] Terzioglu, F.; Rongong, J.A.; Lord, C.E.: The dissipative characteristics of oblate particles in granular dampers. *Proceedings of the XI International Conference on Structural Dynamics*, pp. 4851–4866, 2020. DOI:10.47964/1120.9393.20452.

[TianGai15] Tian, L.; Gai, X.: Wind-induced vibration control of power transmission tower using pounding tuned mass damper. *Journal of Vibroengineering*, Vol. 17, No. 7, pp. 3693–3701, 2015.

[TriguiEtAl13] Trigui, M.; Foltête, E.; Bouhaddi, N.: Prediction of the dynamic response of a plate treated by particle impact damper. *Proceedings of the Institution of Mechanical Engineers, Part C: Journal of Mechanical Engineering Science*, Vol. 228, No. 5, pp. 799–814, 2013. DOI:10.1177/0954406213491907.

[TuleyEtAl10] Tuley, R.; Danby, M.; Shrimpton, J.; Palmer, M.: On the optimal numerical time integration for lagrangian DEM within implicit flow solvers. *Computers and Chemical Engineering*, Vol. 34, No. 6, pp. 886–899, 2010. DOI:10.1016/J.COMPCHEMENG.2009.10.003.

[UrbakhEtAl04] Urbakh, M.; Klafter, J.; Gourdon, D.; Israelachvili, J.: The nonlinear nature of friction. *Nature*, Vol. 430, pp. 525–528, 2004. DOI:10.1038/NATURE02750.

[Verlet67] Verlet, L.: Computer experiments on classical fluids. I. Thermodynamical properties of lennard-jones molecules. *Physical Review*, Vol. 159, No. 1, pp. 98–103, 1967. DOI:10.1103/PHYSREV.159.98.

[WaltonBraun86] Walton, O.R.; Braun, R.L.: Viscosity, granular-temperature, and stress calculations for shearing assemblies of inelastic, frictional disks. *Journal of Rheology*, Vol. 30, No. 5, pp. 949–980, 1986. DOI:10.1122/1.549893.

[WangEtAl15] Wang, X.; Liu, X.; Shan, Y.; He, T.: Design, simulation and experiment of particle dampers attached to a precision instrument in spacecraft. *Journal of Vibroengineering*, Vol. 17, No. 4, pp. 1605–1614, 2015.

[WangEtAl16] Wang, Y.; Liu, B.; Tian, A.; Tang, W.: Experimental and numerical investigations on the performance of particle dampers attached to a primary structure undergoing free vibration in the horizontal and vertical directions. *Journal of Sound and Vibration*, Vol. 371, 2016. DOI:10.1016/J.JSV.2016.01.056.

[WangEtAl17] Wang, W.; Hua, X.; Xiuyong, W.; Chen, Z.; Song, G.: Advanced impact force model for low-speed pounding between viscoelastic materials and steel. *Journal of Engineering Mechanics*, Vol. 143, 2017. DOI:10.1061/(ASCE)EM.1943-7889.0001372.

[WangEtAl19] Wang, Y.; Liu, B.; Tian, A.; Wei, D.; Jiang, X.: Prediction methods for the damping effect of multi-unit particle dampers based on the cyclic iterations of a single-unit particle damper. *Journal of Sound and Vibration*, Vol. 443, pp. 341–361, 2019. DOI:10.1016/J.JSV.2018.10.035.

[WeirTallon05] Weir, G.; Tallon, S.: The coefficient of restitution for normal incident, low velocity particle impacts. *Chemical Engineering Science*, Vol. 60, pp. 3637–3647, 2005. DOI:10.1016/J.CES.2005.01.040.

[WellmannWriggers12] Wellmann, C.; Wriggers, P.: A two-scale model of granular materials. *Computer Methods in Applied Mechanics and Engineering*, Vol. 205-208, pp. 46–58, 2012. DOI:10.1016/J.CMA.2010.12.023.

[WongEtAl09a] Wong, C.; Spencer, A.; Rongong, J.: Effects of enclosure geometry on particle damping performance. *Proceedings of the 50th AIAA/ASME/ASCE/AHS/ASC Structures, Structural Dynamics, and Materials Conference*, 2009. DOI:10.2514/6.2009-2689.

[WongEtAl09b] Wong, C.X.; Daniel, M.C.; Rongong, J.A.: Energy dissipation prediction of particle dampers. *Journal of Sound and Vibration*, Vol. 319, No. 1-2, pp. 91–118, 2009. DOI:10.1016/J.JSV.2008.06.027.

[Wriggers01] Wriggers, P.: *Nonlinear Finite Element Methods*. Berlin: Springer, 2001. DOI:10.1007/978-3-540-71001-1.

[Wriggers06] Wriggers, P.: *Computational Contact Mechanics*. Berlin and Heidelberg: Springer, 2006. DOI:10.1007/978-3-540-32609-0.

[XuEtAl05] Xu, Z.; Wang, M.; Chen, T.: Particle damping for passive vibration suppression: Numerical modelling and experimental investigation. *Journal of Sound and Vibration*, Vol. 279, No. 3, pp. 1097–1120, 2005. DOI:10.1016/J.JSV.2003.11.023.

[Yamada74] Yamada, G.: Vibration damping effect of the impact damper on a piecewise linear mass spring system. *Bulletin of Japan Society of Mechanical Engineers*, Vol. 17, No. 104, pp. 210–217, 1974. DOI:10.1299/JSME1958.17.210.

[YangEtAl05] Yang, M.Y.; Lesieutre, G.A.; Hambric, S.; Koopmann, G.: Development of a design curve for particle impact dampers. *Noise Control Engineering Journal*, Vol. 53, pp. 5–13, 2005. DOI:10.1117/12.540019.

[YaoChen15] Yao, B.; Chen, B.: Investigation on zero-gravity behavior of particle dampers. *Journal of Vibration and Control*, Vol. 21, No. 1, pp. 124–133, 2015. DOI:10.1177/1077546313488157.

[YaoEtAl14] Yao, B.; Chen, Q.; Xiang, H.Y.; Gao, X.: Experimental and theoretical investigation on dynamic properties of tuned particle damper. *International Journal of Mechanical Sciences*, Vol. 80, pp. 122–130, 2014. DOI:10.1016/J.IJMECSCI.2014.01.009.

[YinEtAl17] Yin, Z.; Su, F.; Zhang, H.: Investigation of the energy dissipation of different rheology behaviors in a non-obstructive particle damper. *Powder Technology*, Vol. 321, 2017. DOI:10.1016/J.POWTEC.2017.07.090.

[ZhangEtAl15] Zhang, K.; Chen, T.; Wang, X.; Fang, J.: Rheology behavior and optimal damping effect of granular particles in a non-obstructive particle damper. *Journal of Sound and Vibration*, Vol. 364, 2015. DOI:10.1016/J.JSV.2015.11.006.

[ZhangEtAl17] Zhang, K.; Chen, T.; He, L.: Damping behaviors of granular particles in a vertically vibrated closed container. *Powder Technology*, Vol. 321, pp. 173–179, 2017. DOI:10.1016/J.POWTEC.2017.08.020.

[ZhangEtAl18] Zhang, K.; Yanhui, X.; Chen, T.; Ma, Z.: Experimental studies of tuned particle damper: Design and characterization. *Mechanical Systems and Signal Processing*, Vol. 99, pp. 219–228, 2018. DOI:10.1016/J.YMSSP.2017.06.007.

[Zohdi04] Zohdi, T.I.: Charge–induced clustering in multifield particulate flows. *International Journal for Numerical Methods in Engineering*, Vol. 62, No. 7, pp. 870–898, 2004. DOI:10.1002/NME.1194.